THESIS FOR THE DEGREE OF LICENTIATE OF ENGINEERING

Electrochemical Capacitors for Miniaturized Self-powered Systems

QI LI

Department of Microtechnology and Nanoscience

CHALMERS UNIVERSITY OF TECHNOLOGY

Gothenburg, Sweden 2018

Electrochemical Capacitors for Miniaturized Self-powered Systems
QI LI

ISSN 1652-0769
Technical Report MC2-403

Chalmers University of Technology
Department of Microtechnology and Nanoscience - MC2
Electronics Materials and Systems Laboratory
Micro- and Nanosystems Group
SE-412 96 Gothenburg
Sweden
Telephone + 46 (0)31-772 1000

Printed by Chalmers Reproservice
Gothenburg, Sweden 2018

Dedicated to my parents and grandparents

Electrochemical Capacitors for Miniaturized Self-powered Systems

QI LI

Department of Microtechnology and Nanoscience - MC2
Chalmers University of Technology

Abstract

Miniaturized self-powered systems with harvest-store-use architectures have been recognized as a key enabler to the internet-of-things (IoT), and further the internet-of-everything (IoE), 5G communication and tactile internet. Electrochemical capacitors (ECs), also known as supercapacitors, are promoted to be the energy storage component in such systems, because of their advantages such as an almost limitless cycle life that is ideal for the vision of “fit-and-forget” maintenance-free networks. Moreover, ECs are able to undertake tasks beyond energy storage. For example, high-frequency ECs can potentially replace the bulky electrolytic capacitors as AC line filters, with benefits in sizing down the circuitry boards and thus constructing compact systems which are pursued by the IoT technology.

Bringing the IoT high-level requirements down to the device-level specifications, challenges to ECs are identified in different aspects, including device electrochemical performance, and device encapsulation/integration. Regarding the performance, challenges exist in (1) improving the energy density, (2) maximizing the operating voltage limit, (3) widening the working temperature range, (4) minimizing the self-discharge and leakage current, and (5) enhancing the frequency response property. Regarding the encapsulation and integration aspect, challenges exist in device design and fabrication. Novel encapsulation and integration EC concepts are thus appreciated to be compatible with the surface mount technology, allow for convenient adaption in the form factor and arbitrary choice of the EC materials (electrodes, electrolytes and separators). Moreover, the EC materials should be durable under the ambient conditions that occur during the encapsulation and integration processes, such as high-temperature exposure for the reflow soldering technique.

The thesis research work addresses the device performance challenges. Specifically, the use of redox electrolytes is promoted for improving the energy density of ECs towards a battery-level, and at the same time keeping the capacitor-level power capability and cycling stability. With a redox-active electrolyte KBr, hybrid devices combining the features of both batteries and ECs are constructed, and a 1.9 V maximum operating voltage is achieved in the aqueous system. Furthermore, voltage- and history-dependent behaviors are revealed, reminding the complexity of hybrid systems.

To explore the extreme high-temperature performance, a special measurement setup is customized and an EMImAc (1-Ethyl-3-methylimidazolium acetate) ionic liquid (IL) electrolyte is employed to enable an operation at a maximum of 150 °C. It is observed that the energy and power densities at high temperatures may not be sacrificed when decreasing the operating voltage limit, therefore it is proposed that for neat IL-based ECs, a strategy of trading the voltage limit for gaining stability at extreme high-temperatures can be considered.

With a graphite and carbon nanotubes hybrid material, it is demonstrated that the self-discharge and leakage current can be suppressed by employing a gel polymer electrolyte. Using the same electrode material, high-frequency ECs that are suitable for AC line filtering tasks are fabricated. The working frequency range is up to kHz with a state-of-art level areal (1.38 mF cm^{-2}) and volumetric capacitances (345 mF cm^{-3}), benefiting from a possible covalent bonding between graphite substrate and the CVD grown CNTs.

Not limited to the above research findings, this thesis has critically reviewed and summarized the general strategies and methods to address all the identified challenges to ECs for their application in miniaturized self-powered systems.

Keywords

Electrochemical capacitors; Energy storage; AC line filters; Electrode materials; Electrolyte materials; Miniaturized self-powered systems

Appended publications related to this thesis

[Paper I] **Q. Li**, M. Haque, V. Kuzmenko, N. Ramani, P. Lundgren, A. D. Smith, P. Enoksson, Redox enhanced energy storage in an aqueous high-voltage electrochemical capacitor with a potassium bromide electrolyte, *Journal of Power Sources*, 348 (2017) 219-228.

[Paper II] M. Haque, **Q. Li**, V. Kuzmenko, E. Köhler, P. Lundgren, P. Enoksson, Thermal influence on the electrochemical behavior of a supercapacitor containing an ionic liquid electrolyte, *Electrochimica Acta*, 263 (2018) 249-260.

[Paper III] **Q. Li***, S. Sun*, A. D. Smith, P. Lundgren, Y. Fu, P. Su, T. Xu, L. Ye, L. Sun, J. Liu, P. Enoksson, Compact and low loss electrochemical capacitors using a graphite / carbon nanotube hybrid material for miniaturized systems, submitted. (*Co-first author)

Other publications related to the author not included in the thesis

[01] G. Li, **Q. Li**, L. Li, J. Fan, Q. Ge, D. Xie, J. Zheng, G. Li, Surface element segregation and electrical conductivity of lithium layered transition-metal oxide cathode materials, *Applied Surface Science*, 427 (2018) 226-232.

[02] A. D. Smith, **Q. Li**, A. Anderson, A. Vyas, V. Kuzmenko, M. Haque, H. Staaf, P. Lundgren, P. Enoksson, Toward CMOS compatible wafer-scale fabrication of carbon-based microsupercapacitors for IoT, *Journal of Physics: Conference Series*, 1052 (2018), 012143.

[03] M. Haque, **Q. Li**, V. Kuzmenko, A. D. Smith, P. Enoksson, Ionic liquid electrolyte for supercapacitor with high temperature compatibility, *Journal of Physics: Conference Series,* 922 (2017) 012011.

[04] **Q. Li**, A. D. Smith, M. Haque, A. Vyas, V. Kuzmenko, P. Lundgren, P. Enoksson, Graphite paper/carbon nanotube composite: A potential supercapacitor electrode for powering microsystem technology*, Journal of Physics: Conference Series,* 922 (2017) 012014.

[05] D. Xie, G. Li, **Q. Li**, C. Fu, J. Fan, L. Li, Improved cycling stability of cobalt-free Li-rich oxides with a stable interface by dual doping, *Electrochimica Acta*, 196 (2016) 505-516

[06] Y. Zhang, L. Li, **Q. Li**, J. Fan, J. Zheng, G. Li, Smart solution chemistry to Sn-containing intermetallic compounds through a self-disproportionation process, *Chemistry - A European Journal*, 22 (2016) 14196-14204.

[07] E. Köhler, H. Staaf, V. Kuzmenko, **Q. Li**, P. Enoksson, Flexible supercapacitor for high temperature applications, *PRiME* (2016) 966.

[08] Y. Wang, L. Li, X. Huang, **Q. Li**, G. Li, New insights into fluorinated TiO_2 (brookite, anatase and rutile) nanoparticles as efficient photocatalytic redox catalysts, *RSC Advances*, 5 (2015) 34302-34313.

[09] **Q. Li**, G. Li, C. Fu, D. Luo, J. Fan, D. Xie, L. Li, Balancing stability and specific energy in Li-rich cathodes for lithium ion batteries: a case study of a novel Li-Mn-Ni-Co oxide, *Journal of Materials Chemistry A*, 3 (2015) 10592-10602.

[10] **Q. Li**, G. Li, C. Fu, D. Luo, J. Fan, J. Zheng, D. Xie, L. Li, A study on storage characteristics of pristine Li-rich layered oxide $Li_{1.2}Mn_{0.54}Co_{0.13}Ni_{0.13}O_2$: effect of storage temperature and duration, *Electrochimica Acta*, 154 (2015) 249-258.

[11] D. Luo, G. Li, C. Fu, J. Zheng, J. Fan, **Q. Li**, L. Li, $LiMO_2$ (M = Mn, Co, Ni) hexagonal sheets with (101) facets for ultrafast charging-discharging lithium ion batteries, *Journal of Power Sources*, 276 (2015) 238-246.

[12] J. Fan, G. Li, D. Luo, C. Fu, **Q. Li**, J. Zheng, L. Li, Hydrothermal-assisted synthesis of Li-rich layered oxide microspheres with high capacity and superior rate-capability as a cathode for lithium-ion batteries, *Electrochimica Acta*, 173 (2015) 7-16.

[13] Y. Zhang, L. Li, J. Zheng, **Q. Li**, Y. Zuo, E. Yang, G. Li, Two-step grain-growth kinetics of sub-7 nm SnO_2 nanocrystal under hydrothermal condition, *The Journal of Physical Chemistry C*, 119 (2015) 19505-19512.

[14] S. Chen, L. Li, W. Hu, X. Huang, **Q. Li**, Y. Xu, Y. Zuo, G. Li, Anchoring high-concentration oxygen vacancies at interfaces of CeO_{2-x}/Cu toward enhanced activity for preferential CO oxidation, *ACS Applied Materials & Interfaces*, 7 (2015) 22999-23007.

[15] **Q. Li**, G. Li, C. Fu, D. Luo, J. Fan, L. Li, K^+-doped $Li_{1.2}Mn_{0.54}Co_{0.13}Ni_{0.13}O_2$: a novel cathode material with an enhanced cycling stability for lithium-ion batteries, *ACS Applied Materials & Interfaces*, 6 (2014) 10330-10341.
[16] D. Luo, G. Li, C. Fu, J. Zheng, J. Fan, **Q. Li**, L. Li, A new spinel-layered Li-rich microsphere as a high-rate cathode material for Li-ion batteries, *Advanced Energy Materials*, 4 (2014) 1400062.
[17] C. Fu, G. Li, D. Luo, **Q. Li**, J. Fan, L. Li, Nickel-rich layered microspheres cathodes: lithium/nickel disordering and electrochemical performance, *ACS Applied Materials & Interfaces*, 6 (2014) 15822-15831.

Conference contributions

[01] **Q. Li**, A. D. Smith, A. Vyas, F. Cornaglia, A. Anderson, M. Haque, V. Kuzmenko, E. Khöler, P. Enoksson, Giving micro-supercapacitor fingers?, *29th Micromechanics and Microsystems Europe workshop 2018*, August 26-29, Bratislava, Slovakia.
[02] **Q. Li**, Supercapacitors for miniaturized self-powered systems, *Supercapacitor: Store for the Future 2018*, June 11-13, Gothenburg, Sweden.
[03] **Q. Li**, A. D. Smith, P. Lundgren, P. Enoksson, Electrochemical capacitors as AC line filters for miniaturized system, *Micronano System Workshop MSW 2018*, May 13-18, Espoo, Finland.
[04] **Q. Li**, A. D. Smith, M. Haque, V. Kuzmenko, E. Köhler, H. Staaf, A. Vyas, P. Lundgren, P. Enoksson, A carbon based high frequency electrochemical capacitor for miniaturized smart systems, *MRS Spring Meeting 2018*, April 2-6, Arizona, United States.
[05] **Q. Li**, A. D. Smith, M. Haque, V. Kuzmenko, P. Lundgren, P. Enoksson, High voltage aqueous asymmetric supercapacitor with thin film MnO_2 and carbon nanotube electrodes, *Advanced Energy Materials 2017*, September 11-13, Surrey, United Kingdom.
[06] **Q. Li**, A. D. Smith, M. Haque, A. Vyas, V. Kuzmenko, P. Lundgren, P. Enoksson, Graphite paper/carbon nanotube composite: A potential supercapacitor electrode for powering microsystem technology, *28th Micromechanics and Microsystems Europe workshop 2017*, August 23-25, Uppsala, Sweden.
[07] **Q. Li**, M. Haque, V. Kuzmenko, N. Ramani, P. Lundgren, A. D. Smith, P. Enoksson, Redox enhanced supercapacitor with an aqueous potassium bromide electrolyte, *smart-MEMPHIS Summer School 2017*, June 26-28, Valletta, Malta.
[08] **Q. Li**, V. Kuzmenko, M. Haque, P. Lundgren, E. Khöler, H. Staaf, P. Enoksson, Nanocomposite materials for miniaturized supercapacitors, *International Conference and Exhibition on Integration Issues of Miniaturized Systems 2017*, March 8-9, Cork, Ireland.
[09] **Q. Li**, V. Kuzmenko, M. Haque, P. Lundgren, P. Enoksson, Freestanding 3D nano structured composite material with improved capacitive performance, *Nature Conference on Materials for Energy 2016*, June 11-14, Wuhan, China.

ACKNOWLEDGEMENTS

It has been an amazing experience to me coming a long way to Sweden and starting my PhD at Chalmers. For that, I would like to address my sincere thanks to my main supervisor Prof. Peter Enoksson and co-supervisor Prof. Per Lundgren for taking me into the Micro- and Nanosystems Group. I truly appreciate your trust and guidance throughout my research to build up my knowledge in electrochemical capacitors from almost nothing! Many thanks to Volodymyr Kuzmenko and Anderson D. Smith who also supervise my work. Thank you for scrutinizing the papers and all the good advice!

Thanks to my colleagues Mazharul Haque, Agin Vyas, Elof Khöler, Henrik Staaf, Sadia Farjana, Amir Ghaderi, and those who just graduated from the group Markus Frank, Amin Saleem and Sofia Rahiminejad. Thank you for creating such a nice atmosphere to work with!

Thanks to the EMSL laboratory, Nanofabrication laboratory and MC2 department for the administration and support for my research and study. Special thanks to the EU Horizon 2020 smart-MEMPHIS project for the financial support, and the project consortium for all the inspiring meetings!

I would also like to thank my master program supervisors Prof. Guangshe Li and Prof. Liping Li who are now working at Jilin University, for your continuous care and advice!

Finally, thanks to all my friends for the happy hours. Of course, deepest gratitude to my family for your endless support and understanding!

Göteborg, October 2018

Qi Li

李[illegible]

CONTENTS

Abstract i

Appended publications related to this thesis iii

Acknowledgements v

Contents vii

1 Introduction 1

1.1 The internet of things (IoT) and self-powered systems 1

1.2 Batteries and electrochemical capacitors (ECs) 2

1.3 Challenges to ECs for miniaturized self-powered systems 6

1.4 Scope of thesis 8

2 Fundamentals of electrochemical capacitors 9

2.1 Taxonomy 9

2.2 Key performance metrics 13

2.3 Electrochemical capacitor components 16

3 Device performance challenges 23

3.1 Towards high energy with high power and long cycle life 23

3.2 Towards high operating voltage limit 34

3.3 Towards extreme temperature operation 35

3.4 Towards slow self-discharge and low leakage current 41

3.5 Towards high-frequency response 45

4 Encapsulation and integration challenges 49

4.1 Common COTS electrochemical capacitor configurations 49

4.2 Design considerations for system miniaturization 50

4.3 Unconventional electrochemical capacitors 52

5 Conclusions and future work 53

5.1 Conclusions 53

5.2 Future work 54

6 References 55

1 INTRODUCTION

1.1 The internet of things (IoT) and self-powered systems

Over years, the concept of the internet of things (IoT) has been one of the most common buzzwords in technology circles, becoming the driving force for research innovations in electronics, radio frequency platforms, and system integration. The paradigm of the IoT capitalizes on gaining the identity of objects and environment belonging to our daily life. By means of the internet, objects are characterized by functionalities of self-awareness and interaction with surrounding space to perform data elaboration locally [1]. For example, a *smart* thermostat is a piece of IoT technology. The thermostat learns your family's routines and automatically adjusts the temperature based on when you are at home or away, awake or asleep, feeling hot or cold, to make your house more efficient and help you save on heating and cooling bills. The mobile app allows you editing schedules, changing the temperature away from home, and even receive alerts when it looks like something has gone wrong with your heating or cooling system. The full picture of IoT is far more complex, with applications ranging from home appliance to industrial automation and more.

The implementation of IoT relies on *smart* devices, meaning they collect data locally, perform elaboration and communicate within a network. The number of devices demanded for fulfilling IoT needs is enormous - it is predicted that by 2020 more than 50 billion "things" will be connected to the cloud, i.e. software and services that run on the internet [1, 2] (Figure 1), which could not be done without device miniaturization and densification of functionalities. As IoT massively relies on pervasive wireless technology for communicating, the aspect of power availability and consumption is particularly critical. One solution is to develop ultra-low-power (ULP) electronics, while still using batteries as an energy source, for a prolonged service life of the device/system. However, self-powered systems [3, 4] relying on energy harvesters that transduce environmental energy (ambient light, mechanical vibrations, thermal and RF energy) into electricity provide a more promising solution for real maintenance-free / fit-and-forget networks.

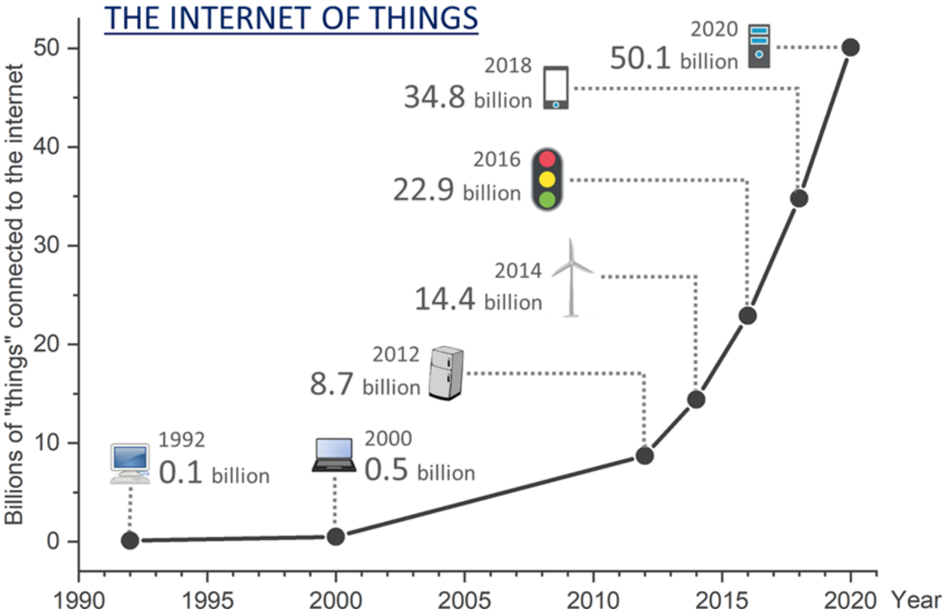

Figure 1. Growth dynamics in the IoT field.

Two different system architectures have been adopted for constructing self-powered systems, i.e. harvest-use and harvest-store-use [4] (Figure 2). The former directly utilizes the energy from an energy harvester for powering the electronics without going through an energy storage device (Figure 2a). It could be cost- and energy- efficient, however, this concept is only applicable when the output power is sufficiently higher than the minimum requirement of the electronics, and the energy harvester must be working continuously to keep the system alive. Therefore, the harvest-use mode has only a narrow range of applications and a limited choice of energy harvester type/size. Comparably, when incorporating an energy storage device, a harvest-store-use self-powered system allows a much greater freedom in selecting energy harvesters. It also improves the systems' quality of service, since the storage device could be used either for storing surplus energy when the harvested energy is more than its current usage, or for accumulating the electricity when the magnitude of the direct output is smaller than needed (Figure 2b). This thesis primarily focuses on the energy storage solutions for miniaturized self-powered systems with the harvest-store-use architecture.

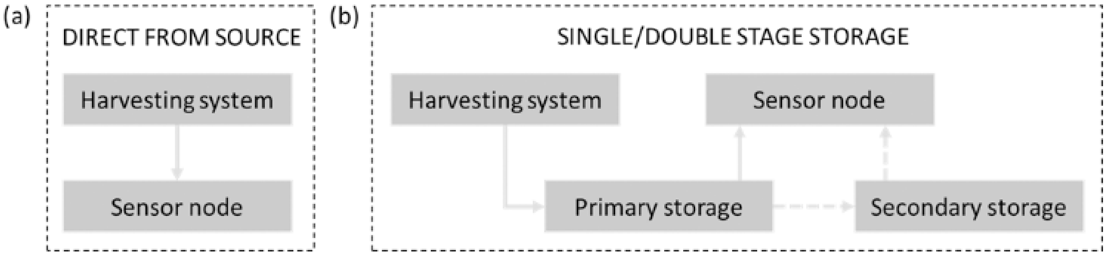

Figure 2. Energy harvesting architectures (a) without and (b) with storage capability [4].

1.2 Batteries and electrochemical capacitors (ECs)

1.2.1 Mechanisms and general performances

Batteries and electrochemical capacitors (ECs) (also called supercapacitors) are the two sophisticated types of energy storage devices which have been used in various self-powered system prototypes [5]. Both devices consist of two electrodes in contact with an electrolyte solution, and the electrodes are usually separated by a porous membrane (separator) to prevent short circuit. Despite similar constructions, the performance metrics (Table 1) is rather different. Noticeably, ECs could be charged in short time, exhibit high power pulse capability and significantly longer cycle/service life, while batteries have a higher voltage and specific energy. The performance differences originate from their different storage mechanisms.

Table 1. Performance metrics of typical ECs and lithium-ion batteries.

	Electrochemical capacitors	**Lithium-ion batteries**
Charge time	1 - 10 s	10 - 60 min
Cycle life	1 million or 30,000 h	500 and higher
Cell voltage	2.3 to 2.75 V	3.6 V nominal
Specific energy (Wh kg^{-1})	5 (typical)	120 - 240
Specific power (W kg^{-1})	Up to 10 000	1 000 - 3 000
Cost per kWh	\$10 000 (typical)	\$250 - \$1 000 (large system)
Service life (industrial)	10 to 15 years	5 to 10 years
Charge temperature	-40 to 65 °C	0 to 45°C
Discharge temperature	-40 to 65 °C	-20 to 60°C

1.2.1.1 Batteries

Batteries store energy obtained from chemical Faradaic reactions at the anode (negative electrode) and cathode (positive electrode). Commonly, Faradaic processes involve electron transfer (1-3 participating electrons per atom or molecule) across electrode surface, which produces chemical state changes in the electroactive materials. The change of chemical states (phase or valence) can be destructive to the material, therefore the cycle life of a battery is normally limited to hundreds of cycles under deep operation. The nature of a Faradaic process also diminishes the power density and lowers the limit of working temperature of a battery, as the redox reactions / phase transformations / ion intercalations are diffusion controlled processes which have slower kinetics compared to non-Faradaic processes such as in typical ECs. The significant benefit of Faradaic processes is an improved energy density (a product of voltage and the amount of charge). Due to high electron density involved in energy storage, a big amount of charges is stored, at a relatively high voltage (up to 5 V vs. Li metal).

The voltage of a battery is defined by the thermodynamics of the involved redox reaction or phase transformation. As a result, a plateau exists on a charge and discharge curve under constant current operation. Because of the polarization caused by the internal resistances of electrolyte and interfaces between components, a potential difference between the charge and discharge curve plateaus is always inevitable. A typical battery curve under constant current operation is shown in Figure 3a. The coulombic efficiency (a ratio of the amount of charge released during discharging process to that being stored during charging) of batteries is extremely high (up to 99.9%), however, since energy is a product of capacity and voltage, the energy efficiency (a ratio of discharged energy to charged energy) is relatively low due to the potential difference of the charge and discharge plateaus. For unstable battery structures, discharge plateau decays over time [6], and polarization increases the gap which exaggerates the problem.

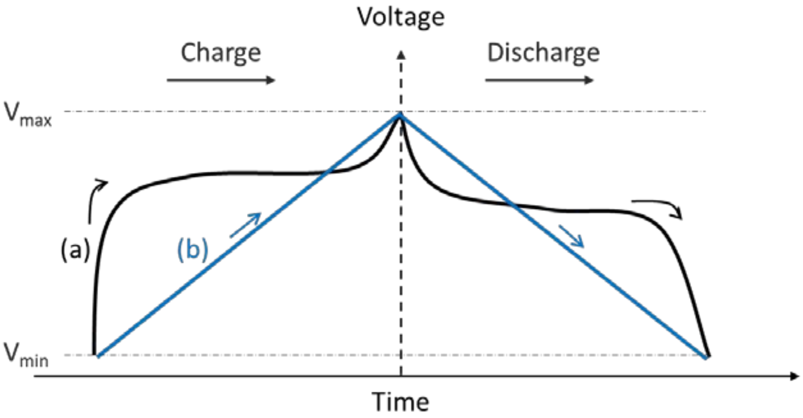

Figure 3. Charging/discharging curves of (a) batteries and (b) ECs.

1.2.1.2 Electrochemical capacitors

In ECs, energy may not be delivered via redox reactions. By orientation of electrolyte ions at the electrode/electrolyte interface, electrical double layers (EDLs) are formed and released, and such ECs are called electrical double layer capacitors (EDLCs). The storage mechanism of EDLCs is driven by non-Faradaic physical processes, involving no electron transfer across electrode/electrolyte interface. Therefore, the aforementioned issues associated with batteries’ Faradaic process nature are overcome in the case of EDLCs, allowing high power density, wide working temperature, and almost limitless cycle life. However, the energy density of EDLCs is low because only 0.18 electrons per carbon atom [7] are involved in energy storage at relatively low voltages.

Different from battery curves, the charge/discharge profile of ECs are linear (Figure 3b). With a simple physical energy storage mechanism of electrostatic adsorption at the electrode/electrolyte interface, the charge/discharge curves of EDLCs are symmetric. Therefore, both the coulombic and energy efficiencies of EDLCs are high.

Besides EDL storage mechanism, some ECs use fast, reversible redox reactions at the surface of active materials (e.g. RuO_2, Fe_3O_4, MnO_2), thus defining what is called the *pseudocapacitive* behavior, and such devices are *pseudocapacitors*. Pseudocapacitors capitalize multi-electron redox reactions, therefore, their energy density exceeds that of EDLCs, with a certain compromise in the cycling stability [8]. It should be noted that the prefix “pseudo” herein means “not actually but having the appearance of”. Therefore, the term “pseudocapacitance” describe the properties of an electrode that has a capacitive behavior reflected into the linear charge/discharge curves under constant current operation (Figure 3b) [9-11]. Although the term definition is clear, many battery-type materials such as $Ni(OH)_2$ have been reported in the literature as pseudocapacitors despite exhibiting Faradaic behavior (plateau charge/discharge curves). The correct understanding and use of the “capacitance” concept is especially important when taking practical applications into account.

1.2.2 Aspects of application in miniaturized self-powered systems

As determined by their respective storage mechanisms, the electrochemical signatures of batteries and ECs are rather different. When employed in the miniaturized self-powered systems, the signatures are translated into pros or cons in various aspects.

The lifespan of an energy storage device in a system is closely related to how often a maintenance work needs to be performed to renew the storage. In this case, the almost limitless cycle life of ECs eliminates storage device being the bottleneck of a system service life, while the substantially shorter cycle life of batteries implies frequent maintenance work, which can be problematic (e.g. when a sensor node is implanted at the hardly reachable locations).

The signature of charge/discharge curves also determines how convenient it is to integrate batteries and ECs as a storage device into a system. A significant drawback of using batteries is the need for a maximum power point tracking (MPPT) component to allow a battery to be charged at a relatively fast speed [12]. Moreover, since batteries have a charging voltage plateau (as shown in Figure 3a) at a specified voltage (e.g. 3.7 V for a $LiCoO_2$ lithium-ion battery), a voltage converter is thus also needed together with MPPT. The charging requirements complicate the power management unit (PMU) design, increase energy loss through MPPT and converter and thus increase the price and size of the system. By contrast, ECs can be charged from 0 V with an energy harvester by trickle current without impairing their long-term stability [4]. Therefore, MPPT and converters can possibly be eliminated, which would simplify the circuitry, minimize energy loss, lower the cost and reduce the size of systems.

A more comprehensive “translation” to implicative benefits of employing ECs in the miniaturized self-powered systems is summarized in Table 2. In short, ECs show more advantages than batteries, thus the thesis promotes ECs as a suitable energy storage device for miniaturized self-powered systems.

Table 2. EC features and their implicative benefits when used in miniaturized self-powered systems.

Advantageous features	Implicative benefits for self-powered systems
Long cycle life	Eliminating the need for replacing batteries; Making maintenance-free systems.
High power density	Effectively absorbing the intermittent energy pulse from energy harvesters (whose output is often pulse-like); Releasing burst energy (depending on application e.g. RF transmitting).
High charge/discharge energy efficiency	Minimizing energy loss during energy conversion.
Linear charging curve	Indicating state-of-charge; Allowing for easy behavior prediction.
Can be charged from 0 V	Allowing for trickle charging; Simplifying charging circuitry, and converter-less design minimizing energy loss.
Wide temperature tolerance range	Being suitable for harsh environment applications.
Function beyond storing energy	Potentially replacing conventional capacitors e.g. electrolytic smoothing capacitors to size down the system.

1.2.3 Type of functions of electrochemical capacitors

Perceiving EC as a “capacitor”, the possible functions of ECs are far beyond just storing electricity. ECs should follow electrical responses that a capacitor is supposed to display, that is the current leads voltage by 90° in AC circuits. The property of an ideal capacitor can be presented in a waveform diagram and phasor diagram in Figure 4, compared to those of resistors and inductors.

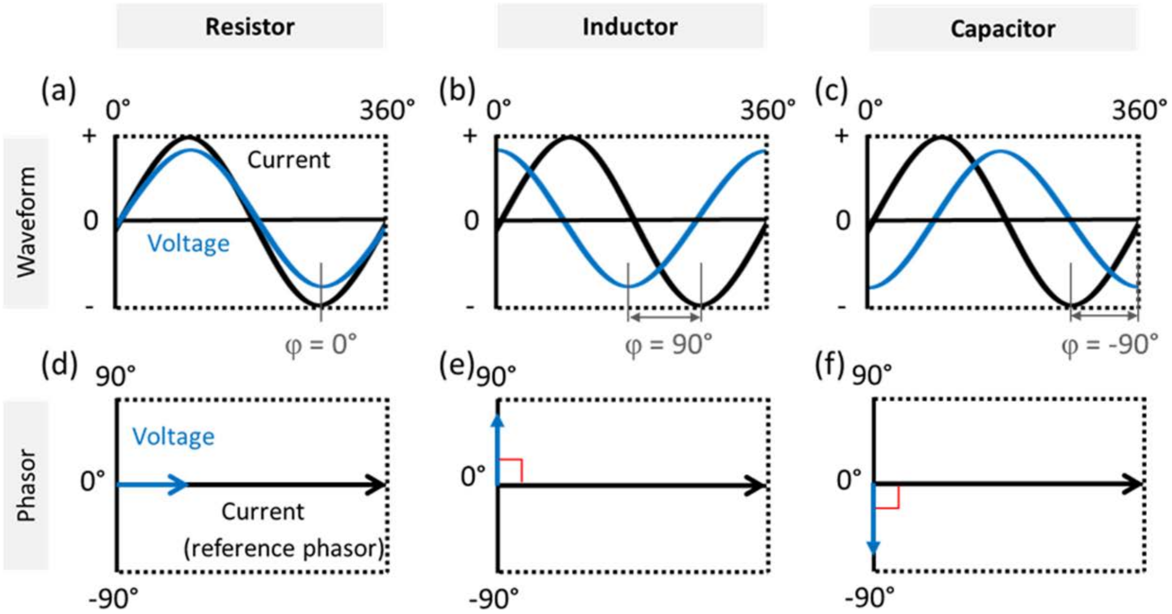

Figure 4. Waveform and phasor diagrams of resistors (a, d), inductors (b, e) and capacitors (c, f).

Capacitors are used in virtually every area of electronics, and they perform a variety of tasks**,** including

- Storing energy;
- Buffering batteries;
- AC line filtering;
- Signal/RF coupling and decoupling;
- Timing.

In principle, ECs could undertake all the tasks, however, for the signal/RF coupling and decoupling purposes, ECs may suffer from a lack of sufficient frequency response property; and for timing, although ECs are capable in terms of performance (linear charge/discharge that indicates the state-of-charge, e.g. in a wirelessly powered implantable pacemaker, a capacitor is used to regulate the pacing rhythm [13]), there is no strong motivation of using ECs. Considering the state-of-art EC technology and its possible developing trend confined by the energy storage physics, as well as the benefit of using ECs instead of conventional capacitors, ECs are preferable to be employed for the first three tasks. Using ECs as an energy storage device is relatively straightforward, as ECs were first invented for such purpose and have greater energy density than normal capacitors. The following texts elaborate the two important types of functions beyond energy storage and their connection to miniaturized self-powered systems for IoT.

Buffering batteries

Capacitors for this application are called *hold up capacitors*. Hold up capacitors are used in parallel with batteries. The charge stored in the capacitors is released to provide power for a short time, thus buffering transient current surges on batteries and extending battery life. In the IoT regime, the buffer capacitor is not uncommon. Self-powered systems usually use low power energy source (e.g. energy harvester with a small battery), but need to support peak power loads for the purpose of RF transmissions, data acquisition, storage, micro-controller start-up, etc. The peak power (current) can be significantly higher than that a battery can handle. In this case, hold-up capacitors are needed. Using ECs instead of conventional capacitors reduces the size of the system because of ECs' advantage in energy density.

AC line filtering

The output of many energy harvesters is alternating signals while electronics works with direct current, therefore rectifying circuits are usually required to convert AC to DC. As shown in Figure 5, assuming the input signal is sinusoidal at a frequency *f*, the resulting signal after a full wave bridge rectifier is a ripple wave with all the negative parts converted to the positive, ranging from 0 to +*V* at a frequency of

$2f$. When inserting an AC line filter, the signal is smoothed out producing a relatively stable ripple voltage. The bigger capacitance the filter has, the smoother signal is obtained, as the ripple voltage ΔV_{Ripple} is defined as

$$\Delta V_{Ripple} = \frac{I_L}{2f \cdot C} \qquad \text{Equation (1)}$$

where I_L is the load current required for the application, f is the frequency of input signal and C is the capacitance of the smoothing capacitor. Because ECs store enormously more charges per weight and volume than conventional capacitors, using ECs for such application is beneficial for constructing compact systems that are pursued by the IoT technology. Note that it is important to select the right type of EC for such application. Typical ECs with porous carbon electrodes work at a low frequency of 1 Hz and below. When being operated at a frequency more than the value, the electrical response deviates from the capacitive behavior. Therefore, there is a growing interest to develop high-frequency ECs that can work up to kHz level. This type of ECs is under investigation in this thesis (Paper III).

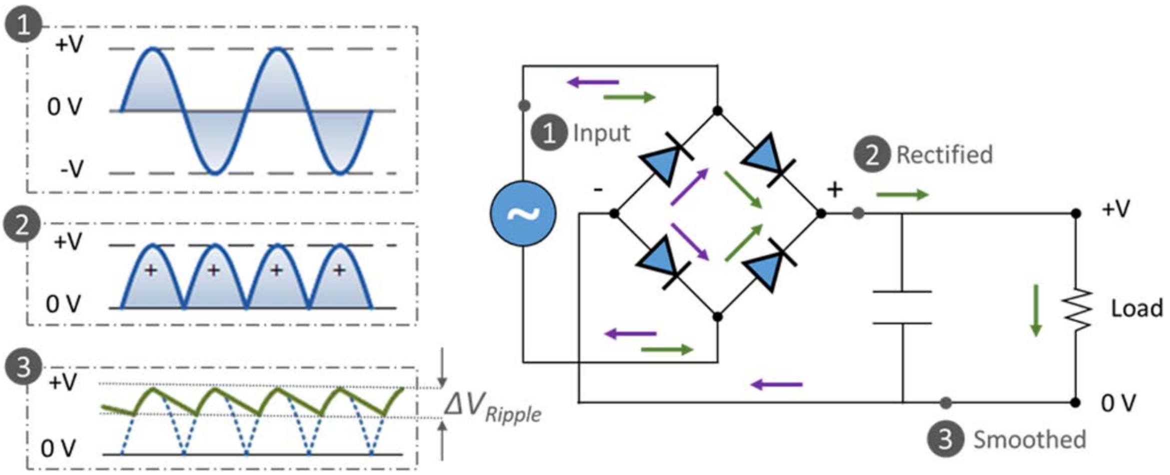

Figure 5. Circuit diagram of rectifying and smoothing circuit, and waveforms at different stages.

1.3 Challenges to ECs for miniaturized self-powered systems

The challenges to ECs for their application in miniaturized self-powered systems are two-folded, i.e. ECs have to meet requirements on device performance, and at the same time to be integratable with heterogeneous components in order to construct a system.

1.3.1 Device performance

Device performance of ECs must satisfy the requirements set by a system design. The system design may put restraints on a number of metrics, including

- Capacitance
- Energy and power
- Equivalent series resistance
- Maximum operating voltage
- Cycle life
- Working temperature range
- Self-discharge and leakage current
- Time constant

Improving the energy density of ECs to a battery level is always of great interest in the academia and industry. The challenge in this regard is to gain the increase in energy while keeping a high power density as well as a long cycle life. The energy enhancement generally relies on an increase in capacitance or maximum operating voltage. Considering the applications in wireless sensor networks, the ECs should be durable with harsh environmental conditions such as extreme temperatures. Moreover, in miniaturized self-powered systems where the amount of the harvested energy can be very small, the self-discharge and leakage current, which characterize an energy loss property of ECs, should be minimized. Leakage current also directly links to the charging behavior at an extremely low current input. Low current charging is a typical feature in miniaturized systems as the current output from an energy harvester could be as low as a few µA. When leakage current is comparable to the charging current, the charging curve deviates from linearity, which potentially deprives ECs of the claimed benefits in Table 2.

1.3.2 Device encapsulation and integration

The second fold of the challenges to ECs for their application in miniaturized self-powered systems lies in the encapsulation and integration aspects. Hermetic encapsulation of the EC materials (electrodes, electrolytes, and separators) should isolate the core materials from ambient humidity and atmosphere, which enables leakage-proof devices with high electrical insulation and good resistance to environmental extremes, thus guaranteeing a long-term operation stability.

Similar to batteries, common commercial off-the-shelf (COTS) ECs can be found encapsulated in coin-, cylindrical-, prismatic- and pouch-type cell configurations. These COTS EC encapsulation concepts are generally advantageous in terms of scaling up to fabricate large EC packs, while drawbacks arise when packaging miniaturized ECs. For example, miniaturization of coin cells results in an increased percentage of “dead” weight and volume from the metal packaging; manufacturing small size cylindrical cells may only allow for axial type of configuration due to increased risk of short-circuiting when arranging the two terminals on the same base plane of cylinder; similar issues exist for prismatic and pouch cell configurations.

Self-powered systems leverage a variety of heterogeneous technologies, spanning from energy harvesting, storage, sensing/actuating to wireless/RF transmission. Bringing an encapsulated EC to the next application level, one should consider its integration with other components to construct a functional system. The existing COTS ECs have a limited choice of the positioning of positive and negative terminals, therefore the system layout design is restricted and space efficiency may not be optimized. New EC encapsulation and integration concepts that allow for easy geometry tailoring and arbitrary assigning the location of terminals is therefore desired for miniaturization and seamless integration.

Moreover, many concurrent encapsulation and packaging techniques for printed circuit board (PCB) electronics, such as reflow soldering [14], are high temperature (HT) processes, which requires the EC to withstand elevated temperature (more than 100 °C) for a certain period of time [15]. Therefore, high-temperature durability is of great interest.

In a nutshell, the challenges to ECs’ application in miniaturized systems can be summarized below.

Device performance challenges

- Improving energy density towards battery-level while keeping high power and long cycling stability
- Increasing the maximum operating voltage limit
- Achieving high power under operations at extreme low-temperature, and high stability at extreme high-temperature
- Minimizing self-discharge and leakage current
- Enhancing frequency response property with a high areal capacitance

Device encapsulation/integration challenges

- Developing new encapsulation and integration concepts allowing for surface mounting with a low profile and compatibility with a wide choice of materials
- Enhancing the tolerance to high-temperature exposure that is required for reflow soldering and/or other encapsulation and integration methods

1.4 Scope of thesis

The pervasiveness of IoT requires miniaturized self-powered systems, and EC technology is believed to be a suitable and important part of these systems. Bringing IoT high-level requirements down to the device-level specifications, challenges to ECs can be identified in various aspects. It is noteworthy that there is not a single perfect EC device that displays superior performance in all metrics discussed above. Different application specifications stress on one or just a few properties. Therefore, the development of ECs for IoT falls within the fences of addressing the most critical issue, while keeping other aspects satisfactory enough for the system.

This thesis research work focuses on the device performance challenges which cover the aspects of improving energy density using a redox-active KBr electrolyte (Paper I), widening working temperature range with an ionic liquid electrolyte (Paper II) and achieving high frequency response as well as reducing loss through self-discharge and leakage current by employing a graphite/carbon nanotubes material (Paper III). Not limited to these, the thesis critically reviews and summarizes the general strategies and methods to address all the challenges. Chapter 2 illustrates the fundamental aspects of ECs, clarifying the taxonomy, performance metrics and constituting components. Chapter 3 explores the solutions to device performance challenges and Chapter 4 is focused on encapsulation and integration aspects. In the end, Chapter 5 summarizes the main findings of the thesis and future prospects.

2 FUNDAMENTALS OF ELECTROCHEMICAL CAPACITORS

To be able to address the challenges regarding the device performance, it is essential to clarify and understand the fundamentals of electrochemical capacitors. The knowledge of ion storage and transport mechanisms builds a strong basis for the development of devices and their resulting performance. This chapter reviews types of ECs, their performance metrics and the constituting components that significantly influence the performance.

2.1 Taxonomy

Depending on the working mechanism, ECs can be divided into three main categories: (1) Electrical double layer capacitors (EDLCs) that primarily works on physical separation of charge forming electrical double layers (EDLs) near the surface of the electrode; (2) Pseudocapacitors that involve Faradaic reactions very close to the surface without bulk phase transformation; (3) Hybrid devices that combine both capacitor- and battery-like processes in energy storage. Based on the device configuration, ECs can also be classified as symmetric or asymmetric devices.

2.1.1 Electrical double layer capacitors (EDLCs)

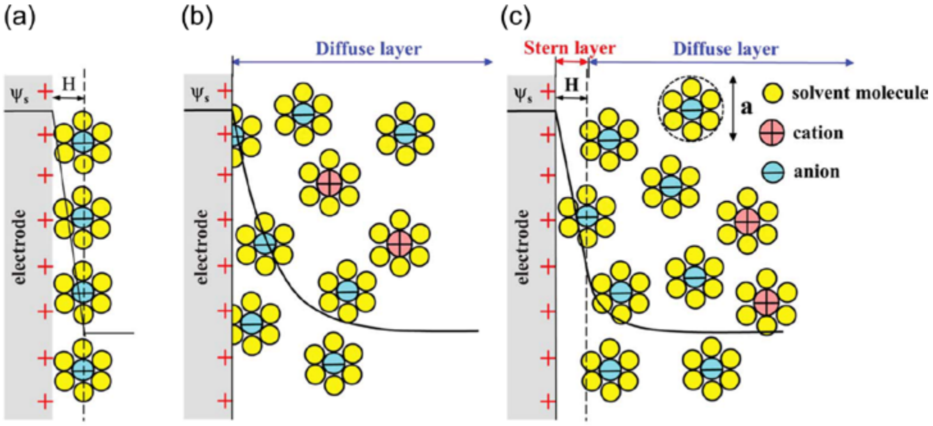

Figure 6. (a) Helmholtz, (b) Gouy-Chapman, and (c) Stern model of the EDL theory [16].

The main storage mechanism of EDLCs is the reversible electrostatic accumulation of ions on the surface of porous carbon electrodes. Helmholtz [17] proposed a theory describing that an nm thick condensed layer parallel to the electrode surface is formed by electrostatic charge separation when an electrode is polarized (Figure 6a). The capacitance is expressed in the same form as parallel plate capacitors, i.e.

$$C_H = \frac{\varepsilon_r \varepsilon_0 \times A}{d} \qquad \text{Equation (2)}$$

where ε_r represents the dielectric constant of the electrolyte, ε_0 is the vacuum permittivity, A is the surface area of the electrode, and d stands for the EDL effective thickness (Debye length). Since porous carbon has an extremely large surface area (up to 3000 $m^2\ g^{-1}$), and Debye length d is within the range of nm, the attainable EDL capacitance is substantially high. Later, Gouy [18] and Chapman [19] improved Helmholtz model by taking into account ion diffusion, where they proposed that the potential decreases exponentially from the electrode surface to the bulk electrolyte (Figure 6b). In 1924, Stern [20] proposed a model combining the Helmholtz and Gouy-Chapman models by recognizing the two regions contributing to the apparent capacitance, i.e. an inner Stern layer and a diffuse layer (Figure 6c). And the double layer capacitance (C_{EDL}) is equivalent to the sum of the Stern layer capacitance (C_H) and diffuse layer capacitance (C_D) by following the form of two capacitors connected in series:

$$\frac{1}{C_{EDL}} = \frac{1}{C_H} + \frac{1}{C_D} \qquad \text{Equation (3)}$$

A schematic of a typical EDLC is presented in Figure 7. When a potential is applied across the electrodes, an excess or deficit of charges appears on the electrode surfaces which in turn attracts the counter ions from the electrolyte solution resulting electrical neutrality. Along the EDL theory, it is generally perceived that double layers formed electrostatically in both positive and negative electrode/electrolyte interfaces during a charging process. Therefore, the whole device is equivalent to two capacitors in series [21], and the device capacitance C_{Device} follows the equation as

$$\frac{1}{C_{\text{Device}}} = \frac{1}{C_{+}} + \frac{1}{C_{-}} \qquad \text{Equation (4)}$$

where C_+ and C_- represent for the positive and negative electrode capacitance, respectively. When $C_+ = C_-$, C_{Device} is half the electrode capacitance. Otherwise, C_{Device} is limited by the electrode which has a lower capacitance.

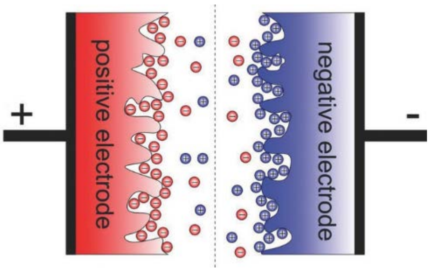

Figure 7. Schematic of a typical EDLC [21].

However, it was found that for some carbon materials with around 1 nm average pore diameter [22, 23], they can only accommodate one or a few ions per pore, therefore no classical double layer is formed. More accurately, their charge storage process arises from the electrosorption of ions by an oppositely charged carbon sponge, similar to physisorption of molecules by the same porous carbons, but driven by electrostatic force [24]. A wire-in-cylinder model [25] was proposed to accurately describe the effect in microporous carbon electrodes, and the theory can well fit experimental data regardless of the types of carbon material and electrolyte employed.

2.1.2 Pseudocapacitors

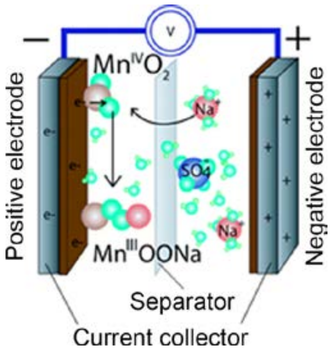

Figure 8. Schematic of a pseudocapacitor [26].

In pseudocapacitive electrodes, capacitance arises due to fast and reversible Faradaic redox reactions between the electrochemically active electrode material and electrolyte. After applying a certain potential, charge transfer occurs across the double layer. Although it involves Faradaic reactions similar to batteries, the working mechanism is different regarding the operating potential [27]. In a battery, the potential between electroactive materials remains ideally constant following Nernst equation whereas in a pseudocapacitor, the potential changes with the extent of charge acceptance ($\Delta V \propto \Delta Q$), and the derivative of $\Delta Q/\Delta V$ is termed as pseudocapacitance [7].

A schematic of a pseudocapacitor based on a MnO_2 material is shown in Figure 8. During a discharging process, Mn oxidation states change from (IV) to (III), and meanwhile, electrolyte cations (Na^+ in this case) is adsorbed on the surface. Electro-adsorption of protons on the surface may also happen, therefore, the charge storage mechanism of MnO_2 can be generically expressed as the reaction:

$$\mathrm{Mn(IV)O_2} + x\mathrm{C}^+ + y\mathrm{H}^+ + (x+y)\mathrm{e}^- \leftrightarrow \mathrm{Mn(III)OOC}_x\mathrm{H}_y \qquad \text{Equation (5)}$$

where C^+ represents the electrolyte cations (K^+, Na^+…). The reaction is fast and surface-confined, resulting in capacitive behavior. Note that there is little interest in symmetric pseudocapacitors because there are no oxidation states available at less than 0 V for MnO_2 [8]. But composite materials of MnO_2 and carbon [28] could overcome the problem and construct symmetric devices that show good performance.

Besides MnO_2, a number of other transition metal oxides (e.g. RuO_2), nitrides (e.g. VN), sulfides (e.g. MoS_2), carbide (e.g. Ti_3C_2) and conducting polymers (e.g. polyaniline and polypyrrole), are all pseudocapacitive provided that a proper electrolyte is applied [27, 29]. The Faradaic processes that occur at the electrodes may be different depending on the type of materials, but no matter which material employed, the obtained electrochemical response is supposed to be capacitor-like in a certain voltage range for pseudocapacitors. The three Faradaic mechanisms that can result in capacitive features are (1) Underpotential deposition, e.g. Pb underpotential-deposition on Au: $\mathrm{Au} + x\mathrm{Pb}^+ + 2x\mathrm{e}^- \rightarrow \mathrm{Au} \cdot x\mathrm{Pb}_{\mathrm{ads}}$; (2) Redox pseudocapacitance, e.g. energy storage in MnO_2 as presented above; (3) Intercalation pseudocapacitance, e.g. lithium-ion storage in Nb_2O_5: $\mathrm{Nb_2O_5} + x\mathrm{Li}^+ + x\mathrm{e}^- \leftrightarrow \mathrm{Li}_x\mathrm{Nb_2O_5}$ [30].

Due to these Faradaic processes occurring on the surface and in the bulk near the surface, the pseudocapacitance is 10 to 100 times larger than the electrostatic capacitance of an EDLC. At the same time, it lacks cycling stability to some extent due to the issues such as volume change during operation [27, 31].

2.1.3 Hybrid devices

It is generally acknowledged that hybrid devices refer to those devices that combine different charge storage mechanisms in the positive and negative electrode materials [24]. The definition may cause confusion since devices constructed with a pseudocapacitive electrode and an EDL electrode apparently fall within the fence of pseudocapacitors. Therefore, the term of hybrid devices is mostly applied when a battery-like behavior is incorporated resulting in battery-capacitor hybrids.

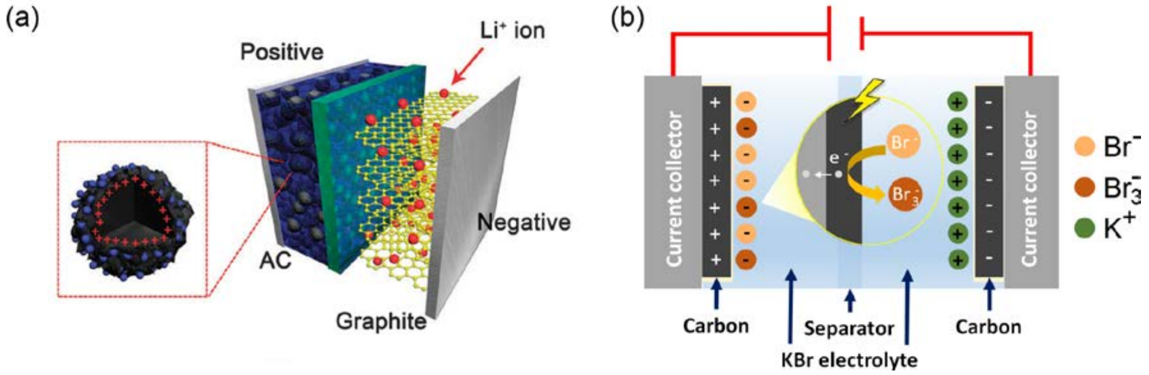

Figure 9. Schematic of hybrid devices: (a) Lithium-ion capacitors [32]; (b) Redox electrolyte based hybrid systems (Paper I).

Battery-capacitor hybrids are believed to be an important future direction for electrochemical energy storage systems, towards high energy and power density beyond what is anticipated from improvements in lithium-ion batteries or ECs [24]. The hybrids are typically constructed with a high-capacity battery-type electrode (source of energy) and a high rate capacitive electrode (source of power). Lithium-ion capacitor (LICs) as shown in Figure 9a is a typical example of a battery-capacitor hybrid system. A LIC utilizes porous carbon (common EDLC electrode material) and a pre-lithiated graphite (common lithium-ion battery anode material) as the positive and negative electrodes, respectively. Lithium-ion intercalation-deintercalation occurs in the graphite electrode while adsorption-desorption of electrolyte anions occurs on the porous carbon electrode. Another approach to construct battery-capacitor hybrids is through the use of redox electrolyte [33, 34]. Simply by replacing the electrochemically inert electrolyte of a common EDLC by a redox-active one (e.g. KBr in Paper I), one can obtain a redox-enhanced EDLC hybrid device. Depending on the redox species, electron transfer occurs on either positive or negative electrode surface, adding Faradaic charge storage to the underlying capacitive mechanism. The charge storage process is detailed in section 2.3.2.5.

2.1.4 Symmetric and asymmetric devices

By examining the device configuration, ECs can also be categorized into symmetric and asymmetric types. Symmetric devices refer to those with identical positive and negative electrodes. Asymmetric devices refer to every combination of positive and negative electrodes whenever there is any difference between the two electrodes (the type of material, weight, thickness…).

Symmetric devices are common for EDLCs where two porous carbon electrodes are used for positive and negative electrodes. This is a standard configuration employed to investigate the properties of electrolytes in Paper I (redox-active electrolyte KBr) and Paper II (ionic liquid electrolyte EMImAc, i.e. 1-Ethyl-3-methylimidazolium acetate). Note that symmetric EDLCs are not always optimized, therefore in some cases, the weight of the two electrodes are imbalanced to extend operating voltage window [35, 36] (discussed in section 3.1.2.2), and the use of two different carbon materials for positive and negative electrodes are also advised to maximize the attainable capacitance (section 3.1.2.3). For pseudocapacitors, they can be symmetric configuration when using composite materials e.g. MnO_2/carbon as electrodes [28]. As pointed out earlier, if one electrode is made of a pure pseudocapacitive material, it has to be coupled with a different material (either EDL capacitive or another pseudocapacitive material) as the counter electrode for the availability of oxidation state change, thereby asymmetric configuration. Battery-capacitor hybrids with a battery electrode are naturally all asymmetric devices, while for the hybrids enabled by redox electrolytes, the terminology is not strictly established. If the two electrodes are identical e.g. in redox-enhanced EDLCs, it can be called symmetric system, however, it is essential to recognize that the storage behaviors of the two electrodes are rather "asymmetric".

2.1.5 Electrical responses in general

Electrical response is an essential source of information that determines the type of application and PMU design in a system. This sub-section compares the electrical responses displayed by cyclic voltammogram (CV, voltage sweeps within a range at a certain scan rate $v = dV/dt$) and galvanostatic charge/discharge curve (GCD, time-dependent change in voltage at a constant current) of EDLCs, pseudocapacitors, and hybrid devices.

From the viewpoint of the *electrode*, three storage behaviors have been identified, i.e. electrostatic charge accumulation (EDL capacitive behavior), surface confined Faradaic redox or intercalation (pseudocapacitive behavior) and semi-infinite diffusion controlled Faradaic redox (battery-like behavior). EDL capacitive behavior is characterized by classic rectangular CVs and a linear GCD curve. Pseudocapacitive behavior, as indicated by the term itself (explained in section 1.2.1.2), should have the same response as the EDL capacitive one. Nonetheless, it is not uncommon that CVs of some materials based on intercalation mechanisms that deviate from standard rectangular shapes are also attributed to pseudocapacitance. These materials are characterized by significantly broadened peaks and little separation in peak position on CV scans [24]. Note that they are intrinsically different from battery behaviors which involve phase transformations, and the current response i in CV is proportional to the square root of scan rate, i.e. $i \propto v^{0.5}$. Both EDL capacitive and pseudocapacitive behaviors involve no phase transformation and exhibit a linear sweep rate dependence on current i.e. $i \propto v$. The CVs of battery behavior have well-resolved peak separation and correspondingly plateaus on GCD curves.

The *device* behavior as a whole is a sum up of its two electrode behaviors. Depending on the device "symmetry", three responses can be recognized in general. (1) Two capacitive (herein capacitive refers to either EDL capacitive or pseudocapacitive) electrodes result in capacitive devices; (2) One capacitive and one battery-like electrode leads to hybrid devices; (3) Two battery-like electrodes constitutes a battery. In principle, EDLCs and pseudocapacitors should follow case (1), and battery-capacitor hybrids follow case (2), but depending on the proportion of contribution from battery-like and capacitive behavior, the response may vary to a large extent from so-called "*supercabattery*" (battery-like behavior dominates) to "*supercapattery*" (capacitive behavior dominates) [37].

2.2 Key performance metrics

Key performance metrics include capacitance, energy and power, equivalent series resistance, maximum operating voltage, cycle life, self-discharge and leakage current, working temperature range and time constant. An overview of their definitions and evaluation methods is given in this section.

2.2.1 Capacitance

Capacitance is a measure of the ability to store electrical charge, given by

$$C = \frac{\Delta Q}{\Delta V} \qquad \text{Equation (6)}$$

where ΔQ and ΔV represents the amount of charge stored and the width of the voltage window, respectively. When calculating capacitances, one should examine whether the behavior is capacitive or rather a battery behavior, in order to avoid wrong interpretation. Capacitance is evaluated from three basic techniques, i.e. CV, GCD, and electrochemical impedance spectroscopy (EIS).

CV measurements apply a linear voltage sweep from the minimum, typically 0 V for ECs, to the maximum operating voltage $V_{\max}$ at a scan rate of v, and a response current i is recorded as a function of elapsed time (Figure 10a). The curve is usually plotted as i vs. V as in Figure 10b.

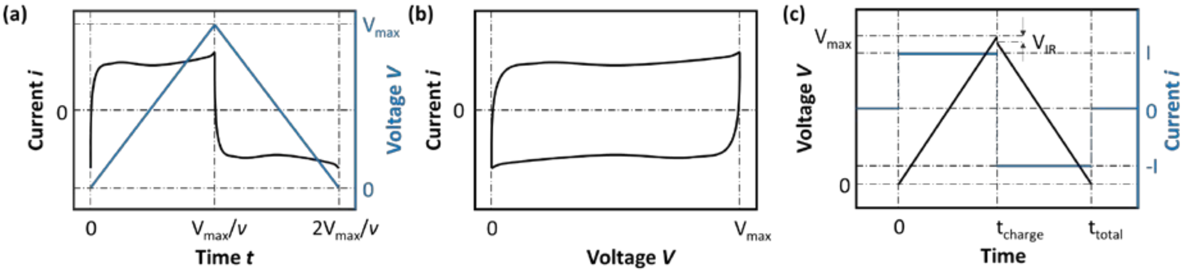

Figure 10. (a) Variation of current and voltage during a CV scan. (b) A typical CV curve. (c) A typical GCD curve with a display of the current variation.

For extraction of the capacitance from CVs, it is recommended to use the whole curve, though calculation can be done by selecting an arbitrary region. The following equation can be adopted

$$C = \frac{\Delta Q}{\Delta V} = \frac{\int_0^{2V_{max}/v} |i| dt}{2V_{max}} \qquad \text{Equation (7)}$$

where i is the current response as a function of time t, v is the scan rate and V_{max} is the maximum voltage.

GCD measurements charge and discharge a device with a constant current, and voltage response is recorded as in Figure 10c. Based on GCD results, the capacitance is

$$C = \frac{\Delta Q}{\Delta V} = \frac{I \cdot (t_{total} - t_{charge})}{V_{max} - V_{IR}} \qquad \text{Equation (8)}$$

where V_{IR} is the IR drop related to the equivalent series resistance.

Capacitance value can also be obtained through EIS technique which measures the impedance of a device as a function of frequency by applying a low-amplitude alternating voltage (normally 5 mV) superimposed on a steady-state potential. By adopting an RC equivalent circuit, the calculation of capacitance is based on the following equations

$$C' = -\frac{-Z''}{2\pi f |Z|^2} \qquad \text{Equation (9)}$$

$$C'' = \frac{Z'}{2\pi f |Z|^2} \qquad \text{Equation (10)}$$

where f is the frequency of the perturbation voltage, $Z = \sqrt{Z'^2 + Z''^2}$ is the overall complex impedance, Z' and Z'' are the real and imaginary part of Z, respectively, C' and C'' are the real and imaginary part of so-called *supercapacitance* [38].

Above calculations generate the absolute capacitance from a measurement. The values are usually further normalized by weight, area or volume thus giving gravimetric capacitances in e.g. F g^{-1}, areal capacitances in e.g. F cm^{-2} and volumetric capacitances in e.g. F cm^{-3}.

2.2.2 Energy and power

Energy and power of ECs can be calculated through

$$E = \frac{1}{2} C V_{max}^2 \qquad \text{Equation (11)}$$

$$P_{peak} = \frac{V_{max}^2}{4ESR} \qquad \text{Equation (12)}$$

where *ESR* represents the equivalent series resistance. Note that the power P_{peak} refers to the highest possible power that the device could deliver for a pulse. This calculation can be useful when considering buffer capacitor applications. Average power can be obtained via dividing *E* by the discharge time, i.e.

$$P_{avg} = \frac{E}{t_{discharge}} \qquad \text{Equation (13)}$$

2.2.3 Equivalent Series Resistance (ESR)

ESR is the sum of various types of resistances including the intrinsic resistance of the electrode material and electrolyte solution, mass transfer resistance of the ions, and the contact resistance between the current collector and the electrode. The resistance of the bulk electrolyte solution and the electrolyte inside the pores tend to dominate the ESR. The evaluation of *ESR* can be done by applying Ohm's law to the IR drop in a GCD measurement as in Figure 10c, i.e.

$$ESR = \frac{\Delta V}{\Delta I} = \frac{V_{IR}}{2I} \qquad \text{Equation (14)}$$

EIS is also a commonly used technique to determine *ESR*, however, the method is not standardized. *ESR* can be evaluated using the real part of the complex impedance at 1 kHz [39], or via interpolation of high-frequency part of a Nyquist plot to the *x*-axis (Paper II).

2.2.4 Maximum operating voltage (V_{max})

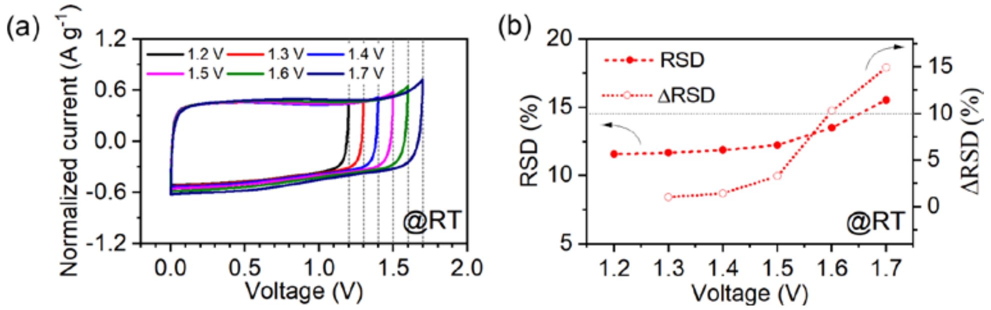

Figure 11. Determining the V_{max} of an EC containing an EMImAc electrolyte: (a) CV curves of different voltage limits. (b) *RSD* and Δ*RSD* as a function of the voltage limit (Paper II).

The maximum operating voltage is decided by the stability window of both electrodes and electrolytes. Experimentally, V_{max} can be determined by CV scans with a stepwise increase of voltage, until a rapid increase of anodic current is observed (e.g. Figure 11a). However, there is a lack of standard defining what a "rapid" increase is. In Paper II, we set up a quantitative benchmark for determining V_{max}, which defines the V_{max} is the highest voltage with less than 10% increase (compared to its adjacent voltage limit) in the relative standard deviation (*RSD*) of anodic current. For example, as in Figure 11a, a stepwise increase of voltage limit measurement is conducted for an EC containing an EMImAc ionic liquid electrolyte at room temperature (RT). The *RSD* of anodic current for each voltage limit is calculated as

$$RSD = \frac{\sigma_{I_a}}{\overline{I_a}} \times 100\% \qquad \text{Equation (15)}$$

where σ_{I_a} is the standard deviation of anodic current, and $\overline{I_a}$ is the average anodic current. They are calculated based on the data points that constituting the anodic branch of a CV curve. Then change of *RSD* at a voltage limit of V_2 compared to *RSD* at V_1 is calculated through

$$\Delta RSD_{V_2} = \frac{RSD_{V_2} - RSD_{V_1}}{RSD_{V_1}} \times 100\% \qquad \text{Equation (16)}$$

ΔRSD can reflect the influence of increasing voltage limit on the degree of change in the storage behavior. A benchmark of 10% is a rule-of-thumb in the study of an EMImAc electrolyte. According to the results in Figure 11b, 1.5 V is the highest voltage with less than 10% ΔRSD, therefore, $V_{\max}$ for the device is set at 1.5 V at room temperature.

2.2.5 Cycle life

Extremely long cycle life is an important feature of ECs enabling “fit-and-forget” IoT systems. Evaluation of cycle life is performed by repeating GCD measurement, and a capacitance retention can be obtained as an indicator of the lifetime. An alternative to the cycling test is the constant load or float test performed by holding the capacitor at the nominal cell voltage and determining the capacitance as a function of time by occasional charge/discharge cycles [40, 41].

2.2.6 Self-discharge and leakage current

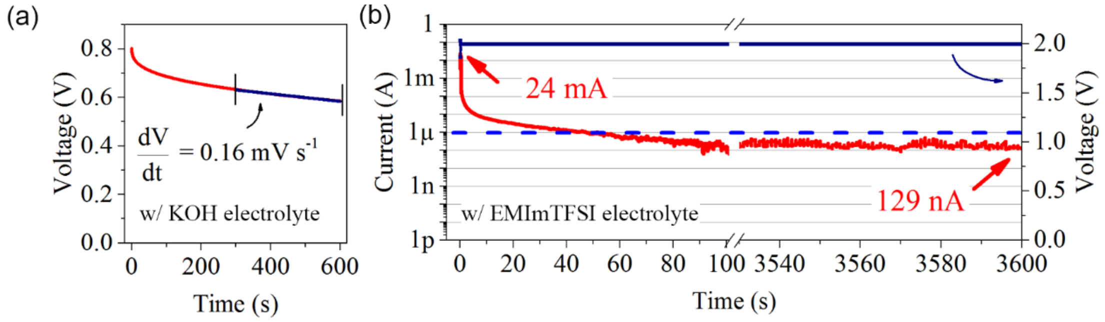

Figure 12. (a) Self-discharge and (b) leakage current measurements of ECs with graphite/VACNTs electrodes (Paper III).

Self-discharge is a voltage loss of a charged device over a period of storage time, which is detrimental to preserving the stored energy. Evaluation can be done by recoding the voltage decay of a charged device under an open circuit condition. Prior to the recording, the device can be held at its nominal voltage for a certain period of time. For the interest of practical applications where fast charging/discharging switch are of immense importance [39], the holding time is preferable to be short. In paper III, a voltage holding of only 5 min is applied for the self-discharge evaluation of an EC containing graphite / vertically aligned carbon nanotubes (graphite/VACNTs) electrodes (Figure 12a).

Leakage current is a compensate current needed to maintain the device at the rated voltage, therefore, it is normally evaluated by recording the current when holding the device at a specified voltage. For example, as in Figure 12b, a leakage current at 2 V is recorded for an EC in Paper III. Two important metrics result in a low loss feature. The first is a low equilibrium current (~100 nA), and the second is a fast rate to reach the equilibrium current (within 100 s from 24 mA to around 100 nA). Leakage current can also be calculated through a self-discharge curve through

$$I_{leakage} = C \cdot \frac{dV}{dt} \qquad \text{Equation (17)}$$

where dV/dt is the self-discharge rate within a certain time period (as in Figure 12a) and C is the device capacitance.

2.2.7 Working temperature range

All the EC metrics can be influenced by thermal effects. A working temperature range is determined by the nature of both electrode and electrolyte, especially the latter. Many commercial ECs have a rated temperature range of -40 to 70 °C, though special applications may require a temperature beyond the range. Determination of temperature range is assisted by examining other performance metrics at different test temperatures. Generally, extreme high-temperature impairs lifetime, and extreme low-temperature significantly increases *ESR* and thus limits the power output. In Paper II, the maximum operating temperature is mainly determined by examining the cycling stability and the average coulombic efficiency.

2.2.8 Relaxation time constant

The relaxation time constant (τ_0) of an EC is an indicator of how fast the device can be charged and discharged, which is measured by EIS in the form of a Bode plot or a phase angle plot. Figure 13 displays the results of two distinct devices in Paper II and Paper III. By identifying the frequencies at which the peak of C'' is reached (Figure 13a) or at which the phase angle is -45° (Figure 13b), time constants can be calculated by taking the reciprocal of the frequency values. For the device consisting of activated carbon (AC) electrodes and an EMImAc electrolyte in Paper II, τ_0 is on the order of 10 s. Thus at least 10 s is required to charge or discharge an EC at room temperature, in comparison with a high-frequency EC constituted by the graphite/VACNTs electrodes and a KOH electrolyte in Paper III, which requires only 0.51 ms.

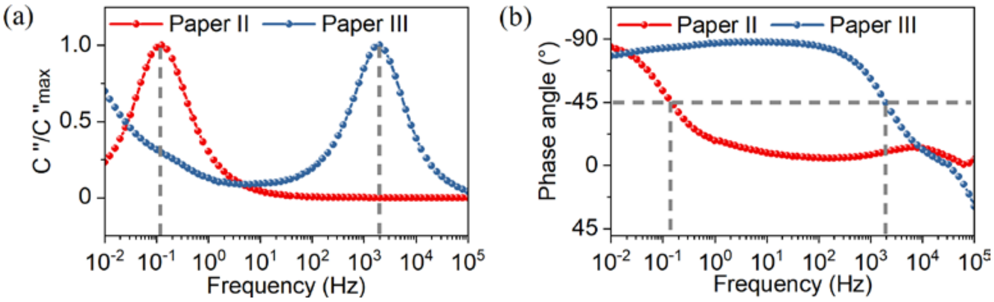

Figure 13. Determination of time constants: (a) Bode plots; (b) Phase angle plots (Paper II and III).

2.3 Electrochemical capacitor components

Regardless of unconventional ECs, a typical structure of a device is depicted in Figure 14 consisting of two electrodes on current collectors which are in direct connection to external metal contacts, an electrolyte, a separator, and an encapsulating package. All components have an influence on device performance. This section briefly outlines their effects and respective material choices.

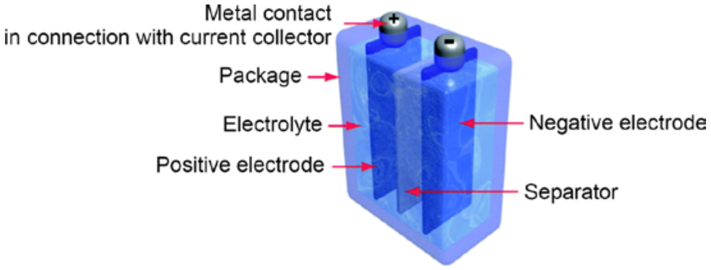

Figure 14. Schematic of an EC showing different components [42].

2.3.1 Electrodes

The electrode material is a critical component of an EC, which dictates the charge storage mechanism and thus the electrical response. In general, materials for EDLCs and pseudocapacitors can be categorized into the following types: carbon, transition metal oxides, nitrides, carbides, and conducting polymers. Under each category, there is a vast range of options available as active electrodes. Bearing in mind that composite materials from any combination of them are all technically viable, the choice of electrode materials is extraordinarily broad, let alone taking into account battery materials when designing hybrid systems, and the R&D in this field constitute a large proportion of reports within the scientific community. Specifically, carbon-based materials construct EDLCs which are of great interest for IoT application due to their long lifetime.

Carbon has been playing a frontier role as EC electrodes due to its versatility and unique properties. Nearly all carbon allotropes are effective in energy storage, including zero-dimensional (0D) structured onion-like carbon (OLC), one-dimensional (1D) carbon nanotubes (CNTs), two-dimensional (2D) graphene and three-dimensional (3D) activated carbon (AC), carbide-derived carbon (CDC) and templated carbon as compared in Table 3. In fact, approximately 80% of the commercially available supercapacitors are made of nanostructured carbonaceous materials [43].

Table 3. Different Carbon Structures Used in EDLCs [44].

Material	OLC	CNTs	Graphene	AC	CDC	Templated carbon
Dimensionality	0D	1D	2D	3D	3D	3D
Conductivity	High	High	High	Low	Moderate	Low
Volumetric capacitance	Low	Low	Moderate	High	High	Low
Cost	High	High	Moderate	Low	Moderate	High
Structure	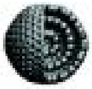	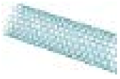	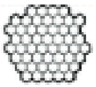	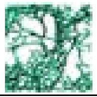	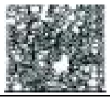	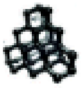

Because of its low cost and relatively high volumetric capacitance (50 - 80 F cm^{-3} [44]), AC is one of the most classic electrode materials that are suitable for large ECs (up to hundreds of Farads). A commercial AC material (Kuraray, YP-80F) with a BET (Brunauer-Emmett-Teller) specific surface area (SSA) of 2 100 m^2 g^{-1}, fabricated with coconut shells as the raw material, is used as the standard electrodes in Paper I and Paper II to examine the properties of the electrolytes. On the other hand, CNTs and graphene have relatively high cost but are highly conductive, and their unique dimensionalities promise the application as the supporting substrates for preparing composite electrodes by decorating the surface with a thin film of redox materials (section 2.3.4). Due to the relatively low density of CNTs (~ 0.3 vs. ~ 0.5 g cm^{-3} for AC [44]) and restacking problems of graphene, these materials are preferable to construct small size devices in the form of thin film electrodes. Combining the nature of high conductivity and less porosity, high-frequency ECs (section 3.5) can be constructed based on graphene or CNTs. Paper III presents such small size ECs based on a hybrid material of graphite and CNTs (Figure 15).

Figure 15. Small size ECs based on graphite/VACNTs electrodes (Paper III).

2.3.2 Electrolytes

The electrolyte is the provider of ions that are fundamental in the charge storage processes. Thermodynamic stability of an electrolyte confines the operating voltage of a device. Moreover, the physicochemical properties of electrolyte also determine the temperature range. Hence, the right selection of an electrolyte can maximize energy density (by enlarging operating voltage) and power density (by both increasing operating voltage and lowering *ESR* due to ionic resistivity) of a device.

The widely used and studied electrolytes are aqueous electrolytes, organic electrolytes, ionic liquid electrolytes, and solid or quasi-solid-state electrolytes. Conventionally, an electrolyte is electrochemically inactive, while a redox electrolyte which contributes Faradaic type of energy storage have aroused broad attention recently.

2.3.2.1 Aqueous electrolytes

Aqueous electrolytes have low resistivity and high ionic conductivity compared to other types of electrolytes. The ionic conductivity of 6 M KOH (applied in Paper III) is 0.6 S cm^{-1} and 1 M H_2SO_4 is up to 0.8 S cm^{-1} at 25 °C, significantly higher than a few tens of mS cm^{-1} for organic ones and even lower values for ionic liquids (applied in Paper II). Aqueous electrolytes are also cheap, safe (due to non-flammability) and require no special condition during fabrication and assembly. A significant drawback is a very narrow voltage window, which restricts the energy and power density of a device [27]. For acid and alkaline electrolytes, the maximum operating voltage is around 1 V, limited by the thermodynamics of water decomposition. Comparably, neutral electrolytes such as alkaline sulfates take advantage of large overpotential for H_2 and O_2 evolution reactions, and their voltage window can be extended to 1.5 V [45, 46]. It is reported that 1 M Li_2SO_4 works stably over 15 000 cycles at an operating voltage of 2.2 V [47]. In Paper I, we demonstrate a KBr solution when employed as a conventional aqueous electrolyte can be operated at up to 1.6 V, with a higher capacitance than other neutral electrolytes such as Li_2SO_4 and Na_2SO_4, and further to 1.9 V when redox activities are involved.

2.3.2.2 Organic electrolytes

Organic electrolytes typically consist of conducting salts dissolved in organic solvents. They provide a wide voltage stability window of 2.5 to 2.8 V. In general, it gives the opportunity to acquire increased energy density, although capacitance of carbons in organic electrolytes is usually lower than that in aqueous ones because organic electrolytes generally have larger solvated ions and lower dielectric constants [32]. Currently, commercial ECs are mostly made of tetraethylammonium tetrafluoroborate ($TEABF_4$) salt dissolved in organic electrolytes [7]. Drawbacks of organic electrolytes are their high cost, low conductivity, safety concerns related to the flammability, volatility, and toxicity. Furthermore, organic electrolytes require strict purification and special conditions for device fabrication, i.e. dry rooms where water content is extremely low.

2.3.2.3 Ionic liquid electrolytes

Recently, room temperature molten salts, also known as ionic liquids (ILs), have gained significant attention due to their very wide potential window up to 4 V. They are composed of bulky, asymmetric organic cations and weakly coordinating inorganic/organic anions. Based on the composition, ILs can be classified as aprotic, protic and zwitterionic types as shown in Figure 16. ILs are also known as solvent-free electrolytes due to the absence of any volatile organic compound [48, 49]. Moreover, ILs have high thermal and chemical stability, low vapor pressure due to their inherently high viscosity, non-flammability, and relatively low harmful effect on the environment. However, compared to conventional electrolytes (aqueous or organic), ILs always give high *ESR* and low conductivities, particularly at lower temperatures. Corresponding remedies include the addition of solvents and mixing two types of ILs to form eutectic mixtures, which are detailed in section 3.3.1.3 and 3.3.2.3. Also, for high-temperature applications, the issue of low conductivity is greatly alleviated, which is demonstrated in Paper II with an imidazolium-based IL EMImAc.

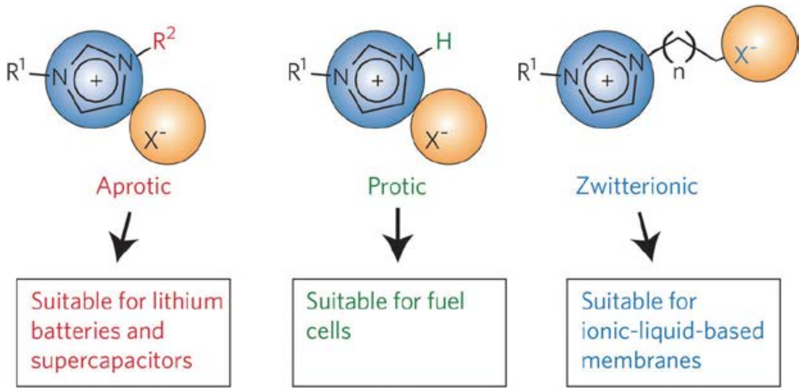

Figure 16. Classification of ionic liquids [50].

2.3.2.4 *Solid- or quasi-solid-state electrolytes*

Solid-state electrolytes are non-liquid electrolytes, mostly polymer-based where conducting salts are distributed in a polymer matrix, and some are based on inorganic matrix [51]. They are in a solid state so that this type of an electrolyte can both serve as an ionic conducting medium and as a separator. Therefore, their liquid-leakage-free nature enables constructing flexible devices. A drawback related to this type of electrolytes is a limited contact surface area between solid-state electrolytes and electrode materials, thus increasing *ESR* and decreasing power capability.

Polymer-based solid-state electrolytes are classified into (1) solid polymer electrolytes (SPEs) which are dry polymer electrolytes, (2) gel polymer electrolytes (GPEs) where there is a liquid phase existing in the framework thus an alternative term is quasi-solid-state electrolytes, and (3) polyelectrolytes where the polymer matrix itself is a conducting salt contributing to conductivity.

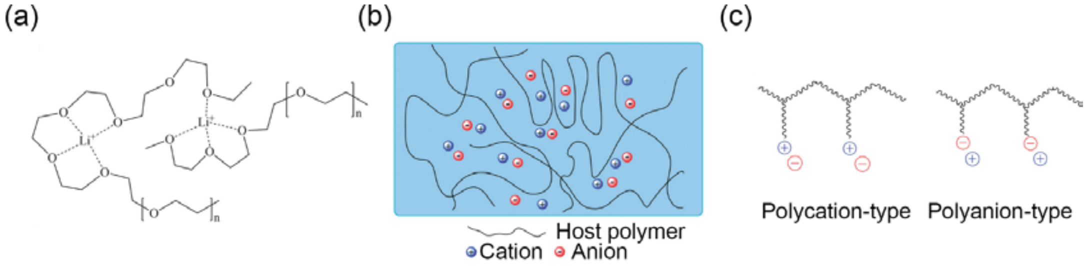

Figure 17. Schematic diagrams of (a) a dry solid-state polymer electrolyte PEO/Li^+, (b) a gel polymer electrolyte, and (c) a polyelectrolyte [32].

SPEs is composed of a polymer and a salt, e.g. PEO/Li^+ as shown in Figure 17a. Due to the absence of a liquid phase, SPEs have good mechanical properties, and the conductivity relies on ion transport within the polymer thus lower than that of GPEs. PVA/H_3PO_4 is a typical example of GPEs (Figure 17b) which consist of PVA as a polymer host swollen in solvent H_2O and H_3PO_4 as an electrolyte. PVA based GPEs are most commonly used because of their easy production, high hydrophilicity, good film forming, non-toxicity, and low cost. A PVA/H_3PO_4 GPE is applied in Paper III to demonstrate flexible low loss ECs.

PVA based electrolytes are also called hydrogel polymer electrolytes characterized by 3D polymeric networks trapping H_2O in the PVA matrix mainly through surface tension [52]. The ions move via the solvent H_2O and show good conductivity, but the mechanical strength and operating temperature and voltage are relatively low. Instead of H_2O, GPEs can also be based on organic solvents thereby the term "organogel" electrolytes. Corresponding polymer matrix options are PEO [53, 54] , PMMA [55, 56], PVP, PEEK [57] and copolymers [58, 59]. Organogel GPEs have an extended maximum operating voltage up to 3 V [54] compared to hydrogel GPEs. Table 4 compares, in general, the metrics of different types of electrolytes discussed above.

Table 4. Typical metric values of liquid and solid- or quasi-solid-state electrolytes

	Liquid electrolytes			Solid- or quasi-solid-state electrolytes		
	Aqueous	Organic	IL	Hydrogel	Organogel	IL-containing
Maximum operating voltage (V)	0.8 to 1.6	2.5-2.8	1-4	0.8 to 1.6	2.5-2.8	1-4
Ionic conductivity @RT (S cm^{-1})	Up to 1	0.05	10^{-3} to 10^{-2}	10^{-3} to 10^{-1}	10^{-3}	10^{-3}
Temperature range (°C)	-10 to 70	-40 to 70	RT to over 100	-10 to 70	-40 to 70	RT to over 100

2.3.2.5 *Redox electrolytes*

Redox electrolytes are a relatively new type of electrolyte being investigated. Different from the conventional ones, redox electrolytes contain redox-active species such as simple or complexes of transition metal ions (e.g. VO^{2+}), halide ions (e.g. I^-, Br^-), quinones and phenylamide. Redox electrolytes can be classified as *redox-additive electrolytes* and *redox-active electrolytes*. The former refers to conventional electrolytes with redox-active species as an additive, while the latter refers to those that are inherently able to undergo fast redox reactions, such as KBr (Paper I).

During a charging process on the positive electrode side as shown in Figure 18a, oxidizable species (R_P) from a redox electrolyte donate electrons and are oxidized to O_P, and on the negative side, reducible species O_N accept electrons to be reduced to R_N. A reversible process happens during a discharging process as in Figure 18b. The electrolyte that contributes R_P is called *catholyte*, and the one that provides O_N is called *anolyte*. Note that a redox electrolyte can contain either one of R_P and O_N, or both species. For example, KBr redox electrolyte (Paper I) contains only R_P, i.e. bromine ions to be oxidized to O_P (Br_3^-), while potassium ions in KBr are just normal cations to be adsorbed on the surface but undergo no redox reactions.

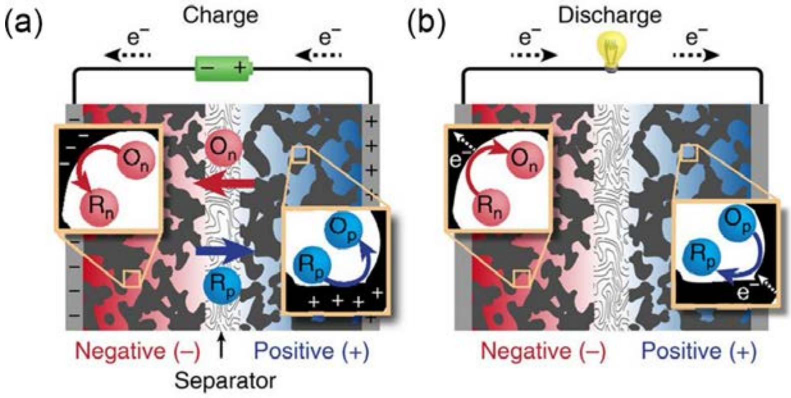

Figure 18. Schematic of redox processes during (a) charging and (b) discharging [60].

The redox reactions proceed on the surface of the electrode [34]. In terms of porous carbon-based systems, redox species in the bulk electrolyte must enter the pores as the first step ($O_{bulk} \rightarrow O_{pore}$ as step (1) for anolyte species, or $R_{bulk} \rightarrow R_{pore}$ as step (1') for catholyte species, Figure 19). It is predicted that a transition state is needed before the electron transfer could happen, i.e. step (2) $O_{pore} \rightarrow O^*$ or step (2') $R_{pore} \rightarrow R^*$. Afterward, transition states convert to adsorbed states through step (3) or (3'), and redox reaction finally happens via step (4). A few exceptional cases are: (1) Transition state species could exchange electrons without going through an adsorbed state; (2) If absorbed species transform via (5) or (5') to soluble species that can diffuse into the bulk electrolyte during charging, the redox enhanced energy storage is not effective, because the product after electron transfer (R_{ads} or O_{ads}) is not recoverable since they have already diffused out of the pore; (3) Redox reaction could also happen outside the pore via (6) or (6') but with little energy contribution due to limited surface area (i.e. active sites for reactions).

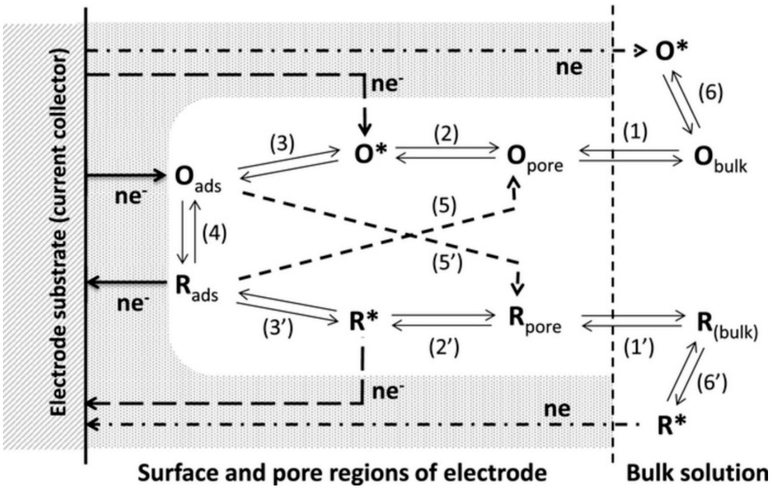

Figure 19. Illustration of charge storage mechanisms in the porous carbon electrode of an EC with a redox electrolyte [34].

The use of redox electrolytes is an easy and low cost yet effective approach to construct hybrid devices with an improved energy density, however, the incorporation of redox processes complicates the energy storage mechanism and therefore the related device behaviors. Paper I, which describes using a KBr redox-active electrolyte, has revealed that the device performance depends on both operating voltage and operation history (discussed in section 3.1.2.4). Understanding the underlying mechanisms is essential to design redox enhanced EDLCs as an energy storage solution towards a specific application.

2.3.3 Separators

The function of separators is to prevent direct contact between positive and negative electrodes and at the same time allow for fast transportation of ionic charge carriers. Separators mainly contribute to *ESR* and therefore have an important influence on power performance. As part of the "dead" weight and volume of ECs, separators are preferred to be light and thin but should also exhibit certain mechanical strength, thermal and chemical stabilities, and be easily wetted by the electrolyte. Commonly used separators are thin porous polymers (polypropylene and polyethylene), cellulose and glass fibers. Recently developed options include graphene oxide (GO) films [61] and eggshell membranes [62]. Some of them have different preference to the type of electrolytes. For example, cellulose separators work well in organic electrolytes but may degrade in aqueous H_2SO_4 electrolytes [63].

Thermal properties of separators are an important consideration when designing high-temperature devices. Thermal shrinkage of the separators happens around their decomposition temperature, leading to short circuits between the two electrodes, which may eventually cause thermal runaway (the shrinkage of separators is required to be less than 5 % after 60 min at 90 °C [64]). At low temperatures when ion mobility is limited, the porosity of separator plays a vital role in overall performance [65, 66].

2.3.4 Current collectors and packages

Current collectors are typically flat metal foils or grids onto which active electrode materials are cast [67]. They should be chemically and electrochemically stable in the presence of an electrolyte and during device operation. For aqueous acid electrolytes, current collectors should be corrosion-resistant. Noble metals such as gold are an ideal option in terms of stability, but the high cost apparently limits their widespread use. Alternative options are indium tin oxide (ITO) [68], carbon [69] and conducting polymers [69]. For aqueous alkaline electrolytes, common collectors are nickel [70], stainless steel [71] and also carbon-based materials such as carbon fabrics [72], carbon nanotubes [73], carbon fiber papers [74] and graphite [75]. Aqueous neutral electrolytes are much less corrosive, therefore the materials for acid and alkaline electrolytes are also applicable to them. For organic and ionic liquid electrolytes, aluminum is the most common current collector material.

Current collectors have an influence on lifetime and *ESR*. It has been found that an aluminum current collector is involved in the ageing of ECs based on organic electrolytes [63] and ionic liquids [76, 77]. An optimal interface between a current collector and an electrode material reduces the internal resistance. Surface treatments of a sol-gel deposit of a conducting carbonaceous material on aluminum current collector have been shown to decrease ohmic drops at the interface [78]. Developing nanostructured current collectors with an increased contact area is clearly a direction towards high-performance devices. The beneficial effect is particularly significant for pseudocapacitive material based ECs. This is because pseudocapacitive materials mostly have low electronic and ionic conductivities, therefore ion access is limited when the material is deposited on planar current collectors in a thick film. With nanostructured current collectors such as a carbon nanotube array (Figure 20a), pseudocapacitive materials can be deposited onto in a conformal way (Figure 20b), and the exposed area to the electrolyte is greatly improved. The electrode material in Paper III can be used as 3D current collectors for this purpose.

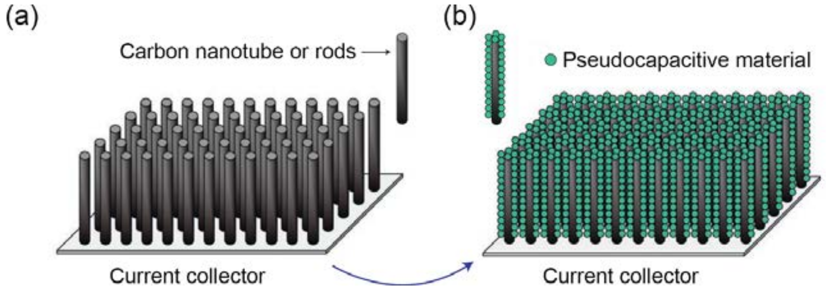

Figure 20. Schematic of (a) carbon nanotube array as a nanostructured current collector and (b) conformal deposition of pseudocapacitive material on the current collector [8].

Packaging materials of ECs depend on the cell configuration and manufacturers. In general, steel is used for coin cells (e.g. stainless steel SS316), cylindrical cells (nickel plated steel sheets [79]) and prismatic cells (heavy gauge steel [80]). Pouch cells use aluminum laminated film [81] for the casing, from outside to inside, the laminated film consists of polyamide layer, aluminum foil, and polypropylene with adhesive layers in between. Some suppliers e.g. Cellergy offer prismatic ECs with polymer-based packages.

Current collectors and package materials are another sources of “dead” weight and volume in addition to separators, therefore ideally they should be light and compact. For state-of-art devices, especially small ones, the weight of the overall device is 5-10 times larger than the total weight of positive and negative electrodes [82]. Therefore, for the design of ECs for miniaturized self-powered systems, it is highly desirable to reduce the “dead” weight and volume in order to maximize device level energy and power densities.

Along the vein of minimizing the weight and volume of current collectors, it is desirable to develop free-standing, highly conductive electrodes to eliminate current collectors. Materials with metallic conductivities such as carbon nanotube [83], graphene [84] and two-dimensional carbides [85] are suitable for such a strategy.

3 DEVICE PERFORMANCE CHALLENGES

This chapter elaborates the strategies and methods aiming to address the challenging issues regarding device performance, identified in Chapter 1. Many of the performance-related issues are not only specific to miniaturized systems but also exist for ECs' application in macro systems, therefore the corresponding strategies and methods can be universal.

3.1 Towards high energy with high power and long cycle life

The mathematical expression of energy, i.e. Equation (11), dictates that the energy is proportional to the capacitance (C) and the square of the maximum operating voltage (V_{max}^2) for capacitive-behavior ECs. It is thus natural to increase either C or V_{max} for energy maximization. The author generalizes the strategies by material-level and device-level optimizations.

3.1.1 Material-level optimization

The push toward high C and V_{max} are directly relevant to materials science and engineering which optimizes material physicochemical properties and structures with respect to the energy storage mechanisms.

3.1.1.1 High capacitance materials

Carbon

Carbon materials represent the most classic type of electrode constructing ECs, i.e. EDLCs that are favored by IoT systems due to their excellent cycle life suits the “fit-and-forget” concept. As pointed out earlier, AC arouses tremendous interest because of its low cost and relatively high volumetric capacitance. Micropores (pore size < 2 nm) and mesopores (2 to 50 nm) created during the activation process (oxidation in water vapor, KOH, or CO_2) are responsible for the high SSA of AC, which can exceed 2000 $m^2\ g^{-1}$. Note that SSA is preferable to be assessed by the Dubinin-Radushkevich (DR) equation or the Density Functional Theory (DFT) model since the BET model (based on multilayer gas adsorption on the solid surface) could overestimate surface area for micro-porous carbons [86]. Nevertheless, no matter which model is applied, a linear increase of specific capacitance as a function of SSA seems to cease at around 1200 $m^2\ g^{-1}$ and then saturate [87, 88]. This is because of a mismatch between pore size and ion size. Optimal capacitance is achievable when the pore size is very close to the size of de-solvated ions, implying that solvated ions could undergo a de-solvation process before entering the pore to be electro-adsorbed. This was supported/proved by a number of experimental and theoretical research [22, 23, 89-99]. Micropores that are smaller than the ions contribute substantially to SSA but little to charge storage due to ion sieving effect [90], while very large pores show worse interaction with ions [95]. Therefore, carbon with both high SSA and relatively narrow pore size distribution (PSD) is preferred to maximize capacitance. The understanding of capacitance origin has boosted the development of carbon-based ECs. Capacitive performance of activated carbon has been greatly improved from about 120 F g^{-1} in the mid-2000s to more than 200 F g^{-1} in organic electrolytes [100].

Templated carbons is an important direction of high-performance carbon-based materials. They are produced by the carbonization of an organic compound in nanospace of a template substance and the liberation of the resulting carbon from the template. The method allows for flexibility in tuning porosity. Carbons of hierarchical porosity where there is an optimal combination of micropores, mesopores and macropores, and a beneficial interplay between different pores present a new benchmark of carbon electrode capacitance beyond 300 F g^{-1} [42]. Within such a hierarchical porous structure, ions subsequently enter the largest pores and then flow into subdivided smaller ones, and finally reach the smallest pores, as shown in Figure 21. An optimal network overcomes the drawback of slow mass transportation within micropore-dominated carbon materials, achieving both high capacitance and high rate capability. The capacitance of carbon can also be increased when doped with heteroatoms such as nitrogen and oxygen which generate pseudocapacitance. By combining the effects both from hierarchical porosity of template carbon and nitrogen doping, a record value of 855 F g^{-1} (at 1 A g^{-1}) has been reported for a few-layer nitrogen-doped (source of pseudocapacitance) mesoporous carbon fabricated from a silica hard template, and an electrode capacitance of 615 F g^{-1} is still retained at 40 A g^{-1} [101].

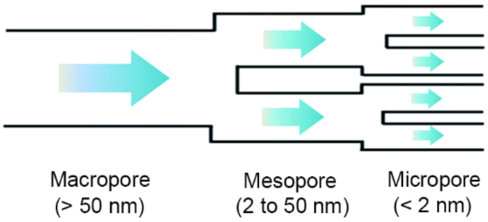

Figure 21. Illustration of an ion diffusion pattern in a typical hierarchical porous structure [42].

Pseudocapacitive materials

Pseudocapacitive materials exhibit higher capacitances than carbons due to their Faradaic nature. The theoretical gravimetric capacitance value (in F g^{-1}) can be calculated through

$$C = \frac{n \cdot F}{M \cdot V} \qquad \text{Equation (18)}$$

where n is the number of electrons transferred in the involved redox reaction, F is the Faraday constant, M is the molar mass of the pseudocapacitive material and V is the maximum operating voltage or potential window. For the most studied MnO_2, the redox reaction proceeds in terms of Equation (5) thus within a potential window of about 0.8 V, thus $n = 1$, $V = 0.8$ V, $M = 86.9$ g mol^{-1} and $F = 96\,485$ C mol^{-1} obtained the capacitance of MnO_2 material roughly equals 1388 F g^{-1}. For the materials that undergo multi-electron reactions, e.g. RuO_2 with oxidation states that can change from (II) to (IV) thus $n = 2$ in terms of

$$RuO_2 + xH^+ + xe^- \leftrightarrow RuO_{2-x}(OH)_x \qquad \text{Equation (19)}$$

where $0 \leq x \leq 2$, maximum capacitance could reach 1400 to 2000 F g^{-1} [102-104] depending on the degree of reaction and the potential window within which the reaction is assumed to complete. Nevertheless, such a high capacitance was rarely achieved in practice [105], generally because of low electronic conductivity (of amorphous RuO_2) resulting in poor charge carrier transport and weak interaction between nanoparticles. An intrinsically low electronic conductivity which leads to low capacitance and inferior power capability is a challenge to almost all other transition metal oxide pseudocapacitive materials.

One of the solutions to the problem is to engineer the material into thin film. The performance of transition metal oxides can thus be greatly improved because the charge carrier transport path is minimized and the interplay between particles is no longer an issue [106]. As a result, the effect of low conductivity is minimized. However, the thin film strategy limits the overall capacity of charge storage, giving low areal capacitance and is suitable only for niche applications. Alternatively, using nanostructured 3D current collectors as a substrate for depositing a conformal layer of materials can be an effective approach to increasing mass loading while still benefiting from the fast dynamics of thin film electrodes.

The other solution to the problem is to improve conductivity by modulating the materials' composition and electronic structure. Introducing oxygen vacancies, as impurity states in the bandgap, into oxides to tune their intrinsic defects is one way to increase the conductivity of transition metal oxides [107]. The vacancies also serve as active sites for reactions. Oxygen vacancies can be obtained through annealing under vacuum or with a reducing gas (e.g. hydrogen, ammonia) [108]. Another approach for improving conductivity is through doping, via the regulation of donor or acceptor densities. Both non-metal [109] and metal [110] atoms have been demonstrated as dopants to optimize the capacitive performance. The modified materials show improved maximum capacitances, smaller *ESR* and increased power densities.

Compared to oxides, transition metal sulfides, nitrides, and carbides have higher electronic conductivity with rich redox chemistry for energy storage [29, 111, 112]. Especially for carbide Ti_3C_2 which exhibits a metallic conductivity of up to 1 500 S cm^{-1}, and an extremely high volumetric capacitance of 900 F

cm^{-3} (correspond to 245 F g^{-1}) [113]. Ti_3C_2 is a member of MXene family which is a new direction of electrode materials for constructing high-performance ECs. Excellent charge storage performance of MXenes is partly because of their 2D structures, representative of a large group of 2D and layered structured materials [29, 111]. These materials are only a few atoms thick and therefore have a large number of immediately accessible electrochemically active sites. On the other hand, the rich active sites lead to an instability of such materials, which is also a common challenge to pseudocapacitive materials. The remedy could be engineering specific microstructure in order to tolerate the volume expansion and thus reduce stains during charging/discharging processes.

Battery-type materials

Precisely, battery-type materials should not be linked to *capacitance*, rather their storage capacity is evaluated as *capacity* Q in a unit of C g^{-1} or mAh g^{-1}, and the energy density is calculated from GCD curves through

$$E = \int V \cdot i\mathrm{d}t = \int V\mathrm{d}Q \qquad \text{Equation (20)}$$

where V is the voltage and i is a constant current. Thanks to the advancement of battery technology, a number of battery electrodes can be readily utilized to construct hybrid EC systems, including intercalation cathodes, phase changing cathodes, metal anodes, alloying anodes, and transition metal compounds. Cycle life remains an issue when employing a battery electrode because ion insertion or phase transformation create dimensional changes that have a negative impact on the integrity of the electrodes. Whether the as constructed device is suitable for self-powered systems or not will depend on application scenario. Besides electrodes, redox electrolytes also belong to battery-type materials that greatly enhance the energy density of ECs. Harnessing multi-electron redox processes through the use of battery-type materials is regarded as an important direction to boost energy storage performance [24].

3.1.1.2 High voltage materials

Electrolyte plays a decisive role in the maximum operating voltage of ECs. As reviewed in the last chapter, in terms of the intrinsic properties of the electrolyte materials themselves, the IL is the best material that brings $V_{\max}$ beyond 3 V. However, ILs severely limit the attainable power density due to their low ionic conductivity, especially at a low temperature. Although aqueous electrolytes of higher conductivity are thermodynamically limited by H_2O decomposition window of 1.23 V, studies have proved that they can be kinetically stable up to a substantially high voltage (more than 2 V) for neutral electrolytes, due to three possible factors. (1) H^+ and OH^- equilibrium. The concentrations of H^+ and OH^- ions in a neutral electrolyte are extremely low, hence neither hydrogen nor oxygen evolution is favored. (2) There is a strong solvation of both cations and anions [47]. Cations and anions exist in the form of hydrated ions, and the surrounding H_2O molecules have to depart from the hydration shell before getting involved in H_2 or O_2 evolution reactions (HER or OER). The extra energy required for dehydration contributes to an overpotential to HER or OER. (3) Hydrogen electrosorption in micropores of the carbon electrode [114, 115]. Carbons with smaller particle and pore sizes would lead to a higher overpotential for HER [114], and surface functional groups also influence overpotential [116]. With a proper selection of electrodes and device design, a 4.2 V aqueous device is possible [117]. Water-in-Salts Electrolyte (WiSE) [118] concept (highly concentrated LiTFSI salt solution) also promises high voltage aqueous electrolytes (2.4 V [119], 2.9 V [120]) enabling high energy devices, but there is clear trade-off between an improved energy density and decreased power density and cycling stability [119]. Concentration optimization is needed to minimize this effect.

Besides electrolyte, electrode materials can also be a limiting factor to $V_{\max}$. The stability window of a variety of common electrode materials in aqueous and organic media is summarized in Figure 22 [112], which can be used as a reference map for selecting electrodes when designing high voltage and high energy ECs.

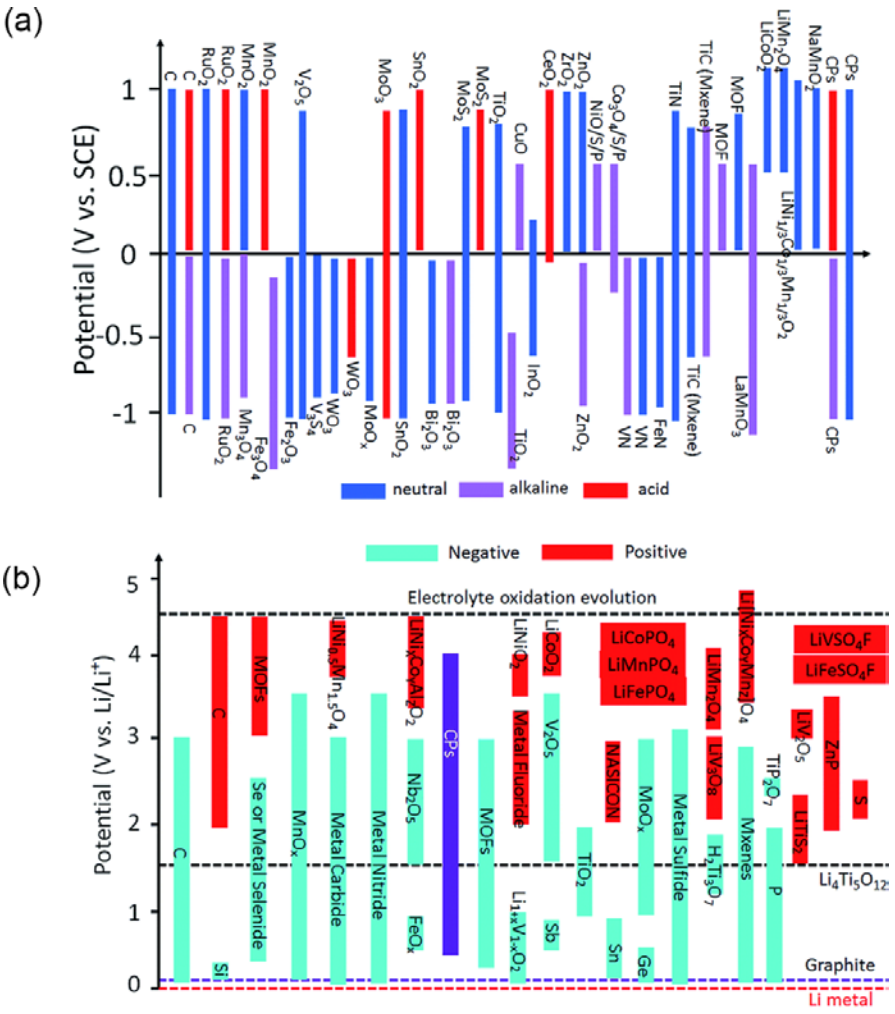

Figure 22. Working potential windows of electroactive materials in (a) aqueous and (b) organic electrolytes [112].

3.1.2 Device-level optimization

A boost in capacitance and maximum operating voltage can also be realized through device engineering, leveraging existing materials. The approach is to reach an optimal match among the positive electrode, negative electrode and electrolyte by designing asymmetric devices.

3.1.2.1 Principles

The benefit of increasing V_{max} is substantial to energy improvement as $E \propto V_{max}^2$. The design of asymmetric devices is an effective tool to enlarge the voltage window by manipulating the two electrodes through

$$m_P C_P E_P = m_N C_N E_N$$

Equation (21)

where m, C and E represents the mass, specific capacitance and working potential window, respectively, and the subscript label P and N refer to positive and negative electrodes. The above equation is simply an expression of the fact that the amount of charge flowing through the positive electrode equals to that through the negative electrode.

In the case of a symmetric EC with identical electrodes, the working potential windows are generally symmetric ($E_P = E_N$). However, the symmetric windows could cause some potential *wasted* on one side of the electrodes. As shown in Figure 23a, assuming that the positive electrode show capacitive behavior within a potential range between E_{P1} to E_{P2}, and the negative electrode is within E_{N1} to E_{N2}, thus the limits of capacitive potential range (*CPR*) of the two electrodes are

$$CPR_P = E_{P2} - E_{P1}$$ Equation (22)

$$CPR_N = E_{N2} - E_{N1}$$ Equation (23)

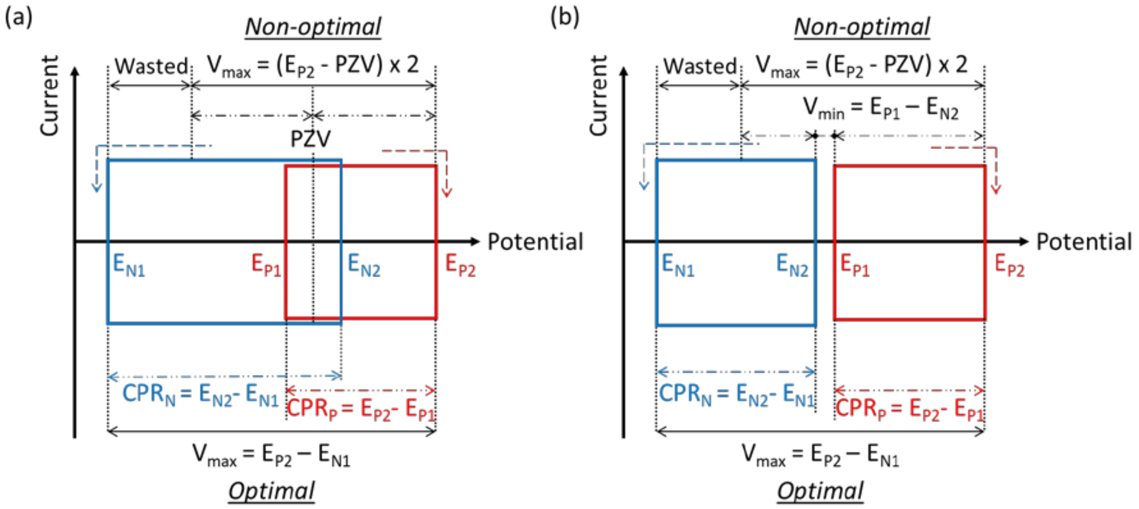

Figure 23. Schematic of electrode potentials and operating voltages in the case of (a) $E_{N2} > E_{P1}$ and (b) $E_{N2} < E_{P1}$.

In many cases, the *CPR* range of the positive electrode overlaps that of the negative electrode, i.e. $E_{N2} > E_{P1}$ (Figure 23a). Then the device can be discharged to 0 V where the potential of positive electrode equals to that of the negative electrode, and the equal potential at 0 V is donated as the potential of zero voltage (*PZV*). If $E_{N2} < E_{P1}$, the EC can only be discharged to a minimum operating voltage V_{min} defined by E_{P1} - E_{N2}, instead of 0 V.

When an EC is being charged, the potential of positive electrode increases while negative electrode potential decreases (following the arrows in Figure 23), so V_{max} is determined till either of the electrodes is ramped up to its potential limit (E_{P2} or E_{N1}). The electrode that first reaches its boundary potential is the *voltage-limiting electrode*. As an example in Figure 23a, the positive electrode is voltage-limiting, then there is a wasted potential on the negative electrode that is not exploited yet applicable for capacitive charge storage. To optimize the system in order to fully maximize V_{max}, the capacitance of the positive electrode should be increased. This can be done by asymmetric design with the following methods.

3.1.2.2 Method 1 - Increasing the mass of the voltage-limiting electrode

When loading a higher amount of material on the positive electrode, i.e. increasing the m_P in Equation (21), the working potential range of negative electrode E_N is accordingly enlarged, since other factors (C_P, E_P, m_N, and C_N) remain unchanged in the equation. Because the reference potential *PZV* is relatively stable in EDLCs [35, 36, 121, 122], the negative electrode potential is stretched to its limit of E_{N1}, and the V_{max} optimization is thus achieved. The theoretical mass ratio can be calculated through

$$\frac{m_P}{m_N} = \frac{C_N \cdot (PZV - E_{N1})}{C_P \cdot (E_{P2} - PZV)}$$ Equation (24)

This requires an experimental determination of electrodes' specific capacitances (C_P and C_N), the potential limits (E_{N1} and E_{P2}, mostly determined by electrolyte stability window) and *PZV*. For this purpose, except the common two-electrode setup as in Figure 24a, a conventional three-electrode cell is needed to examine the stability window of electrolyte, which can also be used for a rough estimation of C_N and C_P (Figure 24b). Besides, a special two electrode system equipped with a reference electrode (T-type Swagelok cell used in Paper I is shown in Figure 24c) to gather information on the real-time change of electrode potential during device operation, measure the *PZV* and exact calculation of electrode capacitances.

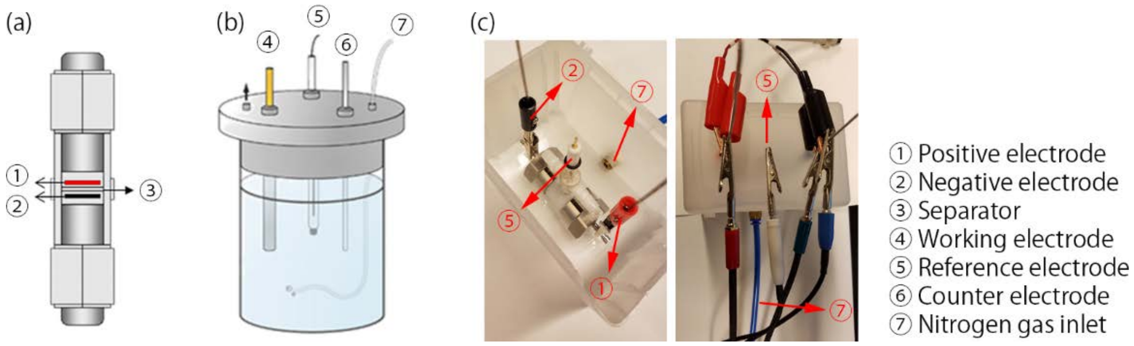

Figure 24. Measurement setups (a) Two-electrode system: Swagelok cell; (b) Conventional three-electrode cell; (c) Three-electrode system: T-type Swagelok cell.

With this method (mass-balancing), it was demonstrated that V_{max} has been optimized in EDLCs with aqueous electrolytes [35, 36, 123], as shown in Figure 25. Similar cases can also be found in ionic liquid systems [124, 125].

It is not established but quite common that the positive electrode is usually the voltage-limiting electrode in symmetric EDLCs, especially in neutral aqueous systems. This may be partly attributed to the fact that negative electrode potential can be extended to a rather low potential by taking advantage of nascent hydrogen storage and thereby large HER overpotential, making a large *CPR* range of the negative electrode.

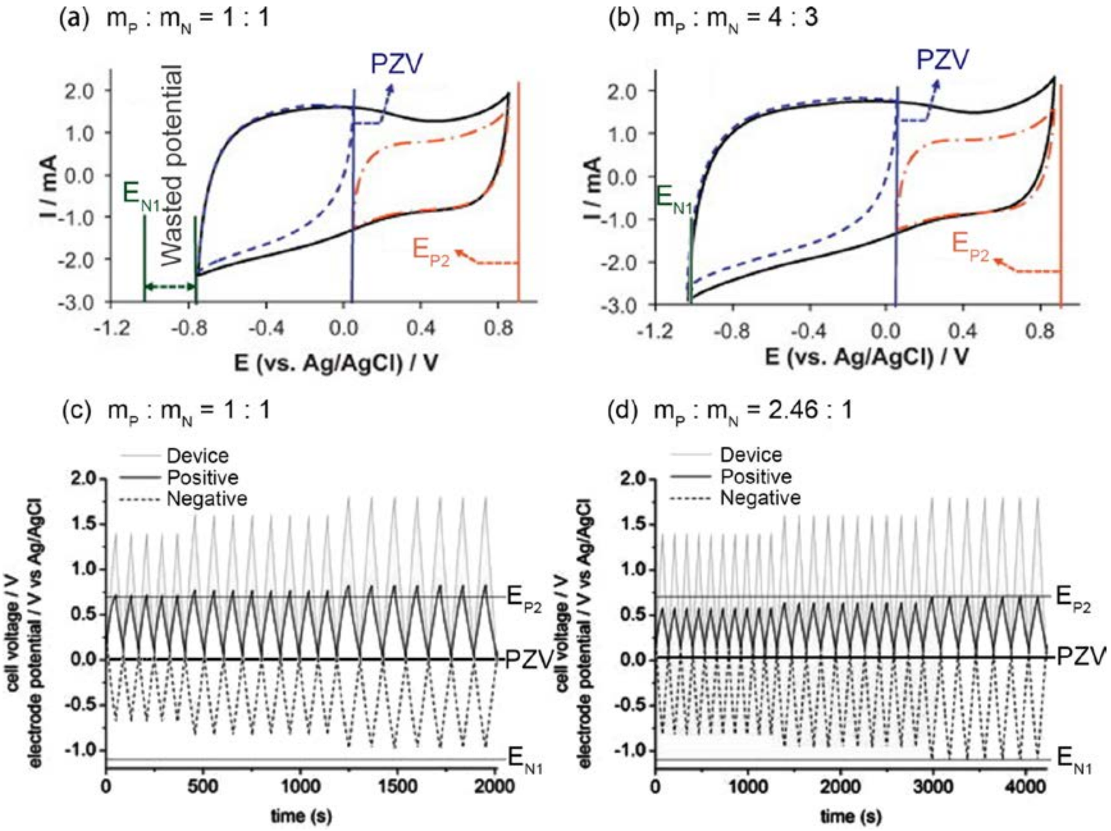

Figure 25. CV curves of a carbon electrode in a conventional three-electrode cell (0.3 mol L^{-1} K_2SO_4) with *PZV* and working potential ranges (dashed curves) determined by a T-type cell: (a) non-optimized and (b) optimized. GCD curves of device and electrodes at an operating voltage of 1.4, 1.6 and 1.8 V with E_{P2} and E_{N1} determined by a conventional three-electrode cell: (c) non-optimized and (d) optimized. Adapted from [35] and [36].

3.1.2.3 Method 2 - Increasing the specific capacitance of the voltage-limiting electrode

Similar to the increase of m_P, a higher value of C_P (while keeping others unchanged) leads to the same effect that E_N is stretched according to Equation (21).

It is worth noticing that a symmetric device might not be optimal. For symmetric EDLCs with the same porous carbon on both sides, the specific capacitance of positive and negative electrodes are *NOT* equal. A maximized specific capacitance is achieved when matching the pore size with the ion size [97, 126]. The sizes of cations and anions in an electrolyte are different, leading to a different degree of matching thereby different capacitances on the two electrodes.

Therefore, one can construct an asymmetric device by using a different carbon material with respect to the selection of electrolyte ions, in order to increase C_P and optimize V_{max}. This method could retain the most power capability and cycling stability of EDLCs. A more substantial change to the system is through replacing carbon with a pseudocapacitive material. This falls into the field of asymmetric pseudocapacitors. Except for a high specific capacitance, another possible beneficial aspect of using pseudocapacitive materials is a high H_2O decomposition overpotential. For example, a high OER overpotential on a MnO_2/CNTs composite was found independent of the electrolyte pH [127] as shown in Figure 26a. Thermodynamically, OER potential at pH = 10 is 0.64 V and at pH = 6.4 is 0.85 V vs. NHE (normal hydrogen electrode). Experimental results show that the MnO_2 material can be polarized to a much higher potential without showing oxygen evolution, making it a suitable positive electrode material candidate. The maximum operating voltage of a device with an activated carbon negative electrode is possible to be over 2 V with optimization (Figure 26).

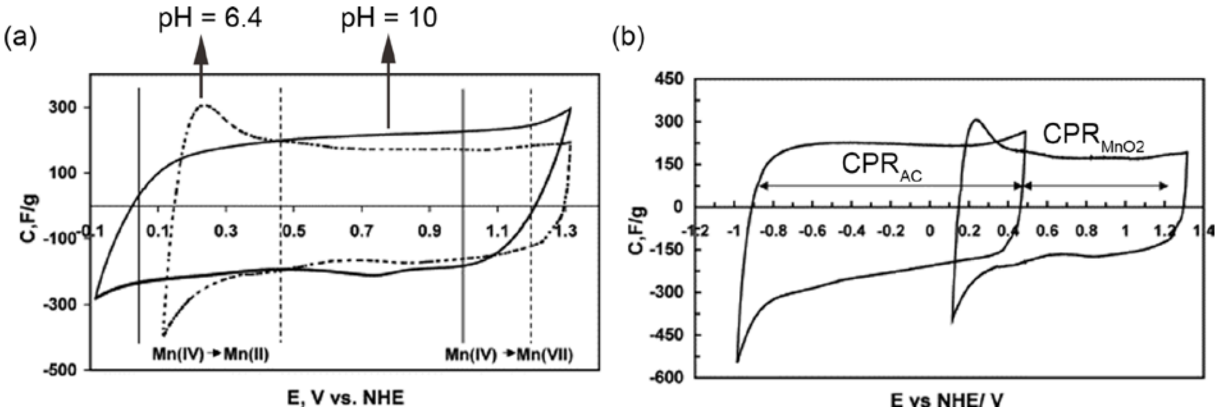

Figure 26. CV curves of MnO_2 in KOH (pH = 10) and KNO_3 (pH = 6.4) and (b) CVs of activated carbon and MnO_2 in KNO_3 solution (pH = 6.4) [127].

Further, replacing the carbon electrode with another pseudocapacitive material will result in asymmetric devices based on all pseudocapacitive electrodes [112]. Constructing this type of devices is an effective approach to maximizing V_{max} in aqueous media, but the application of organic electrolytes for a further boost in voltage limit remains a challenge [8]. Moreover, it is rather clear that a lack of cycling stability is a barrier for this type of devices to be applied in self-powered systems - a considerable amount of demonstrations show a capacitance retention less than 90% over only 5 000 cycles. A solution to this problem relies rather on materials development.

3.1.2.4 Method 3 - Pinning the electrode potential of the voltage-limiting electrode

Another way of perceiving "increasing the capacitance" is slowing down the rate of potential increase during charging, i.e. a smaller slope on its GCD curve. Along this line, an extreme situation is that the potential of the voltage-limiting electrode (E_P in the case of Figure 23) is "pinned" at a certain value, then the potential range of the other electrode is thus stretched according to Equation (21). Pinning the electrode potential is effectively introducing a battery-like behavior which displays a plateau on GCD curves, and therefore hybrid ECs. Since battery behavior cannot be interpreted as capacitance, Equation (21) is converted to Equation (25) for those devices with a battery-like behavior appears on the positive electrode, or Equation (26) for those on the negative electrode.

$$m_P Q_P = m_N C_N E_P \qquad \text{Equation (25)}$$

$$m_P C_P E_P = m_N Q_N \qquad \text{Equation (26)}$$

where Q_P and Q_N refer the specific capacities (C g^{-1} or mAh g^{-1}) of the battery-like electrodes.

It is a perspective that among the two general methods constructing hybrid ECs (incorporating battery electrode material or employing redox electrolytes), the use of redox electrolytes is more effective to improve the energy while keeping the high power and cycling stability since it is developed on the base of EDLCs. The dimensional change caused by e.g. intercalation/deintercalation reactions of battery electrodes significantly impacts their lifetime, detrimental for IoT applications.

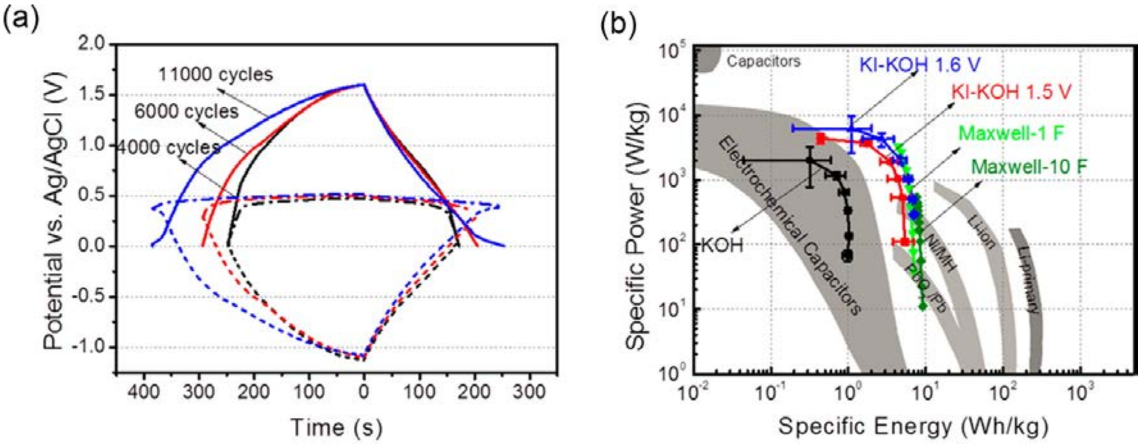

Figure 27. (a) GCD curves f device and electrodes at 1.6 V with KI-KOH electrolyte. (b) Ragone plot comparing energy and power densities with other systems [128].

An example of pinning electrode potential is shown in Figure 27 where the electrolyte is 4 M KI mixed with 1 M KOH [128]. Faradaic energy storage originates from iodine related reactions as

$$I^- + 6OH^- \rightarrow IO_3^- + 3H_2O + 6e^- \qquad \text{Equation (27)}$$

The reaction generates a long plateau on the positive electrode, making the electrode potential E_P to be pinned at around 0.5 V vs. Ag/AgCl reference electrode (Figure 27a). The negative electrode potential is stretched to as low as around -1.1 V, with its *CPR* range fully exploited. The pinned potential prevents the potential going further to invoke OER, therefore H_2O is protected from decomposition by the redox reaction. V_{max} of the aqueous electrolyte device is high up to 1.6 V, even with the presence of an alkaline KOH. The device operating at 1.6 V shows an improved energy density and an EC level power density is retained in this system (Figure 27b).

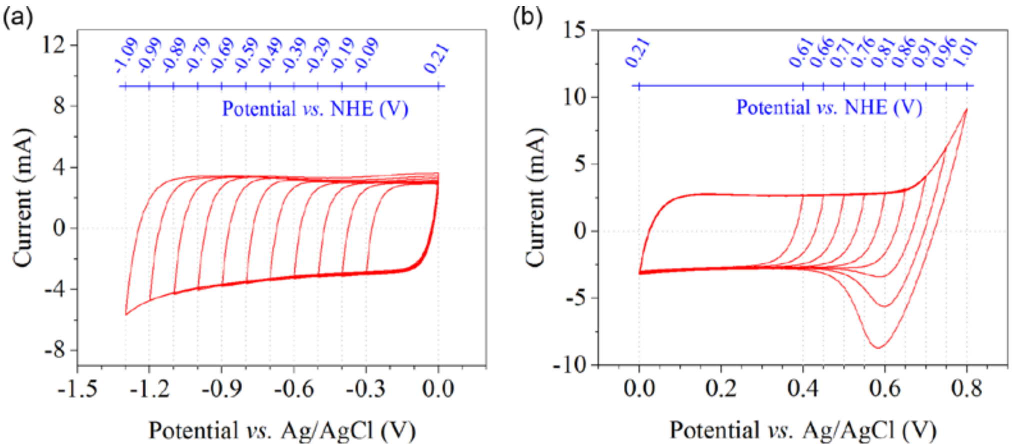

Figure 28. (a) Negative and (b) positive CV scans in a three-electrode cell with 1 M KBr (Paper I).

In Paper I, we have found that KBr in a simple form of salt is an effective redox-active electrolyte and also displays a pinning effect. The redox reaction starts to take place in terms of

$$3Br^{-} \rightarrow Br_3^{-} \qquad \text{Equation (28)}$$

at a potential of about 0.65 V *vs.* Ag/AgCl, determined by CV scans of 1 M KBr with an AC working electrode (Figure 28b). The cathodic current during the negative scan (Figure 28a) increases continuously with the voltage ramping. No dramatic change is observed until -1.30 V although it seems -1.2 V is around the limit for a pure capacitive behavior. This indicates that large overpotential of HER exist on the negative electrode. If E_{P2} is pinned by the redox reaction, E_{N1} will be stretched to a low potential and then a large V_{max} can be expected.

Table 5. Performance metrics of the KBr-containing device at different voltages [a] (Paper I).

V_{max}	0.8 V	1.0 V	1.2 V	1.4 V	1.6 V	1.7 V	1.8 V	1.9 V
Specific capacity, $Q_{electrode}$ (mAh g^{-1})	16.8	20.8	25.6	32.4	38.0	41.6	44.8	48.8
Specific capacitance, $C_{electrode}$ (F g^{-1})	75.2	77.2	80.4	83.2	85.2	88.4	89.6	92.0
Specific energy, E_{device} (Wh kg^{-1})	1.7	2.7	4.0	6.1	8.0	9.4	10.6	12.0
Coulombic efficiency, η_C (%)	99.7	99.7	99.6	99.4	98.7	97.9	97.2	97.5
Energy efficiency, η_E (%)	95.2	95.6	95.8	94.3	93.3	91.4	89.0	87.6

[a] The numbers presented in this table are average values of 100 cycles at specified voltages at 1 A g^{-1}.

We measured the performance of a KBr-containing device with two identical AC electrodes at different V_{max} shown in Figure 29a-b. The performance metrics extracted from GCD measurements are listed in Table 5. The experiment indicated that the device can reach 1.9 V without compromising stability in this aqueous system, which is remarkable considering the simplicity of the system. The electrode potential values were recorded using the T-type Swagelok cell. As shown in Figure 29, E_{P2} finally tends to saturate at around 0.8 V vs. Ag/AgCl when the cell operates at 1.9 V, which is close to the standard electrode potential of 0.84 V vs. Ag/AgCl for the redox reaction. Accordingly, E_{N1} eventually decreases to about -1.1 V. The 1.9 V high voltage aqueous device shows considerable improvement in energy density and its power density remains high (Figure 29d). Moreover, the energy efficiencies are still high as 87.6% when battery-like reactions are heavily involved at 1.9 V.

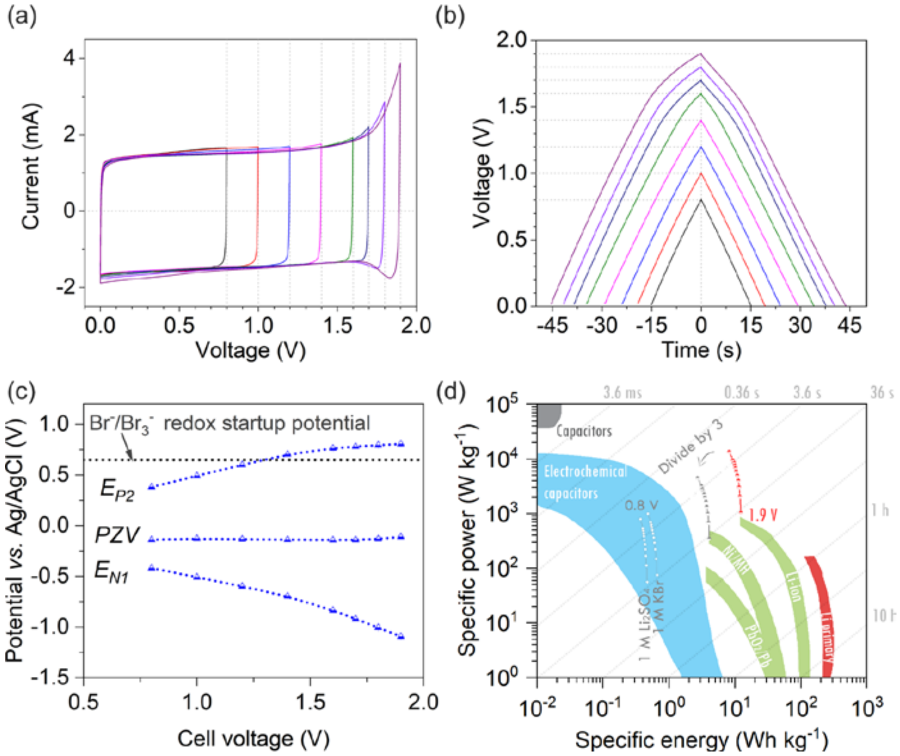

Figure 29. KBr-containing device: (a) CV scans and (b) GCD curves from 0.8 to 1.9 V, (c) variation of electrode potential as a function of operating voltage, and (d) Ragone plot (Paper I).

The approach of pinning electrode potential seems to be effective for developing ECs for self-powered systems, in terms of increasing energy at a high power and high stability. Nevertheless, one should be cautious about the complexity of the system. The introduction of redox activity causes *voltage-dependent behavior* - it behaves as pure EDLC up to 1.6 V, and then hybrid features appear from 1.7 V and above. Moreover, we have also observed a *history-dependent behavior*. As shown in Figure 30, GCD curve "swells" with the cycling process at 1.9 V operation. If the device is pre-cycled at 1.9 V for 500 cycles and then operated at 1.6 V, a small portion of redox activity is "triggered", evidenced by the changing of the GCD curve slope towards the high voltage (Figure 30c), in contrast to the pure EDL behavior when directly operated at 1.6 V (Figure 30a). We donate the pre-cycling process as "triggering operation". The history-dependent behavior is accompanied by a variation of E_{N1}, E_{P2}, and *PZV* caused by complex redox chemistry as well as the transport and storage of redox-active ions. We believe the observations are not unique to KBr, but also to other redox enhanced EDLC systems. Therefore, one should be aware of these changes in storage mechanism, and evaluate them carefully before bringing them into practical application.

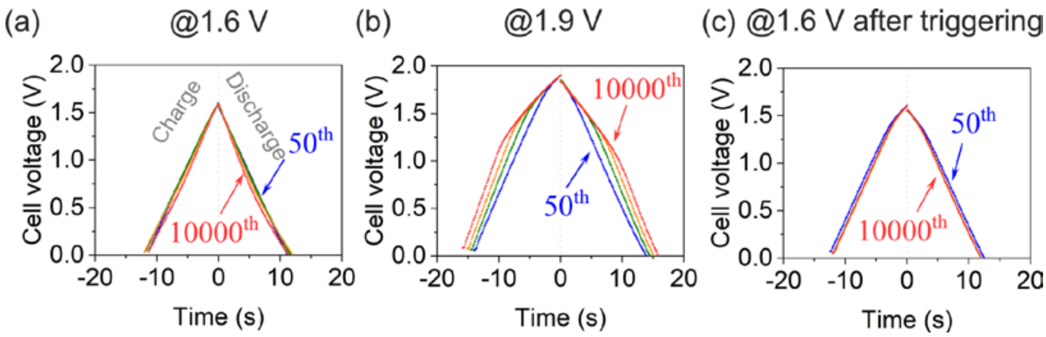

Figure 30. The history-dependent behavior of KBr-containing devices: GCD curves at specified cycle numbers at (a) 1.6 V, (b) 1.9 V and (c) 1.6 V after a triggering operation (Paper I).

3.1.2.5 Method 4 - Tuning PZV

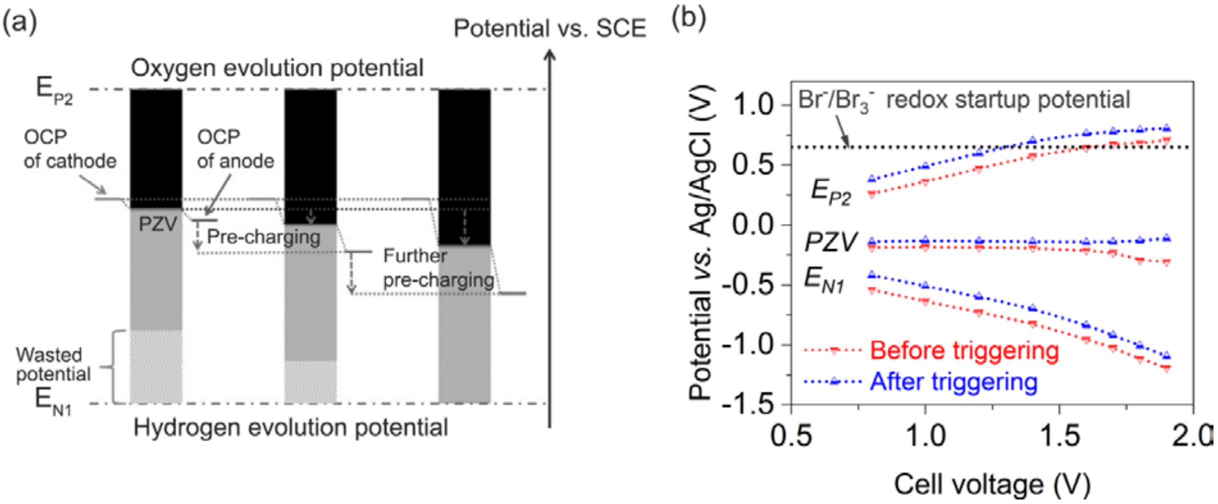

Figure 31. (a) Schematic of *PZV* tuning to maximize operating voltage window [129], (b) *PZV* and electrode potential shift after triggering operation in KBr-containing system (Paper I).

PZV is a reference point of potential with respect to which the two electrodes starts to work against. If *PZV* can be tuned to shift away from the *CPR* of the voltage-limiting electrode, V_{max} is enlarged. For example in Figure 23, a downshift of PZV towards E_{P1} would exploit the maximum *CPR* of the positive electrode, and at the same time, working potential of the negative electrode is enlarged accordingly with regard to a balanced charge flow i.e. Equation (21). Therefore, *PZV* is an important parameter that affects V_{max}, however, it is difficult to predict its exact value in practice, but it is located within the open-circuit potentials of the positive and negative electrode. It is believed that when operated at 0 V, there is a fast potential balance between the two electrodes and *PZV* is determined when the balancing process reaches equilibrium [129]. Along with this vein, researchers pre-charged the voltage-limiting electrode (positive electrode) at lower potential values than its OCP in a conventional three-electrode cell, then assembled the device with the pre-charged positive electrode, and managed to downshift *PZV* to from 0.17 to -0.1 V vs. SCE (standard calomel electrode). The downshift of *PZV* leads to a utilization of wasted potential on the negative electrode, and finally optimized $V_{\max}$ from 1.4 to 1.8 V in 5 M LiCl electrolyte [129]. The schematic of *PZV* tuning by pre-charging is shown in Figure 31. Besides the pre-charging method, there can be other applicable methods, especially when redox reactions involve and the surface charge of the electrode become complex. The complexity can allow for the possibility of more tuning methods or even self-adjustment of *PZV*, e.g. *PZV* shift caused by triggering operation in the KBr-containing system. Future efforts are needed to manipulate the *PZV* more effectively and productively.

3.1.3 Remarks

Improvement of the energy density of ECs relies on a joint effort of both materials science and device engineering. The insight from the viewpoint of *electrode potentials* and a simple theoretical consideration of Equation (21) help to optimize device performance. In the process of enhancing energy, one should be aware of the influence on power and cycling stability, and critically evaluate the device in accordance to application requirements. Among the presented strategies, methods and examples, it is a perspective that high voltage redox electrolyte based EDLC systems is promising for applications in self-powered systems. KBr redox electrolyte enables battery-level energy density with EC-level power density and cycle life, and also very high energy efficiency. The complex yet interesting redox electrochemistry of redox electrolytes allows the possibility for performance manipulating through a triggering operation or *PZV* tuning, while the continuous change of GCD curves at high voltage operation might cause difficulty to accurate power management.

3.2 Towards high operating voltage limit

3.2.1 Bipolar design

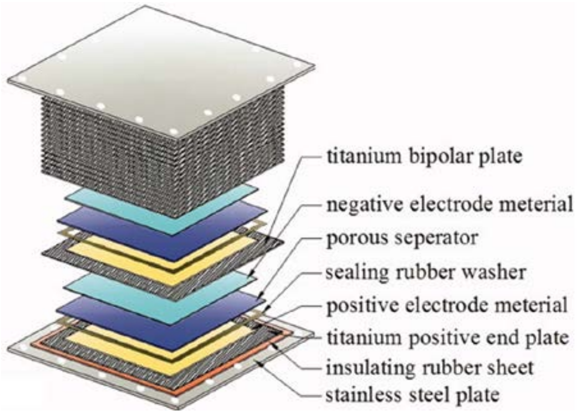

Figure 32. Bipolar design [130].

The maximum operating voltage limit $V_{\max}$ of a single device is determined by the electrode and electrolyte materials and can be optimized through device engineering with the methods stated in the last section. Normal $V_{\max}$ of single devices is 1 to 3 V. For applications that require higher voltage than 3 V, one can use two or even more devices connected in series. The bipolar design aims for higher space-efficiency of series-connection of multiple devices.

In essence, a bipolar design is simply to stack devices, but through bipolar electrode plates. A bipolar electrode plate can serve as a current collector for a positive electrode in one cell, while as a negative electrode's current collector in the adjacent cell. In this way, only N+1 plates are needed for stacking N devices, while normal stacking requires 2N plates together with 2N individual packages. An example of a bipolar device is shown in Figure 32. This device uses titanium as the bipolar plate, and the unit cells are insulated by rubber rings. With this configuration, researchers fabricated a 20 V bipolar device consisting of 19 PPy-CNTs (+) | 3 M KCl | CMPB (-) cells [130]. Other examples of bipolar design devices can be found in references [131-135]. Besides, the author has developed bipolar device prototypes with 3 unit cells encapsulated in CR1220 coin cells for a project application. Graphite papers were used as the bipolar plates, and water-proof double-sided tape was employed for insulation.

3.2.2 Remarks

The bipolar design is desired for high-frequency ECs as the one in Paper III, which utilize a KOH electrolyte and thus $V_{\max}$ of a single device is limited to less than 1 V. A bipolar design is a device-level engineering approach which can absolutely achieve high operating voltages that are not achievable for single devices. Energy and power densities (per weight) of a bipolar cell is at the same level as its unit cells, but the bipolar design is advantageous over the design that externally connects multiple devices, because a bipolar device needs less packaging and current collector materials. Exploiting lighter materials for bipolar plate can further strengthen this advantage. Moreover, when using high voltage bipolar devices for low voltage applications, each unit cell works at only 1/N of the voltage applied on the device, which is beneficial for achieving slow self-discharge or low leakage current, as well as high cycling stability.

The main drawback associated with a bipolar design is its relatively complicated manufacturing process. Unit cells must be isolated from each other, which is challenging when using liquid electrolytes, and especially when fabricating miniature devices for microsystems. Employing solid- or quasi-solid-state electrolytes can alleviate the problem. Furthermore, the bipolar design requires high uniformity of unit cells, meaning that the cells should have the same capacitance, working voltage range, etc. Otherwise, the system is not balanced and lifetime is thus seriously shortened, similar to battery system balancing. Another concern comes with the fact that malfunction of any unit cell in a series connection leads to a failure of the whole device. Therefore, the bipolar design poses very high requirements on manufacture engineering.

3.3 Towards extreme temperature operation

For extreme temperature performance, the electrolyte is the most critical component. At low temperatures, energy and power are limited by ionic conductivity of the electrolytes, while electrolyte decomposition causes safety and reliability issues at high temperatures. Therefore, kinetics-related parameters (such as ionic conductivity) and thermal stability properties are the main factors when evaluating electrolyte for extreme temperature operations.

The influence of temperature on electrolyte physicochemical properties is presented in Figure 33 [136]. Temperature change directly alters the ionic conductivity, viscosity and diffusion coefficient, and the latter two factors are highly relevant to ionic conductivity via different governing rules. All the variations are reflected by the capacitance and *ESR*. The intrinsic properties of an electrolyte, i.e. glass transition temperature (T_g) and decomposition temperature determine the usable temperature range, and T_g also influences ionic conductivity of particularly solid- or quasi-solid state electrolytes. The relation network should help scrutinize electrolyte options for ECs that target extreme working temperatures.

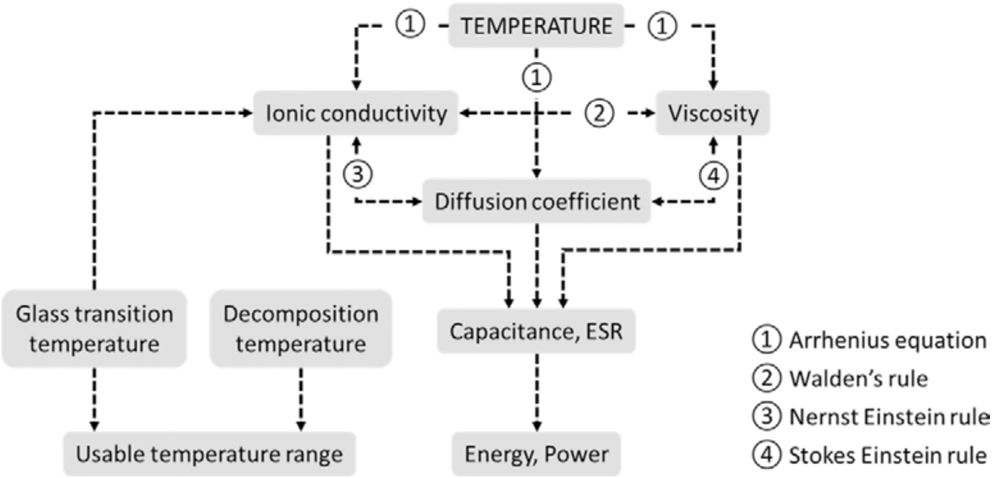

Figure 33. Relation network of temperature and different properties of electrolytes.

3.3.1 Towards extreme low-temperature

3.3.1.1 Aqueous electrolyte systems

It is of industrial interest to develop low-temperature ECs based on aqueous electrolytes because of their low cost compared to other counterpart electrolytes. Aqueous electrolytes typically cease to work when temperature below -10 °C, because most electrolytes start to freeze and solubility of salts sharply decrease which significantly diminishes ionic conductivity, although -52 °C was reported for RuO_2 pseudocapacitor using 39 wt% (5.26 M) H_2SO_4 without no additional treatment [137].

To extend the low-temperature limit, industrial anti-freeze (ethylene glycol, methanol or formamide) can be considered as an electrolyte additive that maintains a liquid phase at extremely low temperatures. An anti-freeze agent of ethylene glycol was added into Li_2SO_4 and achieved a limit of -20 °C for an EDLC [138]. The addition of the same agent into solutions of sodium, lithium, potassium and ammonium sulfate resulted in -30 °C aqueous electrolytes for a MnO_2/carbon pseudocapacitor, and it was found that the addition of ethylene glycol increases viscosity and decreases ionic conductivity [139], therefore alternative electrolyte systems have been developed. Methanol, an alternative to ethylene glycol, was used as an anti-freeze additive in a $NaClO_4$ electrolyte for AC based EDLCs, and a limit of -40 °C was achieved at an operation voltage window of 1.2 V [140]. Further, a 1.6 V window operating at -40 °C in 7:3 volume ratio water/methanol Li_2SO_4 system was reported demonstrating reasonable EDL behavior [141]. In addition, formamide was also used as an anti-freeze agent, and an electrolyte of calcium chloride ($CaCl_2$) dissolved in formamide/water (1:1 volume ratio) was proposed as an electrolyte for down to -60 °C application in a CNTs-based EDLC system.

In general, the use of anti-freeze extends the low-temperature limit, but at the same decreases solubility of salts due to a low dielectric constant of the organic moiety promoting ionic association [142], resulting in low conductivity and impairing room temperature performance. For example, the solubility of Li_2SO_4 is reduced to around 0.7 M in water/methanol (7:3 volume ratio) mixture and the conductivity decreases to 40.6 mS cm^{-1} compared to 64 mS cm^{-1} for 1 M Li_2SO_4 in water at 24 °C, correspondingly capacitance drops from 103 to 89 F g^{-1} for the mixture [141]. In an effort of searching highly conductive neutral (for high voltage operation) electrolytes that withstand freezing conditions, binary mixtures of cholinium chloride $[HOCH_2CH_2N(CH_3)_3]^+Cl^-$ 5 mol kg^{-1} water solution was recently demonstrated as a low-temperature electrolyte capable of working as low as -40 °C with little capacitance loss compared to room temperature performance (from 126 to 106 F g^{-1}) [143].

3.3.1.2 *Organic electrolyte systems*

Many commercial ECs can already work reliably at a low-temperature of -40 °C based on ACN based organic electrolytes. A further extension of the limit is restricted by similar concerns as for aqueous electrolytes, i.e. freezing point of the solvent, the solubility of salts and viscosity, etc. Accordingly, methods of extending low-temperature limit of organic electrolytes include using low freezing/melting point solvent or use such chemicals as co-solvent and employing salts of high solubility to maintain adequate ionic conductivity and minimize *ESR* at low temperatures [144-148].

Adding low melting point co-solvent (such as formates, esters, and cyclic esters) into the $TEABF_4$/ACN electrolyte can enable carbon EDLCs working at -75 °C but the limit is -55 °C with a moderate *ESR* value [144]. Interestingly, the study found that the capacitance value shows less dependency on the electrolyte variation, while *ESR* seems to be quite sensitive. By employing a zeolite-templated porous carbon as the electrode, a low-temperature limit of -70 °C was demonstrated in $SBPBF_4$ (spiro-(1, 1')-bipyrrolidinium tetrafluoroborate) in ACN to show up to 86% of the energy density available at room temperature [147]. Note that the addition of co-solvents could limit the upper-temperature tolerance to 50 °C [149].

3.3.1.3 *Ionic liquid electrolyte systems*

Ionic liquids are well known for their high thermal stability that is suitable for high-temperature operations, however, ILs are restricted for low-temperature applications due to high viscosity, a melting point that is greater than 0 °C, and low conductivity. Strategies to enhance low-temperature performance includes mixing an IL with organic solvents [150-152] and mixing an IL with another IL [149, 153-156]. The former strategy improves ionic conductivity at a cost of thermal stability. Comparably, eutectic mixture of ILs represents an important direction to very wide temperature range electrolytes.

Eutectic mixtures of ILs have large stable liquidus temperature range (the span of temperatures between the freezing point and boiling point of a liquid). The size and symmetry of cations strongly influence the melting points of ILs. Usually, one of the two pairing ions (usually the cation) is particularly large and possesses a low degree of symmetry, leading to inefficient packing of the large irregular cations with small charge-delocalized anions, which is why organic salts have a reduced crystal lattice energy and hence a lower melting point compared to inorganic salts [153].

It was demonstrated that the selection of a proper combination of cations with the same anion prevents an ordered arrangement and crystallization, thereby inhibiting the formation of a lattice. The liquid state of the mixture can then be maintained several tens of degrees lower compared to ILs taken individually [149]. A eutectic mixture of N-methyl-N-propylpiperidinium bis(fluorosulfonyl)imide ($PIP_{13}FSI$) and N-butyl-N-methylpyrrolidinium bis(fluorosulfonyl)imide ($PYR_{14}FSI$) was used as the EC electrolyte in conjunction with exohedral nanostructured carbon (CNTs and OLC) electrodes. The system exhibits a remarkable working temperature range from -50 to 100 °C as shown in Figure 34, with a liquid state maintained down to -80 °C [149]. Recently, a new eutectic IL mixture based on 1-ethyl-3-methylimidazolium bis(trifluoromethylsulfonyl)imide (EMImTFSI) and 1-propyl-3-methylpyrrolidinium bis(trifluoromethylsulfonyl)imide (PMPyrrTFSI) was developed and the low temperature limit has been lowered to -70 °C [157].

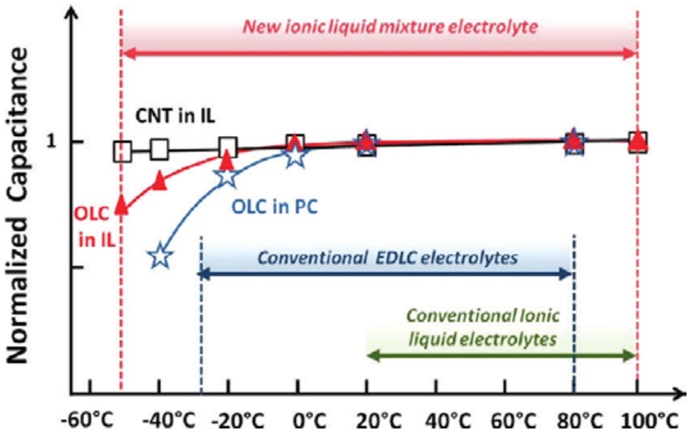

Figure 34. Change of capacitance versus the temperature for OLC and CNT electrodes in $PIP_{13}FSI$-$PYR_{14}FSI$ eutectic IL [149].

3.3.1.4 *Solid- or quasi-solid-state electrolyte systems*

Solid- or quasi-solid-state electrolytes have an advantage in high package compatibility for leak-proof encapsulations and find applications in consumer electronics, microelectronics, and wearable or printable electronics. Application of this type of electrolytes for low-temperature operation is challenging, as their ionic conductivity is already moderate at room temperatures (at a level of 10^{-3} S cm^{-1}). There has been no comprehensive work addressing the low-temperature performance of solid-state electrolytes, but it was shown that the PVA/KOH based electrolyte is capable of working at -20 °C for a NiO-AC system [158].

Ionic conductivity in solid- and quasi-solid-state electrolytes is governed by the concentration of dissociated carrier ions and their mobility. The mobility is highly relevant to the polymer matrix applied. Therefore, it could be beneficial to use low T_g polymers in order to facilitate ion movement.

3.3.2 Towards extreme high-temperature

3.3.2.1 *Aqueous electrolyte systems*

Limited by the water evaporation issue, aqueous electrolytes are not likely to be used at very high temperatures above 80 °C. Some research work demonstrated H_2SO_4 aqueous electrolyte can be operated at up to 73 °C at a 17% capacitance drop compared to room temperature [137]. The capacitance drop can be explained by the increasing thickness of the Helmholtz layer (increased charge separation distance d thus a decreased C in Equation (2) caused by accelerated Brownian motion [159].

Unfortunately, there seems no solid solution from materials development point of view to address the issue. Instead, one can apply thermal management (cooling) systems for aqueous EC packs to keep the temperature constant, however, this measure increases cost and reduces energy density and reliability, and more importantly, it necessitates maintenance which is against the vision of IoT systems and adding a cooling system is basically impractical for miniaturized systems. Therefore, aqueous ECs are not recommended for high-temperature applications.

3.3.2.2 *Organic electrolyte systems*

Typical upper-temperature limit for organic electrolytes is 70 °C. Under extreme high-temperature operation, an organic electrolyte undergoes decomposition causing safety issues and impairing the cycling stability.

PC and ACN based organic electrolytes are most common among commercial products and in research reports. Comparably, PC are less thermally stable than ACN (although in some cases PC based organic electrolytes are used up to 100 °C [160]). ACN has a boiling point of only 80 °C and it is not recommended for temperatures above 70 °C due to safety concerns. In the event of abusive electrical, thermal, or mechanical conditions, a very toxic substance of hydrogen cyanide can be generated. ACN also has a low flash point of about 5 °C, which also poses safety issues. In general, organic electrolytes are not suitable for extreme high-temperature applications, the same as aqueous ones.

3.3.2.3 Ionic liquid electrolyte systems

Ionic liquids are an important candidate for constructing ECs that can withstand extreme high-temperature conditions, due to their high decomposition temperature (typically 200 to 400 °C [161]). Thermal stability of ILs is influenced by water and impurities [162]. In principle, ILs can be used at an operating temperature below the decomposition point. However, at extremely high temperatures, the interaction between different components (electrode, binder, current collector and electrolyte) becomes predominant thus limiting operations under extreme conditions. Moreover, at high temperatures, the thermal expansion of components is not negligible. We have observed that the Swagelok cells (with stainless steel current collector and a Teflon jacket) are not suitable for high-temperature experiments, because of the mismatch in thermal expansion efficiencies of different materials of components. Likewise, coin cells configuration is not qualified because the pressure build-up at relatively high temperatures destroys the encapsulation, and the plastic gasket ring is not thermally stable. Above reasons may justify why a good amount of work demonstrating IL electrolyte working at high temperatures from 60 to 80 °C, while it is rarely reported above 100 °C. To deepen the knowledge of the performance of IL above 100 °C, special measurement set-up may be necessary.

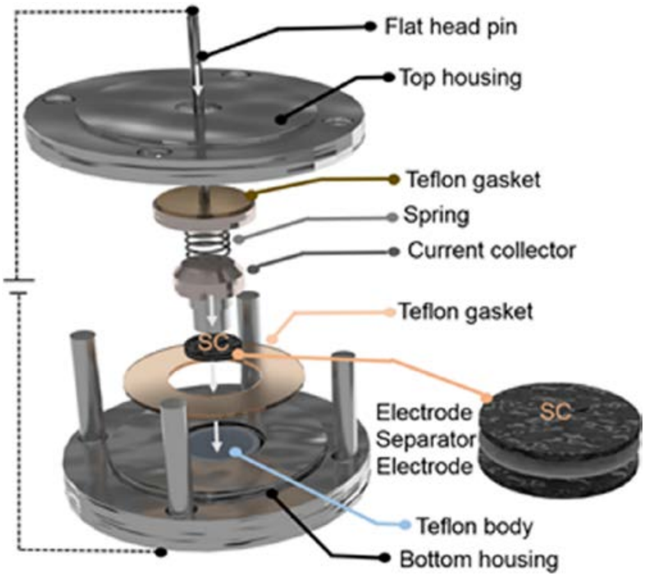

Figure 35. Schematic of the customized chamber and EC cell assembly (Paper II).

In Paper II, a measurement setup for temperatures above 100 °C is custom-made and shown in Figure 35. The customized setup consists of a top and a bottom housing made of stainless steel. The housings provide one end connection to the EC cell from an external power supply. The second end connection is maintained by a flat head pin (made of stainless steel) through the top housing. A thin Teflon gasket is kept between the top housing and the flat head pin in order to avoid any connection with the rest of the housings. The EC cell is placed inside a cavity of the bottom housing. The cell is separated from the wall of the cavity by an inner Teflon body to make sure that the external connection through the housings is maintained only at the one side of the cell. A thin Teflon gasket on the surface of the bottom housing provide isolation for a piston-shaped current collector that is attached to the flat head pin with a stainless steel spring which could compensate thermal expansion issues at elevated temperatures.

3.3.2.4 Trading V_{max} for stability under extreme high-temperature operation

Although a high V_{max} results in a high energy density, it accelerates the ageing process of ECs. An increase of voltage window by 100 mV can reduce lifetime by a factor of two [163]. Charging to a voltage of 200 mV above the rated voltage can increase ageing rate by a factor of 64, equivalent to increasing temperature by 40 °C above room temperature (25 °C) [164]. Therefore, it is not uncommon to lower the voltage limit in order to gain a higher stability at high temperatures. Of particular practical significance, for neat ionic liquid electrolyte systems, this action can gain stability at no energy and power sacrifices.

With the measurement setup in Figure 35, an AC-based EDLC system with an ionic liquid electrolyte EMImAc is evaluated at up to 150 °C. Note that the selection of EMImAc as an electrolyte is mostly driven by the smart-MEMPHIS project which requires device assembly to be conducted in an uncontrolled environment and therefore the component (EMImAc) should be of low toxicity [165, 166] for staff safety. The maximum voltage limits $V_{\max}$ at different temperatures were determined by a series of CV measurements. At room temperature up to 80 °C, the limit is set at 1.5 V, while it is lowered to 1.4 V for 100 and 120 °C, and further down to 1.3 V when operating at 150 °C. The result of a thorough evaluation is listed in Table 6. Due to a high viscosity and low ionic conductivity of the neat IL EMImAc at room temperature, a large IR drop is observed leading to a usable voltage of 1.31 V. With an increased temperature, ionic conductivity increases resulting in higher capacitance and at the same time much smaller IR drop. As a result, the energy and power density are much greater at elevated temperatures than the ones obtained at RT with a higher $V_{\max}$.

Table 6. Performance metrics of EMImAc containing EC (Paper II).

Temperature (°C)	$V_{\max}$ (V)	IR drop [a] (mV)	Useable voltage (V)	Energy density (Wh kg^{-1})	Max. Power density (kW kg^{-1})	Capacitance [b] (F g^{-1})
RT	1.5	186	1.31	4.3	4.6	84
40	1.5	79	1.42	6.1	12.8	98
80	1.5	35	1.46	8.3	30.5	122
100	1.4	29	1.37	7.3	32.5	121
120	1.4	26	1.37	7.4	36.0	121
150	1.3	23	1.28	7.7	35.6	142

[a] IR drop at 3 A g^{-1}; [b] Maximum capacitance is achieved at 1 A g^{-1} while 2 A g^{-1} for 150 °C

Above observation on EMImAc can be universal to other neat IL electrolyte systems. As high temperature greatly enhances the conductivity of neat ILs and therefore increases effective voltage range during a discharge, the energy and power loss as a result of decreasing $V_{\max}$ can be minimal. It is a perspective that neat ILs are very promising candidates for extreme high-temperature operations.

3.3.2.5 Solid- or quasi-solid-state electrolyte systems

Compared to low-temperature applications, there is a great interest in using solid- or quasi-solid-state electrolytes at elevated temperatures. The accelerated ion diffusion rate in the electrolyte with less viscosity results in increased conductivity with operating temperature and good energy storage capability. H_3PO_4 doped proton-conducting film poly[2,5 benzimidazole] (ABPBI) was evaluated up to 120 °C with AC electrodes, showing capacitance increased from 197 to 248 F g^{-1} from room temperature [167]. Similarly, a H_3PO_4-doped poly-[2, 20-m-phenylene-5, 50-bibenzimidazole] (PBI) electrolyte sandwiched between two reduced graphene oxide (rGO) electrodes was demonstrated to have extremely high stability at up to 160 °C [168]. Record temperature of 200 °C was reported for an ionic liquid based ionogel [169] and another ionic liquid infilled with clays [51]. For the most common PVA based electrolytes, typical high-temperature limit is below 70 °C (T_g of PVA is 85 °C), and crosslinking of the PVA matrix may be beneficial in enhancing high-temperature performance [170].

3.3.3 Remarks

IoT systems such as wireless sensor networks with storage units are applied for a wide range of applications in diverse environmental conditions, but it is usually a very rare case when a specific application requires an extremely wide range of temperatures from extremely low e.g. -40 °C to extremely high e.g. 200 °C, which can be probably tolerated only by eutectic ionic liquids without a thermal management system. Therefore, the design is mostly application-specified towards either low temperature or high temperature.

For extreme low-temperature applications, aqueous systems are advantageous because of relatively high conductivity and low cost. For extreme high-temperature, neat ILs are a good option, and trading voltage limit for stability can be considered. The benefit of gaining stability at little or no compromise in energy and power reveal in Paper II may also be observable for other low room-temperature conductivity electrolytes such solid- or quasi-solid-state electrolytes. The use of neat ILs is also favored from a packaging point of view, as the absence of a solvent precludes an evaporation issue during a high-temperature encapsulation. In addition, special encapsulation and a package design may be necessary for extreme high-temperature ECs, taking into account the thermal expansion coefficient of the components.

This section addresses extreme temperature operation from electrolyte options viewpoint, however, the consideration of electrodes, separators, current collectors and their interaction with electrolytes may not be trivial.

3.4 Towards slow self-discharge and low leakage current

Self-discharge and leakage current are detrimental to preserving the harvested energy in a self-powered system. Especially in miniaturized systems where the magnitude of the current (converted from the harvested energy) for charging an EC is at as low as μA or even nA level. Self-discharge dissipates energy through a spontaneous voltage decay under open circuit conditions, while leakage current is relevant to consuming energy for keeping the EC at a constant voltage (for buffering battery applications) and also related to charging behavior at low current. Minimizing self-discharge and leakage current is a critical task for EC development targeting IoT applications.

3.4.1 Mechanisms and mathematical treatments

An ideally polarized capacitor has no pathway for current to leak in an open circuit, and the equivalent circuit can be represented by Figure 36a, in which charging current i_t enters through a resistance R_S into the capacitor C. For a constant voltage V applied, the variation of charging current can be calculated as

$$i_t = i_i \exp[-\frac{t}{R_s C}] \qquad \text{Equation (29)}$$

In reality, self-discharge and/or leakage current set in, and the equivalent circuit contains a potential- and time-dependent leakage resistance, R_{SD}, in parallel to the capacitor [171]. Under constant voltage charging, it is decomposed to i_C that charges the capacitor and the leakage current, i_{SD}, resulted from the self-discharge through R_{SD}. When $R_{SD} >> R_S$, self-discharge is slow and charging current is close to that charging an ideal capacitor as in Equation (29). If $R_{SD} << R_S$, the rate of self-discharge is high and a large leakage current is required to maintain charge stored in the capacitor to sustain a constant voltage.

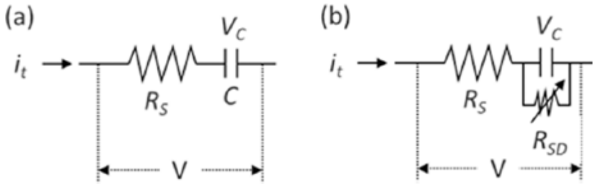

Figure 36. Equivalent circuits of ECs (a) without and (b) with self-discharge / leakage current [171].

The leakage resistance originates from different mechanisms. Conway [7] has classified them into three categories: (1) So-called activation-controlled electrochemical reaction which kinetically follows the Tafel equation. This corresponds to overcharging beyond the respective (plus or minus potential) decomposition limit of the electrolyte. The voltage decay as a function of time is mathematically represented as

$$V = -\frac{RT}{\alpha F}\ln\frac{\alpha F i_0}{RTC} - \frac{RT}{\alpha F}\ln(t + \frac{C\tau}{i_0}) \qquad \text{Equation (30)}$$

where V is the voltage at time t, R is the gas constant, T is the temperature, F is Faradaic constant, α is transfer coefficient, i_0 is the exchange current density, C is the capacitance and τ is an integration constant. Therefore, voltage declines linearly with log t. (2) Discharge through ohmic resistance, physically corresponding to any undesired imperfection of insulating material, e.g. short-circuit leakage currents between adjacent electrodes in imperfectly sealed bipolar configurations. In this case, voltage decay is in the mathematical form of

$$\frac{\mathrm{V}}{\mathrm{V}_0} = \exp(-\frac{t}{RC}) \qquad \text{Equation (31)}$$

where V_0 is the initial voltage, R is the leakage resistance. Therefore, $\ln V$ declines linearly with t. (3) Diffusion-controlled processes. It can correspond to practical examples where some depolarizing impurity is present that can undergo a Faradaic redox reaction within the potential range of charging and that for solvent stability. The dynamics of voltage decay is governed by Fick's law and in the mathematical form of

$$C(V_0 - V) = 2zFAD^{1/2}\pi^{1/2}c_0 t^{1/2} \qquad \text{Equation (32)}$$

where A is the area of flux, D is the diffusion coefficient and c_0 is the initial concentration of the diffusive species. Therefore, V declines linearly with $t^{1/2}$. The pattern of the voltage decay as a function of time is generally used to detect the mechanism of self-discharge.

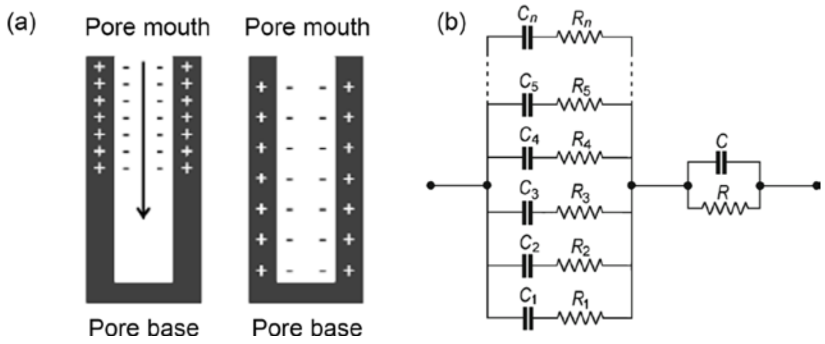

Figure 37. (a) Charge redistribution in a slit pore; (b) Vertical ladder network of TLM [172].

In porous carbon electrodes, *charge redistribution* is an important phenomenon relating to self-discharge [172, 173]. Graphically, charge redistribution within one slit pore is displayed in Figure 37a, where the charge is first accumulated at the pore "mouth" and distributed down to the pore base gradually. To simulate the charge redistribution effect in porous carbon structures, transmission line model (TLM, different RC sub-systems forming a ladder-like circuit) as shown in Figure 37a can be employed. Each R_iC_i system has its own characteristic time τ_i (not necessarily equal to another time constant τ_j), at which it may be charged or discharged. The circuit is proposed to be universal for any porous electrode having non-branching pores [172]. Due to different time constants, the system cannot be charged synchronously, implying that smaller τ_i of RC circuit are firstly charged up and then the charge is redistributed throughout, causing apparent voltage decay, i.e. self-discharge. It was proven that charge redistribution leads to the same mathematical expression of voltage decay as activation controlled Faradaic reactions [173].

For a practical EC, the mechanism of self-discharge and leakage current can be "hybrid", but takes mathematical forms of above. Therefore, the voltage decay can be eventually simulated with the equation below

$$V(t) = V_0 - a\exp\left(\frac{t}{\tau}\right) + bln(t) + c\sqrt{t} \qquad \text{Equation (33)}$$

where a, b and c are all constants [174].

3.4.2 Influences of charging history and temperature

The charging history and the ambient temperature significantly influences the rate of self-discharge and leakage current [175]. Applying a small $V_{\max}$ and charging current, hold the voltage for a long duration at a low temperature will lead to minimal self-discharge and leakage current.

The observation for porous carbon-based ECs can be understood by the charge redistribution model. Bearing in mind the role of pores with different sizes (Figure 21), bigger pores at the periphery adsorb/de-adsorb ions at a faster rate than meso- and micropores due to the higher resistance of the latter. Upon charging at high current for a short period of time, ions accumulate at the big pores and the small pores remain unoccupied. A charge redistribution process will then set in so that the meso- and micropores reach an equilibrium potential with the big pores, and a rapid voltage decay will be observed. However, if the EC is charged for a long time before being open-circuited, the ions reach the micropores of the electrode, and this sudden voltage drop can be averted. The time constant of charge redistribution for porous carbon-based ECs can be more than 50 hours [173]. A low charging current will allow more time for ions distribution into small pores, which in turn alleviate fast voltage decay.

Regarding temperature, Arrhenius equation is used to model its relation with self-discharge current I, in connection to leakage current, and temperature T

$$I(T) = A\exp[-\frac{\Delta E_a}{RT}] \qquad \text{Equation (34)}$$

where E_a is in the order of 40-80 kJ mol^{-1} for Faradaic processes, and 16-20 kJ mol^{-1} for diffusion-controlled processes. Assume an E_a of 40 kJ mol^{-1}, the leakage current is 37 times higher at 70 °C than at 0 °C.

3.4.3 Suppressing self-discharge and leakage current

Similar to batteries, a charged EC is at a relatively high free energy state compared to its discharged state, therefore the phenomenon of self-discharge and leakage current is thermodynamically driven. It cannot be totally prohibited but the process can be kinetically slowed down to a certain degree until meeting application requirements.

To find a solution, one can first identify the mechanism based on the mathematical simulation discussed in section 3.4.1. It is advised to employ three-electrode systems to identify the individual behavior of two electrodes [7, 176]. This procedure is useful if there are different mechanisms or rates of self-discharge at the positive and negative electrodes, which is usually the case. For example, Chen and co-workers [177] used this method and identified that in a hydroquinone/H_2SO_4 redox electrolyte system, self-discharge takes place through the shuttle of redox species BQ (*p*-benzoquinone) between the two electrodes. Accordingly, remedies including using an ion-exchange membrane Nafion® 117 as a separator to block the diffusion pathway of BQ, or selecting a redox electrolyte which is converted into insoluble species during a charging process. Besides, Tevi et al. [178] proposed to deposit an ultra-thin layer of poly (p-phenylene oxide) (PPO) to block electron transfer to prevent reactions related to redox-active impurities of the electrode or electrolyte. Adding electrolyte additive such as surfactants of sodium dodecyl sulfate (SDS) and p-t-octylophenol (Triton X-100) [179], as well as a liquid crystal of 4'-Pentyl-4-biphenylcarbonitrile (5CB) [180], have also been reported to be effective solutions in suppressing self-discharge.

In paper III, we found that the utilization of a GPE electrolyte with graphite/VACNTs electrodes could alter the self-discharge mechanism and result in low loss ECs, compared to aqueous systems. As shown in Figure 38a, 85% of initial voltage was retained after 10 min open circuit for the PVA/H_3PO_4 device, 12% higher than that with a KOH electrolyte. In another comparison in Figure 38b-c, mathematical analyses suggest that the self-discharge mechanism could have been altered by using a different electrolyte. For the gel electrolyte, the self-discharge curve can be fairly well fitted with a governing equation derived from Fick's law, i.e. voltage decays linearly with $t^{1/2}$, suggesting that the self-discharge may mainly originate from diffusion controlled processes while ohmic or Faradaic processes have little contribution. On the other hand, the curve of the device with a KOH electrolyte cannot match any single mechanism, indicating that its self-discharge is governed by multiple processes. The results demonstrate the possibility of achieving slower self-discharge / lower leakage current and capacitive behavior at extremely low current through the kinetics restriction in the electrolytes. However, it should be noted that the effectiveness of using a gel electrolyte for reducing self-discharge in *porous* structures may require special attention to device fabrication, especially to ensure the penetration of gel electrolyte into the porous matrix.

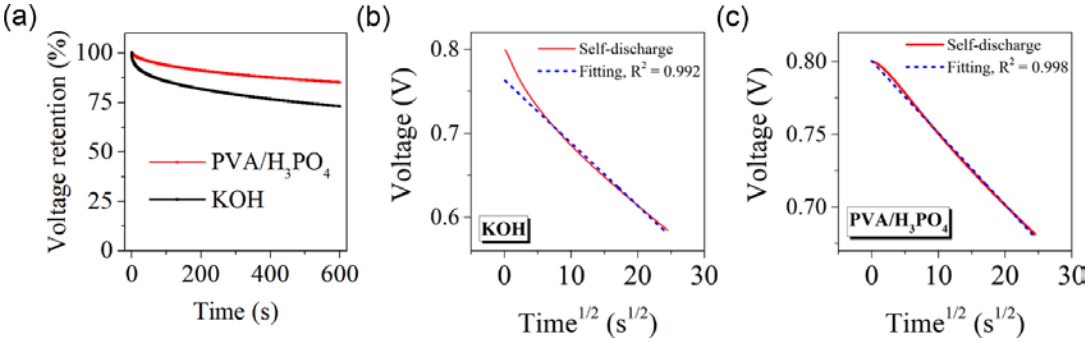

Figure 38. (a) Comparison of self-discharge of graphite/VACNTs electrodes with a PVA/H_3PO_4 GPE electrolyte and a KOH aqueous electrolyte, (b-c) Fitting of voltage decay curve in time$^{1/2}$ as a characteristic of a diffusion-controlled process (Paper III).

3.4.4 Remarks

It has been argued that self-discharge is not necessarily relevant to direct energy loss, considering (1) the charges within porous carbon are not lost but rather redistributed, and (2) the law of energy preservation and no heat dissipation has ever been reported under open-circuit operation (meaning no exchange of energy between the EC and the environment) [174]. Nevertheless, the apparent performance is greatly diminished by the voltage decay according to energy and power calculations that are related to the voltage squared (V^2).

From materials and devices development point of view, the solutions differ from one system to another, with respect to different mechanisms, but it seems most of the measures proven effective would inhibit kinetics of ion movement and therefore would decrease power performance, except an addition of Triton surfactant [179]. The relation between charging history, temperature and self-discharge rate may help to design PMUs that operate the EC in a favorable way for low losses, i.e. applying low current charging and voltage holding at low temperature. Another engineering method is through a bipolar design as stated in section 3.2, in which individual EC units take low voltage distribution on them, thereby achieving low self-discharge while retaining all the other merits of ECs. Yet again, high-level manufacturing control conditions are desirable to minimize the negative effects of non-uniformity of constituting units.

3.5 Towards high-frequency response

3.5.1 Capacitor metrics in relation to high-frequency response property

Every capacitor has a “comfortable” frequency range to work properly, otherwise, the behavior deviates from capacitive features and the device transforms from a capacitor to a resistor if being charged/discharged at an overrated current. The work towards high-frequency EC is driven by the need of system size reduction for IoT systems, where a suitable EC could substitute conventional bulky electrolytic capacitors for line filtering and smoothing ripples on a rectified wave (section 1.2.3). A high-frequency EC as a storage unit is also believed to be able to absorb the energy pulse from an energy harvester in the self-powered systems [181].

As elaborated in Chapter 1, a capacitive behavior of a capacitor implies that the current leads voltage by 90° in an AC circuit. Due to the nature of device structure and working mechanisms, conventional capacitors, i.e. electrostatic capacitors and electrolytic capacitors, can perform as ideal capacitors (phase angle close to -90°) at high frequencies up to the order of 10^7 and 10^4 Hz, respectively. In contrast, common ECs are in a range from a low frequency to 10^{-1} or 10 Hz, depending on the size and material used. The development of high-frequency ECs is intended to increase the operational frequency to a substantial value, hopefully to a kHz level, with EDL mechanism unchanged for a higher energy density than in conventional capacitors.

The laboratory technique to evaluate frequency range is through an EIS measurement, and a phase angle variation against frequency can be obtained as in Figure 39. Of particular interest, the frequency at which phase angle is -45° is a characteristic frequency, also called cut-off frequency f_0. At operation frequencies beyond f_0, the resistive behavior starts to dominate. The reciprocal of f_0 is the relaxation time constant τ_0, i.e. RC time constant in relation to charging an RC circuit in Figure 36a and Equation (29). This is an indicator of how quickly an EC can be charged or discharged. For electrostatic capacitors, τ_0 is generally below 1 µs, and for electrolytic capacitors, the RC product is generally < 1 ms. An ideal capacitor discharges about 63% of its energy during one RC time constant. Another figure of merit is the phase angle at 120 Hz, φ_{120Hz}. For AC line filtering purposes, φ_{120Hz} is normally used for comparison in performances of smoothing ripples of 60 Hz (U.S. city power line frequency) AC after a full-wave rectifying.

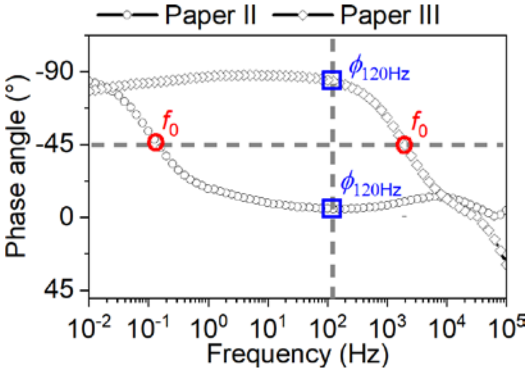

Figure 39. An example phase angle variation with frequency (Paper II and III).

3.5.2 Design guidelines of high-frequency ECs

The understanding of transmission line model from the vertical ladder RC circuits in Figure 37b should provide insights into designing ECs with an excellent frequency response property. The reason that conventional ECs with porous carbon electrode having low f_0 is asynchronous charging. The rich porosity leads to a distribution of the ionic resistance network, corresponding to different branches of the ladder circuit, with each of them having a different RC time constant. Therefore, charge redistribution takes place through different time domains. The resistance of micropores is huge and it can take an enormous amount of time to reach an equilibrium of a fully charged state [173]. If the pores of the electrode are uniform in size and shape, the ladder network can be eventually degenerated into a single branch RC circuit as in Figure 36a. In this way, the EC is charged in a synchronous manner.

Further, if equivalent resistance R is substantially small, together with a moderate capacitance, the RC product i.e. time constant τ_0 could reach down the order of milliseconds, in contrast to seconds for common ECs with porous carbon electrodes.

Based on the above discussion, an ideal electrode material should be of high electronic conductivity with an optimal porosity. The latter implies that the pores are preferably well-connected and relatively large in diameter. Micropores, dead pores and tortuous pore geometry should be avoided. Moreover, *ESR* is a result of an optimized combination of the electrodes, electrolytes and current collectors, therefore, the contact between the components should also be optimal.

In terms of applications in miniaturized systems, the footprint or space allocated for an EC component is limited. This indicates that instead of specific capacitance in Farads per gram, the areal and volumetric capacitance should be examined. Thus, the electrode fabrication is preferably to be scalable in terms of mass loading or thickness, with little compromise in the frequency response property.

3.5.3 State-of-art of high-frequency ECs

The first report on high-frequency ECs was published in 2010 with graphene as an electrode material [182]. Graphene is a compelling material for such application because of extremely high electronic conductivity and a pore-less structure. The monolayer or few-layer graphene-based devices have shown good frequency response [183], but the extremely low mass loading severely limits the energy content (per footprint) of such devices: a basal plane produces only 3 µF cm^{-2}, estimated from a polished graphite electrode in NaF electrolyte [184] or 21 µF cm^{-2} for a 0.3 nm thick graphene layer in BMImPF$_6$ electrolyte [184]. The low areal capacitance is generally a common concern for many nm-layered devices. Although high metrics can be calculated based on the ultrathin layer device, the true performance may not be the same as ultrathin layer devices when scaling up to achieve a desired areal device capacitance [82]. Vertically aligned graphene sheets [182] enable the utilization of edge planes which have a greater areal capacitance of 50 to 70 µF cm^{-2} [184], and therefore a decent capacitance of 0.4 mF cm^{-2} at 0.01 Hz was achieved, though the capacitance is still less than 0.2 mF cm^{-2} at 120 Hz.

A recent review [181] compiled the materials development of high-frequency ECs. The materials option has expanded over nearly all carbon allotropes, and further to some of the pseudocapacitive oxides and conducting polymers. As one can find, increasing areal capacitance remains a challenge to overcome. Most devices rely on thin film electrodes for a high-frequency response property. For example, by reducing a CNT film thickness to nm scale, a cut-off frequency of nearly 16 kHz can be obtained, while areal capacitance is as low as 58 µF cm^{-2} [185]. By increasing the film thickness and mass loading to a proper extent, a higher capacitance can be obtained, however at a certain degree of compromise in frequency response. For instance, a 0.28 mF cm^{-2} EC with 1995 Hz cut-off frequency was demonstrated for a 298 nm thick CNT film on gold-coated Al foil with a vacuum filtration method [185], and a 0.6 mF cm^{-2} device with 1425 Hz cut-off frequency was fabricated with CNT film pressed on gold-coated roughened stainless steel rods [186].

A hybrid structure of graphene/VACNTs can potentially solve the problems associated with their constituting material components. Integrating VACNTs with graphene could increase the areal capacitance of the latter, and graphene as the substrate for VACNTs could be a solution to replace metal layers. The hybrid formation mechanism is preferred to be chemical bonding rather than a mere physical mixture, in order to reduce the contact resistance. A hybrid structure between graphene and VACNTs was investigated by Tour's group [187], and a microsupercapacitor (on a rigid Si substrate) based on this hybrid material was demonstrated exhibiting 1343 Hz cut-off frequency, -81.5° phase angle, 0.23 mF cm^{-2} capacitance at 120 Hz for a 10 µm VACNTs device. The performance is encouraging but this graphene/VACNTs hybrid material requires chemically active copper or nickel metal underlayers for growing single-layer graphene. Moreover, the areal capacitance could be further enhanced.

In paper III, we demonstrate a graphite/VACNTs hybrid material as an electrode with high areal capacitance (1.38 mF cm^{-2}) and volumetric capacitance (345 mF cm^{-3}) at 120 Hz, with phase angle around -85°. This represents the state-of-art performance of high-frequency ECs (Table 7).

The material was fabricated through chemical vapor deposition of CNTs on a highly oriented graphite film with a plasma treatment to introduce oxygen groups for hydrophilicity with an aqueous 6 M KOH electrolyte. The material has a great flexibility (Figure 40a) and roughly 40 μm long CNTs vertically aligned on the substrate (Figure 40b). The length of CNTs is longer than those reported previously [188], which enables a high capacitance (Figure 40d) due to high mass loading, and encouragingly superior frequency response with a cut-off frequency of 1.9 kHz and phase angle of -84.82° at 120 Hz (Figure 40c). The connection between CNTs and the graphite substrate was examined. There is a sign from TEM observations that the CNTs are covalently bonded to the graphite substrate, which optimizes the contact between active electrodes (CNT array) and the current collector (graphite paper). In addition, f_0 shows no clear dependence on CNT length, which is an indirect evidence supporting the covalent bonding claim.

Table 7. Comparison of high-frequency ECs (Paper III).

Material	Electrolyte, Voltage	$\phi_{120\ \mathrm{Hz}}$ (°)	f_0 (Hz)	τ_0 (ms)	$C_{\mathrm{A,\ 120\ Hz}}$ (mF cm^{-2})	$C_{\mathrm{V\text{-}e,\ 120\ Hz}}$ [a] (mF cm^{-3})	$C_{\mathrm{V\text{-}d,\ 120\ Hz}}$ [b] (mF cm^{-3})	Ref.
VACNTs on graphite	**KOH, 0.8 V**	**-84.82**	**1980**	**0.51**	**1.38**	**690**	**345**	**Paper III**
SWCNTs	H_2SO_4, 1.0 V	-81	1425	0.7	0.601	13065	-	[186]
SWCNTs	TEA BF_4, 2.5 V	-82.2	1995	0.501	0.282	4732	69.3	[185]
Graphitic carbon / CNT	TEA BF_4, 2.5 V	-80.3	1000	1	0.3	3947	72.4	[189]
Carbon nanofiber	KOH, 0.9 V	81 [c]	1300	0.77 [c]	2.25	187.5	-	[190]
VOGN [d]	KOH, 1 V	-82	15000	0.06	0.175	1458	24.3	[182]
VOGN [d]	KOH, 0.9 V	-83	10000	0.1	0.3	150	-	[191]
VOGN [d]	KOH, 0.9 V	-82	4000	0.248	0.36	-	7.5	[192]
VOGN [d]	KOH, -	-85	6300	0.16 [c]	0.265	-	17.2	[193]
Holey graphene	KOH, 0.8 V	-81.2	1220	0.819	0.478	1200	-	[194]
rGO	KOH, 0.8 V	-84	4167 [c]	0.24	0.283	70	6.4	[195]
Ketjen black	TEA BF_4, 2.8 V	-79.8	1000	1	0.574	3679	137.8	[196]

[a] $C_{\mathrm{V\text{-}e}}$ is the volumetric capacitance considering only electrode thickness, and $C_{\mathrm{V\text{-}d}}$ is volumetric capacitance considering electrode and current collector thicknesses. Estimated/inferred from presented data. [c] Estimated or derived from the presented data. [d] VOGN stands for vertically oriented graphene nanosheets.

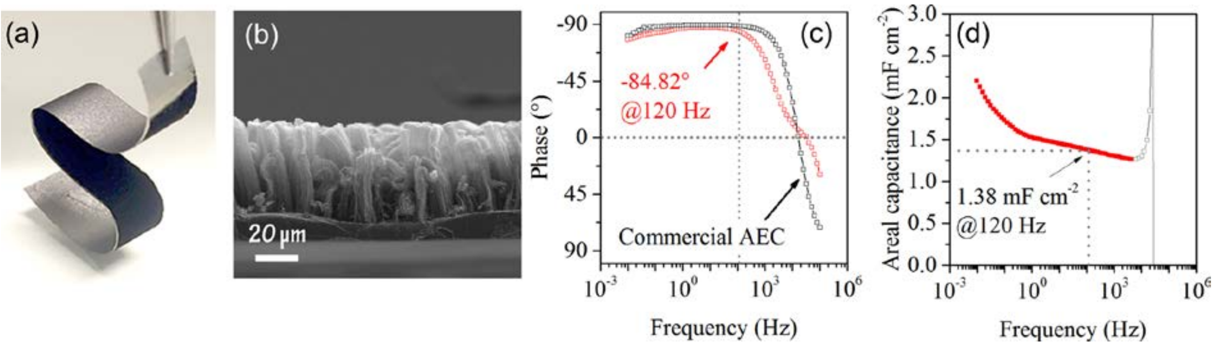

Figure 40. (a) Optical picture and (b) SEM image of graphite/VACNTs electrodes. (c) Phase angle and (d) frequency-dependent capacitance of the graphite/VACNTs based EC (Paper III).

3.5.4 Remarks

High-frequency ECs can replace bulky electrolytic capacitors, one of the biggest components in circuit boards, for smoothing ripples, with advantage in higher energy density and thus size reduction of circuit boards for IoT systems. However, for high operating voltages, designs such as bipolar capacitors must be employed to stack ECs together in series. Since capacitance density of ECs scales up as $1/V^2$ (V is the device operating voltage), and by contrast, capacitance density of an electrolytic capacitor scales like 1/V because the CV product of anodic dielectric is approximately constant [197]. Therefore, the advantage of capacitance density for ECs will disappear at a particular voltage (43 V for the high-frequency EC in Paper III). Fortunately, in portable electronics equipment, 2 V can be sufficient for bypass and filtering purpose capacitors [182]. At such low voltages, the size advantage of ECs is rather significant.

4 ENCAPSULATION AND INTEGRATION CHALLENGES

As a practical device, the best combination of core EC materials, i.e. the electrodes, electrolytes, and separators, must be properly encapsulated in a certain form factor, and then be integrated with other system components such as energy harvesters, sensors and PMUs to construct effective miniaturized self-powered systems. The encapsulation and integration aspects pose mostly engineering challenges in device design and fabrication of ECs, and also materials challenges that the EC materials must be compatible with the ambient conditions that occur during the encapsulation and integration processes. This chapter starts with overviewing common COTS ECs with emphasis on their configurations, then elaborates the call for surface-mount designs for the purpose of high circuitry density and system miniaturization, and in the end briefly discusses the solutions from EC development point of view.

4.1 Common COTS electrochemical capacitor configurations

The configuration design of COTS ECs is strongly linked to targeted market and cost-efficiency. Common options are coin cells, cylindrical (wound) cells, prismatic cells, and pouch cells. Large modules of unit cells in the above configurations connected in series or parallel are also commonly seen in the market for high energy and power applications.

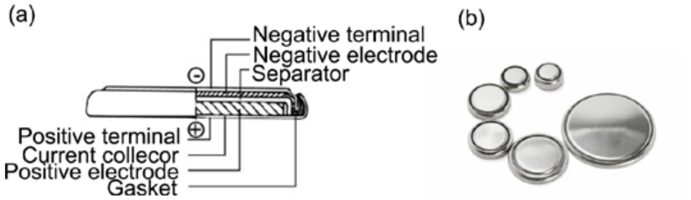

Figure 41. (a) Schematic and (b) picture of coin cells [198].

Coin cells, also known as button cells, are usually shaped like a squat cylinder (Figure 41) typically 5 to 25 mm in diameter and 1 to 6 mm in height. Materials are encapsulated by metal cans separated by an insulating gasket in a coin cell configuration, and the positive and negative terminals are thus located on the opposite side of the squat cylinder.

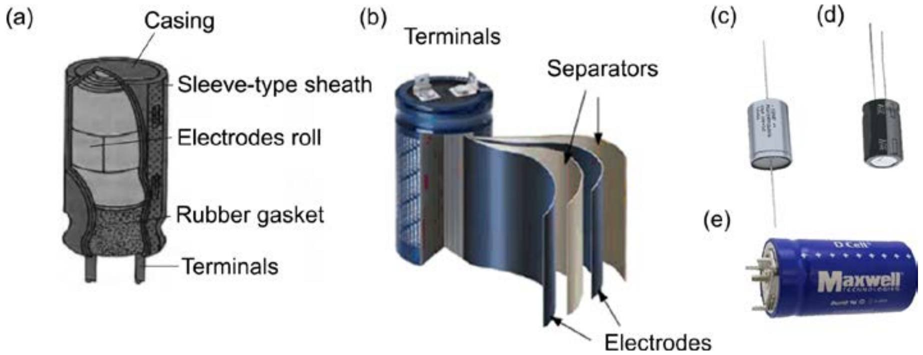

Figure 42. (a-b) Schematic of cylindrical (wound) ECs, and pictures of cylindrical ECs with (c) axial type and (d-e) radial type terminals (picture courtesy of Panasonic, Kemet, and Maxwell).

Cylindrical cells (Figure 42) are also called wound type cells by some manufacturers. The electrode and separator layers are rolled up, fitted with pin connectors and placed in a cylindrical casing. The positive and negative terminals can be arranged either on the same base plane (e.g. radial or radial snap-in type, Figure 42d-e) or on the two different base planes of the cylinder (axial type, Figure 42c). Before the winding process for encapsulation, a rubber gasket is placed on the top, and the case opening is folded over and then pressed into the rubber to form hermetic sealing. A safety vent can be provided for releasing excessive pressure (usually over 7 atm) built up during operation [199].

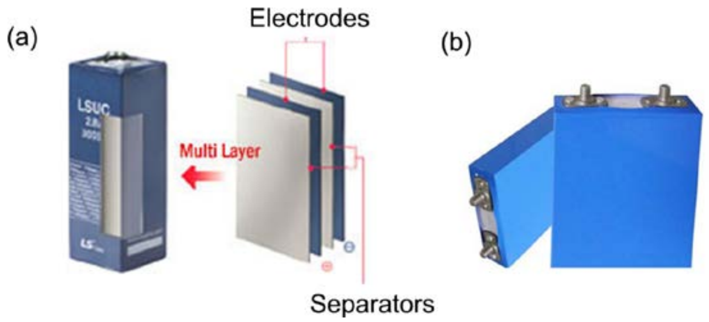

Figure 43. (a) Schematic and (b) picture of prismatic type EC [200].

In prismatic cells (Figure 43), the materials (rolled-up sheets) are wrapped in a metallic housing resembling a box of chewing gum. This configuration is suitable for high energy and power applications since a relatively large surface area in dissipating heat from the cell interior to the exterior is available. There is a debate on which of the cylindrical and prismatic types is better. It is acknowledged that large prismatic cells have a higher energy density, especially when they are assembled in modules for geometric aspects, however, prismatic cells contain more parts than cylindrical cells and are more expensive to manufacture [199].

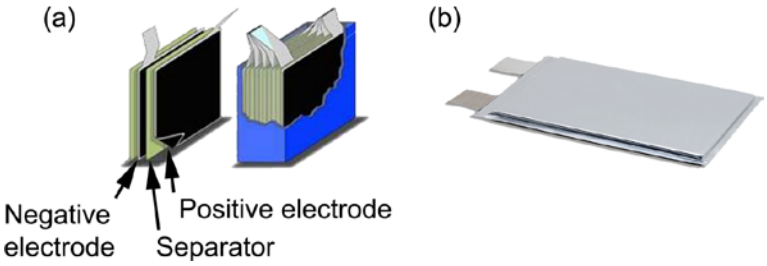

Figure 44. (a) Schematic and (b) picture of pouch type EC [201].

In pouch cells (Figure 44), a number of “positive electrode - separator - negative electrode” stacks are piled up, and the electrodes of the same polarity are connected and welded to the terminal conductive foil-tabs which are brought to the outside in a fully sealed way. The pouch cell makes the most efficient use of space and achieves 90-95% packaging efficiency. However, pouch cell has little tolerance for swelling due to gassing from electrolyte decomposition, and vulnerable to puncture and similar types of mechanical influence because of soft packaging. Pouch cells use aluminum laminated film containing polymer layers [81] for the casing. Polymer-based sealed wraps are not water- and air-tight for long-term application. Thermal management efficiency is low compared to other configurations, though it can be a minor issue for miniaturized systems.

4.2 Design considerations for system miniaturization

4.2.1 Surface-mount ECs

For a small size of the whole system, the constituting unit components should be miniature, then it is essential to consider the method of integration for a high space efficiency. In electronic industries, surface mount technology (SMT) is regarded as a revolutionary change [202]. By mounting flat leaded or leadless components and electronic packages on the surface of printed circuit boards (PCBs), SMT allows a higher degree of automation, higher circuitry density, and smaller volume, as opposed to the counterpart through-hole technology (THT). Using surface mount devices (SMDs) can deliver up to 90% reduction in both weight and volume, compared to using through-hole devices (THDs) [202] as sketched in Figure 45. Therefore, it is advantageous to design surface-mountable ECs for miniaturized self-powered systems based on PCBs.

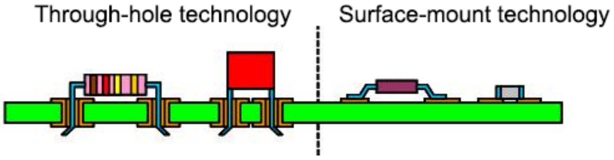

Figure 45. Through-hole technology and surface-mount technology [203].

A few types of surface-mount ECs are available on the market. Some designs are basically a coin type capacitor sitting on a surface mountable holder, which unfortunately leads to a high profile. The same concern comes with the cylindrical type ECs that can sit on a holder, or with their terminal leads designed to be flat for surface mountability. Comparatively, prismatic and pouch cells have smaller dead volumes on the module level and higher degrees of design freedom. The companies of Cap-XX, AVX and muRata have presented a series of pouch type ECs with very thin profiles, down to 0.4 mm for a 35 mF muRata product [204]. The pouch ECs can be surface mountable with flat leads. Cellergy, another player in the market, utilizing conventional screen or stencil printing techniques for the fabrication of prismatic type of ECs. Cellergy ECs are also surface mountable with a low profile by designing flat leads. Using the printing technology, the smallest footprint achievable is 12 × 12.5 (L × W) mm^2, and the highest capacitance of 12 mF is at 2.4 mm thickness and 3.5 V voltage, highest voltage is 6.3 V at 3.4 mm and 7 mF [205]. Specifically, aiming for applications in microsystems, SEIKO and CLC Factory have presented the smallest 3.2 × 2.5 × 0.9 (L × W × H) mm^3 surface-mount chip type ECs with capacitances on the order of 10 mF [206, 207].

The successful commercialization of above devices evidences the effectiveness of their designs. Nevertheless, there is still room for improvement. For example, sizing down of the footprint may be problematic for pouch cells, considering that sufficient sealant area on the edge should be preserved for hermetic sealing, otherwise the device would be more vulnerable to mechanical shocks and pressure build-up caused by gas generation. The water and airtightness may also be questionable under harsh climate conditions. For printing technology, the choice of electrode and electrolyte materials could be limited, indicating that the advanced materials developed in the laboratory cannot be directly utilized. Additional development of stable inks may be necessary. Moreover, the allocation of terminals is difficult to be designed on the flat surface for the conventional configurations. This makes it necessary to use glue or adhesive tape on the flat surface (to attach on PCBs) for mechanical stability, unfortunately aggravating reliability concerns.

In a nutshell, novel encapsulation and integration concepts are always appreciated. Ideally, the design and manufacturing technology should allow for surface mountability, convenient allocation of terminal positions, and easy adaptation in geometry design as well as an arbitrary choice of materials, moreover, compatibility with bipolar designs.

4.2.2 Reflow-soldering

SMDs can be assembled onto PCBs with the used of solder paste reflow, wave soldering or conductive adhesive curing processes. The last is mostly used in some flexible circuit boards or boards with heat sensitive components, while the wave soldering is more efficient for THDs [202].

To start the reflow-soldering process, the solder powder and flux are pre-blended to form a sticky thixotropic solder paste, and the paste is used to temporarily attach SMDs on their contact pads. Afterward, the entire assembly is subjected to controlled heat above the liquidus temperature of the solder paste for a short period of time, which melts the solder, permanently connecting the joint [202]. Although the heat may be applied by soldering individual joints with a hot air pencil, a higher degree of automation and productivity is through the use of reflow oven for batch processing. This could pose challenges to EC technology, since the peak temperature can go up to more than 300 °C, depending on the solder material. Therefore, the EC encapsulation and the core materials are preferred to be durable to high-temperature exposure, usually for a short period of time, on a scale of minutes. The exploitation of ionic liquid electrolytes is a promising solution. For the smart-MEMPHIS project, we have validated that the EMImAc electrolyte could withstand an exposure at 190 °C for up to 2 hours without deteriorating the stability.

4.3 Unconventional electrochemical capacitors

Addressing the encapsulation and integration challenges, on the one hand, relies on an enormous amount of engineering efforts for new encapsulation concepts, and simultaneously, the materials development also facilitates finding the solution. Along with this vein, unconventional EC configurations are being developed (Figure 46a-b). The materials innovation has resulted in prototype devices which are flexible, transparent, stretchable and/or compressible, viable to be of almost arbitrary form factors such as fiber-like, being space efficient. The advancement in solid- or quasi-solid-state electrolytes apparently eases the encapsulation concerns because of their leakage-proof nature. Also, structural ECs serving as an energy storage device that takes zero space provides another option for optimal space efficiency. Micro-supercapacitors, typically interdigital fingers on a planar substrate, offer a possibility of seamless on-chip integrations with other components (Figure 46c).

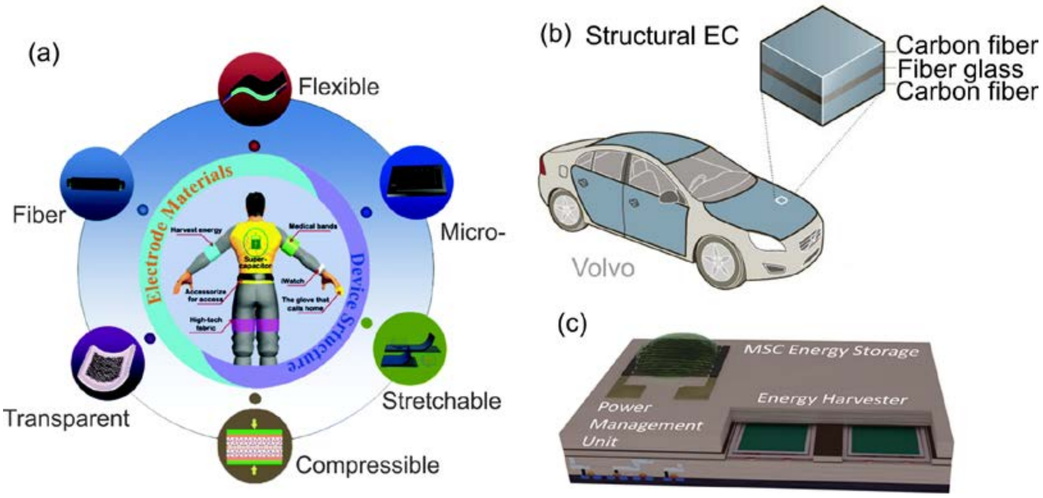

Figure 46. (a-b) Unconventional EC configurations [208, 209], (c) Seamless on-chip integration with a microsupercapacitor (MSC) component.

All the new technologies contribute to constructing miniaturized self-powered systems, but mostly these unconventional ECs are still premature and challenges to their final accomplishments are also encountered. Specifically, encapsulation of microsupercapacitors remains a hurdle for their wide application. The general idea of encapsulation is bonding the device wafer with a lid wafer or cover it with a protective coating. Currently, all the hermetic encapsulation processes (anodic bonding, glass frit bonding, eutectic or diffusion bonding) are usually performed at high temperatures [210]. Therefore, the development of high-temperature durable materials is also needed in this frontier.

5 CONCLUSIONS AND FUTURE WORK

5.1 Conclusions

This thesis focuses on ECs application in miniaturized self-powered systems which is essential for the internet of things (IoTs) and further the internet of everything (IoE), 5G mobile communication and tactile internet. Besides energy storage related purposes, ECs can also be used for AC line filtering, with benefits of system size reduction. Bringing high-level IoT requirements down to a device-level, we have identified that the existing challenges to EC technology in the regard of electrochemical performance and device encapsulation/integration as follows:

Device performance challenges

- Improving energy density towards battery-level while keeping high power and long cycling stability
- Increasing the maximum operating voltage limit
- Achieving high power under operations at extreme low-temperature, and high stability at extreme high-temperature
- Minimizing self-discharge and leakage current
- Enhancing frequency response property with a high areal capacitance

Device encapsulation/integration challenges

- Developing new encapsulation and integration concepts allowing for surface mounting with a low profile and compatibility with a wide choice of materials
- Enhancing the tolerance to high-temperature exposure that is required for reflow soldering and/or other encapsulation and integration methods

The solutions to above challenges are explored in this thesis. Specifically, in relation to the thesis experimental research, we have found in Paper I that constructing hybrid systems with the use of redox-active KBr electrolyte is an effective approach in enhancing the energy density while keeping high power and long lifetime. The redox activity of bromide pins the potential of the positive electrode, thereby stretching the negative electrode potential to much wider stability window. As a result, 1.9 V is achieved in this aqueous system. Battery level energy density is thus achieved with little compromise in capacitor-level power density and cycle life. Moreover, both voltage- and history-dependent behaviors are revealed, reminding the complexity of redox enhanced EDLC systems. The complexity allows for possibility of regulating performance metrics by a triggering operation, but on the other hand it may cause difficulties to power management, therefore, special care is needed before incorporating hybrid ECs into IoT networks.

As an effort in exploring extreme high-temperature ECs in Paper II, we introduced an EMImAc ionic liquid electrolyte which enables an AC based EDLC working at maximum of 150 °C for short period and at 120 °C for long time. Importantly, we point out that maximum operating voltage can be traded for gaining stability at high temperatures, without sacrifice in energy and power densities. This strategy can be applicable for all electrolytes that have a moderate conductivity at room temperature, e.g. neat ionic liquids and solid-state electrolytes. This finding is of practical significance as it provides hints for PMU designers.

Regarding efforts to minimize self-discharge and leakage current, in Paper III, we presented a graphite/VACNT carbon hybrid material, and proved that using a gel polymer electrolyte can mitigate self-discharge and leakage current effectively, compared to using aqueous electrolytes. Moreover, the results indicate that the graphite/VACNT is an excellent material for constructing high frequency ECs that are suitable for AC line filtering. The high frequency response property is achieved along with a state-of-art level areal (1.38 mF cm^{-2}) and volumetric capacitances (345 mF cm^{-3}), benefiting from a possible covalent bonding between graphite substrate and the CVD grown VACNTs.

Not limited to the research work, a more comprehensive review and summary of strategies and methods have been given in this thesis. It is clear that to date, there is no single perfect solution to address all the challenges, rather the development of ECs is always specific to application defined requirements. Overviewing the state-of-art development, it seems current storage technologies are far from being ideal, and there is a need for redesign of the energy storage systems in terms of materials, device configurations and encapsulation techniques as well as integration with other components. To accomplish this goal, extensive parametric experimental studies are required. However, it is almost impractical, considering the tremendous amount of options of materials and configurations, as well as their combinations. There is a perspective that EC development will contribute to the advent of IoT, and finally IoT would boost EC technology in turn, in a way that networking researchers worldwide, building up big database for high throughput calculation and accelerating the screening processes.

5.2 Future work

Among all the identified challenges to ECs, reducing self-discharge and leakage current is regarded as the most difficult tasks because the process is favored by thermodynamics. Taking appropriate measures such as kinetics limitation is supposed to be effective in mitigating the loss. Except device level performance, the knowledge of individual electrode behaviors should be beneficial for a better solution.

Bearing in mind the target application of ECs in self-powered systems, one has to take into account the encapsulation and integration aspects which needs attention in device-level development. New EC device concepts that is compatible with SMT, allow for easy geometry tailoring and arbitrary assigning the location of terminals is highly desired and is part of the ongoing research. Besides, microsupercapacitors offer another viable route for convenient on-board or on-chip integration. The optimization of microsupercapacitors is also being pursued and foreseen to be one of the most attainable goal in the near future.

6 REFERENCES

[1] J. Iannacci, Internet of things (IoT); internet of everything (IoE); tactile internet; 5G - a (not so evanescent) unifying vision empowered by EH-MEMS (energy harvesting MEMS) and RF-MEMS (radio frequency MEMS), Sens. Actuator A: Phys., 272 (2018) 187-198.

[2] V. Afshar, Cisco: Enterprises are leading the internet of things innovation, https://www.huffingtonpost.com/entry/cisco-enterprises-are-leading-the-internet-of-things_us_59a41fcee4b0a62d0987b0c6?guccounter=1, Acessed on August 24, 2018.

[3] P. Glynne-Jones, N. M. White, Self-powered systems: A review of energy sources, Sensor review, 21 (2001) 91-98.

[4] S. Sudevalayam, P. Kulkarni, Energy harvesting sensor nodes: Survey and implications, Ieee Commun Surv Tut, 13 (2011) 443-461.

[5] M. Winter, R. J. Brodd, What are batteries, fuel cells, and supercapacitors?, Chem. Rev., 104 (2004) 4245-4270.

[6] Q. Li, et al., K^+-doped $Li_{1.2}Mn_{0.54}Co_{0.13}Ni_{0.13}O_2$: A novel cathode material with an enhanced cycling stability for lithium-ion batteries, ACS Appl. Mater. Interfaces, 6 (2014) 10330-10341.

[7] B. E. Conway, Electrochemical supercapacitors: Scientific fundamentals and technological applications, first ed., Springer Science & Business Media, New York, 2013.

[8] P. Simon, Y. Gogotsi, Materials for electrochemical capacitors, Nat. Mater., 7 (2008) 845-854.

[9] T. Brousse, et al., To be or not to be pseudocapacitive?, J. Electrochem. Soc., 162 (2015) A5185-A5189.

[10] A. Laheaar, et al., Appropriate methods for evaluating the efficiency and capacitive behavior of different types of supercapacitors, Electrochem. Commun., 60 (2015) 21-25.

[11] G. Z. Chen, Understanding supercapacitors based on nano-hybrid materials with interfacial conjugation, Prog. Nat. Sci.-Mater., 23 (2013) 245-255.

[12] H. G. Lee, N. Chang, Powering the IoT: Storage-less and converter-less energy harvesting, The 20th Asia and South Pacific Design Automation Conference, 2015.

[13] Y. Sun, et al., Wirelessly powered implantable pacemaker with on-chip antenna, Microwave Symposium (IMS), 2017 IEEE MTT-S International, 2017.

[14] M. Brachet, et al., Solder-reflow resistant solid-state micro-supercapacitors based on ionogels, J. Mater. Chem. A, 4 (2016) 11835-11843.

[15] Y. Wang, et al., All-printed paper based surface mountable supercapacitors, IEEE Trans. Dielectr. Electr. Insul., 24 (2017) 676-681.

[16] L. Pilon, et al., Recent advances in continuum modeling of interfacial and transport phenomena in electric double layer capacitors, J. Electrochem. Soc., 162 (2015) A5158-A5178.

[17] H. V. Helmholtz, Studien über electrische grenzschichten, Annalen der Physik, 243 (1879) 337-382.

[18] M. Gouy, Sur la constitution de la charge électrique à la surface d'un électrolyte, J. Phys. Theor. Appl., 9 (1910) 457-468.

[19] D. L. Chapman, Li. A contribution to the theory of electrocapillarity, The London, Edinburgh, and Dublin philosophical magazine and journal of science, 25 (1913) 475-481.

[20] O. Stern, Zur theorie der elektrolytischen doppelschicht, Zeitschrift für Elektrochemie und angewandte physikalische Chemie, 30 (1924) 508-516.

[21] F. Beguin, et al., Carbons and electrolytes for advanced supercapacitors, Adv. Mater., 26 (2014) 2219-2251.

[22] E. Raymundo-Pinero, et al., Relationship between the nanoporous texture of activated carbons and their capacitance properties in different electrolytes, Carbon, 44 (2006) 2498-2507.

[23] J. Chmiola, et al., Anomalous increase in carbon capacitance at pore sizes less than 1 nanometer, Science, 313 (2006) 1760-1763.

[24] M. R. Lukatskaya, et al., Multidimensional materials and device architectures for future hybrid energy storage, Nat. Commun., 7 (2016) 12647.

[25] J. Huang, et al., A universal model for nanoporous carbon supercapacitors applicable to diverse pore regimes, carbon materials, and electrolytes, Chem. Eur. J., 14 (2008) 6614-6626.

[26] K. Jost, et al., Textile energy storage in perspective, J. Mater. Chem. A, 2 (2014).

[27] G. Wang, et al., A review of electrode materials for electrochemical supercapacitors, Chem. Soc. Rev., 41 (2012) 797-828.

[28] C. Choi, et al., Elastomeric and dynamic MnO_2/CNT core-shell structure coiled yarn supercapacitor, Adv. Energy Mat., 6 (2016) 1502119.

[29] X. Yu, et al., Emergent pseudocapacitance of 2D nanomaterials, Adv. Energy Mat., 8 (2018).

[30] V. Augustyn, et al., Pseudocapacitive oxide materials for high-rate electrochemical energy storage, Energy Environ. Sci., 7 (2014) 1597-1614.

[31] B. Conway, et al., The role and utilization of pseudocapacitance for energy storage by supercapacitors, J. Power Sources, 66 (1997) 1-14.

[32] C. Zhong, et al., A review of electrolyte materials and compositions for electrochemical supercapacitors, Chem. Soc. Rev., 44 (2015) 7484-7539.

[33] S. T. Senthilkumar, et al., Redox additive/active electrolytes: A novel approach to enhance the performance of supercapacitors, J. Mater. Chem. A, 1 (2013) 12386.

[34] B. Akinwolemiwa, et al., Redox electrolytes in supercapacitors, J. Electrochem. Soc., 162 (2015) A5054-A5059.

[35] J. H. Chae, G. Z. Chen, 1.9V aqueous carbon-carbon supercapacitors with unequal electrode capacitances, Electrochim. Acta, 86 (2012) 248-254.

[36] S. Vaquero, et al., Mass-balancing of electrodes as a strategy to widen the operating voltage window of carbon/carbon supercapacitors in neutral aqueous electrolytes, Int. J. Electrochem. Sci, 8 (2013) 10293-10307.

[37] G. Z. Chen, Supercapacitor and supercapattery as emerging electrochemical energy stores, Int. Mater. Rev., 62 (2017) 173-202.

[38] P. L. Taberna, et al., Electrochemical characteristics and impedance spectroscopy studies of carbon-carbon supercapacitors, J. Electrochem. Soc., 150 (2003) A292-A300.

[39] S. Zhang, N. Pan, Supercapacitors performance evaluation, Adv. Energy Mat., 5 (2015) 1401401.

[40] D. Weingarth, et al., Cycle versus voltage hold - which is the better stability test for electrochemical double layer capacitors?, J. Power Sources, 225 (2013) 84-88.

[41] P. Ruch, et al., Aging of electrochemical double layer capacitors with acetonitrile-based electrolyte at elevated voltages, Electrochim. Acta, 55 (2010) 4412-4420.

[42] T. Liu, et al., Revitalizing carbon supercapacitor electrodes with hierarchical porous structures, J. Mater. Chem. A, 5 (2017) 17705-17733.

[43] Y. Zhai, et al., Carbon materials for chemical capacitive energy storage, Adv. Mater., 23 (2011) 4828-4850.

[44] P. Simon, Y. Gogotsi, Capacitive energy storage in nanostructured carbon - electrolyte systems, Acc. Chem. Res., 46 (2012) 1094-1103.

[45] L. Demarconnay, et al., A symmetric carbon/carbon supercapacitor operating at 1.6V by using a neutral aqueous solution, Electrochem. Commun., 12 (2010) 1275-1278.

[46] L. Zhao, et al., Carbon nanofibers with radially grown graphene sheets derived from electrospinning for aqueous supercapacitors with high working voltage and energy density, Nanoscale, 5 (2013) 4902-4909.

[47] K. Fic, et al., Novel insight into neutral medium as electrolyte for high-voltage supercapacitors, Energy Environ. Sci., 5 (2012) 5842-5850.

[48] A. Brandt, et al., Ionic liquids in supercapacitors, MRS Bull., 38 (2013) 554-559.

[49] M. Galiński, et al., Ionic liquids as electrolytes, Electrochim. Acta, 51 (2006) 5567-5580.

[50] M. Armand, et al., Ionic-liquid materials for the electrochemical challenges of the future, Nat. Mater., 8 (2009) 621-629.

[51] R. S. Borges, et al., Supercapacitor operating at 200 degrees celsius, Sci. Rep., 3 (2013) 2572.

[52] N. Choudhury, et al., Hydrogel-polymer electrolytes for electrochemical capacitors: An overview, Energy Environ. Sci., 2 (2009) 55-67.

[53] C. Ramasamy, M. Anderson, An activated carbon supercapacitor analysis by using a gel electrolyte of sodium salt-polyethylene oxide in an organic mixture solvent, J. Solid State Electrochem., 18 (2014) 2217-2223.

[54] C. Ramasamy, et al., A 3-V electrochemical capacitor study based on a magnesium polymer gel electrolyte by three different carbon materials, J. Solid State Electrochem., 18 (2014) 2903-2911.

[55] P. M. Dicarmine, et al., Donor-acceptor polymers for electrochemical supercapacitors: Synthesis, testing, and theory, J. Phys. Chem. C, 118 (2014) 8295-8307.
[56] R. Yuksel, et al., Transparent and flexible supercapacitors with single walled carbon nanotube thin film electrodes, ACS Appl. Mater. Interfaces, 6 (2014) 15434-15439.
[57] K.-F. Chiu, S.-H. Su, Lithiated and sulphonated poly (ether ether ketone) solid state electrolyte films for supercapacitors, Thin Solid Films, 544 (2013) 144-147.
[58] M.-F. Hsueh, et al., The synergistic effect of nitrile and ether functionalities for gel electrolytes used in supercapacitors, J. Phys. Chem. C, 117 (2013) 16751-16758.
[59] Y.-D. Chiou, et al., Cycle stability of the electrochemical capacitors patterned with vertically aligned carbon nanotubes in an $LiPF_6$-based electrolyte, Nanoscale, 5 (2013) 8122-8129.
[60] S. E. Chun, et al., Design of aqueous redox-enhanced electrochemical capacitors with high specific energies and slow self-discharge, Nat. Commun., 6 (2015) 7818.
[61] Y. M. Shulga, et al., Graphene oxide films as separators of polyaniline-based supercapacitors, J. Power Sources, 245 (2014) 33-36.
[62] H. Yu, et al., Using eggshell membrane as a separator in supercapacitor, J. Power Sources, 206 (2012) 463-468.
[63] A. Bittner, et al., Ageing of electrochemical double layer capacitors, J. Power Sources, 203 (2012) 262-273.
[64] G. Zhao, Reuse and recycling of lithium-ion power batteries, John Wiley & Sons, 2017.
[65] K. Tõnurist, et al., Influence of mesoporous separator properties on the parameters of electrical double-layer capacitor single cells, J. Electrochem. Soc., 156 (2009) A334-A342.
[66] K. Tõnurist, et al., Specific performance of supercapacitors at lower temperatures based on different separator materials, J. Electrochem. Soc., 160 (2013) A449-A457.
[67] Y. Yue, H. Liang, 3D current collectors for lithium-ion batteries: A topical review, Small Methods, 2 (2018).
[68] I. Ryu, et al., Coaxial RuO_2-ITO nanopillars for transparent supercapacitor application, Langmuir, 30 (2014) 1704-1709.
[69] H. W. Cho, et al., Synthesis and supercapacitive properties of electrodeposited polyaniline composite electrode on acrylonitrile-butadiene rubber as a flexible current collector, Synth. Met., 162 (2012) 410-413.
[70] X. Gong, et al., Nickel-cobalt hydroxide microspheres electrodepositioned on nickel cobaltite nanowires grown on Ni foam for high-performance pseudocapacitors, J. Power Sources, 267 (2014) 610-616.
[71] F. Xiang, et al., Far-infrared reduced graphene oxide as high performance electrodes for supercapacitors, Carbon, 75 (2014) 201-208.
[72] N. A. Alhebshi, et al., Conformal coating of $Ni(OH)_2$ nanoflakes on carbon fibers by chemical bath deposition for efficient supercapacitor electrodes, J. Mater. Chem. A, 1 (2013) 14897-14903.
[73] R. Zhou, et al., High-performance supercapacitors using a nanoporous current collector made from super-aligned carbon nanotubes, Nanotechnology, 21 (2010) 345701.
[74] J. Xu, et al., Flexible asymmetric supercapacitors based upon Co_9S_8 nanorod//Co_3O_4@RuO_2 nanosheet arrays on carbon cloth, ACS nano, 7 (2013) 5453-5462.
[75] J. Ji, et al., Nanoporous $Ni(OH)_2$ thin film on 3D ultrathin-graphite foam for asymmetric supercapacitor, ACS nano, 7 (2013) 6237-6243.
[76] R.-S. Kühnel, A. Balducci, Comparison of the anodic behavior of aluminum current collectors in imide-based ionic liquids and consequences on the stability of high voltage supercapacitors, J. Power Sources, 249 (2014) 163-171.
[77] A. Brandt, et al., An investigation about the use of mixtures of sulfonium-based ionic liquids and propylene carbonate as electrolytes for supercapacitors, J. Mater. Chem. A, 1 (2013) 12669-12678.
[78] C. Portet, et al., Modification of Al current collector surface by sol-gel deposit for carbon-carbon supercapacitor applications, Electrochim. Acta, 49 (2004) 905-912.
[79] T. Takahashi, et al., Properties of nickel-coated steel sheets for battery case, Nippon Steel & Sumitomo Metal Technical Report, (2015).
[80] Targray, Targray packaging materials for battery manufacturing, https://www.targray.com/li-ion-battery/packaging-materials, Acessed on September 11, 2018.

[81] MTI, Aluminum laminated film for pouch cell case, http://www.mtixtl.com/AluminumLaminatedFilmforPolymerBatteryCase100mmWx210mmL50pcs.aspx, Acessed on September 11, 2018.
[82] Y. Gogotsi, P. Simon, Materials science. True performance metrics in electrochemical energy storage, Science, 334 (2011) 917-918.
[83] C. Niu, et al., High power electrochemical capacitors based on carbon nanotube electrodes, Appl. Phys. Lett., 70 (1997) 1480-1482.
[84] D. Li, et al., Processable aqueous dispersions of graphene nanosheets, Nat. Nanotechnol., 3 (2008) 101-105.
[85] M. R. Lukatskaya, et al., Cation intercalation and high volumetric capacitance of two-dimensional titanium carbide, Science, 341 (2013) 1502-1505.
[86] T. Centeno, F. Stoeckli, The assessment of surface areas in porous carbons by two model-independent techniques, the dr equation and dft, Carbon, 48 (2010) 2478-2486.
[87] G. Gryglewicz, et al., Effect of pore size distribution of coal-based activated carbons on double layer capacitance, Electrochim. Acta, 50 (2005) 1197-1206.
[88] O. Barbieri, et al., Capacitance limits of high surface area activated carbons for double layer capacitors, Carbon, 43 (2005) 1303-1310.
[89] G. Salitra, et al., Carbon electrodes for double-layer capacitors I. Relations between ion and pore dimensions, J. Electrochem. Soc., 147 (2000) 2486-2493.
[90] L. Eliad, et al., Ion sieving effects in the electrical double layer of porous carbon electrodes: Estimating effective ion size in electrolytic solutions, J. Phys. Chem. B, 105 (2001) 6880-6887.
[91] L. Eliad, et al., Assessing optimal pore-to-ion size relations in the design of porous poly (vinylidene chloride) carbons for edl capacitors, Appl. Phys. A, 82 (2006) 607-613.
[92] C. Vix-Guterl, et al., Electrochemical energy storage in ordered porous carbon materials, Carbon, 43 (2005) 1293-1302.
[93] J. Chmiola, et al., Desolvation of ions in subnanometer pores and its effect on capacitance and double-layer theory, Angew. Chem. Int. Ed. Engl., 47 (2008) 3392-3395.
[94] M. Deschamps, et al., Exploring electrolyte organization in supercapacitor electrodes with solid-state NMR, Nat. Mater., 12 (2013) 351-358.
[95] H. Nishihara, et al., Investigation of the ion storage/transfer behavior in an electrical double-layer capacitor by using ordered microporous carbons as model materials, Chem. Eur. J., 15 (2009) 5355-5363.
[96] J. Chmiola, et al., Effect of pore size and surface area of carbide derived carbons on specific capacitance, J. Power Sources, 158 (2006) 765-772.
[97] C. Largeot, et al., Relation between the ion size and pore size for an electric double-layer capacitor, J. Am. Chem. Soc., 130 (2008) 2730-2731.
[98] G. Feng, et al., Ion distribution in electrified micropores and its role in the anomalous enhancement of capacitance, ACS nano, 4 (2010) 2382-2390.
[99] C. Merlet, et al., On the molecular origin of supercapacitance in nanoporous carbon electrodes, Nat. Mater., 11 (2012) 306-310.
[100] L. Wei, et al., Hydrothermal carbonization of abundant renewable natural organic chemicals for high-performance supercapacitor electrodes, Adv. Energy Mat., 1 (2011) 356-361.
[101] T. Lin, et al., Nitrogen-doped mesoporous carbon of extraordinary capacitance for electrochemical energy storage, Science, 350 (2015) 1508-1513.
[102] C.-C. Hu, W.-C. Chen, Effects of substrates on the capacitive performance of $RuO_x·nH_2O$ and activated carbon-RuO_x electrodes for supercapacitors, Electrochim. Acta, 49 (2004) 3469-3477.
[103] C.-C. Hu, et al., How to achieve maximum utilization of hydrous ruthenium oxide for supercapacitors, J. Electrochem. Soc., 151 (2004) A281-A290.
[104] C.-C. Hu, et al., Design and tailoring of the nanotubular arrayed architecture of hydrous RuO_2 for next generation supercapacitors, Nano Lett., 6 (2006) 2690-2695.
[105] L. Chen, et al., Toward the theoretical capacitance of RuO_2 reinforced by highly conductive nanoporous gold, Adv. Energy Mat., 3 (2013) 851-856.
[106] M. Toupin, et al., Charge storage mechanism of MnO_2 electrode used in aqueous electrochemical capacitor, Chem. Mater., 16 (2004) 3184-3190.

[107] X. Lu, et al., Oxygen-deficient hematite nanorods as high-performance and novel negative electrodes for flexible asymmetric supercapacitors, Adv. Mater., 26 (2014) 3148-3155.

[108] Y. L. Huang, et al., Recent smart methods for achieving high-energy asymmetric supercapacitors, Small Methods, 2 (2018) 1700230.

[109] K. Karthikeyan, et al., Fluorine-doped Fe_2O_3 as high energy density electroactive material for hybrid supercapacitor applications, Chemistry ‐ An Asian Journal, 9 (2014) 852-857.

[110] G. Wang, et al., Facile synthesis of highly photoactive α-Fe_2O_3-based films for water oxidation, Nano Lett., 11 (2011) 3503-3509.

[111] Y. Guo, et al., Layer structured materials for advanced energy storage and conversion, Small, 13 (2017) 1701649.

[112] J. Sun, et al., Recent progresses in high-energy-density all pseudocapacitive-electrode-materials-based asymmetric supercapacitors, J. Mater. Chem. A, 5 (2017) 9443-9464.

[113] M. Ghidiu, et al., Conductive two-dimensional titanium carbide 'clay' with high volumetric capacitance, Nature, 516 (2014) 78-81.

[114] K. Jurewicz, et al., Towards the mechanism of electrochemical hydrogen storage in nanostructured carbon materials, Appl. Phys. a-Mater., 78 (2004) 981-987.

[115] K. Fic, et al., Interfacial redox phenomena for enhanced aqueous supercapacitors, J. Electrochem. Soc., 162 (2015) A5140-A5147.

[116] M. P. Bichat, et al., High voltage supercapacitor built with seaweed carbons in neutral aqueous electrolyte, Carbon, 48 (2010) 4351-4361.

[117] W. Shimizu, et al., Development of a 4.2 V aqueous hybrid electrochemical capacitor based on MnO_2 positive and protected li negative electrodes, J. Power Sources, 241 (2013) 572-577.

[118] L. Suo, et al., “Water-in-salt” electrolyte enables high-voltage aqueous lithium-ion chemistries, Science, 350 (2015) 938-943.

[119] P. Lannelongue, et al., “Water-in-salt” for supercapacitors: A compromise between voltage, power density, energy density and stability, J. Electrochem. Soc., 165 (2018) A657-A663.

[120] N. Kumar Thangavel, et al., Water-in-salt electrolytes for high-voltage supercapacitors, 233rd ECS Meeting, 2018.

[121] Q. Gao, et al., Exploring the large voltage range of carbon/carbon supercapacitors in aqueous lithium sulfate electrolyte, Energy Environ. Sci., 5 (2012) 9611-9617.

[122] Q. Abbas, et al., Sodium molybdate - an additive of choice for enhancing the performance of AC/AC electrochemical capacitors in a salt aqueous electrolyte, Faraday Discuss., 172 (2014) 199-214.

[123] I. Piñeiro-Prado, et al., Design of activated carbon/activated carbon asymmetric capacitors, Front. Mater., 3 (2016) 16.

[124] M. Lazzari, et al., High voltage, asymmetric EDLCs based on xerogel carbon and hydrophobic IL electrolytes, J. Power Sources, 178 (2008) 490-496.

[125] M. Lazzari, et al., Mesoporous carbon design for ionic liquid-based, double-layer supercapacitors, Fuel Cells, 10 (2010) 840-847.

[126] N. Jackel, et al., Increase in capacitance by subnanometer pores in carbon, ACS Energy Letters, 1 (2016) 1262-1265.

[127] V. Khomenko, et al., Optimisation of an asymmetric manganese oxide/activated carbon capacitor working at 2V in aqueous medium, J. Power Sources, 153 (2006) 183-190.

[128] X. Wang, et al., High energy density aqueous electrochemical capacitors with a KI-KOH electrolyte, ACS Appl. Mater. Interfaces, 7 (2015) 19978-19985.

[129] M. Yu, et al., Boosting the energy density of carbon-based aqueous supercapacitors by optimizing the surface charge, Angew. Chem. Int. Ed. Engl., 56 (2017) 5454-5459.

[130] X. Zhou, et al., 20 V stack of aqueous supercapacitors with carbon (−), titanium bipolar plates and CNT ‐ polypyrrole composite (+), AlChE J., 58 (2012) 974-983.

[131] J. Chae, et al., Nanostructured materials for the construction of asymmetrical supercapacitors, Proceedings of the Institution of Mechanical Engineers, Part A: Journal of Power and Energy, 224 (2010) 479-503.

[132] K. K. Lian, et al., Electrochemical cell having symmetric inorganic electrodes, Patent No. 5,587,872, December 24, 1996.

[133] K. C. Ng, et al., Individual and bipolarly stacked asymmetrical aqueous supercapacitors of CNTs/sno$_2$ and CNTs/MnO$_2$ nanocomposites, J. Electrochem. Soc., 156 (2009) A846-A853.
[134] P. Staiti, F. Lufrano, Design, fabrication, and evaluation of a 1.5 F and 5 V prototype of solid-state electrochemical supercapacitor, J. Electrochem. Soc., 152 (2005) A617-A621.
[135] X. Zhou, G. Z. Chen, Electrochemical performance of screen-printed composite coatings of conducting polymers and carbon nanotubes on titanium bipolar plates in aqueous asymmetrical supercapacitors, J. Electrochem, 18 (2012) 548-565.
[136] G. Xiong, et al., Thermal effects in supercapacitors, Springer, 2015.
[137] J. Zheng, T. Jow, High energy and high power density electrochemical capacitors, J. Power Sources, 62 (1996) 155-159.
[138] R. Vellacheri, et al., High performance supercapacitor for efficient energy storage under extreme environmental temperatures, Nano Energy, 8 (2014) 231-237.
[139] A. J. Roberts, et al., Low temperature water based electrolytes for MnO$_2$/carbon supercapacitors, Phys. Chem. Chem. Phys., 15 (2013) 3518-3526.
[140] J. Yin, et al., Anti-freezing aqueous electrolytes for electric double-layer capacitors, Electrochim. Acta, 88 (2013) 208-216.
[141] Q. Abbas, F. Béguin, High voltage AC/AC electrochemical capacitor operating at low temperature in salt aqueous electrolyte, J. Power Sources, 318 (2016) 235-241.
[142] S. P. Pinho, E. A. Macedo, Solubility of nacl, nabr, and kcl in water, methanol, ethanol, and their mixed solvents, J. Chem. Eng. Data, 50 (2005) 29-32.
[143] Q. Abbas, F. Beguin, Sustainable carbon/carbon supercapacitors operating down to -40 °C in aqueous electrolyte made with cholinium salt, ChemSusChem, 11 (2018) 975-984.
[144] E. J. Brandon, et al., Extending the low temperature operational limit of double-layer capacitors, J. Power Sources, 170 (2007) 225-232.
[145] E. Perricone, et al., Safe and performant electrolytes for supercapacitor. Investigation of esters/carbonate mixtures, J. Power Sources, 239 (2013) 217-224.
[146] A. Jänes, E. Lust, Use of organic esters as co-solvents for electrical double layer capacitors with low temperature performance, J. Electroanal. Chem., 588 (2006) 285-295.
[147] Y. Korenblit, et al., In situ studies of ion transport in microporous supercapacitor electrodes at ultralow temperatures, Adv. Funct. Mater., 22 (2012) 1655-1662.
[148] W. C. West, et al., Double-layer capacitor electrolytes using 1, 3-Dioxolane for low temperature operation, J. Electrochem. Soc., 155 (2008) A716-A720.
[149] R. Lin, et al., Capacitive energy storage from -50 to 100 °C using an ionic liquid electrolyte, The Journal of Physical Chemistry Letters, 2 (2011) 2396-2401.
[150] L. Dagousset, et al., Electrochemical characterisations and ageing of ionic liquid/γ-butyrolactone mixtures as electrolytes for supercapacitor applications over a wide temperature range, J. Power Sources, 359 (2017) 242-249.
[151] L. Dagousset, et al., Ionic liquids and γ-butyrolactone mixtures as electrolytes for supercapacitors operating over extended temperature ranges, Rsc Adv., 5 (2015) 13095-13101.
[152] V. Ruiz, et al., Ionic liquid-solvent mixtures as supercapacitor electrolytes for extreme temperature operation, Rsc Adv., 2 (2012) 5591-5598.
[153] W.-Y. Tsai, et al., Outstanding performance of activated graphene based supercapacitors in ionic liquid electrolyte from -50 to 80 °C, Nano Energy, 2 (2013) 403-411.
[154] P. H. Huang, et al., On-chip micro-supercapacitors for operation in a wide temperature range, Electrochem. Commun., 36 (2013) 53-56.
[155] Z. Lin, et al., Graphene-based supercapacitors using eutectic ionic liquid mixture electrolyte, Electrochim. Acta, 206 (2016) 446-451.
[156] Y. Zhou, et al., High performance supercapacitor under extremely low environmental temperature, Rsc Adv., 5 (2015) 71699-71703.
[157] R. Newell, et al., A new high performance ionic liquid mixture electrolyte for large temperature range supercapacitor applications (-70 to 80 °C) operating at 3.5V cell voltage, Electrochim. Acta, 267 (2018) 15-19.
[158] C. Yuan, et al., Effect of temperature on the hybrid supercapacitor based on NiO and activated carbon with alkaline polymer gel electrolyte, Solid State Ionics, 177 (2006) 1237-1242.

[159] H. Michel, Temperature and dynamics problems of ultracapacitors in stationary and mobile applications, J. Power Sources, 154 (2006) 556-560.
[160] K. Hung, et al., Wide-temperature range operation supercapacitors from nanostructured activated carbon fabric, J. Power Sources, 193 (2009) 944-949.
[161] C. Maton, et al., Ionic liquid thermal stabilities: Decomposition mechanisms and analysis tools, Chem. Soc. Rev., 42 (2013) 5963-5977.
[162] M. E. Van Valkenburg, et al., Thermochemistry of ionic liquid heat-transfer fluids, Thermochim. Acta, 425 (2005) 181-188.
[163] G. Xiong, et al., Graphitic petal micro-supercapacitor electrodes for ultra-high power density, Energy Technology, 2 (2014) 897-905.
[164] O. Bohlen, et al., Ageing behaviour of electrochemical double layer capacitors: Part I. Experimental study and ageing model, J. Power Sources, 172 (2007) 468-475.
[165] T. Liebert, T. Heinze, Interaction of ionic liquids with polysaccharides. 5. Solvents and reaction media for the modification of cellulose, BioResources, 3 (2008) 576-601.
[166] M. Zavrel, et al., High-throughput screening for ionic liquids dissolving (ligno-)cellulose, Bioresour. Technol., 100 (2009) 2580-2587.
[167] R. Hastak, et al., All solid supercapacitor based on activated carbon and poly [2, 5-benzimidazole] for high temperature application, Electrochim. Acta, 59 (2012) 296-303.
[168] S.-K. Kim, et al., Extremely durable, flexible supercapacitors with greatly improved performance at high temperatures, ACS nano, 9 (2015) 8569-8577.
[169] X. Liu, et al., Tough bmimcl-based ionogels exhibiting excellent and adjustable performance in high-temperature supercapacitors, J. Mater. Chem. A, 2 (2014) 11569.
[170] H. Fei, et al., Flexible all-solid-state supercapacitors based on graphene/carbon black nanoparticle film electrodes and cross-linked poly (vinyl alcohol)-H_2SO_4 porous gel electrolytes, J. Power Sources, 266 (2014) 488-495.
[171] J. Niu, et al., Comparative studies of self-discharge by potential decay and float-current measurements at c double-layer capacitor and battery electrodes, J. Power Sources, 135 (2004) 332-343.
[172] S. Fletcher, et al., A universal equivalent circuit for carbon-based supercapacitors, J. Solid State Electrochem., 18 (2013) 1377-1387.
[173] J. Black, H. A. Andreas, Effects of charge redistribution on self-discharge of electrochemical capacitors, Electrochim. Acta, 54 (2009) 3568-3574.
[174] A. Lewandowski, et al., Self-discharge of electrochemical double layer capacitors, Phys. Chem. Chem. Phys., 15 (2013) 8692-8699.
[175] J. Kowal, et al., Detailed analysis of the self-discharge of supercapacitors, J. Power Sources, 196 (2011) 573-579.
[176] H. A. Andreas, Self-discharge in electrochemical capacitors: A perspective article, J. Electrochem. Soc., 162 (2015) A5047-A5053.
[177] L. Chen, et al., Mechanism investigation and suppression of self-discharge in active electrolyte enhanced supercapacitors, Energy Environ. Sci., 7 (2014) 1750-1759.
[178] T. Tevi, et al., Application of poly (p-phenylene oxide) as blocking layer to reduce self-discharge in supercapacitors, J. Power Sources, 241 (2013) 589-596.
[179] K. Fic, et al., Electrochemical properties of supercapacitors operating in aqueous electrolyte with surfactants, Electrochim. Acta, 55 (2010) 7484-7488.
[180] M. Y. Xia, et al., Suppressing self-discharge of supercapacitors via electrorheological effect of liquid crystals, Nano Energy, 47 (2018) 43-50.
[181] Z. Y. Fan, et al., Towards kilohertz electrochemical capacitors for filtering and pulse energy harvesting, Nano Energy, 39 (2017) 306-320.
[182] J. R. Miller, et al., Graphene double-layer capacitor with ac line-filtering performance, Science, 329 (2010) 1637-1639.
[183] Z. S. Wu, et al., Bottom-up fabrication of sulfur-doped graphene films derived from sulfur-annulated nanographene for ultrahigh volumetric capacitance micro-supercapacitors, J. Am. Chem. Soc., 139 (2017) 4506-4512.
[184] J. P. Randin, E. Yeager, Differential capacitance study of stress-annealed pyrolytic graphite electrodes, J. Electrochem. Soc., 118 (1971) 711-714.

[185] Y. Yoo, et al., 2.5 V compact supercapacitors based on ultrathin carbon nanotube films for AC line filtering, J. Mater. Chem. A, 3 (2015) 11801-11806.

[186] Y. Rangom, et al., Carbon nanotube-based supercapacitors with excellent ac line filtering and rate capability via improved interfacial impedance, ACS Nano, 9 (2015) 7248-7255.

[187] Y. Zhu, et al., A seamless three-dimensional carbon nanotube graphene hybrid material, Nat. Commun., 3 (2012) 1225.

[188] J. Lin, et al., 3-dimensional graphene carbon nanotube carpet-based microsupercapacitors with high electrochemical performance, Nano Lett., 13 (2013) 72-78.

[189] Y. Yoo, et al., Fast-response supercapacitors with graphitic ordered mesoporous carbons and carbon nanotubes for AC line filtering, J. Mater. Chem. A, 4 (2016) 5062-5068.

[190] N. Islam, et al., High-frequency electrochemical capacitors based on plasma pyrolyzed bacterial cellulose aerogel for current ripple filtering and pulse energy storage, Nano Energy, 40 (2017) 107-114.

[191] G. F. Ren, et al., Kilohertz ultrafast electrochemical supercapacitors based on perpendicularly-oriented graphene grown inside of nickel foam, Carbon, 71 (2014) 94-101.

[192] G. F. Ren, et al., Ultrahigh-rate supercapacitors with large capacitance based on edge oriented graphene coated carbonized cellulous paper as flexible freestanding electrodes, J. Power Sources, 325 (2016) 152-160.

[193] M. Cai, et al., Fast response, vertically oriented graphene nanosheet electric double layer capacitors synthesized from C_2H_2, ACS Nano, 8 (2014) 5873-5882.

[194] Q. Zhou, et al., Nitrogen-doped holey graphene film-based ultrafast electrochemical capacitors, ACS Appl. Mater. Interfaces, 8 (2016) 20741-20747.

[195] K. Sheng, et al., Ultrahigh-rate supercapacitors based on eletrochemically reduced graphene oxide for ac line-filtering, Sci. Rep., 2 (2012) 247.

[196] Y. Yoo, et al., Development of 2.8 V ketjen black supercapacitors with high rate capabilities for AC line filtering, J. Power Sources, 360 (2017) 383-390.

[197] J. R. Miller, Introduction to electrochemical capacitor technology, IEEE Electrical Insulation Magazine, 26 (2010) 40-47.

[198] B. University, Bu-301a: Types of battery cells, https://batteryuniversity.com/learn/article/types_of_battery_cells, Acessed on September 19, 2018.

[199] M. Lu, et al., Supercapacitors: Materials, systems and applications, John Wiley & Sons, 2013.

[200] A. Energy, Discover how the supercapacitor can enhance the battery, http://atlascoenergy.com/projects/supercapacitor/, Acessed on September 19, 2018.

[201] J. Gabay, Supercapacitor options for energy-harvesting systems, https://www.digikey.com/en/articles/techzone/2013/aug/supercapacitor-options-for-energy-harvesting-systems, Acessed on September 19, 2018.

[202] N.-C. Lee, Reflow soldering processes, Elsevier, 2002.

[203] C. T. Lhii, El proyecto, http://bga.blog.tartanga.eus/descripcion-del-proyecto/, Acessed on September 19, 2018.

[204] Murata, DMH series, https://www.murata.com/en-us/products/capacitor/edlc/dmh, Acessed on October 3, 2018.

[205] Cellergy, Cellergy supercapacitor product specification, https://www.cellergycap.com/images/download/Cellergy_Spec_-_rev35_1.pdf, Acessed on October 3, 2018.

[206] CLC Factory, CLC3225 model surface mount type, http://www.clcfactory.co.kr/?act=shop.goods_view&GS=6&GC=GD00, Acessed on October 3, 2018.

[207] Seiko, Cpx capacitors cpx3225a752d, https://www.sii.co.jp/en/me/datasheets/chip-capacitor/cpx3225a752d/, Acessed on October 3, 2018.

[208] L. Liu, et al., Unconventional supercapacitors from nanocarbon-based electrode materials to device configurations, Chem. Soc. Rev., 45 (2016) 4340-4363.

[209] S. Anthony, Structural power technology turns car doors into batteries, https://uk.pcmag.com/feature/106908/structural-power-technology-turns-car-doors-into-batteries, Acessed on October 3, 2018.

[210] N. A. Kyeremateng, et al., Microsupercapacitors as miniaturized energy-storage components for on-chip electronics, Nat. Nanotechnol., 12 (2017) 7-15.

PAPER I

Journal of Power Sources 348 (2017) 219–228

Contents lists available at ScienceDirect

Journal of Power Sources

journal homepage: www.elsevier.com/locate/jpowsour

Redox enhanced energy storage in an aqueous high-voltage electrochemical capacitor with a potassium bromide electrolyte

Qi Li [a], [*], Mazharul Haque [a], Volodymyr Kuzmenko [a], Namrata Ramani [b], Per Lundgren [a], Anderson D. Smith [a], Peter Enoksson [a]

[a] Department of Microtechnology and Nanoscience, Chalmers University of Technology, Gothenburg 41296, Sweden
[b] Department of Materials Science and Engineering, University of California, Los Angeles, CA 90095, United States

HIGHLIGHTS

- An aqueous electrochemical capacitor with stable operation at 1.9 V.
- The EDLC transforms into a redox-EDLC when increasing the operation voltage.
- Br^-/Br_3^- enhances the energy storage at 1.6 V after a triggering operation.
- Electro-oxidation and Br^-/Br_3^- kinetics are proposed causes to the phenomenon.

ARTICLE INFO

Article history:
Received 19 December 2016
Received in revised form
17 February 2017
Accepted 25 February 2017

Keywords:
Redox-EDLC
Aqueous supercapacitor
Redox electrolyte
High voltage
Electrode potential

ABSTRACT

This paper reports a detailed electrochemical investigation of a symmetric carbon-carbon electrochemical device with a potassium bromide (KBr) electrolyte. Below 1.6 V, KBr gives electrochemical double layer behavior. At higher voltages the Br^-/Br_3^- redox reaction comes into effect and enhances the energy storage. The redox-enhanced device has a high energy density, excellent stability, as well as high coulombic and energy efficiencies even at 1.9 V. More importantly, the redox contribution can be “triggered” by pre-cycling at 1.9 V, and remains beneficial after switching to 1.6 V. The triggering operation leads to a 22% increase in stored energy with negligible sacrifice of power. The intriguing behavior is accompanied by a series of complex variations including the shifts of electrode potential limits and the shift of potential of zero voltage. The electro-oxidation of the positive electrode and kinetics of the Br^-/Br_3^- electrode reactions are proposed to be the main causes for the triggering phenomenon. These findings provide means to improve the design and operation of devices that contain bromine, or other redox species with a comparably high electrode potential.

1. Introduction

Electrochemical double layer capacitors (EDLCs) are capable of rapid energy delivery, work with less complicated circuits and have almost limitless lifetime [1–4]. Although an EDLC stores far more energy than a conventional dielectric capacitor, its storage capacity lags behind that of a battery. Therefore, the application of EDLCs is presently limited and energy density enhancement of EDLCs has thus attracted significant attention among researchers [5,6]. Recent reports have demonstrated that replacing an inert electrolyte with a redox-active one introduces multi-electron faradaic reactions as another source of energy in addition to electrostatic energy storage [7–13]. This provides a new route towards energy enhancement, in addition to surface engineering of carbon electrodes [14–16]. The implantation of different catholytes (the portion of an electrolyte near a cathode) and anolytes (the portion of an electrolyte near an anode) in one system is a remarkable way to optimize the device performance [12,17,18]. An efficient design can further increase the energy density several times [12].

Applicable to all EDLC systems, the maximization of cell voltage (U) should be taken into account when designing electrochemical capacitors since the stored energy is proportional to U^2. The voltage limit is mostly determined by the electrochemical stability window of an electrolyte (solvent). In this regard, organic electrolytes used commercially enable a range over 2 V. The energy of an organic

---

[*] Corresponding author.
E-mail address: qili@chalmers.se (Q. Li).

http://dx.doi.org/10.1016/j.jpowsour.2017.02.082
0378-7753/

EDLC can be further enhanced by a redox electrolyte [19]. Compared with organic electrolytes, aqueous electrolytes have more industrial potential since they have higher power capability, convenient fabrication at ambient conditions and less safety concerns [1,20]. Therefore, there is an ongoing effort to develop high performance aqueous EDLC systems. The incorporation of redox functionality to construct aqueous redox-EDLCs is recognized to be a promising approach [17].

In aqueous redox-EDLC systems, a smart design for energy maximization utilizes redox couples whose electrode potential is close to the H_2O decomposition window. This strategy allows the highest potential of a redox reaction before water splitting. Explicitly, the potential should be around the oxygen evolution potential (OEP) for catholytes, and correspondingly, it should be close to the hydrogen evolution potential (HEP) for anolytes. Among various couples mentioned in recent reports, Br^-/Br_3^- has the highest electrode potential of 1.05 V *vs.* NHE (normal hydrogen electrode), 0.23 V higher than the OEP of 0.82 V at pH 7. Considering the overpotential of water decomposition in neutral media, Br^-/Br_3^- is an ideal catholyte species. The effectiveness of the Br^-/Br_3^- redox couple was first shown in an ionic liquid based device [12] where EMImBr was used as a redox additive. This resulted in an 81% capacitance increase compared to the pure $EMImBF_4$. Another effort of using KBr as an additive in acidic media (1 M H_2SO_4) was reported by Melo et al. [21] and led to a 22% capacitance increase in the voltage window from 0 to 1 V. In neutral systems, the bromine chemistry is rarely studied. Some information can be found in the recent report by Boettcher's group [12] which provides further evidence of the high efficiency of Br^-/Br_3^- for energy enhancement. However, that detailed electrochemical study on a Br-containing aqueous electrolyte was limited to 1.0 V, and investigated only a particular case where the positive and negative electrodes were mass-imbalanced.

In addition, due to the rather high electrode potential of 1.05 V *vs.* NHE for Br^-/Br_3^-, the correlation between cell voltage and energy storage properties is an important feature that should be investigated for Br-containing devices. At a low cell voltage, the electrode potential may not be able to reach the 1.05 V required to initiate redox activity, causing the device to behave as a regular EDLC. In contrast, when the cell voltage is sufficiently high, Br^-/Br_3^- reactions take place, thus turning the cell into a redox-EDLC. The "boundary voltage" may not be clearly defined, considering the complex hybrid EDLC and battery-like behavior. However, this complexity makes it possible to adjust the performance by means of specific cell operations. For instance, an initial polarization to a redox-active voltage may influence the behavior at a lower voltage. This possibility exists for all high-electrode-potential redox couples besides Br^-/Br_3^-, and implies that the performance of a redox-EDLC may be highly dependent on cell operation history. This scenario is comparable to the "formation cycles" [22–24] which are critical in the battery industry. However, there is currently not sufficient attention given to such an issue in redox-EDLC studies.

As a highly soluble species with a high electrode potential in neutral aqueous media, a Br-containing electrolyte is a promising candidate for inexpensive high-voltage aqueous electrochemical devices. Herein, we investigate bromine's redox effect in a neutral aqueous symmetric carbon-carbon prototype using KBr. KBr is found to outperform many other electrolytes in different aspects. To the best of our knowledge, we demonstrate for the first time that an aqueous symmetric supercapacitor device with a KBr electrolyte can perform steadily up to 1.9 V. Moreover, a controllable transition in the energy storage mechanism related to cell operation is revealed. These findings provide important hints for the design and operation of electrochemical devices which contain Br, as well as other high-electrode-potential redox species.

2. Experimental

2.1. Electrode preparation

Activated carbon (AC, Kuraray, YP-80F) was used as received without further treatment. The surface area and average pore size of the AC were calculated to be 2112 $m^2\ g^{-1}$ and 1.32 nm, respectively, using the Brunauer-Emmett-Teller (BET) equation and quenched solid density functional theory (QSDFT) [25]. The electrodes used in this work were prepared by thorough mixing of AC, carbon black and polytetrafluoroethylene (PTFE) binder (60 wt. % dispersion in H_2O) in a weight ratio of 80:10:10. After water evaporation in a 75 °C water bath, the mixture was processed into a freestanding film by a rolling press. Φ10 mm pellets were punched out from the film and used as electrodes. A single electrode was around 3 mg in mass and 100 μm in thickness.

2.2. Electrochemical measurements

Three different types of setup were used for electrochemical measurements. A traditional three electrode setup which consisted of a counter electrode (10 mm × 10 mm Pt plate), a reference electrode (Ag/AgCl, 3 M KCl) and a working electrode (an electrode pellet attached to a graphite rod with conductive carbon paste). A two electrode setup was assembled by sandwiching a glass fiber separator (Φ12 mm, thickness 200 μm Whatman®) between two electrode pellets in a two-electrode Swagelok® cell (SS316 current collector). Approximately 100 μL of electrolyte was added into the devices. The other setup was a T-type Swagelok® cell customized from the two-electrode Swagelok® cell by adding an Ag/AgCl reference electrode. The measurements were carried out on a Gamry Reference 3000AE and a Neware BTS 2000 multi-channel potentiostat at room temperature (21 °C).

For the device performance (measurements in two-electrode and T-type Swagelok® cells), the specific capacitance of an electrode, $C_{electrode}$ (F g^{-1}) was calculated from cyclic voltammetry (CV) or galvanostatic charge/discharge (GCD) measurements. Equation (1) was applied to CV profiles:

$$C_{electrode} = \frac{1000}{2M\nu(V_2 - V_1)} \int_{V_1}^{V_2} |I(V)|dV \qquad (1)$$

where M (mg) is the mass of both electrodes including the PTFE binder and carbon black, ν (mV s^{-1}) is the scan rate, V_1 and V_2 are the lower and upper limits of the voltage range in V, and $I(V)$ is the current response in mA. For GCD profiles, equations (2) and (3) were applied for capacitance $C_{electrode}$ (F g^{-1}) and capacity $Q_{electrode}$ (mAh g^{-1}) calculations, respectively:

$$C_{electrode} = \frac{2I_{dis}t_{dis}}{MV} \qquad (2)$$

$$Q_{electrode} = \frac{2I_{dis}t_{dis}}{M} \qquad (3)$$

where I_{dis} (mA) is the constant discharge current, t_{dis} (s) is the discharge time, and V is the maximum cell voltage. The specific energy density of the device, E_{device} (Wh kg^{-1}), was derived from the integration area beneath the discharge curves by applying equation (4):

$$E_{device} = \frac{I_{dis}}{M}\int_{0}^{t_{dis}} V(t)dt \tag{4}$$

where $V(t)$ is the voltage response against time. The specific power P_{device} (W kg^{-1}) was calculated using the following equation:

$$P_{device} = \frac{3600E_{device}}{t_{dis}} \tag{5}$$

The coulombic and energy efficiencies (η_C and η_E) of the device were calculated by equations (6) and (7):

$$\eta_C = \frac{Q_{electrode}}{Q_{ch}} \tag{6}$$

$$\eta_E = \frac{E_{electrode}}{E_{ch}} \tag{7}$$

where Q_{ch} (mAh g^{-1}) and E_{ch} (Wh kg^{-1}) are the charges and the energy accumulated during the charging process, calculated by equations (8) and (9), respectively.

$$Q_{ch} = \frac{2I_{ch}t_{ch}}{M} \tag{8}$$

$$E_{ch} = \frac{I_{ch}}{M}\int_{0}^{t_{ch}} V(t)dt \tag{9}$$

where I_{ch} (mA) and t_{ch} (s) are the constant charging current and charging time.

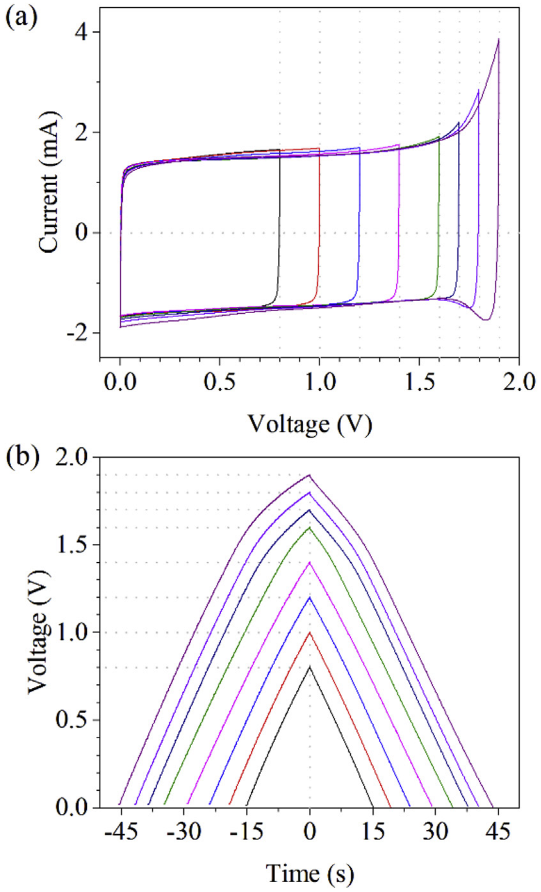

Fig. 1. (a) CV scans at 20 mV s^{-1} and (b) GCD curves at 1 A g^{-1} of a Swagelok® cell at different voltage limits.

3. Results and discussion

3.1. Device performance and the "triggering operation"

The performance of a device consisting of two identical AC electrodes and 1 M KBr electrolyte is initially evaluated with a two-electrode setup. The CV curves sweeping from 0 V to different upper voltage limits are recorded at a scan rate of 20 mV s^{-1} (Fig. 1a). In general, the KBr electrolyte enables ideal EDL behavior up to 1.6 V, giving high coulombic efficiencies (over 97%). Sweeping beyond the limit causes a distortion from the ideal rectangular CV shape. From 1.6 up to 1.9 V cell operation, a significant increase of the anodic current is observed and an associated hump appears in the beginning period of the cathodic scan, suggesting the presence of redox activities in the system. Coulombic efficiencies remain high, i.e. 96, 95 and 93% for 1.7, 1.8 and 1.9 V operations respectively. Representative GCD curves at selected voltages are displayed in Fig. 1b. As in the CV measurements, significant deviations from an ideal EDLC behavior take place after 1.6 V; the slope of the charge/discharge curve is reduced at high voltages. Further, charging beyond 1.9 V causes a severe decrease in stability and efficiency (see supporting information, Fig. S1). Therefore, the voltage limit is set at 1.9 V.

According to the features of the CV and GCD curves in Fig. 1, we assume that the device is principally an EDLC up to 1.6 V, since the CV curves maintain a rather rectangular shape and the voltage response in the GCD test is approximately proportional to the total amount of stored charge (charge/discharge time). A kinetics examination of the CV scan rate dependence at 1.6 V (Fig. S3) is performed by using equation (10) [26]:

$$i(V) = k_1 v + k_2 v^{1/2} \tag{10}$$

where $i(V)$ is the current response at a specific voltage, k_1v and $k_2v^{1/2}$ correspond to the current contributions from the surface capacitive effects and the diffusion-controlled redox process, respectively [26]. The calculation quantitatively confirms the high proportion of EDL capacitive contribution - 89% at a scan rate of 20 mV s^{-1} and 94% at 100 mV s^{-1}. On the other hand, at higher voltages (1.7 V and above), the voltage response severely deviates from the linear feature due to redox reactions, hence the device should be considered as a hybrid device (rather than a pseudocapacitor) [27]. It is worth noting that the concept of "capacitance" is not ideally applicable for hybrid devices, but could be practically used in this case where the EDL behavior still dominates over battery-behavior [28]. For hybrid devices, the coulombic efficiency has been found to be inconclusive in reflecting the device effectiveness, wherefore energy efficiency is of particular interest in this case [28,29]. As exhibited in Table 1, the coulombic efficiencies at specified voltage limits are higher than 97%. In contrast, the energy efficiency drops from 95.2% at 0.8 V to 87.6% at 1.9 V. The 4.8% energy loss at 0.8 V can be at least partly resulting from heat dissipation [30], and at higher voltages, additional energy is lost through overpotential of the Br-related redox activities, which will be revealed in section 3.2.2.

A stepwise cyclic charge-discharge (CCD) test is conducted by performing 2000 cycles at each specified voltage from 0.8 to 2 V, and the results confirm the stability of the system (Fig. S1, rapid decrease is observed only at 2.0 V). The performance of a device

Table 1
Performance metrics of the KBr-containing device at different voltages.[a]

	0.8 V	1.0 V	1.2 V	1.4 V	1.6 V	1.7 V	1.8 V	1.9 V
Specific capacity, $Q_{electrode}$ (mAh g^{-1})	16.8	20.8	25.6	32.4	38.0	41.6	44.8	48.8
Specific capacitance, $C_{electrode}$ (F g^{-1})	75.2	77.2	80.4	83.2	85.2	88.4	89.6	92.0
Specific energy, E_{device} (Wh kg^{-1})	1.7	2.7	4.0	6.1	8.0	9.4	10.6	12.0
Coulombic efficiency, η_C (%)	99.7	99.7	99.6	99.4	98.7	97.9	97.2	97.5
Energy efficiency, η_E (%)	95.2	95.6	95.8	94.3	93.3	91.4	89.0	87.6

[a] The numbers presented in this table are average values of 100 cycles at specified voltages with a current density of 1 A g^{-1}.

directly polarized to 1.6 V is exhibited in Fig. 2a. As expected, the cell at 1.6 V shows almost no capacitance decrease over 10000 cycles with an average value around 85 F g^{-1} for a single electrode. The specific energy is also rather stable and an average value of 7.4 Wh kg^{-1} is obtained. For the cell working at 1.9 V, the specific capacitance is 91 F g^{-1} in the beginning and stabilizes at 101 F g^{-1} in the end of cycling (Fig. 2c). Likewise, specific energy displays a 12% increase from 9.7 to 10.9 Wh kg^{-1}.

Both the 1.6 and 1.9 V cells are very efficient in charge and energy utilization, exhibiting almost 100% coulombic efficiency and energy efficiency around 90%. In order to gain more details of the behavior change during cycling stability tests, the charge/discharge curves at 50th, 1000th, 5000th and 10000th cycles were extracted from the corresponding CCD test and compared in Fig. 2b and d. The amount of charge being stored or released during the charging or discharging process is proportional to the respective time, and the amount of energy can be graphically reflected by the enclosed area under the GCD plot. For the cell working at 1.6 V, the GCD curves collected along the cycling tests are rather linear and represent predominant EDL behavior. The curves are well overlapped showing no significant change in charge/discharge time and shape, indicating essential stability of the energy storage mechanism. In sharp contrast, when the cell is operated at 1.9 V, the slopes of the GCD curves are markedly lower at the high voltage part of the cycle,

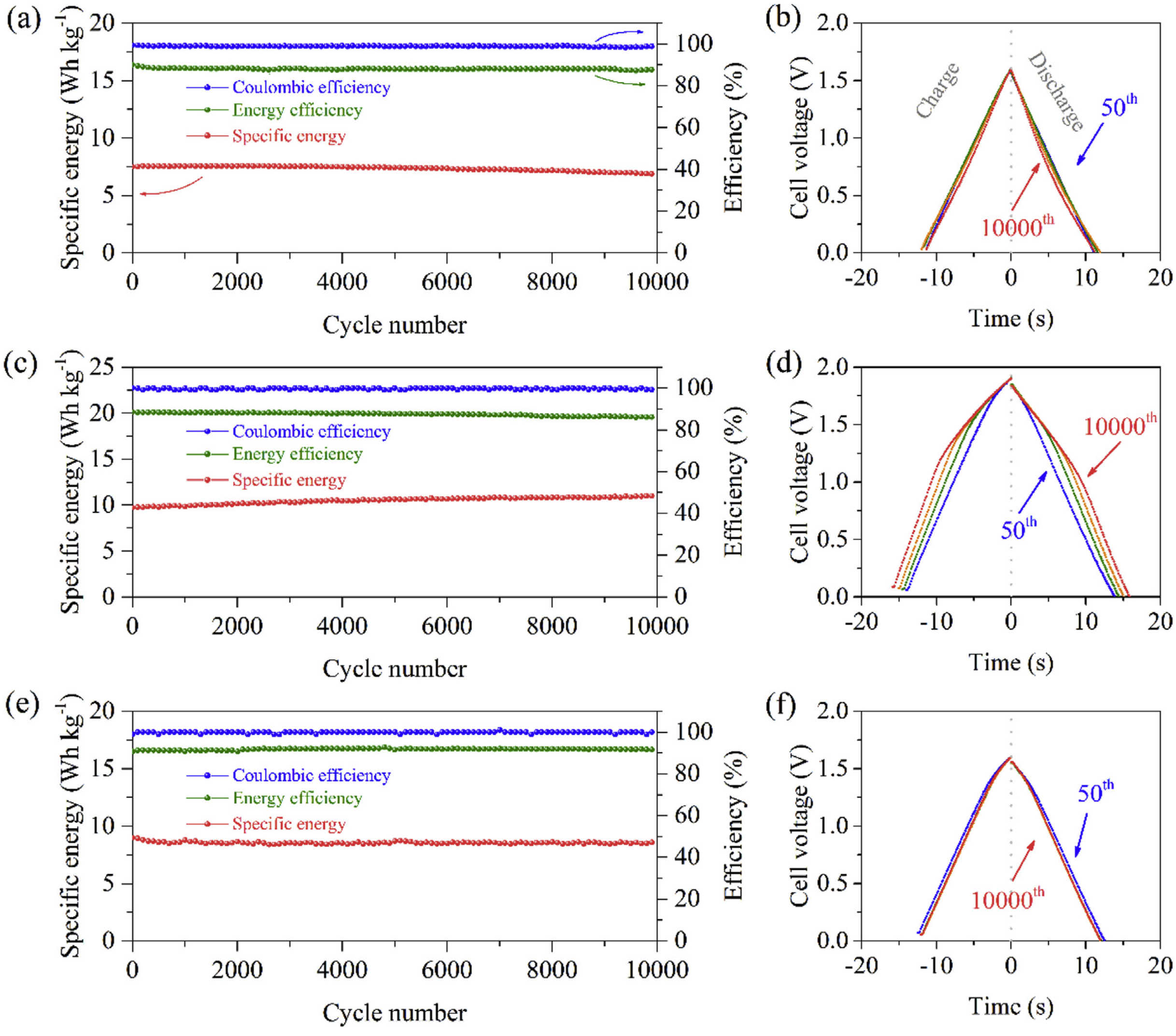

Fig. 2. Cycling stability and GCD curves at selected cycle numbers of two-electrode Swagelok® cells operating at 1.6 V (a, b), 1.9 V (c, d) and 1.6 V after triggering operation (e, f).

and this phenomenon develops with cycling. The evolution of the GCD curves suggests that more and more redox activities are coming into effect, which results in the increases of capacitance or capacity (charge/discharge time) and specific energy (enclosed area). The capacitance and energy increase with cycling is also observed for KI (Fig. S4) which is consistent with previous reports [11,31,32]. Although the underlying mechanism remains to be explained, we propose that it might be related to the kinetics of redox species – a possibility which will be discussed in section 3.3.

As the cycle number increases, the deviation from linearity starts to take place at lower and lower voltages (Fig. 2d). At the 10000th cycle, linear deviation occurs above 1.2 V, which means that at this junction, the redox activity could be utilized at a cell voltage lower than 1.6 V. This feature suggests that the onset of redox reaction can be manipulated by pre-cycling at 1.9 V for a certain number of cycles, and thereafter be utilized at lower voltages. Since redox activities are usually diffusion-controlled reactions with slow kinetics [31], they contribute additional energy to an EDLC and simultaneously decrease the power capability. The manipulation of redox activity is thus necessary, in order to assemble an effective supercapacitor with properly enhanced energy density while maintaining a high power capability. Otherwise, the device turns out to be a mediocre battery. The trade-off has been observed in several cases [17,19], and also applies in the present system. The device working at 1.6 V shows a high rate capability (capacitance retention at 15 A g^{-1}, normalized to the value at 1 A g^{-1}) of 92%, whereas at 1.9 V the value is 81% after 10000 cycles (Fig. S5).

Figs. 2e–f demonstrate the energy enhancement of an EDLC at a minimum sacrifice of power. After pre-cycling at 1.9 V for 500 cycles, the cell voltage is lowered to 1.6 V and cycled for 10000 cycles. The initial specific capacitance and energy density at 1.6 V after pre-cycling are 97 F g^{-1} and 9.0 Wh kg^{-1}, corresponding to 22% increase based on the results in Fig. 2a before pre-cycling, thereafter the device stabilizes at 94 F g^{-1} and 8.6 Wh kg^{-1}. As exhibited in Fig. 2f, the curves at the specified cycles are almost perfectly overlapped, suggesting an extraordinarily stable system with no further evolution of redox species. As compared to the curves in Fig. 2b, the GCD profiles show the features of redox activity after initial high voltage (1.9 V) cycling. The rate capability is calculated to be 88%. This value is slightly lower than for the pure EDLC, but significantly higher than the value when redox activity is heavily involved. Moreover, it is worth mentioning that another advantage of manipulation of the redox activity is a reduced risk of current collector corrosion. This is especially relevant when stainless steel collectors are used in halogen-containing systems [33]. For convenience, we denote the effect of the pre-cycling at 1.9 V as "triggering" of redox activity.

The relationship between energy and power in the neutral aqueous carbon-carbon device is measured and compared to published reference data [2] in a Ragone chart (Fig. 3). The specific energy for the device at 1.6 V, 1.9 V and 1.6 V after triggering is 7.9, 12.1 and 9.0 Wh kg^{-1} at a current density of 1 A g^{-1}. The maximum specific power is around 12, 15 and 14 kW kg^{-1} respectively achieved at 15 A g^{-1}. The gravimetric values are reported by normalizing to the mass of both electrodes (including additives). The mass of the KBr electrolyte is excluded, considering that KBr performs as a redox-active electrolyte and it has a comparable molar mass (119.0 g mol^{-1}) to conventional electrolytes [28]. In practical applications, carbon materials account for approximately 1/3 of the total mass of the packaged commercial device; dividing by a factor of 3 thus gives an extrapolation to a real device performance [34]. The re-calculated metrics at the three different conditions are still located outside the reference area of electrochemical capacitors in the Ragone plot. A few conventional electrolytes are also measured. Note that in acid or alkaline electrolytes, carbon materials usually show higher capacitance than in neutral media – the specific capacitance in 1 M KBr is 20% lower than in 6 M KOH (Table S1). Therefore, it is considered to be an effective practice to use KBr as a redox additive to these non-neutral electrolytes, in order to further enhance the energy storage capacity. However, there presents a few drawbacks in terms of strict requirements on anti-corrosion equipment, current collectors and the loss of maximum voltage due to the low electrochemical stability window of acidic and alkaline electrolytes. In contrast, fewer concerns exist for pure KBr as a neutral electrolyte. Comparing with some other commonly used electrolytes (Figs. S2, S4), KBr exhibits competitive merits in specific capacitance, maximum working voltage and/or energy efficiencies. Taking all these into account, KBr is seen as a promising electrolyte candidate for practical applications.

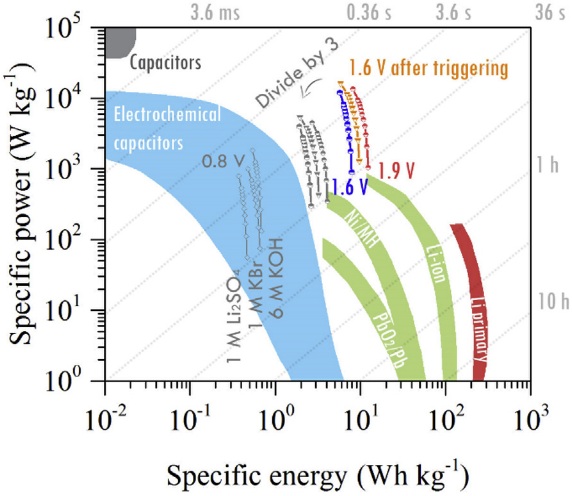

Fig. 3. Ragone plot of the KBr-containing high-voltage electrochemical device. Adapted by permission from Macmillan Publishers Ltd [2].

3.2. Detailed electrochemical analyses

The low-cost aqueous high-voltage electrochemical device with a KBr electrolyte fills a gap between high-power batteries and traditional EDLCs. It is necessary to further investigate the electrochemistry – especially the as-described behavior change after the "triggering operation" in redox-EDLC systems. The phenomenon suggests a method to harness the redox activity and prevents the transformation of an EDLC into a low-energy battery with slightly improved power. More detailed electrochemical analyses are conducted as an effort in further understanding the redox energy enhancement phenomenon.

3.2.1. The electrochemical stability window of 1 M KBr

A traditional three electrode cell is employed to investigate the electrochemical stability window of 1 M KBr electrolyte with AC as the working electrode. Fig. 4 shows the recorded CV curves at the negative and positive potential region *vs.* an Ag/AgCl reference electrode (3 M KCl, 0.21 V *vs.* NHE). The cathodic current during the negative scan increases continuously with the voltage ramping (Fig. 4a). However, no dramatic change is observed till −1.30 V *vs.* Ag/AgCl. The mild current increase could originate from the enhanced hydrogen electrosorption on carbon. A very strong cathodic polarization is observed by stretching the negative limit beyond −1.40 V *vs.* Ag/AgCl (Fig. S6), which is an effect of irreversible hydrogen evolution. On the positive scan, quasi-

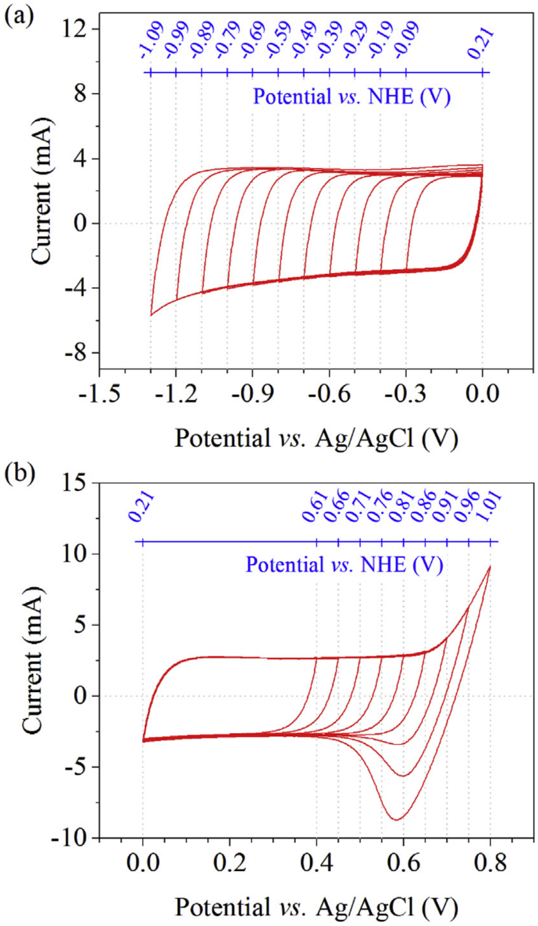

Fig. 4. (a) Negative and (b) positive CV scans of a three electrode cell in 1 M KBr electrolyte at a scan rate of 20 mV s^{-1}.

rectangular CV curves are obtained from 0 to 0.65 V. Extension of the potential window towards more positive values demonstrates significant Br^-/Br_3^- redox activity.

By combining the three electrode measurements in both the negative and positive regions, it can be concluded that the capacitive potential range (CPR) of the KBr electrolyte ranges roughly from −1.30 to +0.65 V *vs.* Ag/AgCl, i.e. around 1.95 V for cell operation. This value is much higher than the theoretical water decomposition window of 1.23 V. The large CPR of KBr in the presence of a porous carbon electrode is a beneficial feature of neutral electrolytes and could be a result of three factors: (1) H^+ and OH^- equilibrium. The concentrations of H^+ and OH^- ions in a neutral electrolyte are extremely low, hence neither hydrogen nor oxygen evolution is favored. (2) There is a strong solvation of both cations and anions [35]. K^+ and Br^- exist in the form of hydrated ions, and the surrounding H_2O molecules have to depart from the hydration shell before getting involved in H_2 or O_2 evolution. Extra energy required for dehydration contributes to the overpotential; (3) hydrogen electrosorption in micropores of the carbon electrode [36,37]. Before irreversible H_2 evolution, the hydrogen species are stored inside the micropores in *statu nascendi*, i.e. as a monoatomic molecule, H_{ad}. The H_{ad} atoms can be reversibly adsorbed/desorbed, which postpones the rapid current increase on the CV scan.

Despite the large CPR of more than 1.9 V, the device performance has suggested that redox activities come into place when the cell operation voltage reaches 1.7 V in the symmetric carbon-carbon system (Fig. 1). This suggests that the potential of zero voltage (*PZV*) is not positioned in the middle of the CPR [38]. Regarding the triggering operation, the shift of the *PZV* and electrode potentials is complex in the redox-EDLC system. A customized T-type Swagelok® cell equipped with an Ag/AgCl reference electrode is further employed to reveal the phenomenon underlying the electrode potential behavior.

3.2.2. *The electrode potential evolution*

The triggering operation is reproduced with a T-type Swagelok® cell. The GCD curves of the cells, as well as positive and negative electrodes are obtained at four different stages (Fig. 5). The cell is firstly polarized to 1.6 V and the curves are recorded for future comparison (Fig. 5c). Thereafter, the device is further polarized to 1.9 V (Fig. 5a) to start the triggering operation. The profiles at the end of triggering are shown in Fig. 5b, and the curves of the cell operated at 1.6 V after triggering are exhibited in Fig. 5d. At least 20 cycles at each stage were recorded, and the curves were collected when the cell was stabilized (open circuit potential variation rate lower than 2 mV min^{-1}).

In general, the negative electrode shows EDL capacitive behavior throughout the process. On the other hand, except the non-triggered cell at 1.6 V (Fig. 5c), the positive electrode shows two distinct time charging regimes, suggesting the co-existence of capacitive and battery-like (redox) behaviors. Redox activities start to take place around 0.65 V *vs.* Ag/AgCl, which is in good agreement with the electrochemical stability window of KBr (Fig. 4). The redox activity produces a plateau in the charging phase and a concomitant one during the discharge. The voltage of the latter is slightly lower than the charging plateau, as a consequence of the overpotential. Such an overpotential causes energy loss because the energy is a product of capacity and voltage. The energy loss on the positive electrode side accounts for the majority loss at a cell level. For instance, 5.2 mW is lost for the whole cell and 4.5 mW of it is lost from the positive electrode in the case of Fig. 5b.

The following potential values are determined by the T-type Swagelok® cell measurements: the electrode potential limit of the positive electrode (*PL*), and of the negative electrode (*NL*) as well as the *PZV*. From the results in Fig. 5, one can observe a positive shift of those parameters after triggering. Further, the position of the *PL* is essential for understanding the varied behaviors at different stages. The redox activity comes into effect when the *PL* goes beyond 0.65 V. Beyond this limit, a higher *PL* value corresponds to more energy contribution from redox reaction. The potential values, as functions of cell voltage, are also examined (Fig. 6a, Table S2). A positive shift of the *PL*, *NL* and *PZV* is observed at all the specified voltages and makes the cell reach the redox activity region earlier on the positive side – sparing more un-utilized capacitive range on the negative side.

The above measurements have explicated the triggering phenomenon from both cell voltage and electrode potential aspects. It can be inferred that the phenomenon is essentially constituted by the shifts of the *PL*, *NL* and *PZV*. The triggering effect is an example of the Br-containing device's susceptibility to operation conditions. The electrochemical system is complex and many important issues, e.g. factors influencing the *PZV*, remain unclear [11]. In section 3.3, a qualitative explanation of the observed phenomena is provided.

3.3. *Discussion*

3.3.1. *Electro-oxidation of the positive electrode*

The electro-oxidation of the positive electrode could be at least partially responsible for the potential shifts. During the cycling at 1.9 V, the *PL* is always higher than the theoretical oxygen evolution potential (OEP, 0.61 V *vs.* Ag/AgCl). It means that H_2O oxidation is potentially happening in addition to strong Br^- oxidation during

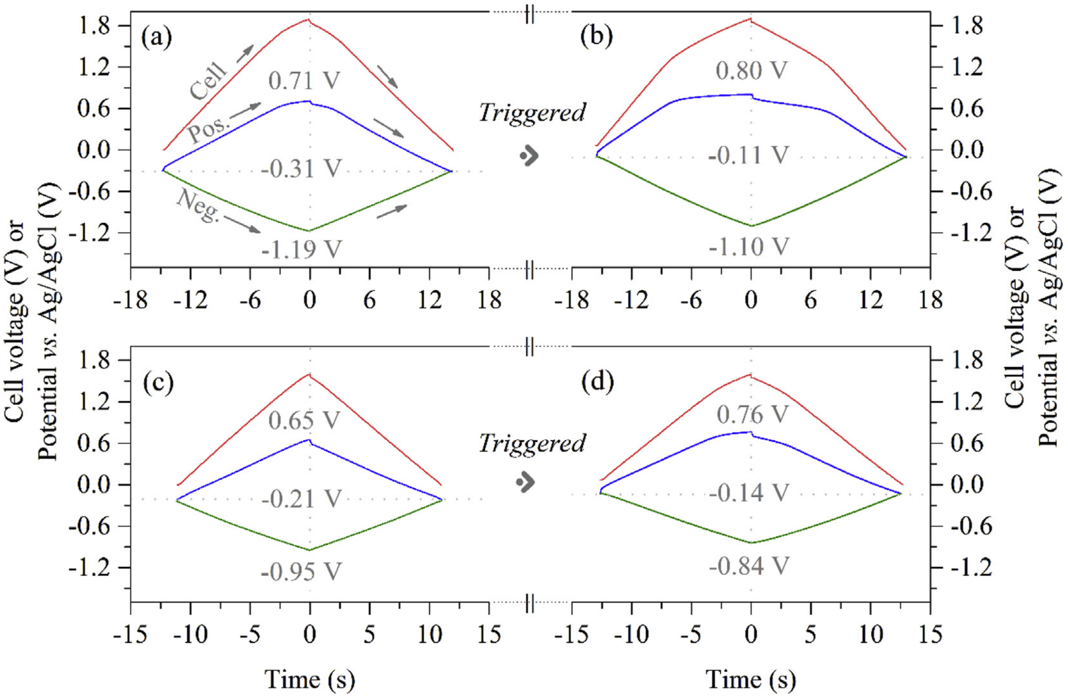

Fig. 5. GCD curves (3 A g^{-1}) of the cell, the positive and negative electrodes at (a) 1.9 V, (b) 500th cycle at 1.9 V, (c) 1.6 V and (d) 1.6 V after triggering operation.

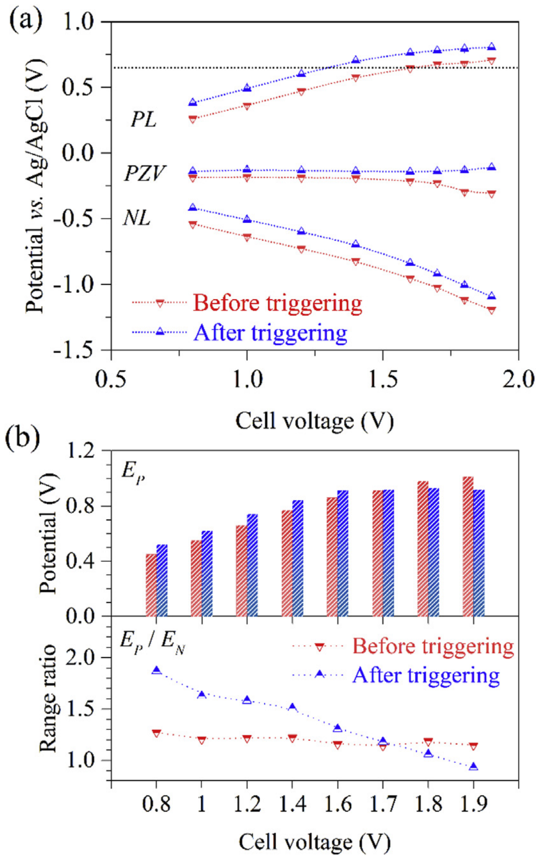

Fig. 6. (a) Evolution of positive, negative limit and *PZV* as a function of cell voltage, (b) a comparison of E_P and E_P/E_N ratios at different cell operation voltages. The dotted line in (a) represents the redox startup potential (0.65 V) as defined in Fig. 4.

charging. Working in the highly active potential region, the positive electrode keeps being electro-oxidized. Correspondingly, the charge storage ability should be deteriorated. The calculation from T-type Swagelok® cell measurements find that C_P (the specific capacitance of the positive electrode) at 0.8 V decreases by 32% after the triggering operation (Table S3). The working potential range must be increased to compensate the decrease of C_P, in order to keep the balance of charge flow in terms of equation (9):

$$m_P C_P E_P = m_N C_N E_N \tag{11}$$

where m is the mass of electrode, C is the specific capacitance (or "claimed capacitance" [28] for non-EDL behaviors), and E represents the working potential range. Since the *PZV* is relatively stable against the cell voltage as observed in Fig. 6a, as well as in previous studies [10,39], the *PL* has to shift positively to enlarge the E_P ($E_P = PL - PZV$). As presented in Fig. 6b, E_P is indeed enlarged after triggering, except when very strong redox activity occurs, e.g. at 1.9 V. Correspondingly, the ratio of E_P/E_N increases significantly. Given that $m_P = m_N$, the result that $E_P > E_N$ suggests $C_P < C_N$.

The mass ratio between positive and negative electrodes has been demonstrated to be critical to the device performance [40,41]. With the unequalisation strategy [42], the cell voltage is possible to be pushed to a higher limit. In this work, all the devices are designed to be mass balanced. The maximum difference between m_P and m_N is 0.03 mg, and the actual m_P/m_N ranges from 0.99 to 1.02. Therefore, the influence of mass imbalance on the maximum cell voltage should be negligible in the initial states. However, electro-oxidation might break the balance by creating m_P mass loss. Such mass loss could be due to the gas (CO_2, CO) evolution induced by further oxidation of surface groups that are generated by electro-oxidation [39,43]. Similar to the C_P decrease, mass loss also leads to the enlargement of the working range E_P, and pushes the potential limit beyond 0.65 V *vs.* Ag/AgCl to involve Br^-/Br_3^- redox at lower voltages. Overall, the electro-oxidation causes the loss of capacitive energy storage. A supplementary measurement indicates that a short-term cycling at 1.9 V decreases the cell capacitance at 0.8 V by approximately 2% (Fig. S7b).

3.3.2. Possible changes in electrolyte composition

Adsorption is one of the most essential energy storage mechanisms for redox-EDLC systems. It is sensitive to the matching between micropores of an electrode material and ion sizes [44], ion/ion or ion/solvent interactions related to diffusion coefficients of the species in solution, or the ion mobility and polarizability [35,45]. Adsorption of the charge carrier species could change the electric double layer, and thereby capacitance and potential of an electrode. A previous study has indicated strong adsorption of Br_3^- in a porous carbon electrode, leading to a lowered electrode potential than standard values [12]. Therefore, the electrolyte composition is an important aspect that helps to understand the triggering phenomenon.

Ideally, the redox reactions that are involved in a redox-EDLC system is completely reversible. Correspondingly, at a discharged state, the charge carrier species in the electrolyte should always be K^+ and Br^- in a certain hydrated form. However, the triggering phenomenon contradicts the 100% reversibility assumption. As exhibited in the cell-level measurements, there is an increasing energy trend during the cycling at 1.9 V (Figs. 2c–d), and a subsequent enhanced energy storage with excellent stability at 1.6 V (Figs. 2e–f). The former qualitatively indicates that some reaction keeps being developed at 1.9 V, while the latter verifies that certain “irreversible species” associated with that reaction remain in the system, thus the electrolyte composition being changed. This change might be associated with kinetics of the redox reaction.

In Br-containing electrochemical devices, the involved redox is acknowledged to be Br^-/Br_3^- [12,19,21]. It is speculated that, in a redox-EDLC system, the redox species must reach a transition state before electron transfer [28]. Therefore, the process can be formulated as two consecutive steps: $Br^- \leftrightarrow Br^*$ and $Br^* \leftrightarrow Br_3^-$ (here we use the symbol of Br^* to represent the transition state), and the overall redox path can be summarized as Fig. 7a. During the charging process, Br_b^- (ions in the bulk electrolyte) firstly enter into the pores of AC and becomes Br_p^-. With the cell voltage and electrode potential ramping up, Br_p^- start to be involved in redox reactions, and is oxidized into Br_3^- via a transition state Br^*.

Previous studies indicate that three elementary steps are involved in a Br^-/Br_3^- reaction [46–50], which can be generally presented as follows for a discharging process: (1) $Br_3^- \rightarrow Br_2 + Br^-$; (2) $Br_2 + e^- \rightarrow Br\cdot + Br^-$; (3) $Br\cdot + e^- \rightarrow Br^-$. In this scenario, Br_2 and/or $Br\cdot$ could be regarded as the transition state Br^*. The electrochemical studies on the $Br_3^-/Br_2/Br^-$ redox kinetics suggest that the first dissociation of Br_3^-, i.e. step (1) is kinetically fast, while step (2) and (3) are comparably rate-limiting [46–50]. This is interpreted that $Br^- \leftrightarrow Br^*$ (Br_2, $Br\cdot$) transformation is relatively slow. At the above given considerations, Br^* that is produced during charging cannot completely transform back into Br^- during a single discharging process. The consequence could be a progressive Br^* accumulation over cycling. It implies a disequilibrium state for the $Br^- \leftrightarrow Br^*$ transformation: R_c (the reaction rate of $Br^- \rightarrow Br^*$ during charging) is higher than R_d (the reaction rate of $Br^* \rightarrow Br^-$ during discharging). Assuming $R_c > R_d$ at 1.9 V, only a small proportion of Br^- completes the Br^-/Br_3^- redox and a few Br^* remains (Fig. 7b-1). With repeated cycling, Br^* accumulates in the system, and the presence of Br^* may facilitate Br^-/Br_3^- reaction thus producing more Br_3^- (Fig. 7b-2). Correspondingly, the energy increases slightly. Fig. 7b-3 represents the imaginary species variation during 1.9 V cycling. Br_b^- is abundant in the bulk solution, so the change after cycling is considered to be negligible. The Br^* accumulation in the system is accompanied by the increase of Br_3^- and decrease of Br_p^- at a fully charged state. On the other hand, the stable energy at 1.6 V after triggering could be explained if the system reaches a

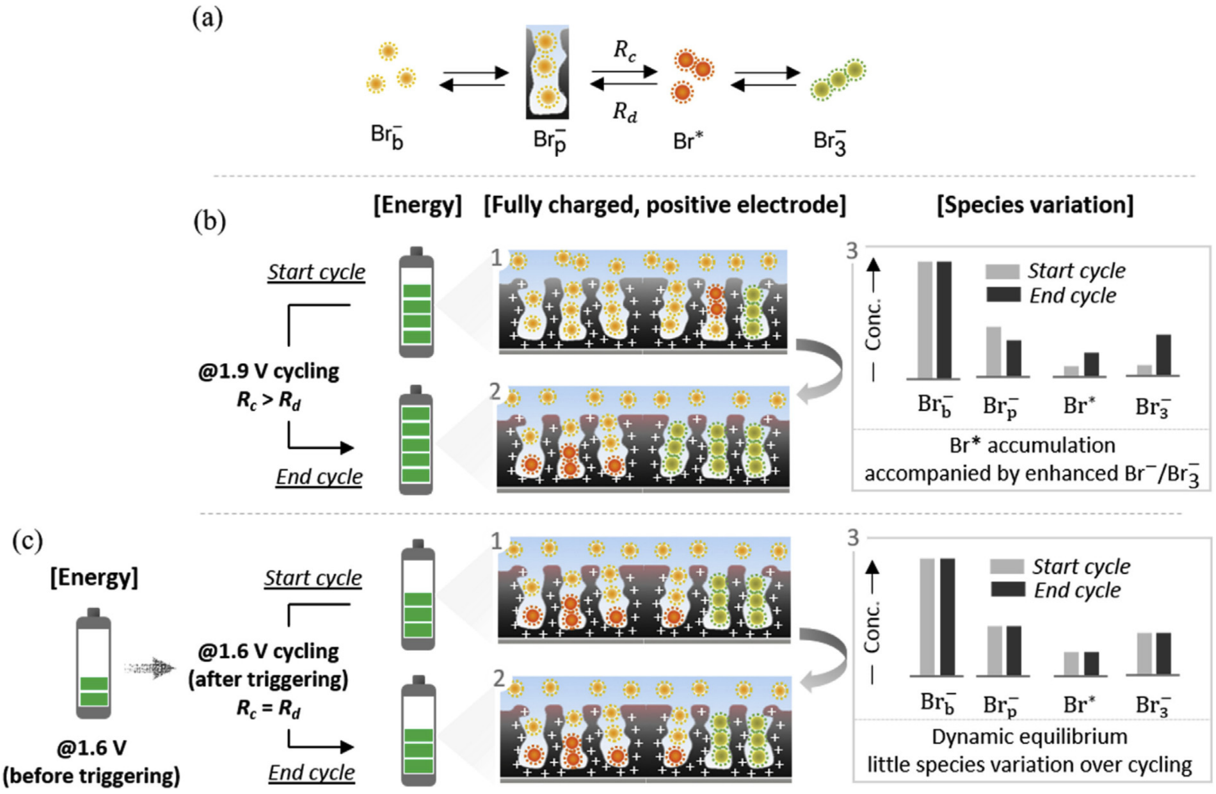

Fig. 7. Schematic of possible explanation of the triggering phenomenon: (a) redox path, (b–c) speculated variation during cycling at 1.9 V and 1.6 V after triggering.

dynamic equilibrium in $Br_p^- \leftrightarrow Br^* \leftrightarrow , Br_3^-$ complying $R_c = R_d$ as in Fig. 7c. In this case, there should be little change in the electrode status (Figs. 7c-1, 2). The electrolyte composition should also be constant (Fig. 7c-3). As a result, the electrode potential as well as the device energy is stabilized over the cycling process. The energy at 1.6 V after triggering operation is lower than that at 1.9 V but is improved than at 1.6 V before triggering, which is experimentally observed in Figs. 2c–f, and briefly described in Fig. 7.

It should be noted that the proposed hypothesis is only a simplified picture with a focus on the positive electrode. The hypothesis provides a qualitative understanding of the experimental observations regarding the triggering phenomenon. Although through some supplementary electrochemical tests (Fig. S7), postmortem materials analysis (Fig. S8) and impedance measurements (Fig. S9), a few tentative evidences that support part of the hypothesis can be obtained, the opportunity remains to study the exact mechanism *in situ*, with the aid of e.g. *in situ* gas analysis techniques [43]. In addition, the reversible hydrogen storage [36], and electrochemical processes on the negative electrode should also be considered.

4. Conclusions

We demonstrate that Br^-/Br_3^- is an effective redox couple in enhancing the energy storage capacity of an EDLC. The symmetric carbon-carbon electrochemical device with an aqueous KBr electrolyte principally performs as a regular EDLC up to 1.6 V. Beyond this voltage threshold, the Br^-/Br_3^- redox reaction comes into effect and the device transforms into a redox-EDLC with an enhanced energy storage capacity. The aqueous device has a maximum voltage of 1.9 V, working with a high energy density, excellent stability and efficiencies. More interestingly, pre-cycling at 1.9 V “triggers” the redox activity and increases the energy storage capacity at 1.6 V with little compromised power. Investigation into the electrode potential suggests that the triggering phenomenon is the positive shift of electrode potential metrics including *PL*, *NL* and *PZV*. We speculate that these observations can be qualitatively explained by the possible electro-oxidation of the positive electrode and the slow kinetics of Br^-/Br_3^- electrode reaction. Our results shed lights on the interesting bromine chemistry, and provide possible insight into to the design and operation of other redox-EDLCs.

Acknowledgement

This work was supported by the European Union's Horizon 2020 Research and Innovation program [grant number 644378, smart-MEMPHIS project]. The authors also thank Anne Wendel for her help with materials analysis.

Appendix A. Supplementary data

Supplementary data related to this article can be found at http://dx.doi.org/10.1016/j.jpowsour.2017.02.082.

References

[1] B.E. Conway, Electrochemical Supercapacitors: scientific fundamentals and technological applications, first ed., Springer Science & Business Media, New York, 2013.

[2] P. Simon, Y. Gogotsi, Materials for electrochemical capacitors, Nat. Mater. 7 (2008) 845–854.

[3] H. Staaf, P. Lundgren, P. Enoksson, Present and future supercapacitor carbon electrode materials for improved energy storage used in intelligent wireless sensor systems, Nano Energy 9 (2014) 128–141.

[4] A.M. Saleem, V. Desmaris, P. Enoksson, Performance enhancement of carbon nanomaterials for supercapacitors, J. Nanomater. 2016 (2016) 1–17.

[5] P. Simon, Y. Gogotsi, B. Dunn, Where do batteries end and supercapacitors begin? Science 343 (2014) 1210–1211.

[6] Y. Wang, Y. Xia, Recent progress in supercapacitors: from materials design to system construction, Adv. Mater. 25 (2013) 5336–5342.

[7] G. Lota, E. Frackowiak, Striking capacitance of carbon/iodide interface, Electrochem. Commun. 11 (2009) 87–90.

[8] S. Roldan, C. Blanco, M. Granda, R. Menendez, R. Santamaria, Towards a further generation of high-energy carbon-based capacitors by using redox-active electrolytes, Angew. Chem. Int. Ed. Engl. 50 (2011) 1699–1701.

[9] H. Yu, L. Fan, J. Wu, Y. Lin, M. Huang, J. Lin, Z. Lan, Redox-active alkaline electrolyte for carbon-based supercapacitor with pseudocapacitive performance and excellent cyclability, Rsc Adv. 2 (2012) 6736–6740.

[10] Q. Abbas, P. Ratajczak, F. Beguin, Sodium molybdate - an additive of choice for enhancing the performance of AC/AC electrochemical capacitors in a salt aqueous electrolyte, Faraday Discuss. 172 (2014) 199–214.

[11] X. Wang, R.S. Chandrabose, S.E. Chun, T. Zhang, B. Evanko, Z. Jian, S.W. Boettcher, G.D. Stucky, X. Ji, High energy density aqueous electrochemical capacitors with a KI-KOH electrolyte, ACS Appl. Mater. Interfaces 7 (2015) 19978–19985.

[12] S.E. Chun, B. Evanko, X. Wang, D. Vonlanthen, X. Ji, G.D. Stucky, S.W. Boettcher, Design of aqueous redox-enhanced electrochemical capacitors with high specific energies and slow self-discharge, Nat. Commun. 6 (2015) 7818.

[13] S.T. Senthilkumar, R.K. Selvan, N. Ponpandian, J.S. Melo, Y.S. Lee, Improved performance of electric double layer capacitor using redox additive (VO^{2+}/VO_2^+) aqueous electrolyte, J. Mater. Chem. A 1 (2013) 7913–7919.

[14] D. Hulicova-Jurcakova, M. Seredych, G.Q. Lu, T.J. Bandosz, Combined effect of nitrogen- and oxygen-containing functional groups of microporous activated carbon on its electrochemical performance in supercapacitors, Adv. Funct. Mater. 19 (2009) 438–447.

[15] V. Kuzmenko, O. Naboka, H. Staaf, M. Haque, G. Goransson, P. Lundgren, P. Gatenholm, P. Enoksson, Capacitive effects of nitrogen doping on cellulose-derived carbon nanofibers, Mater. Chem. Phys. 160 (2015) 59–65.

[16] V. Kuzmenko, O. Naboka, M. Haque, H. Staaf, G. Goransson, P. Gatenholm, P. Enoksson, Sustainable carbon nanofibers/nanotubes composites from cellulose as electrodes for supercapacitors, Energy 90 (2015) 1490–1496.

[17] E. Frackowiak, K. Fic, M. Meller, G. Lota, Electrochemistry serving people and nature: high-energy ecocapacitors based on redox-active electrolytes, ChemSusChem 5 (2012) 1181–1185.

[18] B. Wang, J.A. Macia-Agullo, D.G. Prendiville, X. Zheng, D. Liu, Y. Zhang, S.W. Boettcher, X. Ji, G.D. Stucky, A hybrid redox-supercapacitor system with anionic catholyte and cationic anolyte, J. Electrochem. Soc. 161 (2014) A1090–A1093.

[19] S. Yamazaki, T. Ito, M. Yamagata, M. Ishikawa, Non-aqueous electrochemical capacitor utilizing electrolytic redox reactions of bromide species in ionic liquid, Electrochim. Acta 86 (2012) 294–297.

[20] J.R. Miller, P. Simon, Electrochemical capacitors for energy management, Science 321 (2008) 651–652.

[21] S.T. Senthilkumar, R.K. Selvan, Y.S. Lee, J.S. Melo, Electric double layer capacitor and its improved specific capacitance using redox additive electrolyte, J. Mater. Chem. A 1 (2013) 1086–1095.

[22] P.C.J. Chiang, M.S. Wu, J.C. Lin, A novel dual-current formation process for advanced lithium-ion batteries, Electrochem Solid St. 8 (2005) A423–A427.

[23] J. Li, E. Murphy, J. Winnick, P.A. Kohl, The effects of pulse charging on cycling characteristics of commercial lithium-ion batteries, J. Power Sources 102 (2001) 302–309.

[24] J. Vetter, P. Novak, M.R. Wagner, C. Veit, K.C. Moller, J.O. Besenhard, M. Winter, M. Wohlfahrt-Mehrens, C. Vogler, A. Hammouche, Ageing mechanisms in lithium-ion batteries, J. Power Sources 147 (2005) 269–281.

[25] M. Aslan, D. Weingarth, P. Herbeck-Engel, I. Grobelsek, V. Presser, Polyvinylpyrrolidone/polyvinyl butyral composite as a stable binder for castable supercapacitor electrodes in aqueous electrolytes, J. Power Sources 279 (2015) 323–333.

[26] J. Wang, J. Polleux, J. Lim, B. Dunn, Pseudocapacitive contributions to electrochemical energy storage in TiO_2 (anatase) nanoparticles, J. Phys. Chem. C 111 (2007) 14925–14931.

[27] T. Brousse, D. Belanger, J.W. Long, To be or not to be pseudocapacitive? J. Electrochem. Soc. 162 (2015) A5185–A5189.

[28] B. Akinwolemiwa, C. Peng, G.Z. Chen, Redox electrolytes in supercapacitors, J. Electrochem. Soc. 162 (2015) A5054–A5059.

[29] A. Laheaar, P. Przygocki, Q. Abbas, F. Beguin, Appropriate methods for evaluating the efficiency and capacitive behavior of different types of supercapacitors, Electrochem. Commun. 60 (2015) 21–25.

[30] Y. Dandeville, P. Guillemet, Y. Scudeller, O. Crosnier, L. Athouel, T. Brousse, Measuring time-dependent heat profiles of aqueous electrochemical capacitors under cycling, Thermochim. Acta 526 (2011) 1–8.

[31] E. Frackowiak, M. Meller, J. Menzel, D. Gastol, K. Fic, Redox-active electrolyte for supercapacitor application, Faraday Discuss. 172 (2014) 179–198.

[32] J. Menzel, K. Fic, M. Meller, E. Frackowiak, The effect of halide ion concentration on capacitor performance, J. Appl. Electrochem. 44 (2014) 439–445.

[33] M. De Castro, B. Wilde, The corrosion and passivation of iron in the presence of halide ions in aqueous solution, Corros. Sci. 19 (1979) 923–936.

[34] Y. Gogotsi, P. Simon, True performance metrics in electrochemical energy storage, Science 334 (2011) 917–918.

[35] K. Fic, G. Lota, M. Meller, E. Frackowiak, Novel insight into neutral medium as electrolyte for high-voltage supercapacitors, Energy Environ. Sci. 5 (2012)

5842–5850.

[36] K. Jurewicz, E. Frackowiak, F. Beguin, Towards the mechanism of electrochemical hydrogen storage in nanostructured carbon materials, Appl. Phys. a-Mater. 78 (2004) 981–987.

[37] K. Fic, M. Metier, E. Frackowiak, Interfacial redox phenomena for enhanced aqueous supercapacitors, J. Electrochem. Soc. 162 (2015) A5140–A5147.

[38] Z. Dai, C. Peng, J.H. Chae, K.C. Ng, G.Z. Chen, Cell voltage versus electrode potential range in aqueous supercapacitors, Sci. Rep. 5 (2015) 9854.

[39] Q. Gao, L. Demarconnay, E. Raymundo-Pinero, F. Beguin, Exploring the large voltage range of carbon/carbon supercapacitors in aqueous lithium sulfate electrolyte, Energy Environ. Sci. 5 (2012) 9611–9617.

[40] J.H. Chae, G.Z. Chen, 1.9V aqueous carbon-carbon supercapacitors with unequal electrode capacitances, Electrochim. Acta 86 (2012) 248–254.

[41] S. Vaquero, J. Palma, M. Anderson, R. Marcilla, Mass-balancing of electrodes as a strategy to widen the operating voltage window of carbon/carbon supercapacitors in neutral aqueous electrolytes, Int. J. Electrochem. Sci. 8 (2013) 10293–10307.

[42] C. Peng, S. Zhang, X. Zhou, G.Z. Chen, Unequalisation of electrode capacitances for enhanced energy capacity in asymmetrical supercapacitors, Energy Environ. Sci. 3 (2010) 1499.

[43] M.L. He, K. Fic, E. Frackowiak, P. Novak, E.J. Berg, Ageing phenomena in high-voltage aqueous supercapacitors investigated by in situ gas analysis, Energy Environ. Sci. 9 (2016) 623–633.

[44] J. Chmiola, G. Yushin, Y. Gogotsi, C. Portet, P. Simon, P.L. Taberna, Anomalous increase in carbon capacitance at pore sizes less than 1 nanometer, Science 313 (2006) 1760–1763.

[45] G. Lota, K. Fic, E. Frackowiak, Alkali metal iodide/carbon interface as a source of pseudocapacitance, Electrochem. Commun. 13 (2011) 38–41.

[46] Z.S. Wang, K. Sayama, H. Sugihara, Efficient eosin Y dye-sensitized solar cell containing Br$^-$/Br- 3electrolyte, J. Phys. Chem. B 109 (2005) 22449–22455.

[47] G. Faita, G. Fiori, T. Mussini, Electrochemical processes of the bromine/bromide system, Electrochim. Acta 13 (1968) 1765–1772.

[48] S. Ferro, A.D. Battisti, The bromine electrode. Part I: adsorption phenomena at polycrystalline platinum electrodes, J. Appl. Electrochem. 34 (2004) 981–987.

[49] S. Ferro, C. Orsan, A.D. Battisti, The bromine electrode Part II: reaction kinetics at polycrystalline Pt, J. Appl. Electrochem. 35 (2005) 273–278.

[50] S. Ferro, The bromine electrode Part III: reaction kinetics at highly boron-doped diamond electrodes, J. Appl. Electrochem. 35 (2005) 279–283.

Supporting Information

Redox Enhanced Energy Storage in an Aqueous High-Voltage Electrochemical Device with KBr Electrolyte

Qi Li [a*], Mazharul Haque [a], Volodymyr Kuzmenko [a], Namrata Ramani [b], Per Lundgren [a],

Anderson D. Smith [a], Peter Enoksson [a]

[a] Department of Microtechnology and Nanoscience, Chalmers University of Technology, Gothenburg 41296, Sweden

[b] Department of Materials Science and Engineering, University of California, Los Angeles, California 90095, United States

*Email: qili@chalmers.se

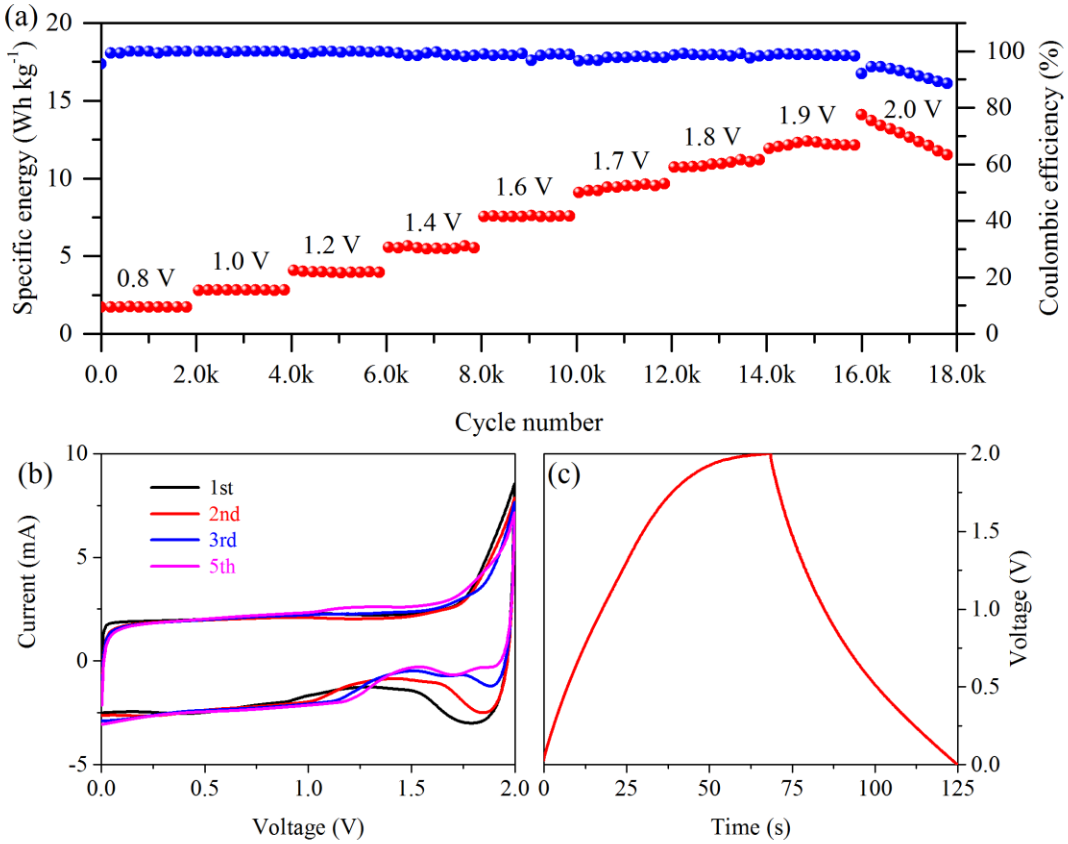

Fig. S1 | Supplementary electrochemical measurements on the two-electrode Swagelok cell. (a) A stepwise cyclic stability test at a current density of 1 A g^{-1}. Rapid energy decrease is observed at 2.0 V, otherwise the device exhibits good stability. (b) CV curves at 20 mV s^{-1} scan rate between 0 and 2.0 V. The successive CV test indicates the instability of this system. (c) Representative GCD curve at 1 A g^{-1}, 2.0 V. The charge/discharge curves are asymmetric, giving low coulombic and energy efficiencies.

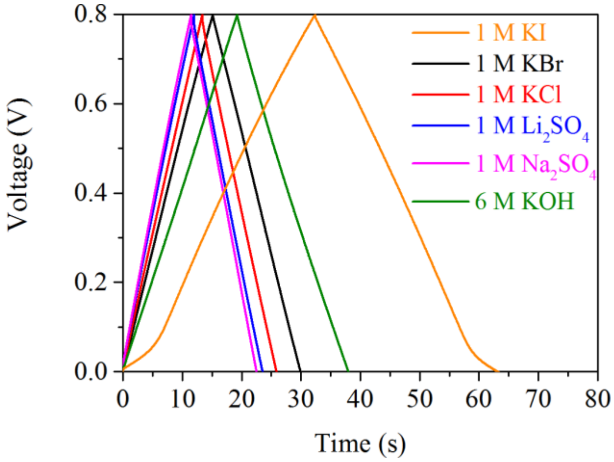

Fig. S2 | Representative GCD curves at 0.8 V, 1 A g^{-1} of AC electrode in different electrolytes. To compare the capacitive performance of different electrolytes, the cells are tested in a voltage range from 0 to 0.8 V. The calculated specific capacitances are listed in Table S1. Except KI, all electrolytes exhibit EDL behavior, showing triangular GCD curves. KBr enables a higher specific capacitance than some other neutral electrolytes. In consistent with previous reports, significant redox contribution can be observed even at a rather low cell voltage 0.8 V in KI electrolyte. The value is thus much higher than for pure EDLCs.

Table S1 | Specific capacitance of AC electrode in different electrolytes

	1 M KI	1 M KBr	1 M KCl	1 M Li_2SO_4	1 M Na_2SO_4	6 M KOH
Specific capacitance, F g^{-1}	153 [a]	75	63	58	56	94

[a] Precisely, the value is a $\Delta Q/\Delta V$ ratio.

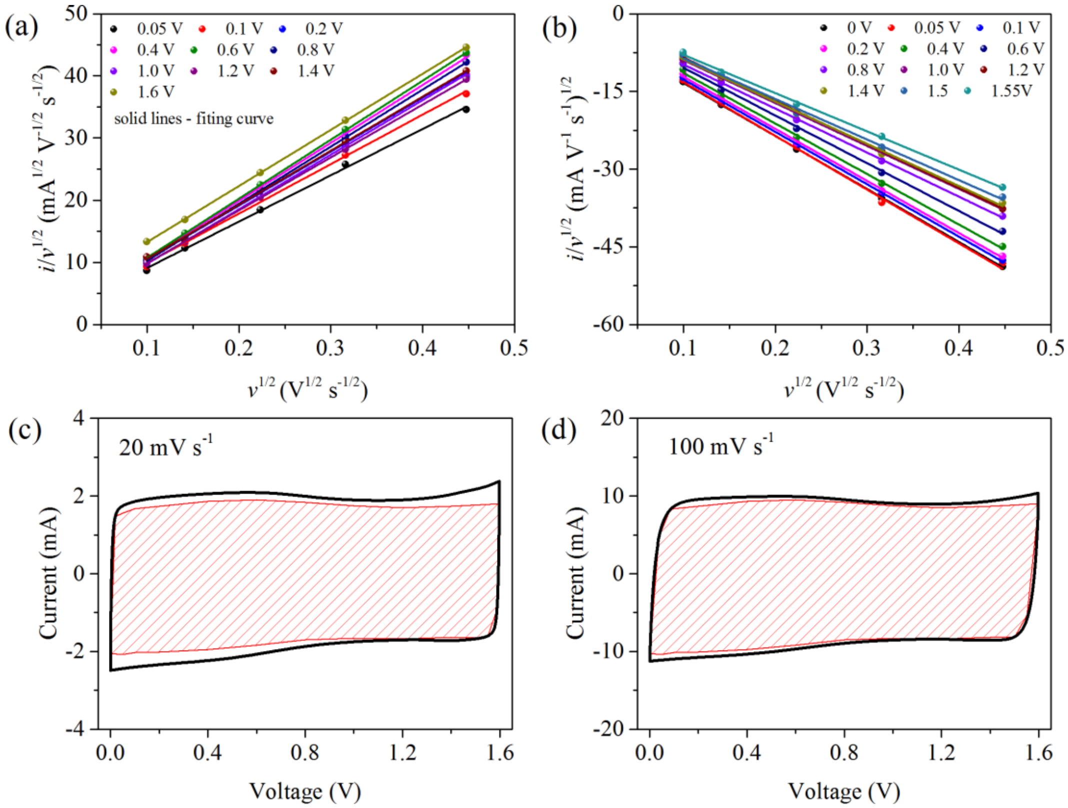

Fig. S3 | The proportion of capacitive energy storage at 1.6 V. (a-b) Linear fitting the experimental data of anodic and cathodic scans, respectively. (c-d) Voltammetric response (1.6 V at scan rates of 20 and 100 mV s^{-1}) for the two-electrode Swagelok cell with AC electrode and KBr electrolyte. The total current (black line) is obtained experimentally. The capacitive currents (shaded regions) are determined by using equation $i(V) = k_1 v + k_2 v^{1/2}$, where *i(V)* is the current response at a specific voltage, $k_1 v$ and $k_2 v^{1/2}$ correspond to the current contributions from the surface capacitive effects and the diffusion-controlled redox process, respectively. The symbol *v* stands for the scan rate, k_1 and k_2 are coefficients and determined by the analysis in (a-b): by rearranging the equation as $i(V)/v^{1/2} = k_1 v^{1/2} + k_2$, k_1 and k_2 can be obtained by the linear fitting of $i(V)/v^{1/2}$ against $v^{1/2}$. The capacitive proportion is calculated as the ratio of the shadowed area to the overall enclosed area of the CV loop in Figure S3c-d. The capacitive proportion is about 89 and 94% at 20 and 100 mV s^{-1} scan rates, respectively.

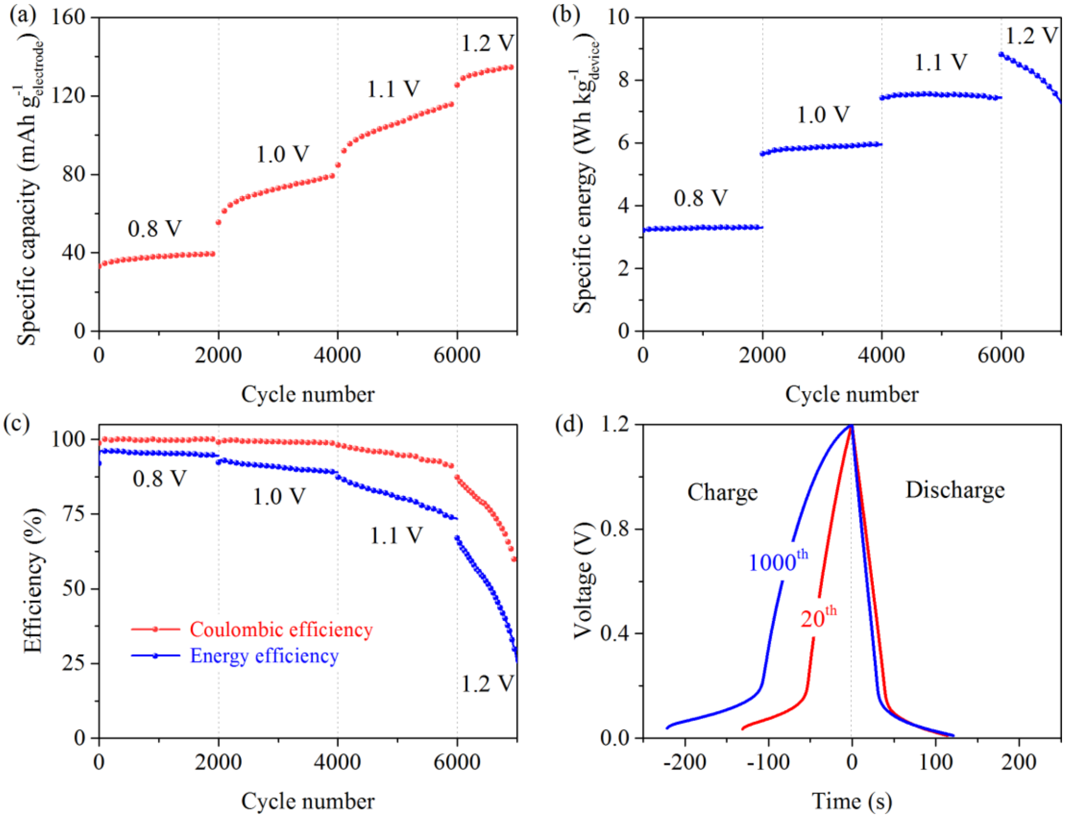

Fig. S4 | Cycling performance of a Swagelok cell with AC electrode and 1 M KI electrolyte. A stepwise cycling stability test at 1 A g^{-1}: (a) capacity, (b) Specific energy and (c) efficiency against cycle number. (d) GCD curves at 1.2 V.

The capacity increases with cycling process throughout the process, while the calculated energy is observed to be relatively stable till 1.1 V cell voltage. Beyond this limit, energy decreases even though capacity still increases. On the other hand, efficiency decreases significantly with pushing the voltage limit to higher values, especially the energy efficiency. By comparing the GCD curves at the specified cycle number, one can see the charging curve is greatly expanded to sustain a similar discharge performance. The above results suggest that the KI system may be suitable for working at 0.8 V, for a sufficient stability and high efficiency.

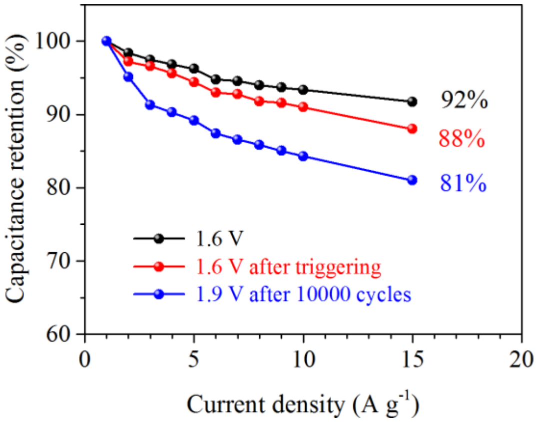

Fig. S5 | Rate capabilities of a KBr-containing device at different stages (two-electrode Swagelok cell). The measurements were conducted at a current density of 1 A g^{-1}.

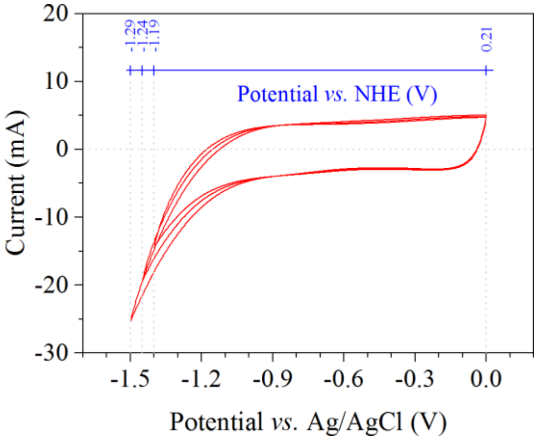

Fig. S6 | Extended negative CV scans of 1 M KBr electrolyte at a scan rate of 20 mV s^{-1} (three-electrode cell).

Table S2 | *PL*, *NL* and *PZV* values at different cell voltages (T-type Swagelok cell) [a]

	Before triggering			After triggering		
	PL	*NL*	*PZV*	*PL*	*NL*	*PZV*
0.8 V	0.26	-0.54	-0.18	0.38	-0.42	-0.14
1.0 V	0.36	-0.64	-0.18	0.49	-0.51	-0.13
1.2 V	0.47	-0.73	-0.19	0.60	-0.60	-0.13
1.4 V	0.58	-0.82	-0.19	0.70	-0.70	-0.14
1.6 V	0.65	-0.95	-0.21	0.76	-0.84	-0.14
1.8 V	0.68	-1.02	-0.23	0.78	-0.92	-0.14
1.9 V	0.68	-1.12	-0.29	0.79	-1.01	-0.13

[a] The numbers are the average values of at least 20 cycles at each voltage, and are collected after the cell is stabilized (open circuit potential variation rate lower than 2 mV min^{-1})

Table S3 | Metrics of positive and negative electrodes (T-type Swagelok cell) [a]

	0.8 V		1.6 V		1.9 V	
	Before triggering	After triggering	Before triggering	After triggering	Before triggering	After triggering
E_P, V *vs.* Ag/AgCl	0.44	0.52	0.86	0.91	1.01	0.92
E_N, V *vs.* Ag/AgCl	0.36	0.28	0.74	0.69	0.89	0.98
E_P/E_N ratio	1.22	1.86	1.13	1.31	1.15	0.94
C_P, F g^{-1}	67.7	46.2	75.7	73.6	81.4	105.2
C_N, F g^{-1}	81.5	85.8	88.0	94.6	94.3	96.7
$C_{electrode}$, F g^{-1}	73.4	60.1	81.4	82.8	87.4	100.8

[a] Calculated from the recorded GCD curves with the T-type Swagelok cell.

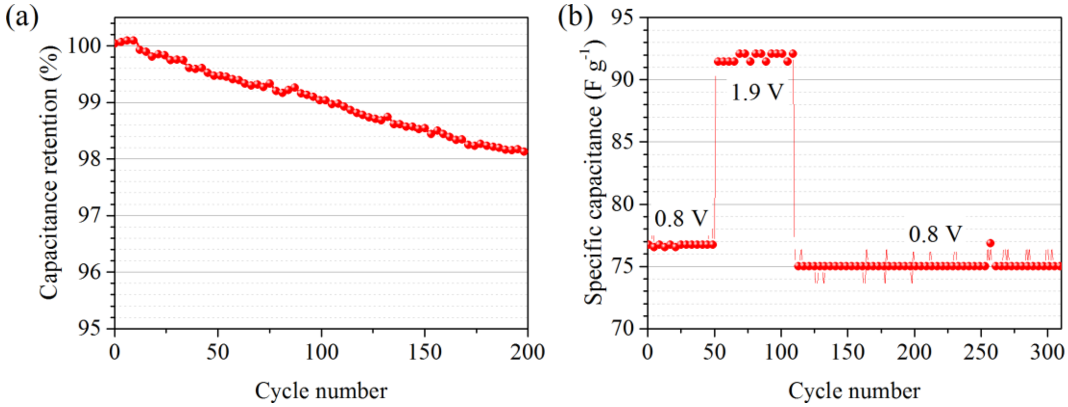

Fig. S7 | Supplementary measurements (two-electrode Swagelok cell, AC electrode, 1 M KBr electrolyte). (a) Cycling stability at 1.9 V, current density of 0.5 A g^{-1}. (b) A comparison of specific capacitance of AC electrode at 0.8 V before and after cycling at 1.9 V, 1 A g^{-1}.

In contrast to the increasing trend at 3 A g^{-1}, the device working at a low current density of 0.5 A g^{-1} shows a slight decrease in capacitance (approx. 2% over 200 cycles). Cycling stability of the Br-containing device is dependent on the charge/discharge current density, which indicates that kinetics concern might exist in the present system. The variation of the cycling stability trend at different current densities can also be found in some other redox-EDLC systems [1].

References

[1] S.E. Chun, B. Evanko, X. Wang, D. Vonlanthen, X. Ji, G.D. Stucky, S.W. Boettcher, Design of aqueous redox-enhanced electrochemical capacitors with high specific energies and slow self-discharge, Nat. Commun., 6 (2015) 7818.

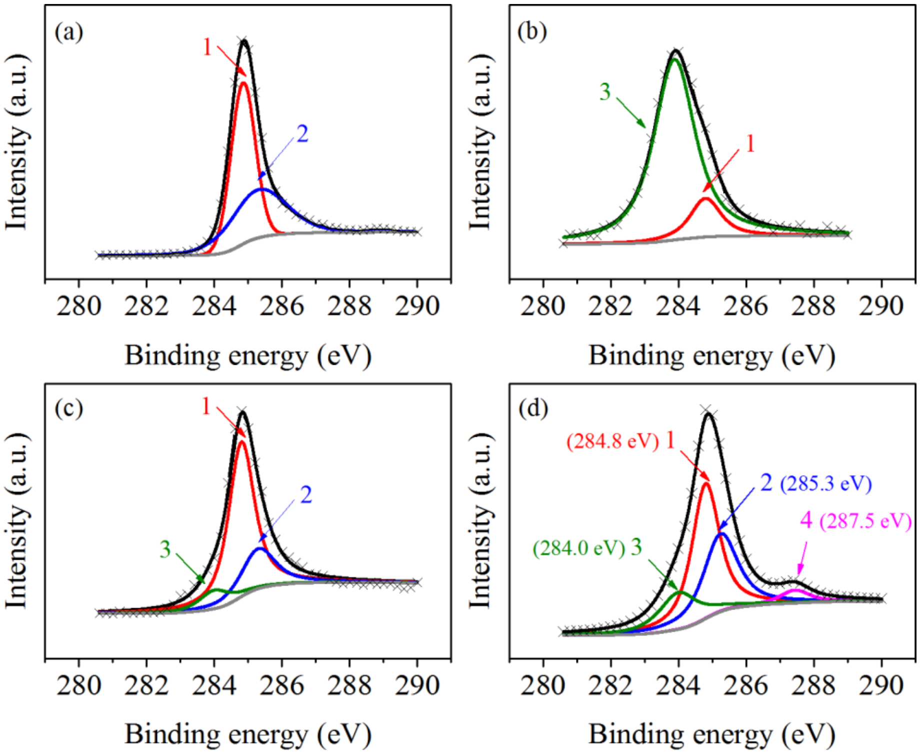

Fig. S8 | C 1s spectrum of (a) Fresh electrode, (b) KBr crystal on a fresh electrode, (c) Negative electrode and (d) Positive electrode. The XPS (X-ray photoelectron spetroscopy) measurements were performed with the Quantum 2000 scanning XPS microprobe from Physical Electronics. An Al Ka (1486.6 eV) X-ray source was used and a beam size was 100 mm. The charging shift was calibrated using a PET (polyethylene terephthalate) reference, C 1s photoemission line at binding energy of 284.8 eV. Shirley-type background are used for the analyses.

A *ex situ* XPS analysis was conducted on the positive and negative electrodes that were recovered from a cycled device (1.9 V, 1000 cycles). A fresh electrode as well as KBr crystal (on a fresh electrode) were also measured to obtain reference data.

The C 1s band of the fresh electrode (Fig. S8a) can be deconvoluted into peak 1 at 284.8 eV and peak 2 at 285.3 eV. Peak 1 is assigned to the C-C bonding as graphitic carbon, and peak 2 can be attributed to C-OH [1, 2], which could be from surface bonding of the raw AC material, and conductive additives. The spectra of KBr that is crystalized on a AC electrode substrate is shown in Fig. S8b, consisting of peak 1 (from the carbon substrate) and peak 3 at around 284.0 eV. C 1s of the negative electrode is a combination of peak 1-3. In contrast, the positive exhibits additional signal at around 287.5 eV, i.e. peak 4. Peak 4 is assigned to carbonyl groups (C=O)[2-4]. This surface group might be generated by electro-oxidation during the cycling at 1.9 V.

References

[1] D. Bar-Tow, E. Peled, L. Burstein, A study of highly oriented pyrolytic graphite as a model for the graphite anode in Li-ion batteries, J. Electrochem. Soc., 146 (1999) 824-832.

[2] M. Nie, J. Demeaux, B.T. Young, D.R. Heskett, Y. Chen, A. Bose, J.C. Woicik, B.L. Lucht, Effect of vinylene carbonate and fluoroethylene carbonate on SEI formation on graphitic anodes in Li-ion batteries, J. Electrochem. Soc., 162 (2015) A7008-A7014.

[3] Q. Gao, L. Demarconnay, E. Raymundo-Pinero, F. Beguin, Exploring the large voltage range of carbon/carbon supercapacitors in aqueous lithium sulfate electrolyte, Energy Environ. Sci., 5 (2012) 9611-9617.

[4] M. Zhu, C.J. Weber, Y. Yang, M. Konuma, U. Starke, K. Kern, A.M. Bittner, Chemical and electrochemical ageing of carbon materials used in supercapacitor electrodes, Carbon, 46 (2008) 1829-1840.

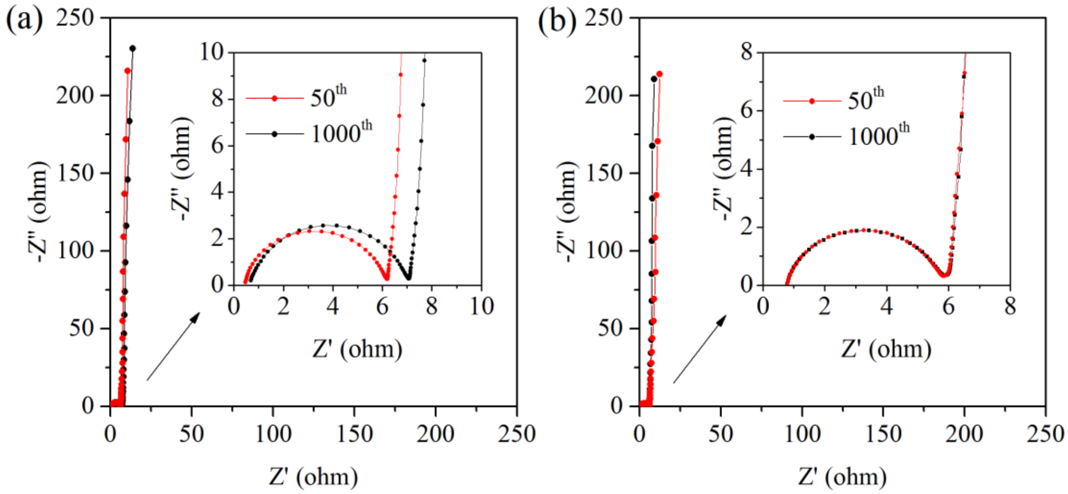

Fig. S9 | Impedance test: Nyquist plots after 50 and 1000 cycles at (a) 1.9 V and (b) 1.6 V after triggering. The tests were carried out in the frequency range of 100 kHz -10 mHz with a 5 mV ac amplitude on a Gamry Reference 3000AE.

We conducted EIS (electrochemical impedance spectroscopy) measurements on two devices working at 1.9 V and 1.6 V after a triggering operation, respectively. The Nyquist plots obtained after 50 and 1000 cycles are displayed in Fig. S9. All the Nyquist plots consist of a semicircle in the high frequency region and a nearly vertical line in the low-frequency region. The x-intercept of the plot is series resistance, R_s, which reflects the internal resistance including solution resistance and resistance from electrical connections of the device; The diameter of the semicircle defines the charge transfer resistance, R_{ct} [1-3].

In the beginning period at 1.9 V cycling, R_s is 0.47 ohm, and increases slightly to 0.68 ohm after 1000 cycles. R_{ct} also shows an increasing trend from 5.73 to 6.40 ohm. In contrast, for the device working at 1.6 V after triggering, the Nyquist plots are almost identical, indicating the excellent stability of the system which is in agreement with the stability test in Fig. 2e-f. The resistance increase at 1.9 V could be a sign of electro-oxidation. It was reported that electro-oxidation could reduce the electrode integrity and contact with the current collector due to evolution of gases (CO, CO_2, etc.) [4, 5].

References

[1] A.J. Rennie, V.L. Martins, R.M. Smith, P.J. Hall, Influence of particle size distribution on the performance of ionic liquid-based electrochemical double layer capacitors, Sci. Rep., 6 (2016) 22062.
[2] D. Yuan, J. Chen, S. Tan, N. Xia, Y. Liu, Worm-like mesoporous carbon synthesized from metal-organic coordination polymers for supercapacitors, Electrochem. Commun., 11 (2009) 1191-1194.
[3] B. Abdulhakeem, B. Farshad, M. Damilola, T. Fatemeh, F. Mopeli, D. Julien, M. Ncholu, Morphological characterization and impedance spectroscopy study of porous 3D carbons based on graphene foam-PVA/phenol-formaldehyde resin composite as an electrode material for supercapacitors, Rsc Adv., 4 (2014) 39066.
[4] Q. Gao, L. Demarconnay, E. Raymundo-Pinero, F. Beguin, Exploring the large voltage range of carbon/carbon supercapacitors in aqueous lithium sulfate electrolyte, Energy Environ. Sci., 5 (2012) 9611-9617.
[5] M.L. He, K. Fic, E. Frackowiak, P. Novak, E.J. Berg, Ageing phenomena in high-voltage aqueous supercapacitors investigated by in situ gas analysis, Energy Environ. Sci., 9 (2016) 623-633.

PAPER II

Electrochimica Acta 263 (2018) 249–260

Contents lists available at ScienceDirect

Electrochimica Acta

journal homepage: www.elsevier.com/locate/electacta

Thermal influence on the electrochemical behavior of a supercapacitor containing an ionic liquid electrolyte

Mazharul Haque*, Qi Li, Anderson D. Smith, Volodymyr Kuzmenko, Elof Köhler, Per Lundgren, Peter Enoksson

Department of Microtechnology and Nanoscience, Chalmers University of Technology, Gothenburg, 41296, Sweden

ARTICLE INFO

Article history:
Received 21 September 2017
Received in revised form
2 December 2017
Accepted 4 January 2018
Available online 6 January 2018

Keywords:
Supercapacitor
Ionic liquid electrolyte
High temperature
Cyclic stability
Relaxation time constant

ABSTRACT

Emerging demands on heat-durable electronics have accelerated the need for high temperature supercapacitors as well as for understanding the influence of elevated temperatures on the capacitive behavior. In this work, we present a comprehensive study of the thermal influence on a supercapacitor containing 1-ethyl-3-methylimidazolium acetate (EMIM Ac) electrolyte and activated carbon (AC) electrodes. The performance variation as a function of temperature in a range from 21 °C to 150 °C reveals that a high specific capacitance of 142 $\mathrm{F\,g^{-1}}$ can be achieved at 150 °C at a current density of 2 $\mathrm{A\,g^{-1}}$ with a rate capability of 87% at 15 $\mathrm{A\,g^{-1}}$ (relative to 2 $\mathrm{A\,g^{-1}}$). At 150 °C, equivalent series resistance (ESR) is only 0.37 $\Omega\,\mathrm{cm^2}$, which is a result of improved ionic conductivity of the electrolyte at elevated temperature. The ESR value of 2.5 $\Omega\,\mathrm{cm^2}$ at room temperature reflects a good compatibility between EMIM Ac and AC. In addition, a capacitance retention of more than 95% (in the end of 1000 cycles) is maintained up to 120 °C followed by 85% at 150 °C. These results confirm EMIM Ac as a suitable candidate for carbon-based high temperature supercapacitors, and the observations regarding the thermal influence on performance metrics e.g. usable operation voltage could be applicable to other energy storage devices.

1. Introduction

Electrochemical capacitors or supercapacitors (SCs) are receiving strong attention as a result of their ability of ultrafast energy delivery and limitless lifetime. Consequently, they have become an integral part of modern electronics either as a primary storage device or as a backup device [1].

In recent years, intensive research efforts are focusing on high temperature applications of supercapacitors. The ability to operate at high temperatures is especially important in electric vehicles (EVs) or hybrid electric vehicles (HEVs) where SCs are used in place of, or in combination with, batteries that provide acceleration power and store energy form regenerative braking, and in turn improve the battery lifetime [2]. Capacitor banks used in such systems can heat up to 60 °C by a nearby combustion chamber. Therefore, thermal stability is one of the most important considerations prior to designing any system of this kind [3]. As shown in Fig. 1, there are a number of other applications that operate at a wide range of elevated temperatures and require energy storage devices [4]. These applications include underground drilling tools, military equipment, aircraft power electronics and wireless sensors operating in harsh environments [5]. Moreover, SCs, aimed for room temperature (RT) application, can also be exposed to temperature variation due to changes in air temperature or self-heating during device operation [3]. Operating SCs at off-design temperatures often lead to problems with safety, reliability and performance through accelerated ageing and thermal runaway [3], which makes this task very challenging.

Among the essential constituents of a SC device, electrolyte plays the most critical role in stable high temperature performance compared to electrodes and separator. Organic electrolytes used in commercial SCs are not well suited for high temperatures (above 70 °C) due to their high flammability, possible evolution of toxic gasses and low boiling points of solvents [3,6]. Aqueous electrolytes are limited by low boiling point of water and are not preferable to be used at more than 80 °C [3]. In this regard, ionic liquids (ILs) can satisfy high temperature requirements due to their unique physiochemical properties such as high thermal and chemical stability, wide voltage range, non-flammability and negligible vapor pressure [7]. ILs are molten salts that remain liquid at or close to room

---

* Corresponding author.
E-mail address: mhaque@chalmers.se (M. Haque).

https://doi.org/10.1016/j.electacta.2018.01.029

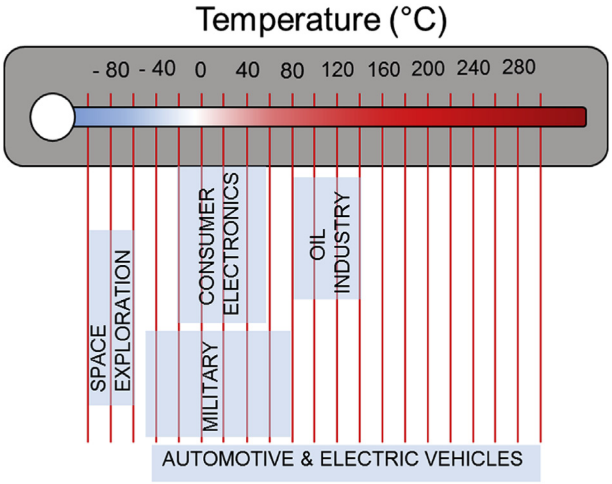

Fig. 1. Temperature requirements of storage devices in different applications. Adapted from Ref. [4] with permission from The Royal Society of Chemistry.

temperature (RT), as they cannot easily form an ordered crystal structure [8,9]. They consist of a relatively large asymmetric organic cation (limiting the negative potential window) and a weakly bonded inorganic or organic anion (limiting the positive potential window and melting point/temperature range) [10]. Due to the bulky nature of ions, ILs are generally more viscous compared to conventional electrolytes, and therefore exhibit inferior capacitance and power density at RT. It was shown that the best performance for an IL is expected at a temperature around 60 °C [3,11,12].

A number of research groups have investigated the thermal stability and capacitive performance of IL containing SCs in combination with different electrodes that can operate at a maximum temperature of 100 °C [11,13–18]. Studied SCs exhibited quite high equivalent series resistance (ESR) due to unsuitable combinations of electrodes and electrolytes and low ionic conductivity of electrolytes. As a strategy to improve the ionic conductivity, some works have been focused on mixtures of ILs and organic solvents [19–23]. However, for high temperature applications, especially above 100 °C, the thermal stability of such a device is endangered due to the presence of organic solvents. Besides, another study showed that the addition of solvents with low dielectric constant (acetonitrile, regardless of being highly polar) can actually decrease the conductivity of the corresponding neat IL by promoting ionic association [24]. Therefore, a solvent with high dielectric constant, for example water is favorable for the dissociation of the ions that increases the conductivity of IL [24]. With a very small amount of water, often water molecules exist as clusters and stay isolated, whereas, with a relatively larger amount, ILs form a three dimensional network linked by a strong hydrogen bond among anion, cation and water [25]. The solvation in IL can result in a significant change in the chemical reactivity of solute water as it is strongly bound to solvent anions. In fact, water have a very large negative excess chemical potential (-29 kJ mol^{-1}) in imidazolium-based ILs [26], meaning a higher energy is needed to decompose the water present in the system.

Theoretically, neat ILs possess adequate ionic conductivity at elevated temperatures and the absence of solvents allows high ionic concentration, which could facilitate good capacitive performance. In this work, we use a new IL electrolyte EMIM Ac with a certain amount of water content for a SC containing AC electrodes and carry out a thorough electrochemical investigation. The main purpose of this study is to demonstrate high temperature tolerance and common trends for the temperature dependence of the device performance. An [EMIM]$^+$ cation-based IL is chosen due to its high conductivity (10 mS cm^{-1}) compared to most of the ILs [27] and less chance of forming aggregates [25]. Additionally, the water present in the EMIM Ac should associate itself with the [Ac]$^-$ anion by a strong hydrogen bond network due to its small size (0.15 nm) and highly polar nature. Consequently, it should reduce the direct coulombic interaction between [EMIM]$^+$ and [Ac]$^-$ ions and that can result in even higher ionic conductivity. Additionally, the large solvation shell due to the small size of the acetate ions (0.15 nm) is expected to be guided by the large amount of mesopores available in the prepared AC electrode and eventually fit in the vast majority of the micropores (average pore size 0.85 nm) [28]. Moreover, acetate-based ILs have low toxicity and corrosiveness with a favorable biodegradability [8]. Lower toxicity allows less critical operation requirements, which fits well with our customized high-temperature electrochemical test cell. The customized test cell also eliminates thermal expansion issues, indicating that the observed performance variations should mainly originate from the interaction between electrode and electrolyte. This study reveals that an EMIM Ac containing SC can function at a temperature as high as 150 °C and enables a specific capacitance that is even greater than most aqueous-based SCs at RT.

2. Experimental

2.1. Materials and characterization

1-Ethyl-3-methylimidazolium acetate 97% (EMIM Ac, with impurities ≤ 0.5% water, Sigma Aldrich), was used as an electrolyte solution without further purification. Commercially available glassfiber sheet (GF, Whatman®) with 200 µm thickness and a diameter of 12 mm was used as separator.

AC (Kuraray®, YP-80F) was used as the main component of the electrodes. First, the AC powder and carbon black (Sigma Aldrich) were mixed and finely grinded in a quartz mortar. Subsequently, the mixture was added to a beaker containing acetone and polytetrafluoroethylene (PTFE) binder (60 wt % in H_2O). The weight ratio of the AC powder, carbon black and PTFE was 80:10:10. Then the mixture was kept in sonication for 30 min and later on transferred to a 75 °C water bath for solvent (acetone) evaporation. Afterwards, a dough was obtained from the mixture and processed into a freestanding film by a rolling press technique. The film was subsequently dried in vacuum for 24 h at 80 °C. Pellets with 10 mm diameter were punched out from the dried film and used as electrodes. A single electrode was around 2.5 mg in mass, 100 µm in thickness and 10 mm in diameter.

The surface area and porosity of commercial AC material (Kuraray®, YP-80F) has been reported in Ref. [29], where nitrogen gas sorption measurements at 77 K were conducted, surface area of 2112 m^{2}g^{-1} was determined with Brunauer-Emmett-Teller (BET) method, and average pore size of 1.31 nm were calculated with quenched solid density function theory (QSDFT) method. To examine the difference in surface area between AC powder and the AC electrode pellet (80% YP-80F AC, 10% PTFE and 10% carbon black), the same nitrogen sorption measurement at 77 K was conducted on TriStar 3000 V6.05 A and BET surface area was calculated accordingly (Fig. S1). Prior to measurements, the samples were degassed under vacuum at 150 °C for 3 h.

Electron spectroscopy for chemical analysis (ESCA) was performed with the Quantum 2000 scanning ESCA microprobe from Physical Electronics to evaluate the elemental composition of the AC powder (Fig. S2). An Al Kα (1486.6 eV) X-ray source was used with a beam size of 100 µm.

The surface morphology of the AC powder and AC electrode material was investigated with scanning electron microscopy (SEM, Leo Ultra 55 FEG SEM, Zeiss) in a secondary electron mode at an acceleration voltage of 3 kV (Fig. S3).

2.2. Thermal characterization

Thermal stability measurements of the pure EMIM Ac electrolyte and the mixture of EMIM Ac and AC electrode were performed by thermal gravimetric analysis (TGA) using a Mettler Toledo TGA/DSC 3+ instrument. Pure EMIM Ac weighing 9.7909 mg and the mixture of EMIM Ac and AC electrode weighing 9.9523 mg were placed into aluminum crucibles. Then the samples were heated in air from 30 °C to 600 °C with a heating rate of 10 °C min^{-1} followed by a flow rate of 20 mL min^{-1}.

2.3. Device configuration and high temperature profile

A symmetrical two electrode SC cell was prepared according to AC|| (GF/EMIM Ac) ||AC configuration and assembled in a customized chamber (Fig. 2) consisting of a top and a bottom housing made of stainless steel. The housings provided one end connection to the SC cell from external power supply. The second end connection was maintained by a flat head pin (made of stainless steel) through the top housing. A thin Teflon gasket was kept between the top housing and the flat head pin in order to avoid any connection with the rest of the housings. The SC cell was placed inside a cavity of the bottom housing. The cell was separated from the wall of the cavity by an inner Teflon body to make sure that the external connection through the housings was maintained only at the one side of the cell. A thin Teflon gasket on the surface of the bottom housing provided isolation for a piston shaped current collector that was attached to the flat head pin with a stainless steel spring which could compensate thermal expansion issues at elevated temperatures.

Electrochemical measurements at room temperature were carried out 24 h after cell assembly, in order to provide enough time for electrolyte absorption. Approximately 100 μL of electrolyte was injected into the cell.

The cell was characterized at a wide temperature range in the following order: RT (21 °C) → 40 °C → 80 °C → 100 °C → 120 °C → cooled back to RT after 120 °C (RT/120 °C) → 150 °C. High temperature exposure was achieved by placing the cell in a DZF-6020 oven (temperature fluctuation ± 1 °C). Temperature was additionally monitored by a UT61B Modern Digital Multimeter coupled with a thermal sensor connected to the cell. The accuracy of the sensor is ± (1.2% ± 3) in a temperature range of −40 °C to 1000 °C. Once the cell reached a pre-defined temperature, it was maintained at that constant temperature for at least 4 h before electrochemical measurements were performed. This ensured that critical dynamical processes in the cell reached thermal equilibrium prior to characterization.

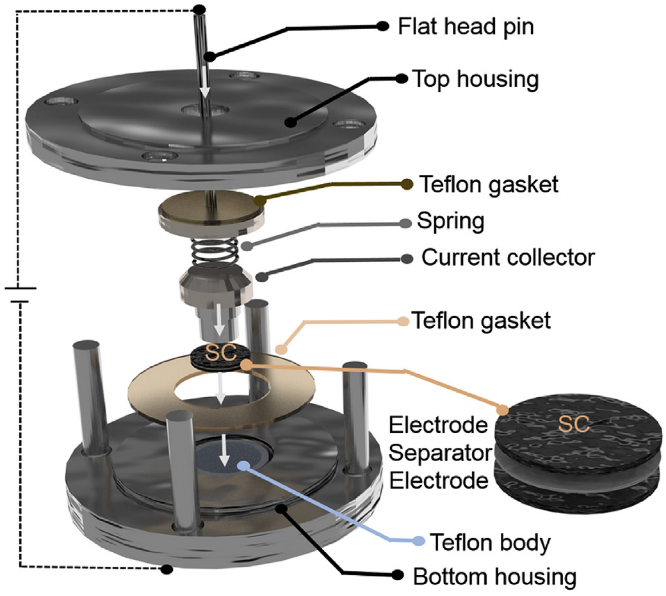

Fig. 2. Schematic of customized chamber and SC cell assembly.

2.4. Electrochemical characterization

Different electrochemical measurements were conducted at RT and elevated temperatures. Specifically, cyclic voltammetry (CV) with scan rates ranging from 10 to 3000 mV s^{-1}, galvanostatic charge discharge (GCD) with a normalized current from 1 to 100 A g^{-1} and cyclic charge discharge (CCD) with a normalized current of 7 A g^{-1} were performed. In addition, electrochemical impedance spectroscopy (EIS) was carried out at a frequency range of 100 kHz to 10 mHz at 0 V with an alternating current (ac) perturbation of 5 mV at open circuit potential. All electrochemical measurements were conducted using a Gamry Reference 3000AE Galvanostat/Potentiostat workstation with a current accuracy (±10 pA ± 0.3%) and voltage accuracy of (±1 mV ± 0.3%) of reading.

Capacitance was calculated from both CV and GCD measurements according to the following equations:

$$C_s = \frac{4}{m\Delta V v_s}\int_{V_1}^{V_2} I(V)dV \quad (\text{F g}^{-1}) \tag{1}$$

$$C_s = \frac{4 \times I_d \times t_d}{m \times \Delta V} \quad (\text{F g}^{-1}) \tag{2}$$

where C_s is the specific capacitance of a single electrode, $I(V)$ is the current response, V_1 and V_2 are lower and upper limits of the potential range respectively, ΔV is the working voltage range, v_s is the scan rate, I_d is the discharge current, t_d is the discharge time and m is the total mass of both electrodes (each electrode had approximately the same mass). The factor of 4 modifies the device capacitance (normalized to mass of two electrodes) to the capacitance of a single electrode [30].

Power density and energy density of the device were calculated from GCD measurements based on the following equations:

$$C = \frac{C_s}{4} \quad (\text{F g}^{-1}) \tag{3}$$

$$E = \frac{C\Delta V^2}{2 \times 3.6} \quad \left(\text{Wh kg}^{-1}\right) \tag{4}$$

$$P_{max} = \frac{\Delta V^2}{4 \times R_s \times m} \quad \left(\text{kW kg}^{-1}\right) \tag{5a}$$

$$P_{avg} = \frac{E \times 3600}{t_d} \quad \left(\text{W kg}^{-1}\right) \tag{5b}$$

$$R_s = \frac{V_{ir}}{2 \times I_d} \quad (\Omega) \tag{6}$$

where C is the specific device capacitance, ΔV is the voltage range excluding internal resistance (V_{ir}) drop, E is the energy density of the device, P_{max} is the maximum power density of the device, P_{avg} is the average power density of the device, t_d is the discharge time, and R_s is the equivalent series resistance from GCD measurements.

3. Results and discussion

3.1. Cyclic voltammetry (CV)

In order to determine the operating voltage limit at RT, CV of the SC containing EMIM Ac electrolyte was carried out in different voltage windows ranging from 1.2 V to 1.7 V with a scan rate of 20 mV s^{-1} (Fig. 3a). An anodic current increase leads to a noticeable deviation from the rectangular cyclic voltammogram (CV) loop at higher voltages. The deviation should be a result of oxygen evolution due to decomposition of residual H_2O in the electrolyte, which involves electron transfer through the interface. This effect is more significant at slower scan rates and higher temperature. Therefore, identifying the voltage related to the accelerated increase of anodic current deviation can be a fair approximation of defining the maximum voltage window. According to the recorded CVs, 1.5 V, the highest voltage with less than 10% accelerated relative standard deviation (RSD) of anodic current is set to be the voltage limit at RT (Fig. 3b). The calculations are made according to the following equations:

$$RSD = \frac{\sigma_{I_a}}{\overline{I_a}} \times 100\% \tag{7}$$

$$Change\ of\ RSD = \frac{RSD_{V_2} - RSD_{V_1}}{RSD_{V_1}} \times 100\% \tag{8}$$

where σ_{I_a} is the standard deviation of anodic current, $\overline{I_a}$ is the average anodic current, RSD_{V_1} is the relative standard deviation of anodic current at voltage V_1 and RSD_{V_2} is the relative standard deviation of anodic current at voltage V_2.

Fig. 3c displays CVs at different scan rates in a voltage range of 0–1.5 V at RT. The rectangular shape of the CVs at slow scan rates are indicative of a characteristic capacitive behavior. Consequently, the transformation into a more oval shape at fast scan rates points out a deviation from ideal capacitive performance. The specific capacitance at a slow scan rate of 10 mV s^{-1} is calculated to be 1.7 times higher than the specific capacitance at 200 mV s^{-1} (54 F g^{-1}). The drop of capacitance at fast scan rates is a consequence of several factors. First, due to electrode and electrolyte intrinsic resistance, a potential loss in the system is unavoidable, which renders the actual potential smaller than the applied potential. When the response current increases with increasing scan rates the potential loss is enhanced, and a smaller potential is left to drive the ions into or from the electrode. Second, at faster scan rates, the electrolyte ions have a shorter transport time and are able to access only a small portion of the active surface [31].

Due to their inherent high viscosity, most IL electrolytes provide much lower capacitance and higher ESR than aqueous and organic electrolytes [10,22,32,33]. Despite that, a maximum specific capacitance of 93 F g^{-1} is achieved at a scan rate of 10 mV s^{-1} with EMIM Ac, which is comparable to aqueous KOH [34] and acetate-based [35] aqueous electrolytes. Moreover, a capacitance retention (ratio of capacitance at 200 mV s^{-1} to the one at 10 mV s^{-1}) of 58% is maintained at 200 mV s^{-1}. Such a high capacitance and reasonable rate capability is believed to be a benefit from the relatively low viscosity (0.16 Pa s) [36] of the EMIM Ac electrolyte. Moreover, presence of a certain amount of H_2O in the current system (Fig. S4) would reduce the viscosity to one-half of that value [36].

To further explore the voltage limit at elevated temperatures, CV voltage-ramp measurements were performed at 100 °C, 120 °C and 150 °C, respectively. Corresponding CVs at a scan rate of 20 mV s^{-1} are presented in Fig. 4a–c. A quasi-rectangular shape with less than 10% accelerated increase of the anodic current is maintained up to 1.4 V at 100 °C and 120 °C followed by 1.3 V at 150 °C (Fig. 4d), which sets the maximum voltage for EDL type behavior at elevated temperatures for this particular system. This trend of shrinkage of the voltage window with elevated temperature is reasonable as there will be an increase of hydrogen chemisorption from the cation either by reorientation of the imidazolium ring or removal of the anion from the surface [37]. And the extent of the phenomenon might depend on the amount of water present in system [38]. However, the shrinkage of the voltage window with elevated temperature can also be noticed in dry ILs [39], which originates from a very fundamental reason: the change in dielectric constant. As the temperature increases, the random thermal motion of the molecules or ions increases to a large extent resulting in a decrease of the dielectric constant that consequently reduces the voltage window.

Therefore, a reduction in voltage at elevated temperature is highly required in order to achieve a good capacitive behavior with high thermal stability.

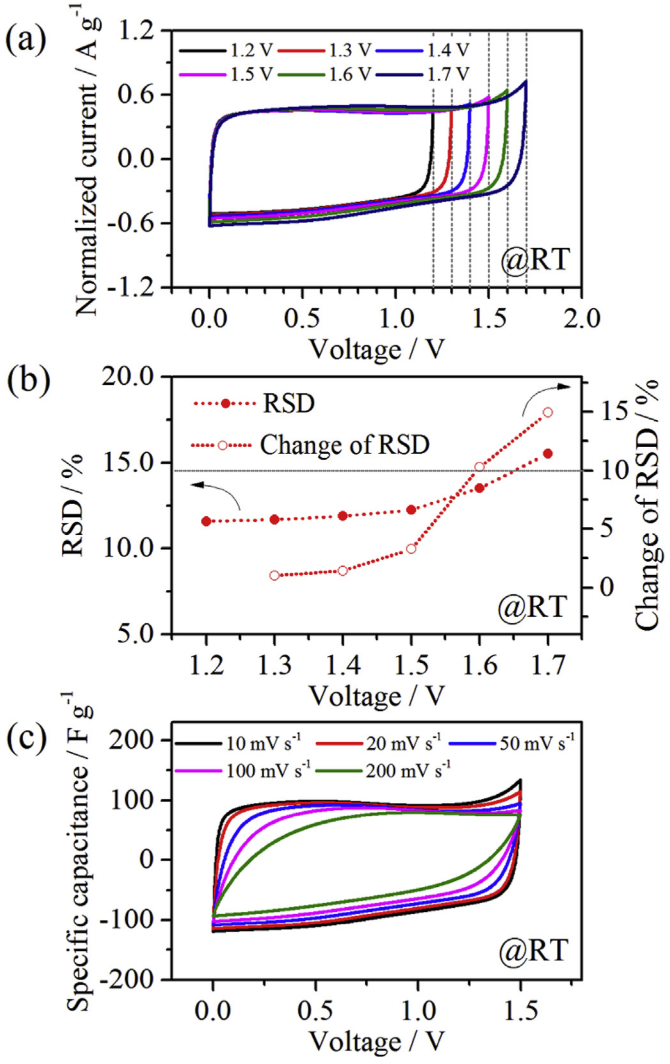

Fig. 3. (a) CV plots at different voltage ranges (at 20 mV s^{-1}, RT), (b) relative standard deviation (RSD) and change of RSD of anodic current as a function of voltage, and (c) CV plots at different scan rates (voltage range 1.5 V, RT).

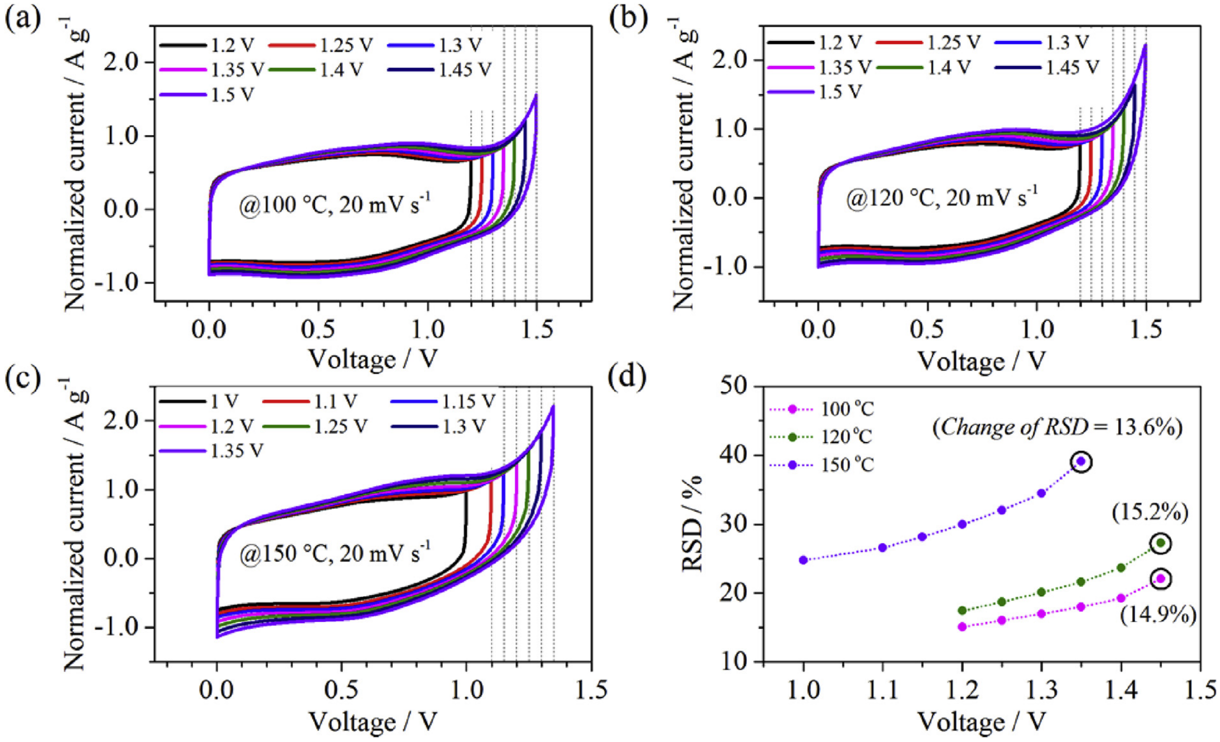

Fig. 4. CV profile within different voltage ranges at (a) 100 °C, (b) 120 °C, (c) 150 °C, and (d) relative standard deviation (RSD) of anodic current as a function of voltage.

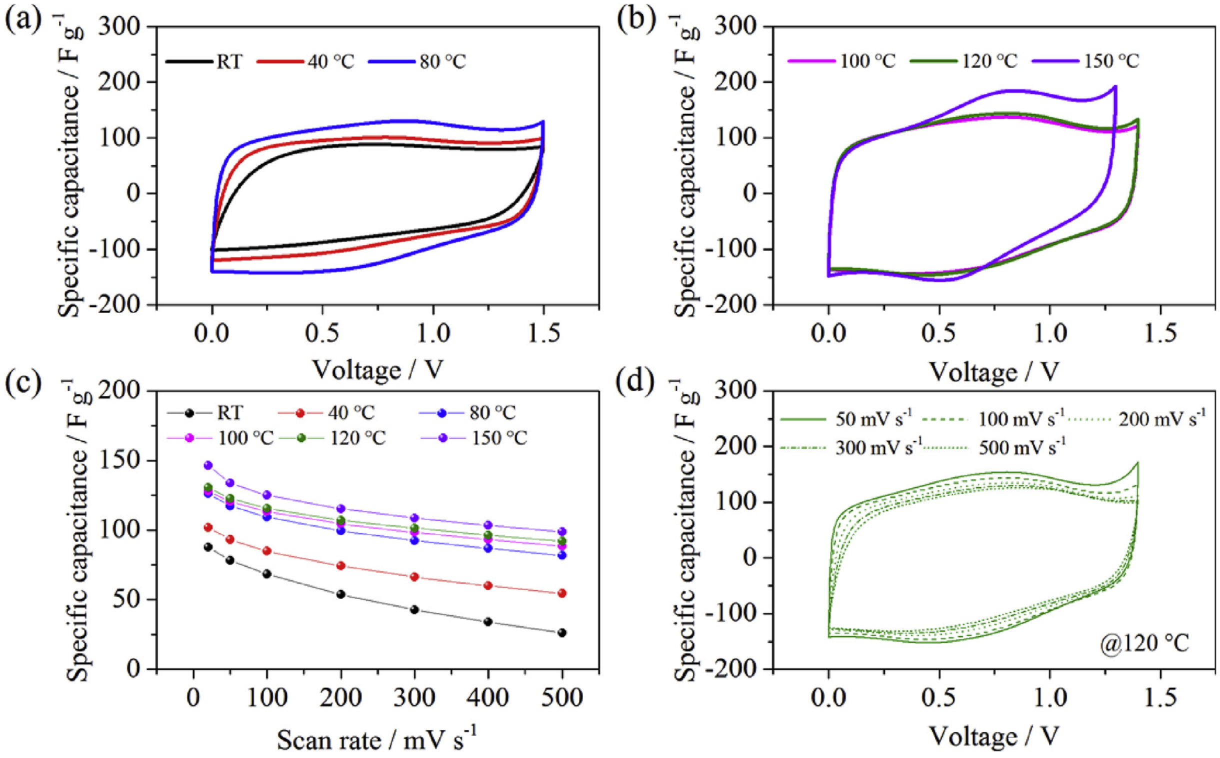

Fig. 5. (a, b) Comparison of CV plots at a scan rate of 100 mV s^{-1} among RT, 40, 80, 100, 120 and 150 °C, (c) variation of specific capacitance at different temperatures with scan rates of 20, 50, 100, 200, 300, 400 and 500 mV s^{-1}, and (d) CVs at 120 °C with different scan rates.

CVs at a scan rate of 100 mV s^{-1} obtained for cells at different temperatures are compared and presented in Fig. 5. The working voltage of the supercapacitor cell remains the same (1.5 V) for RT, 40 °C, and 80 °C (Fig. 5a), indicating that the limited temperature increase hardly has any effect on the maximum voltage. Instead, the shape of the CV curves widens and results in an improved capacitive behavior even at a high scan rate of 100 mV s^{-1} (Fig. 5a–b). The specific capacitance is 125 F g^{-1} at 150 °C, 115 F g^{-1} at 120 °C, 113 F g^{-1} at 100 °C, 99 F g^{-1} at 80 °C, 85 F g^{-1} at 40 °C and 68 F g^{-1} at RT. Since the electrical conductivity of carbon electrodes does not vary significantly with elevated temperature [6], the observed capacitance improvement is possibly attributed to an increased ionic conductivity of the electrolyte, resulting in greater charge accumulation at the electrode/electrolyte interface. This increase of the ionic conductivity of EMIM Ac electrolyte could be explained from the following reasoning: due to a strong affinity of the $[Ac]^-$ anion to abstract hydrogen from water (nearest water molecule from acetate), the formation of acetic acid, especially at elevated temperatures could be expected [40,41], therefore, the acetic acid could increase the ionic conductivity of the IL by two orders of magnitude [42], considering the conformations arising from the hydrogen atom of water.

However, with elevated temperature, the water content from the bulk EMIM Ac solution will be reduced, consequently, attraction of the $[Ac]^-$ anion to create the hydrogen bond will shift towards the hydrogen atom (aromatic acidic proton) in the imidazolium ring (attached to the carbon atom present between the nitrogen atoms), which will lead to the formation of carbenes (intrinsic impurities in dry EMIM Ac) in the system [41].

During charging of the supercapacitor these protonated carbenes diffuse deeply into the micropores and become confined. As a result, the mobility of carbenes is constrained compared to the rest of the bulk solution. At a later event, when the rest of the ions or ionic species from the bulk electrolyte solution are driven to the pores as a result of diffusion caused by electrical or thermal fields, the confined carbenes remain available for re-protonation [38]. A strong carbene protonation/re-protonation can be noticed by the presence of reversible peaks on both anodic and cathodic scans at 150 °C, which contributes to the enlargement of the CV area (Fig. 5b) and thus to the specific capacitance. In fact, the extent of the reversible reaction is noticeable already at 100 °C and 120 °C to a certain extent.

Fig. 5c presents the trend of specific capacitance variation with different scan rates at each temperature. An improved rate capability of the device can be noticed with increased temperature. A capacitance retention (ratio of capacitance at 500 mV s^{-1} to the value at 20 mV s^{-1}) of 71% is maintained at 120 °C, which is over 2 times greater than the retention at RT (30%). CV measurements performed at 120 °C with different scan rates (Fig. 5d) maintain the capacitive behavior with moderately rectangular shape (even at 500 mV s^{-1}), ensuring a good rate performance and thermal tolerance of the device.

Taking all of the above into account, the maximum voltage at different temperatures has been determined, as listed in Table 1. Although the present system could be functional even at 150 °C within 0–1.3 V, the reliability is still questionable for long-term operations at this voltage range. Therefore, for less risk of cell failure, 120 °C is suggested as approaching an upper temperature limit for the SC operation within a decent voltage range of 0–1.4 V.

3.2. Galvanostatic charge discharge (GCD)

Fig. 6a–b illustrate the comparison of GCD curves at a normalized current of 3 A g^{-1}. Symmetrical and nearly linear slopes of the voltage response represent typical capacitive behavior of the SC device, which becomes more apparent with increasing temperature up to 120 °C. Similar to the CV results, a wide bending of the GCD profile at 150 °C confirms the presence of side reactions.

Fig. 6c–d display the specific capacitance and IR drop of the SC cell as a function of normalized current in the temperature range of RT to 150 °C. In general, the specific capacitance decreases with the increase of normalized current. At RT, the cell is not able to charge at a current more than 10 A g^{-1} due to high voltage loss. At 120 °C, the charging capability of the cell improves significantly – it is chargeable at a current of more than 30 A g^{-1}. Therefore, an improved rate capability (the ratio of capacitance at 7 A g^{-1} to the value at 1 A g^{-1}) of 85% can be achieved at 120 °C compared to 62% at RT.

When the current increases the IR drop becomes larger due to its direct proportionality to the current. In addition, the IR drop shows a descending trend with the gradual increase of operating temperature. This decrease of the IR drop facilitates a larger usable voltage at the same current (Table 1). For example, even though the maximum voltage at 120 °C is 0.1 V lower than 1.5 V at RT, the usable working voltage is actually larger. The IR drop at RT is 186 mV, reducing the active working voltage to 1.31 V, whereas the IR drop at 120 °C gives only a modest 26 mV reduction. The energy density is directly proportional to the capacitance and the square of the useable voltage; hence the energy density at elevated temperature (120 °C) is 1.7 times higher than the energy density at RT. A similar trend is observed for each temperature, as shown in Table 1. High power density is the main characteristic of a SC. Therefore, improving energy density without sacrificing the power density should be highly prioritized. The tested SC cell delivers a remarkable maximum power density (Table 1) due to its low internal resistance (V_{ir}) and at the same time ability to function with a high current. The values compare well to other reports (Table S1). Also, the applied current has a significant influence on the average power density and energy density of the device at each temperature. A Ragone plot comparing the performance variation can be seen in Fig. S6.

Fig. 6e shows the GCD profile of the SC operating at 120 °C. All the curves display nearly symmetric triangular shape, which indicates the dominance of EDLC behavior in the system. The IR drop increases with increasing normalized current but still it remains as low as 128 mV at 15 A g^{-1}.

Table 1
Performance metrics of the supercapacitor from GCD measurements.

Temperature (°C)	Max. voltage (V)	IR drop [a] (mV)	Useable voltage (V)	Energy density (Wh kg^{-1})	Max. Power density (kW kg^{-1})	Rate capability (%)	Capacitance [b] (F g^{-1})
RT	1.5	186	1.31	4.3	13.9	62	84
40	1.5	79	1.42	6.1	38.2	78	98
80	1.5	35	1.46	8.3	92.4	82	122
100	1.4	29	1.37	7.3	97.4	85	121
120	1.4	26	1.37	7.4	107.5	85	121
RT/120	1.5	134	1.36	4.9	20.8	66	88
150	1.3	23	1.28	7.7	107.1	87	142

[a] IR drop at 3 A g^{-1}

[b] Maximum capacitance is achieved at 1 A g^{-1} while 2 A g^{-1} for 150 °C.

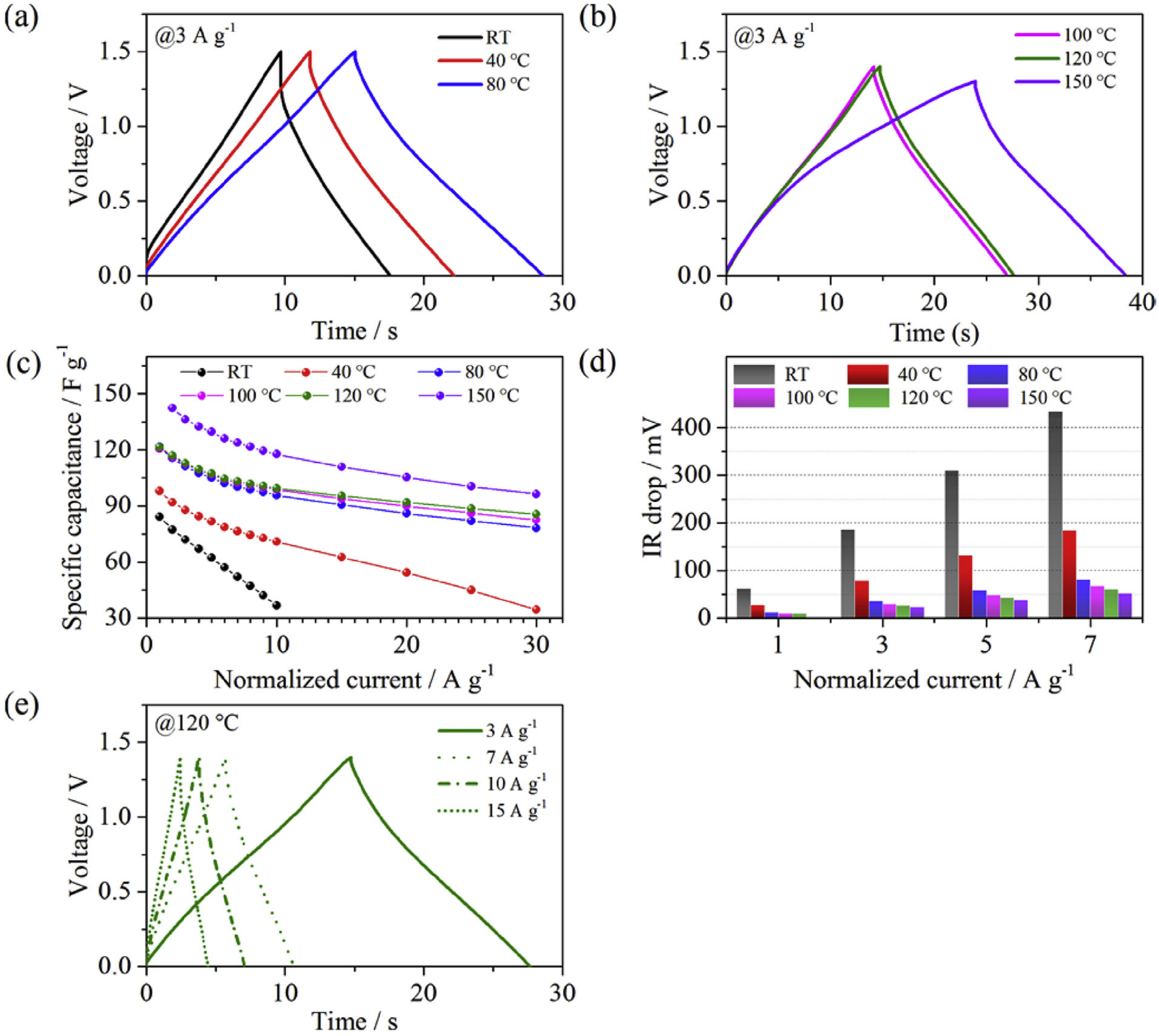

Fig. 6. (a, b) Comparison of GCD plots measured at different temperatures at a normalized current of 3 A g^{-1}, (c) variation of specific capacitance at different temperatures with normalized current of 1–10 A g^{-1}, 15 A g^{-1}, 20 A g^{-1}, 25 A g^{-1} and 30 A g^{-1}, (d) IR drop with different normalized current, and (e) GCD profile at 120 °C with different current densities.

3.3. *Electrochemical impedance spectroscopy (EIS)*

EIS measurements have been conducted in order to distinguish the temperature dependence of the capacitive and resistive parts of the SC. Fig. 7a presents a typical Nyquist plot consisting of different impedance contribution of the SC cell. In the high frequency region, the intersection point of the depressed semi-circle on the Z_{re}-axis closest to the origin is due to equivalent series resistance (ESR) that generally comprises electrolyte solution resistance, separator and external circuit resistances, where the electrolyte solution resistance usually contributes the most [43,44]. The ESR value is fairly low (Table 2) at RT compared to values reported for other systems containing IL (Table S1). The intersection points are shifting towards the origin with an increase in the operating temperature. Hence, a definite decrease of ESR (Table 2) confirms an enhanced ionic conductivity of the EMIM Ac electrolyte with increasing temperature, which essentially speeds up the dynamics of the charge accumulation in the double layer formation. At elevated temperatures, the electrostatic forces between cations and anions become weaker, resulting in a lower viscosity of the electrolyte. The viscosity (Pa·s) decreases by a factor of 32 from RT to 120 °C [36].

The second intersection point of the semi-circle in the middle frequency region is associated with the ion migration across the bulk electrolyte and electrode interface (interfacial resistance, R_{int} [44] in the current EDLC-dominated system. Note that for pseudocapacitive systems, R_{int} is replaced by R_{ct} (charge transfer resistance) that defines the kinetics of electrochemical reaction in the electrode/electrolyte interface [43,45]. According to the recorded values (Table 2), R_{int} keeps decreasing with temperature increase, until the second intersection of the semi-circle is hardly visible at 80 °C and beyond, revealing an enhanced affinity between AC electrode and EMIM Ac electrolyte.

A transition from high to low frequency can be recognized through the presence of a leaning line with a slope of 45° on Nyquist plots and is indicative of transmission line behavior represented by the Warburg impedance. The Warburg region becomes shorter with increasing temperature, indicative of a better ion diffusion into the porous AC electrode [46]. After the Warburg region, a long spike, parallel to the Z_{im}-axis, with a slope of nearly 90° appears in the low frequency region, which is associated with an ideally polarizable mass capacitance [21]. However, for temperatures above 40 °C, the low-frequency part deviates from ideal

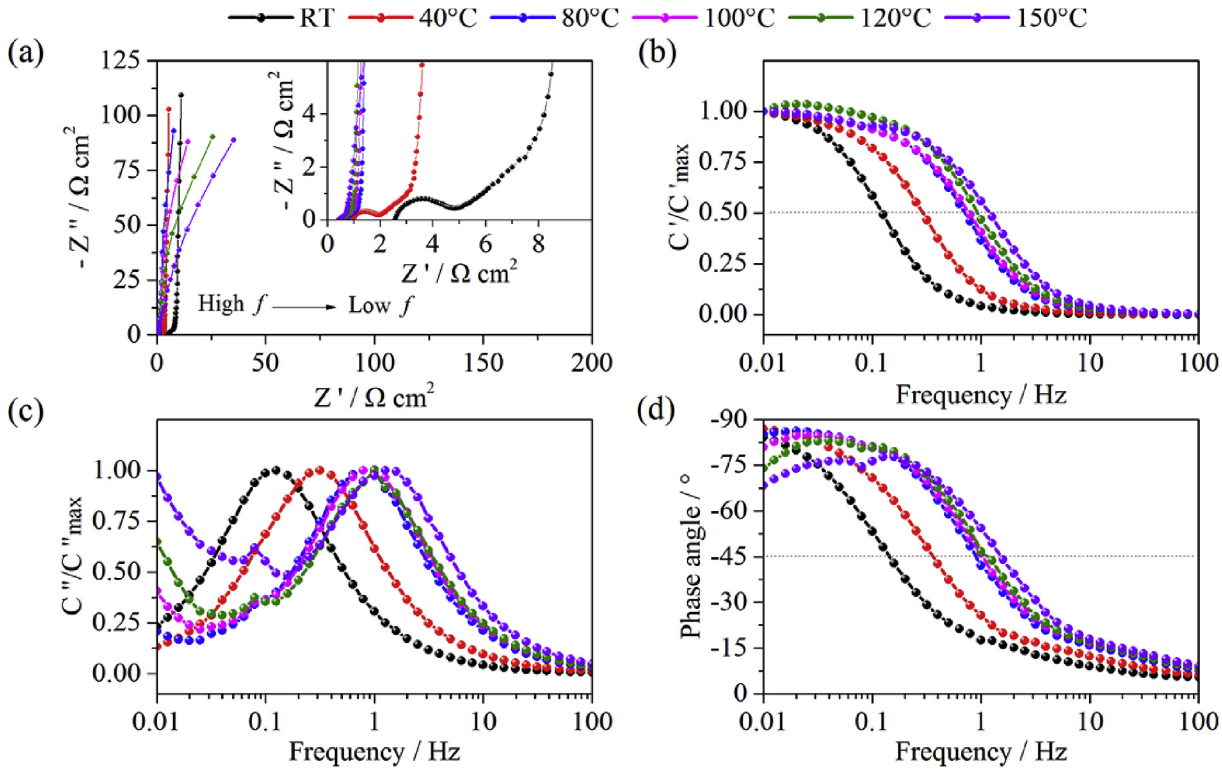

Fig. 7. EIS measurements at different temperatures, (a) Nyquist plots, (b) normalized real capacitance as a function of frequency, (c) normalized imaginary capacitance as a function of frequency, and (d) phase angle as a function of frequency, Bode plots.

Table 2
Performance metrics of the supercapacitor from EIS measurement.

Temperature (°C)	ESR (Ω cm^2)	R_{int} (Ω cm^2)	Phase angle at 10 mHz (°)	Phase angle at 20 mHz (°)	Peak Frequency, f_p (Hz)	Relaxation time constant, τ_o (s)
RT	2.52	2.06	−84	−80	0.13	7.9
40	0.91	0.93	−87	−85	0.32	3.1
80	0.48	0.22	−85	−86	0.80	1.2
100	0.46	0.17	−81	−85	0.80	1.2
120	0.44	0.15	−74	−81	1.0	1.0
RT/120	1.96	1.42	−84	−81	0.16	6.3
150	0.37	0.09	−68	−74	1.3	0.8

capacitive features (parallel to Z_{im}-axis). The degree of inclination with the abscissa is related to the extent of leakage current [21,47]. Generally, leakage current arises due to parasitic side reactions or charge redistribution and increases with elevated temperature [48–50]. This behavior can be better explained in terms of time constant and dielectric relaxation time constant of the SC cell through the complex capacitance analysis. In this way it is possible to resolve the capacitive performance at low frequency, unlike in the Nyquist plot, which is best suited for observing the resistive response at high frequency and which requires sophisticated nonlinear fitting of increasing complexity for elevated temperatures [51,52].

With an alternating signal at frequency ω, a complex capacitance can be defined in terms of a complex permittivity and complex impedance in the following manner [22,53,54]:

$$\begin{aligned} C(\omega) &= C^{'}(\omega) - iC^{''}(\omega) \\ &= \frac{A}{d} \times \left[\varepsilon^{'}(\omega) - i\varepsilon^{''}(\omega)\right] \quad (\mathrm{F}) \end{aligned} \tag{9}$$

$$C^{'} = \frac{-Z^{''}(\omega)}{\omega\left|Z(\omega)\right|^{2}} \quad \left(\mathrm{Fg}^{-1}\right) \tag{10}$$

$$C^{''} = \frac{Z^{'}(\omega)}{\omega\left|Z(\omega)\right|^{2}} \quad \left(\mathrm{Fg}^{-1}\right) \tag{11}$$

where, $C(\omega)$ is the frequency dependent complex capacitance, C' being its real part and C'' its imaginary, A is the geometrical area of the electrode, d is the double layer thickness, $\varepsilon^{'}(\omega)$ and $\varepsilon^{''}(\omega)$ are the real and imaginary part of the complex permittivity, $|Z(\omega)|$ is the frequency dependent impedance, $Z'(\omega)$ is the real part of the impedance, $Z''(\omega)$ is the imaginary part of the impedance.

Fig. 7b–c demonstrate the change of real and imaginary capacitance (complex capacitance) with frequency. The real capacitance is essentially the deliverable capacitance, which increases with elevated temperatures. More importantly, the frequency at which the capacitance reaches half of its maximum (stored energy is not fully accessible above this frequency) has been remarkably increased with temperature increase (Fig. 7b). It is worth mentioning that the total dielectric polarization of ILs is a combination of electronic polarization as a result of the molecular polarizability and the orientation polarization caused by the permanent dipole moment of the ions [55]. In an alternating field, the average dipole orientation requires a characteristic time to align with the changing field direction. This is known as the dielectric relaxation time, which can be extracted from the characteristic frequency corresponding to the maximum capacitance in the imaginary capacitance plot (Fig. 7c): $\tau_o = 1/f_p$. τ_o is the dielectric relaxation time and f_p is the peak frequency. The dielectric relaxation time is the minimum time required to deliver the stored energy with an efficiency of more than 50% [54,56], meaning that a high characteristic frequency (equivalent to a low relaxation time constant) is a reflection of high power capability with improved rate performance [57]. As shown in Table 2, the peak frequency at RT is 0.13 Hz which is two times higher than what was reported for an EMIM BF_4 containing SC [15]. With increasing temperature, the peak frequency shifts towards higher frequency and the relaxation time constant decreases significantly (Table 2). The increasing characteristic frequency at elevated temperatures follows similar trend as reported for an (1-butyl-1-methylpyrrolidinium bis-(trifluoromethylsulfony) imide (BMPY TFSI) containing SCs [6] but with higher operating frequency (Table 2). The high characteristic frequency is believed to be a consequence of good affinity between AC and EMIM Ac and thus a low ohmic resistance at elevated temperatures.

It can be noticed from Fig. 7c that there are some resistive tails in the low frequency region at high temperatures (80 °C and beyond) in addition to the capacitive peak. The extent of the leakage current can be estimated from the magnitude of these resistive tails [58]. By taking into account the presence of leakage current, another time constant can be defined as a product of total capacitance and leakage resistance. The time constant can be extracted from the frequency corresponding to the resistive tail: $\tau_1 = 1/f_t$, where τ_1 is the time constant and f_t is the tail frequency. When τ_1 is sufficiently larger than τ_o, the leakage current is smaller [58]. The time constants are calculated to be 40 s, 25 s, 20 s and 6 s for 80, 100, 120, and 150 °C, respectively. By comparing the time constants (τ_1) with the dielectric relaxation time constants (τ_o) (Table 2), it can be estimated that with increasing temperature the leakage current also increases. The enhanced leakage current under thermal influence is a common observation in various systems, because the extent of charge redistribution increases significantly at high temperature as a consequence of increased ionic mobility [59,60]. Besides, in the EMIM Ac electrolyte, the abstraction of hydrogen atoms by the acetate anion may occur, especially when the electrolyte is dry, leading to charge transfer caused by the formation of carbenes (an intrinsic impurity of pure EMIM Ac) [41,61]. Therefore, the extent of the leakage current could be further increased as a result of these parasitic side reactions. On the other hand, leakage current is comparatively low at lower temperatures possibly due to two factors. First, charge redistribution is mitigated as a result of slow ionic mobility. Second, the presence of higher H_2O content (around 10%, Fig. S4) reduces the carbene formation [41] and further decreases the leakage current. The former is believed to be the main contributor.

Fig. 7d represents the impedance data in a Bode plot. The phase angle of an ideal capacitor is −90° but slight deviations are very common in reality due to the presence of intrinsic resistance in the system. The greater deviation with increasing temperature can be clearly seen at very low frequency (10 mHz), with the largest deviation occurring at 150 °C (Table 2). The phase angle at 20 mHz (Table 2) for temperatures above 40 °C approaches −90°, which indicates that the capacitive behavior is improving at a comparatively higher frequency at elevated temperatures.

3.4. Cyclic charge/discharge (CCD)

CCD measurements were carried out for 1000 cycles at each temperature with a normalized current of $7\,A\,g^{-1}$ (Fig. 8a). The inset compares the 50th and 1000th cycles of GCD curves. The change of the curves is insignificant after cycling, except a small reduction in charging and discharging time. The deviation of the triangular shape is only evident at 150 °C, which indicates that cycle life degradation occurs and puts an upper limit on the device operating temperature.

Fig. 8a–b present capacitance retention at 1000 cycles and average coulombic efficiency over the temperature range from 40 °C to 150 °C. A capacitance retention of more than 95% (specifically 98% at 40 °C, 97% at 80 °C, 96% at 100 °C, 95% at 120 °C) is maintained up to 120 °C, while at 150 °C it is 85%. A high average coulombic efficiency of 98% is maintained up to 100 °C followed by 96% at 120 °C and 81% at 150 °C.

As stated in section 3.1, even though the device can function at 150 °C at 1.3 V and the capacitance retention in the end of cycling is fairly high (85%), it should not be operated at this temperature and voltage for long time period due to a higher risk of device failure. An interesting result was revealed when the SC cell was cycled for 1000 cycles at 1 V prior to 1.3 V: a capacitance retention of 95% was maintained in the end of cycling (Fig. S5). Therefore, as the working

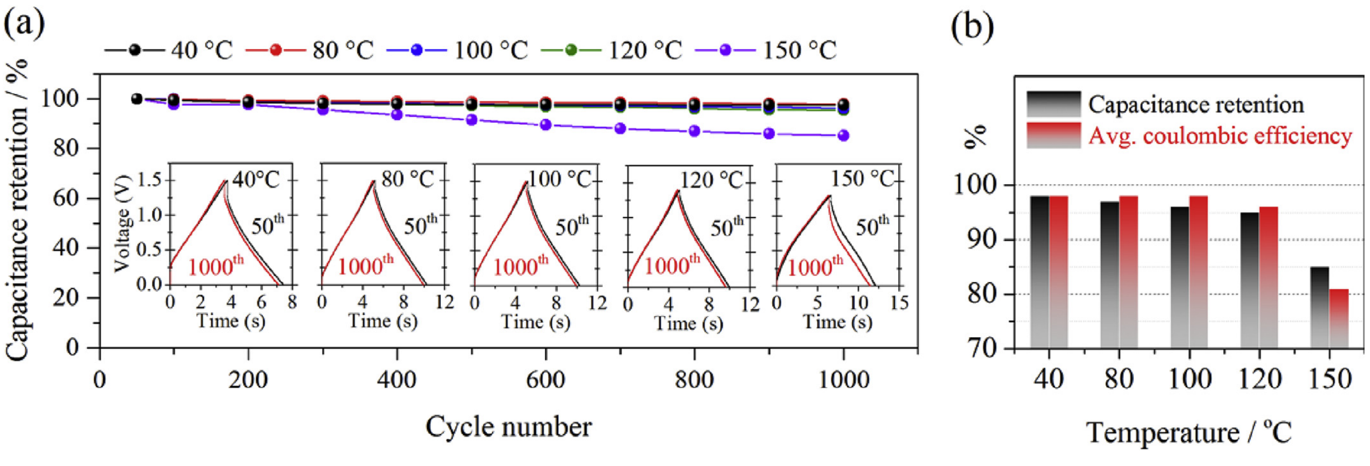

Fig. 8. (a) CCD test at 40, 80, 100, 120 and 150 °C for 1000 cycles (b) capacitance retention at 1000th cycle and average coulombic efficiency as a function of temperature.

voltage is very sensitive to temperature due to enhanced electrochemical activity, a relatively low operating voltage can ensure an improved long-term stability at elevated temperatures.

3.5. Influence of high temperature exposure on room temperature performance

All electrochemical measurements such as CV (with a scan rate from 10 to 3000 mV s^{-1}), GCD (1–100 A g^{-1}), CCD (1000 cycles) and EIS have been carried out on the same cell with a gradual increase of temperature in the following way RT, 40, 80, 100 and 120 °C, over a period of 30 days. Afterwards, the cell was cooled down to RT, and the performance was examined again to investigate whether there is a hysteresis caused by the thermal treatment or operation history (Fig. 9).

Interestingly, the electrochemical performance of the cell has been measurably improved compared to the initial RT performance. Both the CV (Fig. 9a) and GCD (Fig. 9b) measurements illustrate ideal EDLC behavior. At RT, a specific capacitance of 88 F g^{-1} has been calculated from the CV, and this value increases to 92 F g^{-1} after 120 °C exposure. From the GCD profile, the charging and discharging time also increased with a reduced IR drop (from 62 mV to 44 mV). The Nyquist plot (Fig. 9c) follows a similar trend with a reduced ESR and R_{int} (Table 2). This improvement suggests that the enhanced surface modification at high temperature remains in the system to some extent even if the system cools down to RT. Also, it is speculated that the high temperature exposure and repeated charging/discharging might have improved the interface in terms of more complete wetting of AC electrode surface with the EMIM Ac electrolyte. More importantly, the capacitive signature of the cell remains similar after all the cycling and high temperature exposure. Therefore, the progressive change on the performance of the cell validates the robustness of the device. At the same time, the evidence of the performance improvement due to high temperature treatment can also be considered as a potential strategy to improve the RT performance of other supercapacitor systems containing carbon electrodes and IL electrolytes.

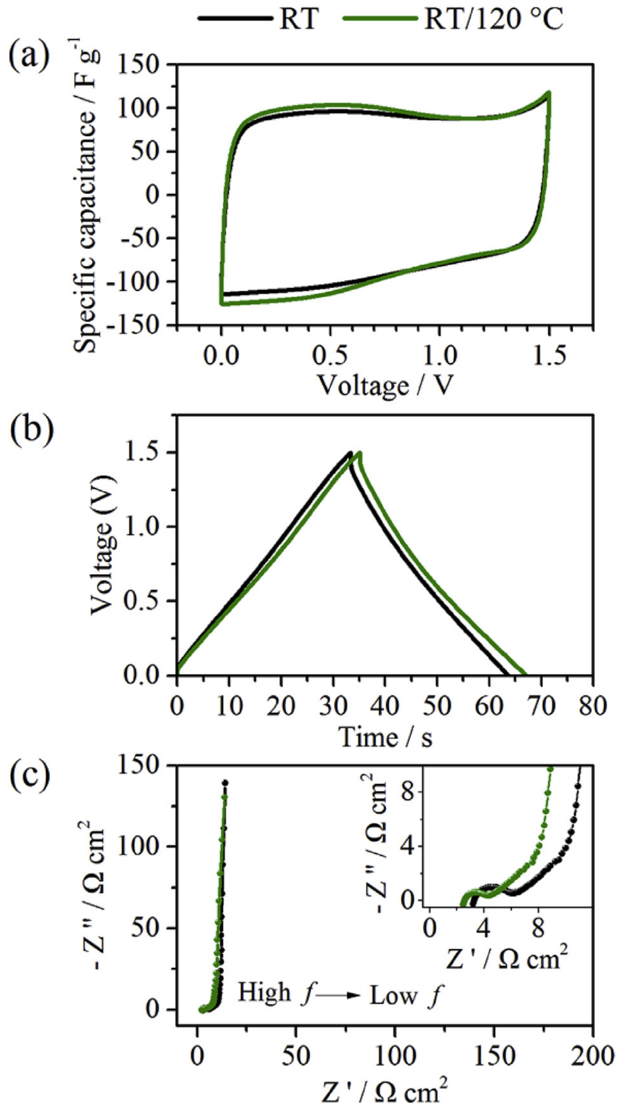

Fig. 9. Electrochemical performance of the supercapacitor before and after high temperature (120 °C) exposure, (a) CV at 20 mV s^{-1}, (b) GCD at 1 A g^{-1} and (c) Nyquist plot. Measurements are performed at RT.

4. Conclusions

A thorough electrochemical study of a supercapacitor containing EMIM Ac electrolyte and AC electrodes has been carried out in a wide temperature range from RT to 150 °C. These results manifest for the first time that EMIM Ac could be a prospective electrolyte for carbon-based supercapacitors, especially for high temperature applications. The AC/EMIM Ac system is found to be functional at up to 150 °C within 0–1.3 V while 120 °C is suggested to be the maximum operating temperature and 1.4 V as the voltage limit for long-term use. Both good affinity between EMIM Ac and AC, and a reduction of the dielectric relaxation time constant with temperature increase are revealed by the devices' impedance behavior. The study points out that maximum operation temperature could be gained at an expense of the voltage range. However, the usable voltage range (and thus the energy density and power density) may not necessarily be compromised thanks to a lower IR drop at elevated temperatures. The trade-off between maximum operation temperature and maximum voltage as well as the performance enhancement after thermal treatment could be of major practical significance for designing high temperature electrochemical capacitor systems.

Acknowledgment

This work was funded by the European Union's Horizon 2020 research and innovation program [grant number 644378, smart-MEMPHIS project], and Vinnova UDI project Energy Harvesting Toolkit. The authors thank Jonna Hynynen and David Philip Anderson for assistance with the (TGA) and BET surface area measurement.

Appendix A. Supplementary data

Supplementary data related to this article can be found at https://doi.org/10.1016/j.electacta.2018.01.029.

References

[1] R. Kotz, M. Carlen, Principles and applications of electrochemical capacitors, Electrochim. Acta 45 (2000) 2483–2498.
[2] A. Burke, H. Zhao, Applications of supercapacitors in electric and hybrid vehicles, in: 5th European Symposium on Supercapacitor and Hybrid Solutions (ESSCAP), Brasov, Romania, 23–25 April 2015.
[3] G. Xiong, A. Kundu, T.S. Fisher, Thermal effects in Supercapacitors, Springer, New York, 2015.
[4] X. Lin, M. Salari, L.M. Arava, P.M. Ajayan, M.W. Grinstaff, High temperature electrical energy storage: advances, challenges, and frontiers, Chem. Soc. Rev. 45 (2016) 5848–5887.
[5] R.A. Norman, First high-temperature electronics products survey 2005, Sandia

report, California, 2006.

[6] H. Wang, Z. Xu, A. Kohandehghan, Z. Li, K. Cui, X. Tan, T.J. Stephenson, C.K. King'ondu, C.M. Holt, B.C. Olsen, J.K. Tak, D. Harfield, A.O. Anyia, D. Mitlin, Interconnected carbon nanosheets derived from hemp for ultrafast supercapacitors with high energy, ACS Nano 7 (2013) 5131–5141.

[7] C. Maton, N. De Vos, C.V. Stevens, Ionic liquid thermal stabilities: decomposition mechanisms and analysis tools, Chem. Soc. Rev. 42 (2013) 5963–5977.

[8] H.F.D. Almeida, H. Passos, J.A. Lopes-da-Silva, A.M. Fernandes, M.G. Freire, J.A.P. Coutinho, Thermophysical properties of five acetate-based ionic liquids, J. Chem. Eng. Data 57 (2012) 3005–3013.

[9] M.G. Freire, P.J. Carvalho, A.M. Fernandes, I.M. Marrucho, A.J. Queimada, J.A. Coutinho, Surface tensions of imidazolium based ionic liquids: anion, cation, temperature and water effect, J. Colloid Interface Sci. 314 (2007) 621–630.

[10] A. Balducci, R. Dugas, P.L. Taberna, P. Simon, D. Plee, M. Mastragostino, S. Passerini, High temperature carbon-carbon supercapacitor using ionic liquid as electrolyte, J. Power Sources 165 (2007) 922–927.

[11] C. Arbizzani, M. Biso, D. Cericola, M. Lazzari, F. Soavi, M. Mastragostino, Safe, high-energy supercapacitors based on solvent-free ionic liquid electrolytes, J. Power Sources 185 (2008) 1575–1579.

[12] M. Armand, F. Endres, D.R. MacFarlane, H. Ohno, B. Scrosati, Ionic-liquid materials for the electrochemical challenges of the future, Nat. Mater. 8 (2009) 621–629.

[13] R.S. Borges, H. Ribeiro, R.L. Lavall, G.G. Silva, Temperature stable supercapacitors based on ionic liquid and mixed functionalized carbon nanomaterials, J. Solid State Electrochem. 16 (2012) 3573–3580.

[14] M. Anouti, L. Timperman, M. el Hilali, A. Boisset, H. Galiano, Sulfonium bis(-trifluorosulfonimide) plastic crystal ionic liquid as an electrolyte at elevated temperature for high-energy supercapacitors, J. Phys. Chem. C 116 (2012) 9412–9418.

[15] L. Wei, M. Sevilla, A.B. Fuertes, R. Mokaya, G. Yushin, Polypyrrole-derived activated carbons for high-performance electrical double-layer capacitors with ionic liquid electrolyte, Adv. Funct. Mater. 22 (2012) 827–834.

[16] L. Timperman, P. Skowron, A. Boisset, H. Galiano, D. Lemordant, E. Frackowiak, F. Beguin, M. Anouti, Triethylammonium bis(tetrafluoromethylsulfonyl)amide protic ionic liquid as an electrolyte for electrical double-layer capacitors, Phys. Chem. Chem. Phys. 14 (2012) 8199–8207.

[17] S. Leyva-Garcia, D. Lozano-Castello, E. Morallon, T. Vogl, C. Schutter, S. Passerini, A. Balducci, D. Cazorla-Amoros, Electrochemical performance of a superporous activated carbon in ionic liquid-based electrolytes, J. Power Sources 336 (2016) 419–426.

[18] N. Handa, T. Sugimoto, M. Yamagata, M. Kikuta, M. Kono, M. Ishikawa, A neat ionic liquid electrolyte based on FSI anion for electric double layer capacitor, J. Power Sources 185 (2008) 1585–1588.

[19] V. Ruiz, T. Huynh, S.R. Sivakkumar, A.G. Pandolfo, Ionic liquid-solvent mixtures as supercapacitor electrolytes for extreme temperature operation, Rsc Adv. 2 (2012) 5591–5598.

[20] W.W. Liu, X.B. Yan, J.W. Lang, Q.J. Xue, Effects of concentration and temperature of EMIMBF4/acetonitrile electrolyte on the supercapacitive behavior of graphene nanosheets, J. Mater. Chem. 22 (2012) 8853–8861.

[21] P. Sivaraman, S.P. Mishra, D.D. Potphode, A.P. Thakur, K. Shashidhara, A.B. Samui, A.R. Bhattacharyya, A supercapacitor based on longitudinal unzipping of multi-walled carbon nanotubes for high temperature application, Rsc Adv. 5 (2015) 83546–83557.

[22] A. Lewandowski, A. Olejniczak, M. Galinski, I. Stepniak, Performance of carbon-carbon supercapacitors based on organic, aqueous and ionic liquid electrolytes, J. Power Sources 195 (2010) 5814–5819.

[23] A. Krause, A. Balducci, High voltage electrochemical double layer capacitor containing mixtures of ionic liquids and organic carbonate as electrolytes, Electrochem. Commun. 13 (2011) 814–817.

[24] W. Li, Z. Zhang, B. Han, S. Hu, Y. Xie, G. Yang, Effect of water and organic solvents on the ionic dissociation of ionic liquids, J. Phys. Chem. B 111 (2007) 6452–6456.

[25] B. Bhargava, Y. Yasaka, M.L. Klein, Computational studies of room temperature ionic liquid–water mixtures, Chem. Commun. 47 (2011) 6228–6241.

[26] R. Lynden-Bell, N. Atamas, A. Vasilyuk, C. Hanke, Chemical potentials of water and organic solutes in imidazolium ionic liquids: a simulation study, Mol. Phys. 100 (2002) 3225–3229.

[27] M. Galiński, A. Lewandowski, I. Stępniak, Ionic liquids as electrolytes, Electrochim. Acta 51 (2006) 5567–5580.

[28] B. Dyatkin, V. Presser, M. Heon, M.R. Lukatskaya, M. Beidaghi, Y. Gogotsi, Development of a green supercapacitor composed entirely of environmentally friendly materials, ChemSusChem 6 (2013) 2269–2280.

[29] M. Aslan, D. Weingarth, P. Herbeck-Engel, I. Grobelsek, V. Presser, Polyvinylpyrrolidone/polyvinyl butyral composite as a stable binder for castable supercapacitor electrodes in aqueous electrolytes, J. Power Sources 279 (2015) 323–333.

[30] M.D. Stoller, R.S. Ruoff, Best practice methods for determining an electrode material's performance for ultracapacitors, Energy Environ. Sci. 3 (2010) 1294–1301.

[31] J.H. Chae, G.Z. Chen, Influences of ions and temperature on performance of carbon nano-particulates in supercapacitors with neutral aqueous electrolytes, Particuology 15 (2014) 9–17.

[32] H. Zhang, G.P. Cao, Y.S. Yang, Z.N. Gu, Capacitive performance of an ultralong aligned carbon nanotube electrode in an ionic liquid at 60 degrees C, Carbon 46 (2008) 30–34.

[33] M. Ue, M. Takeda, A. Toriumi, A. Kominato, R. Hagiwara, Y. Ito, Application of low-viscosity ionic liquid to the electrolyte of double-layer capacitors, J. Electrochem. Soc. 150 (2003) A499–A502.

[34] Q. Li, M. Haque, V. Kuzmenko, N. Ramani, P. Lundgren, A.D. Smith, P. Enoksson, Redox enhanced energy storage in an aqueous high-voltage electrochemical capacitor with a potassium bromide electrolyte, J. Power Sources 348 (2017) 219–228.

[35] J. Piwek, A. Platek, K. Fic, E. Frackowiak, Carbon-based electrochemical capacitors with acetate aqueous electrolytes, Electrochim. Acta 215 (2016) 179–186.

[36] S. Fendt, S. Padmanabhan, H.W. Blanch, J.M. Prausnitz, Viscosities of acetate or chloride-based ionic liquids and some of their mixtures with water or other common solvents, J. Chem. Eng. Data 56 (2010) 31–34.

[37] R. Costa, C.M. Pereira, F. Silva, Double layer in room temperature ionic liquids: influence of temperature and ionic size on the differential capacitance and electrocapillary curves, Phys. Chem. Chem. Phys. 12 (2010) 11125–11132.

[38] B. Gorska, L. Timperman, M. Anouti, F. Béguin, Effect of low water content in protic ionic liquid on ions electrosorption in porous carbon: application to electrochemical capacitors, Phys. Chem. Chem. Phys. 19 (2017) 11173–11186.

[39] K.L. Van Aken, J.K. McDonough, S. Li, G. Feng, S.M. Chathoth, E. Mamontov, P.F. Fulvio, P.T. Cummings, S. Dai, Y. Gogotsi, Effect of cation on diffusion coefficient of ionic liquids at onion-like carbon electrodes, J. Phys. Condens. Matter. 26 (2014) 284104.

[40] J.M. Woo, K.M. Yang, S.U. Kim, L.M. Blank, J.B. Park, High temperature stimulates acetic acid accumulation and enhances the growth inhibition and ethanol production by saccharomyces cerevisiae under fermenting conditions, Appl. Microbiol. Biotechnol. 98 (2014) 6085–6094.

[41] M. Brehm, H. Weber, A.S. Pensado, A. Stark, B. Kirchner, Proton transfer and polarity changes in ionic liquid-water mixtures: a perspective on hydrogen bonds from ab initio molecular dynamics at the example of 1-ethyl-3-methylimidazolium acetate-water mixtures–part 1, Phys. Chem. Chem. Phys. 14 (2012) 5030–5044.

[42] T.J. Meng, K.H. Young, D.F. Wong, J. Nei, Ionic liquid-based non-aqueous electrolytes for nickel/metal hydride batteries, Batteries 3 (2017) 4.

[43] J. Kang, J.Z. Wen, S.H. Jayaram, A.P. Yu, X.H. Wang, Development of an equivalent circuit model for electrochemical double layer capacitors (EDLCs) with distinct electrolytes, Electrochim. Acta 115 (2014) 587–598.

[44] H.D. Yoo, J.H. Jang, J.H. Ryu, Y. Park, S.M. Oh, Impedance analysis of porous carbon electrodes to predict rate capability of electric double-layer capacitors, J. Power Sources 267 (2014) 411–420.

[45] T. Bordjiba, M. Mohamedi, L.H. Dao, Synthesis and electrochemical capacitance of binderless nanocomposite electrodes formed by dispersion of carbon nanotubes and carbon aerogels, J. Power Sources 172 (2007) 991–998.

[46] B. Abdulhakeem, B. Farshad, M. Damilola, T. Fatemeh, F. Mopeli, D. Julien, M. Ncholu, Morphological characterization and impedance spectroscopy study of porous 3D carbons based on graphene foam-PVA/phenol-formaldehyde resin composite as an electrode material for supercapacitors, Rsc Adv. 4 (2014) 39066–39072.

[47] C. Masarapu, H.F. Zeng, K.H. Hung, B. Wei, Effect of temperature on the capacitance of carbon nanotube supercapacitors, ACS Nano 3 (2009) 2199–2206.

[48] J. Black, H.A. Andreas, Effects of charge redistribution on self-discharge of electrochemical capacitors, Electrochim. Acta 54 (2009) 3568–3574.

[49] J. Kowal, E. Avaroglu, F. Chamekh, A. S'enfelds, T. Thien, D. Wijaya, D.U. Sauer, Detailed analysis of the self-discharge of supercapacitors, J. Power Sources 196 (2011) 573–579.

[50] H.A. Andreas, Self-discharge in electrochemical capacitors: a perspective article, J. Electrochem. Soc. 162 (2015) A5047–A5053.

[51] C.Z. Yang, C.Y.V. Li, F.J. Li, K.Y. Chan, Complex impedance with transmission line model and complex capacitance analysis of ion transport and accumulation in hierarchical core-shell porous carbons, J. Electrochem. Soc. 160 (2013) H271–H278.

[52] J.H. Jang, S.M. Oh, Complex capacitance analysis of porous carbon electrodes for electric double-layer capacitors, J. Electrochem. Soc. 151 (2004) A571–A577.

[53] J. Yew, T. Saha, A. Thomas, Impact of temperature on the frequency domain dielectric spectroscopy for the diagnosis of power transformer insulation, in: IEEE Power Engineering Society General Meeting, Montreal, 2006, p. 7.

[54] P.L. Taberna, P. Simon, J.F. Fauvarque, Electrochemical characteristics and impedance spectroscopy studies of carbon-carbon supercapacitors, J. Electrochem. Soc. 150 (2003) A292–A300.

[55] E.I. Izgorodina, M. Forsyth, D.R. Macfarlane, On the components of the dielectric constants of ionic liquids: ionic polarization? Phys. Chem. Chem. Phys. 11 (2009) 2452–2458.

[56] D. Pech, M. Brunet, H. Durou, P. Huang, V. Mochalin, Y. Gogotsi, P.L. Taberna, P. Simon, Ultrahigh-power micrometre-sized supercapacitors based on onion-like carbon, Nat. Nanotechnol. 5 (2010) 651–654.

[57] R. Farma, M. Deraman, Awitdrus, I.A. Talib, R. Omar, J.G. Manjunatha, M.M. Ishak, N.H. Basri, B.N.M. Dolah, Physical and electrochemical properties of supercapacitor electrodes derived from carbon nanotube and biomass

carbon, Int. J. Electrochem. Sci. 8 (2013) 257–273.

[58] J.H. Jang, S. Yoon, B.H. Ka, Y.H. Jung, S.M. Oh, Complex capacitance analysis on leakage current appearing in electric double-layer capacitor carbon electrode, J. Electrochem. Soc. 152 (2005) A1418–A1422.

[59] B.W. Ricketts, C. Ton-That, Self-discharge of carbon-based supercapacitors with organic electrolytes, J. Power Sources 89 (2000) 64–69.

[60] Q. Zhang, J.P. Rong, D.S. Ma, B.Q. Wei, The governing self-discharge processes in activated carbon fabric-based supercapacitors with different organic electrolytes, Energy Environ. Sci. 4 (2011) 2152–2159.

[61] H. Rodriguez, G. Gurau, J.D. Holbrey, R.D. Rogers, Reaction of elemental chalcogens with imidazolium acetates to yield imidazole-2-chalcogenones: direct evidence for ionic liquids as proto-carbenes, Chem. Commun. 47 (2011) 3222–3224.

Supplementary information

Thermal Influence on the Electrochemical Behavior of a Supercapacitor Containing an Ionic Liquid Electrolyte

Mazharul Haque [a*], Qi Li [a], Anderson D. Smith [a], Volodymyr Kuzmenko [a], Elof Köhler [a], Per Lundgren [a], Peter Enoksson [a]

[a] Department of Microtechnology and Nanoscience, Chalmers University of Technology, Gothenburg 41296, Sweden

*E-mail: mhaque@chalmers.se

1. Material characterization

1.1 Surface area difference between AC powder and AC electrode pellet

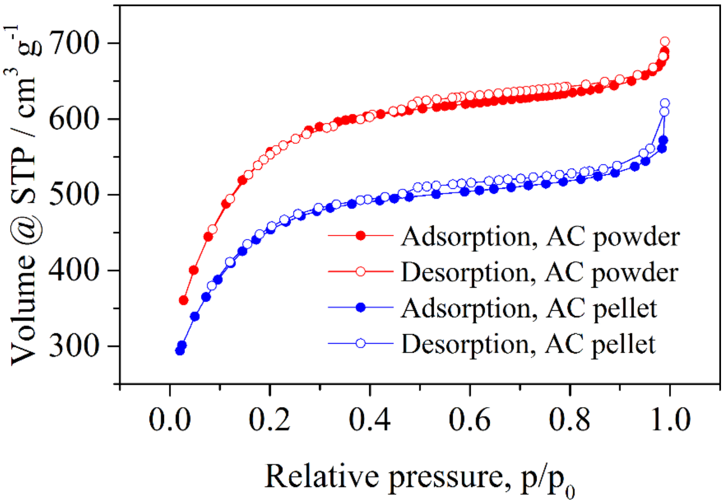

Fig. S1. Nitrogen adsorption and desorption isotherm of AC powder and AC electrode pellet

The nitrogen adsorption/desorption isotherm of AC powder and AC pellet is shown in Fig. S1. Both isotherms are a combination of type I and type IV curve, which suggests a good combination of micropores and mesopores are distributed in the materials. The calculated BET surface area is 2028 ± 24 m^{2}g^{-1} for AC powder and 1565 ± 30 m^{2}g^{-1} for the AC electrode pellet (80% YP-80F AC, 10% PTFE and 10% carbon black). A relatively lower surface area of the AC electrode pellet is reasonable due to the presence of binder [1]. The shape of the isotherms and the BET surface area are similar to those in a recent report [2], indicating a little difference in the material's properties.

1.2 Elemental composition of AC Powder

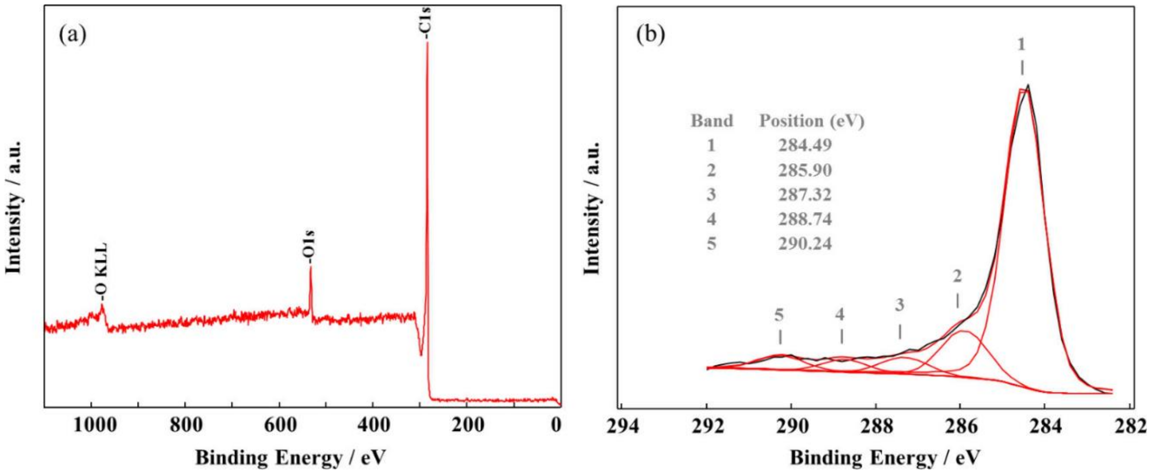

Fig. S2. Typical survey scan (a) and C 1s ESCA spectra (b) of AC powder

ESCA (electron spectroscopy for chemical analysis) spectra of AC is shown Fig. S2. Typical survey scan in Fig. S2 (a) shows that AC material contains 5.90 at.% oxygen along with 94.1 at.% carbon. Fig. S2 (b) shows the C 1s spectra of the AC material that can be resolved into 5 peaks with major C-C (graphitic carbon) peak in the lowest energy [3]. The other 4 bands are C-O (phenols and ethers), C=O (carbonyl groups), O-C=O (carboxyl groups, lactones) and minor shake-up satellite peaks due to π-π* transitions in aromatic rings [3-5]. The functional groups have good affinity to organic electrolytes, which could lead to good wettability. Besides, the presence of the mesopores also facilitates electrolyte penetration.

1.3 Surface morphology

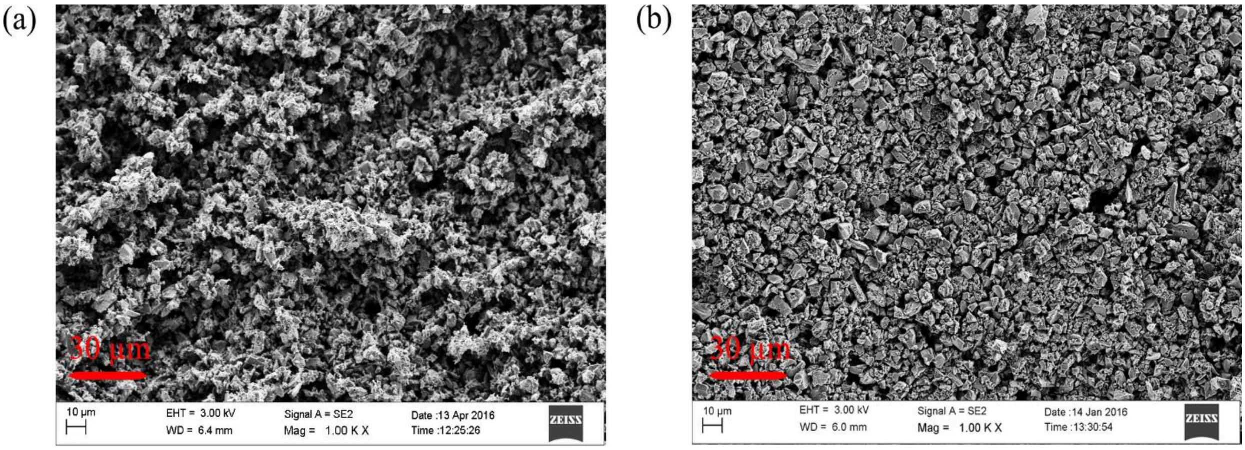

Fig. S3. SEM images of (a) AC powder and (b) AC electrode pellet

SEM image in Fig. S3 (a) shows the porous nature of the AC powder as expected. Moreover, the particles are homogeneously distributed in AC electrode pellet without any sign of agglomeration, Fig. S3 (b). The electrodes have a fairly smooth surface with the typical grain morphology expected of AC powder.

2. Thermal stability

TGA analysis of the pure EMIM Ac electrolyte and a mixture of electrolyte and AC electrode was conducted and shown in Fig. S4. The result reveals that the presence of water in both cases is around 10%. Both the samples show a similar two-step mass loss. The first step occurs below 200 °C and is attributed to the crystalline water desorption. The second step of mass loss, with its inflection point at 240 to 250 °C is due to thermal degradation of EMIM Ac.

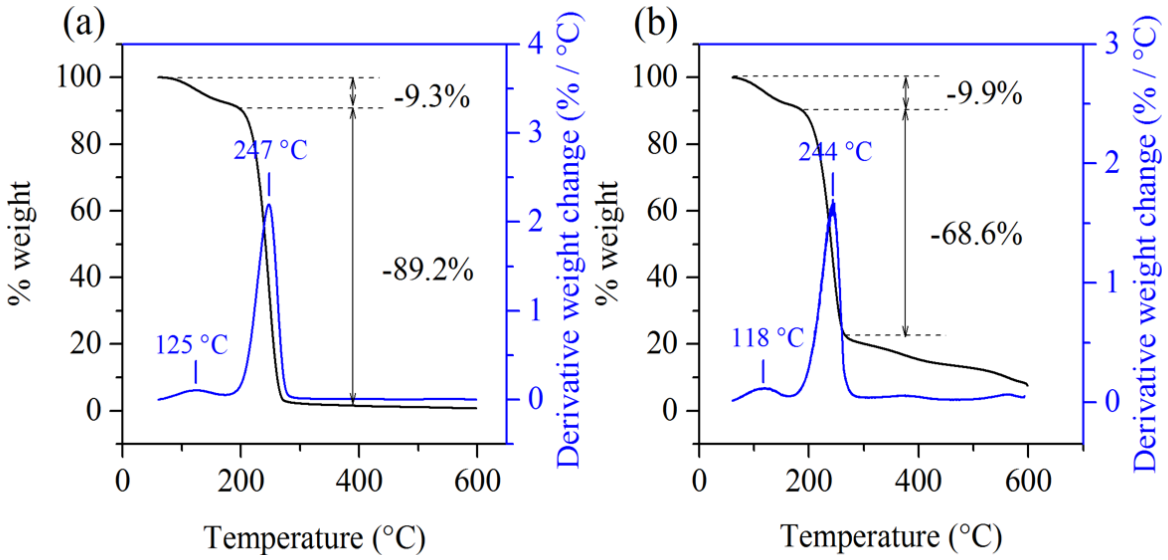

Fig. S4. TGA-thermal gravitograms and TGA-derivatograms of (a) EMIM Ac, and (b) mixture of EMIM Ac and AC electrode pellet

The maximum rate of weight change of crystalline water is similar, which is around 125 °C for pure EMIM Ac and 118 °C for the mixture of EMIM Ac and AC electrode, indicating that the most of the electrochemical performance variation should originate from the electrolyte.

There are two additional steps of mass loss that can be noticed in Fig. S4 (b): one is at 350 - 400 °C originating from the surface residues on the AC electrode and the one observed at 550 - 600 °C is due to the degradation of polytetrafluoroethylene (PTFE) that was used as a binder for the AC electrode material [6].

3. Cyclic charge discharge at 150 °C

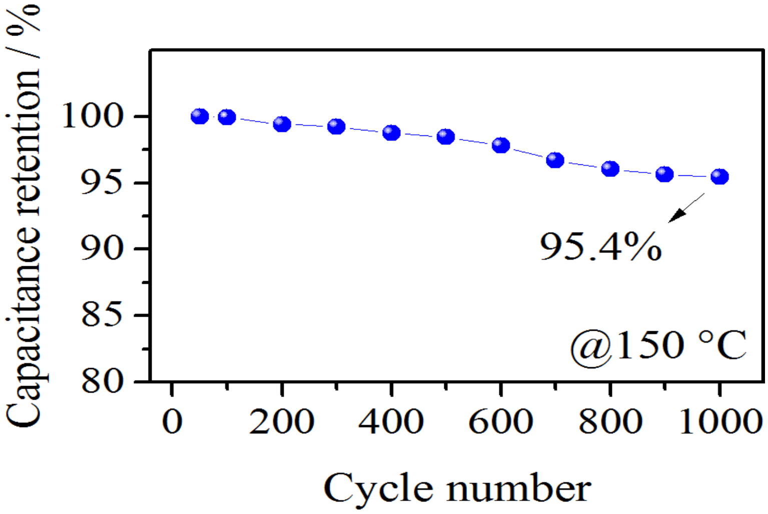

Fig. S5. Cyclic charge discharge for 1000 cycles at 1V prior to 1.3V

4. Ragone plot

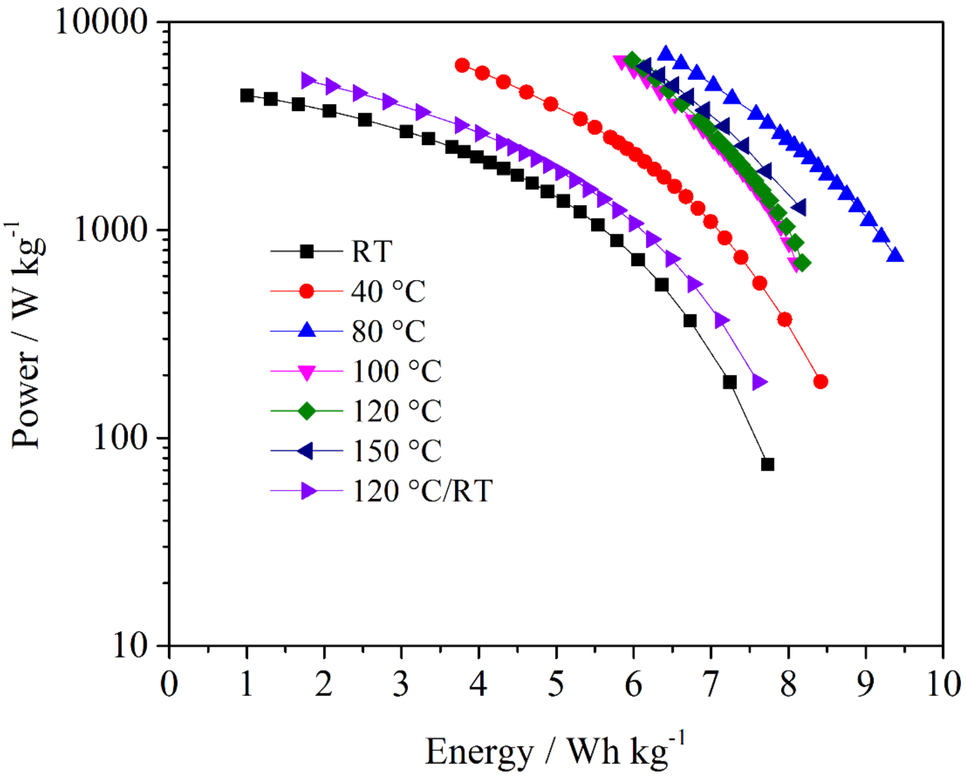

Fig. S6. Ragone plot (average power density vs energy density) at different temperature with different current density

Table S1. Performance metrics of ionic liquid-based supercapacitors with carbon electrodes

Electrolyte/ Electrode	Voltage (V) / Temperature (°C)	Specific capacitance (F g^{-1}) / CV(mV s^{-1}) or GCD (A g^{-1})	Energy density (Wh Kg^{-1})	Power density (kW Kg^{-1})	ESR (Ω)	Cyclic Stability (cycles) / Capacitance retention (%)	Rate capability (%)	Time constant (s)	Ref.
EmIm TFSA / AC	3/ RT	35 (0.1 A g^{-1})	-	-	-	-	-	-	[7]
BmIm TF$_6$ / AC	3/ RT	45 (0.1 A g^{-1})	-	-	-	-	-	-	[7]
EmIm BF$_4$ / AC	3/ RT	80 (0.1 A g^{-1})	6 [a]	-	-	500 / 50	-	-	[7]
PyrrNO3 (0.8) + PyrrTFSI / AC	2/ RT	148 (5 mV s^{-1})	-	-	-	Floating at 2 V for 110 h / >80	-	-	[8]
EMIBF$_4$ / ACNT	-1.5 to 1.5/ RT	23 (0.05 A g^{-1})		1.7 [b]	38.1	10000 /98		5	[9]
	-1.5 to 1.5/ 60	27 (0.05 A g^{-1})	2.1 [d]	4.3 [c]	16.4	10000 /97	50 [l]	2	[9]
BDMIM-TFSI / DWCNT	4/ 25	38.2 (100 mV s^{-1})	3 to 7	-	70 [e] to 75 [f]	2000 [i] / 70			[10]
BDMIM-TFSI / DWCNT-GON	4/ 25	43.1 (100 mV s^{-1})							
BDMIM-TFSI / DWCNT	4/ 100	43.9 (100 mV s^{-1})			11 [g] to 14 [h]				
BDMIM-TFSI / DWCNT-GON	4/ 100	47.6 (100 mV s^{-1})							
1, 2-dimethyl-3-propylimdazolium /AC	2.6/ 15	45 (0.002 mA)	-	-	12.1	-	61 [m]	-	[11]
	2.6/ 25	51 (0.002 mA)			7.37		54 [m]		
	2.6/ 40	57 (0.002 mA)			5.27		84 [m]		
DEME-BF$_4$/AC	2.5/ 25	25.4	-	-	-	500 [j] / 85	-	-	[12]
	2.5/ 40	25.5							
	2.5/ 70	25.7							
	2.5/ 100	23.7							
	2.5/ 130	21.3							
	2.5/ 150	17.5							
EMI-BF$_4$/AC	2.5/ 25	26.3	-	-	-	-	-	-	[12]
	2.5/ 40	26.6							
	2.5/ 70	23.9							

MPPipNTf$_2$/AC cloth	3.5/ RT	66	198 [q]	4.1	58	-	-	100	[13]
MPPyrNTf$_2$/AC cloth	3.5/ RT	69	215 [r]	7.9	30.2	-	-	63	[13]
EMImNTf$_2$/AC cloth	3.0/ RT	75	171 [s]	11.6	15.4	-	-	39	[13]
EMImBF$_4$/ AC cloth	3.0/ RT	87	196 [t]	30	6	-	-	15	[13]
[Me$_3$S] [TFSI] / AC	3.0/ 50	151 (347 mA g^{-1})	47.19	0.31	-	-	-	-	[14]
[Me$_3$S] [TFSI] / AC	3.0/ 80	141 (347 mA g^{-1})	44.10	0.32	-	-	78 [n]	-	[14]
EMIM Ac/ AC	1.5/ 80	122 (1 A g^{-1})	8.3 [u]	2.2 [w]	0.48 (Ω cm^2)	1000 [k] /97	82 [p]	1.2	This work
EMIM Ac/ AC	1.4/ 120	121 (1 A g^{-1})	7.4 [v]	2.0 [x]	0.44 (Ω cm^2)	1000 [k] /95	85 [p]	1	This work

[a, b, c, d] Recalculated for device

[e, f, g, h] Extrapolated from Nyquist plot

[i] Cycling stability test at a temperature of 60 °C at 1 mA cm^{-2} at 3 V

[j] Cycling stability test at a temperature of 100 °C at 15 mA at 2.5 V

[k] Cycling stability test at a temperature of 120 °C at 7 A g^{-1}

[l] Rate capability at 20 A g^{-1} relative to 0.05 A g^{-1}

[m] Rate capability at 0.016 mA relative to 0.002 mA

[n] Rate capability at 20 mV s^{-1} relative to 2 mV s^{-1}

[p] Rate capability at 7 A g^{-1} relative to 1 A g^{-1}

[q, r, s, t] Unit of energy density is kJ kg^{-1}

[u, v] Energy density at 3 A g^{-1}

[w, x] Average power density at 3 A g^{-1}

References

[1] J. Piwek, A. Platek, K. Fic, E. Frackowiak, Carbon-based electrochemical capacitors with acetate aqueous electrolytes, Electrochim. Acta 215 (2016) 179-186.
[2] M. Aslan, D. Weingarth, P. Herbeck-Engel, I. Grobelsek, V. Presser, Polyvinylpyrrolidone/polyvinyl butyral composite as a stable binder for castable supercapacitor electrodes in aqueous electrolytes, J. Power Sources 279 (2015) 323-333.
[3] S. Biniak, G. Szymański, J. Siedlewski, A. Światkowski, The characterization of activated carbons with oxygen and nitrogen surface groups, Carbon 35 (1997) 1799-1810.
[4] H.P. Boehm, Surface oxides on carbon and their analysis: a critical assessment, Carbon 40 (2002) 145-149.
[5] C. Moreno-Castilla, M. Lopez-Ramon, F. Carrasco-Marın, Changes in surface chemistry of activated carbons by wet oxidation, Carbon 38 (2000) 1995-2001.
[6] S. Aliasghari, P. Skeldon, G.E. Thompson, Plasma electrolytic oxidation of titanium in a phosphate/silicate electrolyte and tribological performance of the coatings, Appl. Surf. Sci. 316 (2014) 463-476.
[7] M. Karnan, K. Subramani, P. Srividhya, M. Sathish, Electrochemical studies on corncob derived activated porous carbon for supercapacitors application in aqueous and non-aqueous electrolytes, Electrochim. Acta 228 (2017) 586-596.
[8] L. Timperman, A. Vigeant, M. Anouti, Eutectic mixture of protic oonic liquids as an electrolyte for activated carbon-based supercapacitors, Electrochim. Acta 155 (2015) 164-173.
[9] H. Zhang, G.P. Cao, Y.S. Yang, Z.N. Gu, Capacitive performance of an ultralong aligned carbon nanotube electrode in an ionic liquid at 60 degrees C, Carbon 46 (2008) 30-34.
[10] R.S. Borges, H. Ribeiro, R.L. Lavall, G.G. Silva, Temperature stable supercapacitors based on ionic liquid and mixed functionalized carbon nanomaterials, J. Solid State Electrochem. 16 (2012) 3573-3580.
[11] S.I. Fletcher, F.B. Sillars, R.C. Carter, A.J. Cruden, M. Mirzaeian, N.E. Hudson, J.A. Parkinson, P.J. Hall, The effects of temperature on the performance of electrochemical double layer capacitors, J. Power Sources 195 (2010) 7484-7488.
[12] T. Sato, G. Masuda, K. Takagi, Electrochemical properties of novel ionic liquids for electric double layer capacitor applications, Electrochim. Acta 49 (2004) 3603-3611.
[13] A. Lewandowski, A. Olejniczak, M. Galinski, I. Stepniak, Performance of carbon-carbon supercapacitors based on organic, aqueous and ionic liquid electrolytes, J. Power Sources 195 (2010) 5814-5819.
[14] M. Anouti, L. Timperman, M. el Hilali, A. Boisset, H. Galiano, Sulfonium Bis(trifluorosulfonimide) plastic crystal ionic liquid as an electrolyte at elevated temperature for high-energy supercapacitors, J. Phys. Chem. C 116 (2012) 9412-9418.

PAPER III

Compact and low loss electrochemical capacitors using a graphite / carbon nanotube hybrid material for miniaturized systems

Qi Li[1][+], Shuangxi Sun[1, 2, 3][+], Anderson D. Smith[1], Per Lundgren[1], Yifeng Fu[1],

Peng Su[1], Tao Xu[4], Lilei Ye[5], Litao Sun[4], Johan Liu[1, 2*], Peter Enoksson[1*]

[1] Electronics Materials and Systems Laboratory, Department of Microtechnology and Nanoscience,
Chalmers University of Technology, SE - 412 96 Gothenburg, Sweden

[2] SMIT Center, School of Mechanical Engineering and Automation, Shanghai University, 201800
Shanghai, P. R. China

[3] Fingerprint Cards AB, Kungsgatan 20, SE - 411 19 Gothenburg, Sweden

[4] SEU-FEI Nano-Pico Center, Key Lab of MEMS of Ministry of Education, Southeast University, 210096
Nanjing, P. R. China

[5] SHT Smart High Tech AB, SE - 411 33 Gothenburg, Sweden

*Email: johan.liu@chalmers.se; peter.enoksson@chalmers.se

[+] These authors contributed equally

Abstract

With the establishment of the internet of things (IoT) and the rapid development of advanced microsystems, there is a growing demand to develop electrochemical capacitors (ECs) to replace bulky electrolytic capacitors on circuit boards for AC line filtering, and as a storage unit in energy autonomous systems. For this purpose, ECs must be capable of handling sufficiently high signal frequencies, display minimum energy loss through self-discharge and leakage current as well as maintaining an adequate capacitance. Here, we demonstrate ECs based on mechanically flexible, covalently bonded graphite / vertically aligned carbon nanotubes (graphite/VACNTs) hybrid materials. The ECs employing a KOH electrolyte exhibit a phase angle of -84.82º, an areal capacitance of 1.38 mF cm^{-2} and a volumetric capacitance (device level) of 345 mF cm^{-3} at 120 Hz, which is among the highest values for carbon based high frequency ECs. Additionally, the performance as a storage EC for miniaturized systems is evaluated. We demonstrate capacitive charging/discharging at µA current with a gel electrolyte, and sub-µA leakage current reached within 50 seconds, and 100 nA level stabilized leakage within 100 seconds at 2.0 V floating with an ionic liquid electrolyte.

Keywords

Supercapacitors; hybrid material; AC line filter; energy storage; internet of things

1. Introduction

Electrochemical capacitors (ECs, also known as supercapacitors or ultracapacitors) are well acknowledged for being capable of rapid energy uptake and delivery, and almost limitless cycle life [1]. ECs have now been widely used in macro-scale systems [2]. For example, in uninterruptible power supply (UPS) systems, ECs smooth out the energy demand on batteries whose lifetime can thus be extended [3]; in combustion engine and hybrid vehicles, ECs constitute start-stop modules that start the vehicle with high efficiency. With the establishment of the internet of things (IoT) concept and the rapid development of advanced micro-scale systems, the market of EC technology is expanding to alternating current (AC) line-filters and storage components in energy autonomous devices.

In the line-filter regime, the use of EC facilitates compact circuit design. Nowadays, aluminum electrolytic capacitors (AECs) are the primary component for ripple / noise filtering and decoupling on circuit boards. However, AECs usually are among the largest components found in any electronic circuit [4]. The bulky feature of AECs limits their applications in miniaturized systems such as portable electronics and wireless sensor networks. Since carbon based ECs have significantly higher storage capacity, they are promising candidates to replace low-voltage AECs for circuit board downscaling. For this purpose, the ECs must have an adequate frequency response: at an application-specified frequency, the phase angle should be as close to -90° as possible. In terms of 60 Hz AC line power in the United States, the critical frequency is 120 Hz and the phase angle at 120 Hz is usually a metric to be compared in the research community. Similarly, for 50 Hz AC line power in Europe and other parts of the worlds, 100 Hz is the critical frequency for examining the filter performance.

In the energy autonomous systems regime, EC is well suited as an energy storage component. The use of ECs simplifies the circuitry design compared to lithium batteries due to the compatibility with the trickle charging mode [5], and more importantly, ECs have merits of high energy efficiency (charge to discharge energy), almost infinite recharge cycles, withstanding deep discharge and operability in a wide temperature range. The challenge is, while maintaining the merits above, to achieve sufficient energy storage capacity, minimal loss through self-discharge / leakage current and good capacitive response at *low* current input [6, 7]. Researchers claim that the energy storage EC should also respond to high frequencies in order to efficiently store scavenged pulse electricity from an energy harvester or nanogenerator [8].

The two application areas described above require the development of ECs whose performance are characterized by high cut-off frequency (kHz) and/or low self-discharge / leakage current (μA) with at least moderate capacitance (mF). The research on high frequency ECs in recent years has propelled progress in understanding some key design factors for such devices. For a high cut-off frequency, porous electrodes, e.g. activated carbon, are normally less preferable due to non-uniformity in pore size and wall chemistry, thereby leading to asynchronous charging and poor frequency response. Reducing porosity enables synchronous charging, diminishes the distribution of RC time constants, and as a result, the cut-off frequency is improved. S. Fletcher et al. [9] proved that synchronous charging minimizes self-discharge as well, corresponding to a reduced leakage current. Low electronic resistance and low ionic resistance are also keys to a fast response. The electronic resistance originates from electron transport inside the electrode material and across the electrode/collector interface, while ionic resistance arises from the transport of charged species in the bulk electrolyte and inside the pore structure. Taking all these into account, one should accordingly consider binder-free high surface area materials with less porosity and high conductivity.

Graphene is a compelling material that has extremely high electronic conductivity and a pore-less structure which are favored features for high frequency and low loss ECs. The monolayer or few-layer graphene based devices have shown good frequency response [10], but the extremely low mass loading severely limits the energy content (per footprint) of such devices (a basal plane produces only 3 $\mu F\ cm^{-2}$, estimated from a polished graphite electrode in NaF electrolyte [11]; 21 $\mu F\ cm^{-2}$ for a 0.3 nm thick graphene layer in BMIM PF_6 electrolyte [11]). The low areal capacitance is generally a common concern for many nm-layer devices: Although high volumetrics based on the ultrathin layer device can be calculated, the true performance when scaling up to achieve a desired areal device capacitance may not be the same as ultrathin layer devices [12]. Vertically aligned graphene sheets [4] enable the utilization of edge planes which have a greater capacitance of 50 to 70 μF cm^{-2} [11], and therefore a decent capacitance of 0.4 mF cm^{-2} at 0.01 Hz was achieved, though the capacitance is still less than 0.2 mF cm^{-2} at 120 Hz.

CNTs are another promising material for constructing ECs for microsystems due to high electronic conductivity and reasonable surface area for high capacitance [13-15]. For AC line filtering purpose, CNT based ECs fabricated by solution processes have a slow frequency response if the CNT film is thick, due to the high interfacial resistance from CNT-CNT and CNT-substrate interfaces. Reducing the CNT film thickness to nm scale, a cut-off frequency of nearly 16 kHz was obtained, while as pointed out, the limitation is a low areal capacitance (58 μF cm^{-2}) [14]. By increasing the film thickness and mass loading to a proper extent, a higher capacitance can be obtained with certain compromise in frequency response. For instance, a 0.28 mF cm^{-2} EC with 1995 Hz cut-off frequency was demonstrated for a 298 nm thick CNT film on gold coated Al foil with a vacuum filtration method [14], and a 0.6 mF cm^{-2} device with 1425 Hz cut-off frequency was fabricated with CNT film pressed on gold-coated roughened stainless steel rods [13]. In both cases, a gold-coated current collector is a prerequisite to further minimize the contact resistance for good high frequency response. Compared with solution-based methods, vertically aligned CNTs (VACNTs) grown by CVD methods have an advantage in lower interfacial contact resistance because of orientation order. Theoretically, only a small ohmic resistance exists between the grown CNTs and the substrate [16]. Successful growth on Al substrates has been demonstrated (Al foil [17] or Al underlayer [18]) which unfortunately limits the choice of electrolyte in practical applications [19].

A hybrid structure of graphene/VACNTs potentially solve the problems associated with their constituting material components. Integrating VACNTs with graphene could increase the areal capacitance of the latter, and graphene as the substrate for VACNTs could be a solution to replace metal layers. The hybrid formation mechanism is preferred to be chemical bonding rather than a mere physical mixture, in order to reduce the contact resistance. For example, a hybrid structure between graphene and VACNTs was investigated by Tour's group [16], and a microsupercapacitor (on a rigid Si substrate) based on this hybrid material was demonstrated [20] exhibiting 1343 Hz cut-off frequency, -81.5° phase angle, 0.23 mF cm^{-2} capacitance at 120 Hz for a 10 μm VACNTs device, and a slower self-discharge rate compared to a rGO device [21]. The performance is encouraging but the graphene/VACNTs hybrid material still requires chemically active copper or nickel metal underlayers for growing single layer graphene. Moreover, the areal capacitance could be further enhanced.

The progress in high frequency carbon based EC development is substantial since the first report in 2010 [4], nevertheless, there is still room for developing more compact devices for AC line filters and low loss energy storage units in miniaturized systems. Towards this goal, we investigated ECs based on a graphite/VACNTs hybrid material. Graphite was selected in this study as substrate with the aim to eliminate the need for growing fragile single layer graphene on metal substrates, at no sacrifice in performance. Therefore, it is an easy, relatively cheap and scalable fabrication method, and the graphite/VACNTs material is likely to be compatible with a wide variety of electrolytes. With 6 M KOH (an electrolyte to exploit the highest capacitive performance of carbon, but it corrodes Al, Cu and potentially Ni), the EC exhibits a very good high frequency response showing -84.82° phase angle, 1.38 mF cm^{-2} areal capacitance and a device level volumetric capacitance of 345 mF cm^{-3} at 120 Hz, which is among the best values reported for carbon-based high frequency ECs. The graphite/VACNTs hybrid is a freestanding material, thus the obtained device has an excellent form factor for a wide range of applications in micro systems. Moreover, the material has outstanding heat dissipation performance, which is beneficial for high current and voltage line filtering. As an energy storage unit, ECs based on the graphite/VACNTs with a gel electrolyte could exhibit capacitive behavior at μA working current, and with an ionic liquid electrolyte the device has a minimum energy loss through leakage current since the stabilization to 100 nA level leakage at 2.0 V is fairly quick. The evaluations validate that the graphite/VACNTs hybrid is a promising material to construct application specified ECs for miniaturized systems.

2. Experimental

Materials fabrication: The graphite film was supplied by Panasonic Co. The surface of this graphite film was prepared for VACNTs growth by deposition of a 2 nm Fe film. On top of that, a 3 nm thick layer of Al_2O_3 was deposited in situ by electron-beam evaporation. Here, the Fe serves as a catalyst for VACNT growth while the Al_2O_3 layer serves to facilitate the formation of tip grown VACNTs [22]. A VACNT array was synthesized on the surface of the graphite film through chemical vapor deposition (CVD). After loading the film, the chamber was pumped down to below 0.1 mbar before an 837 sccm flow of H_2 was introduced. Thereafter, the substrate heater was ramped up to 500 °C at a rate of 300 °C min^{-1}, and when this intermediate temperature was reached, the heater was maintained at this temperature for 3 minutes for reducing the catalyst [23]. The heater temperature was then rapidly increased to 720 °C, while the carbon feedstock acetylene at a rate of 240 sccm was introduced into the chamber for 5 minutes, allowing the VACNT array to grow from the surface of the graphite film. Since the process is a tip-growth process, the Fe catalyst and the 3 nm Al_2O_3 layer are separated from the surface of the film during growth ending up at the top of the VACNT array (Figure S1). An Ar plasma treatment was performed at 100 W for 30 seconds, and a freestanding hybrid film was obtained.

Materials characterization: A scanning electron microscope (SEM, Zeiss Supra 60 VP) was employed to characterize the morphology of the graphite/VACNTs hybrid material. In order to verify the bonding between the graphite and the VACNTs, (scanning) transmission electron microscope (TEM/STEM, FEI Technai G20/Titan) characterization was carried out. XPS measurements were conducted on PHI 5000 Versa Probe system equipped with a monochromatic Al Kα X-ray source. The charging shift was calibrated using the C_{1s} photoemission line at binding energy 284.8 eV. For Raman measurements, confocal Raman equipment (XploRA™, manufactured by Horiba Scientific) with a 638 nm laser was employed. The contact angle was evaluated using the sessile droplet technique (4 µm droplet volume) with the Attension Theta contact angle meter.

Electrochemical measurements: Three types of ECs with different electrolytes were fabricated and measured. First, the VACNT array grown on the graphite film was used as the electrode, a glass fiber membrane as the separator and 6 M KOH as the electrolyte. Another type of EC was constructed with a gel PVA/H_3PO_4 electrolyte for the demonstration of electrochemical performance. The device was vacuum dried at 80 °C for 2 hours and then the edges were encapsulated with Kapton® film. For the comparison of self-discharge, an additional glass fiber membrane was used for the PVA/H_3PO_4 device to keep the same configuration as for the KOH device. Before encapsulated in the two-electrode setup (Swagelok® cell), the device was also vacuum dried at 80 °C for 2 hours. The third type of EC was fabricated in the same way as the KOH device, but using a neat ionic liquid EMIM TFSI (1-Ethyl-3-methylimidazolium bis(trifluoromethylsulfonyl)imide) electrolyte.

The electrochemical measurements were performed on Gamry Reference 3000 AE. The areal capacitance C_A was calculated from the GCD curves using the following equation:

$$C_A = \frac{I_d \cdot t}{A \cdot \Delta V} \tag{1}$$

where I_d is the discharge current, t is discharge time, A is the area of the device (i.e. the area of one electrode) and ΔV is the voltage window excluding the IR drop. The AC impedance characterization was carried out in the frequency range 0.01 Hz to 100 kHz. The frequency response of the real (C') and imaginary parts (C'') of supercapacitance [22] can be calculated according to the following equations:

$$C'(f) = \frac{-Z''(f)}{2\pi f A|Z(f)|^2} \tag{2}$$

$$C''(f) = \frac{Z'(f)}{2\pi f A|Z(f)|^2} \tag{3}$$

where f is the frequency, $Z'(f)$ and $Z''(f)$ are real and imaginary parts of the impedance; $|Z(f)|$ is the absolute value of the impedance.

3. Results and discussion

3.1. Material characterization

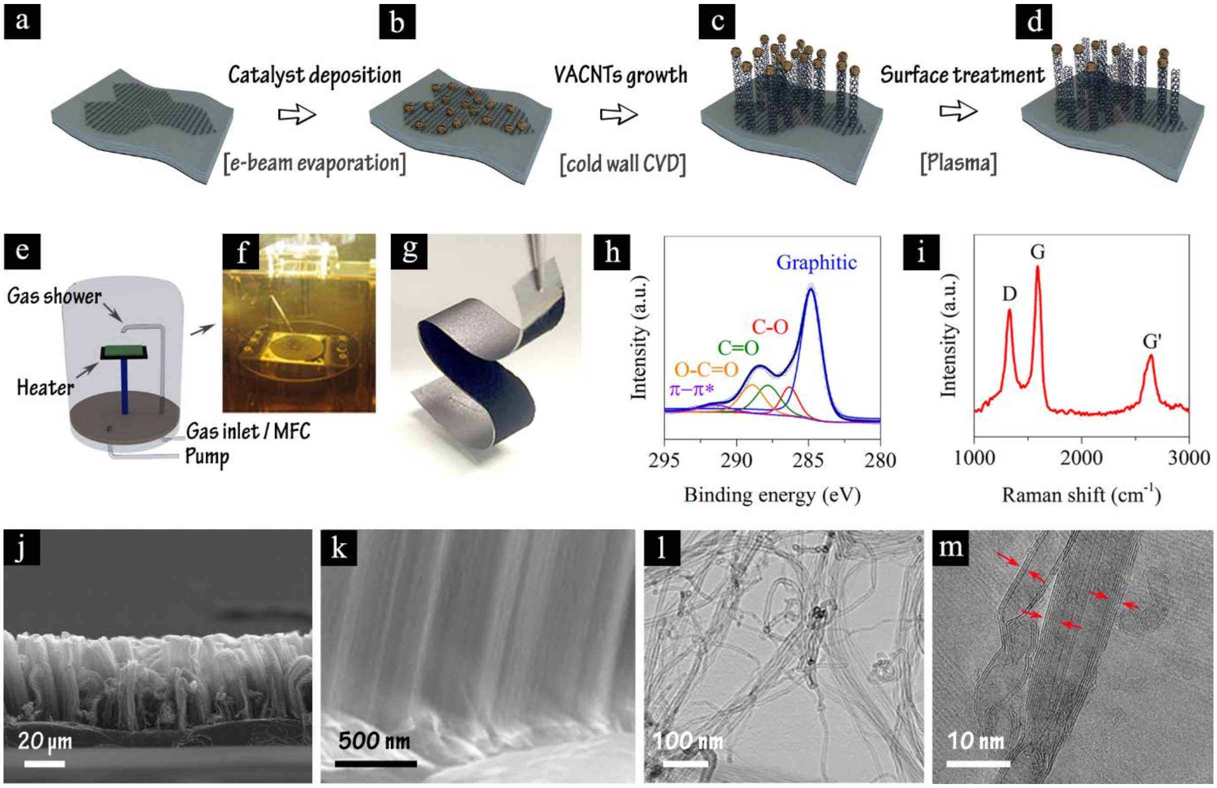

Figure 1. a - d) Schematic diagram presenting the fabrication procedure for the graphite/VACNTs hybrid material. e - f) Schematic diagram and optical picture of the cold-wall CVD reactor. g) Demonstration of material flexibility. h) Raman spectrum of the graphite/VACNTs hybrid material. i) C_{1s} core level spectrum of the graphite/VACNTs hybrid material in cross-section. j-k) SEM images. l-m) TEM images of the graphite/VACNTs hybrid.

The fabrication process of the graphite/VACNTs composite is shown in Figure 1a-d. A freestanding highly oriented pyrolytic graphite film (Figure 1a) supplied by Panasonic co. was used as the supporting substrate for VACNT growth. A catalyst layer of 2 nm Fe and 3 nm Al_2O_3 was successively deposited on the graphite film surface by e-beam evaporation (Figure 1b). The design of the catalyst layer sequence results in tip-growth of VACNTs, which is essential to achieve low equivalent series resistance (ESR) for the EC device. For the tip-growth method, the catalyst particles reside on the top of tip-grown VACNTs thus enabling the direct contact between VACNTs and the substrate [23]. After catalyst evaporation, the graphite film substrate was placed onto a graphite heater in a cold-wall CVD chamber (Figure 1e-f) for VACNTs growth under 720 °C with acetylene as carbon source. Afterwards the material was treated by a mild Ar plasma (Figure 1d). The plasma treatment could partially eliminate the evaporated metal layers [24]. Moreover, this step introduces surface functional groups and therefore leads to a hydrophilic surface. The C_{1s} core level of the surface treated material constitutes more significant signals at a high binding energy, compared to the pristine sample (Figure S2). The high resolution C_{1s} XPS spectrum of the final product is displayed in Figure 1h. Except the main band at 284.8 eV which is assigned to sp^2 graphitic carbon [25-27] and a minor band at 291.5 eV from π-π* shake-up [26, 28, 29], the deconvoluted spectrum (Table S1) consists of the other 3 bands at around 286.3 eV, 287.8 eV and 288.9 eV originating from C-O (e.g. in ether), C=O (e.g. in ketone and quinone) and O-C=O (e.g. in ester) functional groups [26-30]. The atomic concentration ratio of oxygen to carbon content at the surface increased significantly from 5:1 to 99:1 after the plasma treatment (Figure S2). The increased oxygen-containing groups render a hydrophilic surface with a contact angle to H_2O decreases from 139.8° to 43.0° (Figure S2b and S2d). The hydrophilic surface is believed to be beneficial when deploying an aqueous electrolyte for electrochemical capacitors.

The Raman spectrum of the graphite/VACNTs material with G, D and G' band signals is shown in Figure 1i. The G band at around 1575 cm^{-1} is attributed to the longitudinal optical phonons / stretching of the C-C atoms in sp^2 hybridized carbon samples, the D band is related to sp^3 hybridization and is a disorder induced vibration mode, and G' is regarded as the second order Raman overtones [31, 32]. The D-/G-band intensity ratio is an indicator to quantitatively determine the degree of graphitization or defect concentrations [31-36]. The ratio is around 0.7 for the material after plasma treatment (Figure S3c); the initial value was approximately 0.45 indicating that the graphitization decreased and/or defect sites (sp^3-hybridization) increased after plasma treatment, possibly because C-O, C=O and O-C=O functional groups (Figure 1h) may have covalently bonded to the nanotube framework. The increased D-/G-band intensity ratio after plasma treatment was also observed previously [34, 37] and considered as evidence of sidewall functionalization induced by defect sites from argon bombardment of the CNT surface.

The electron microscope images of the mechanically flexible graphite/VACNTs material (Figure 1g) are shown in Figure 1j-m. Uniform VACNT mats were grown on the graphite film, and VACNTs still keep aligned with each other at a height of 40-50 µm (Figure 1j). In order to clearly visualize the interface between VACNTs and the graphite film, the root region of the samples were studied (Figure 1k) which suggests that the VACNTs were grown directly from the graphite substrate at a perpendicular angle with no clear interfacial layer in between (the Fe/Al_2O_3 layer resides at the tip, Figure S1). The structure of individual CNTs were further examined. The grown VACNTs are multi-wall CNTs with diameters ranging from 5 to 20 nm (Figure 1l-m). In addition, the bonding structure between the VACNTs and the graphite substrate was investigated (Figure S4). Ring-like features were observed which resembles those reported by Y. Zhu et al. [16] as indicative of covalent bonding between a graphene substrate and VACNTs.

3.2 High frequency ECs

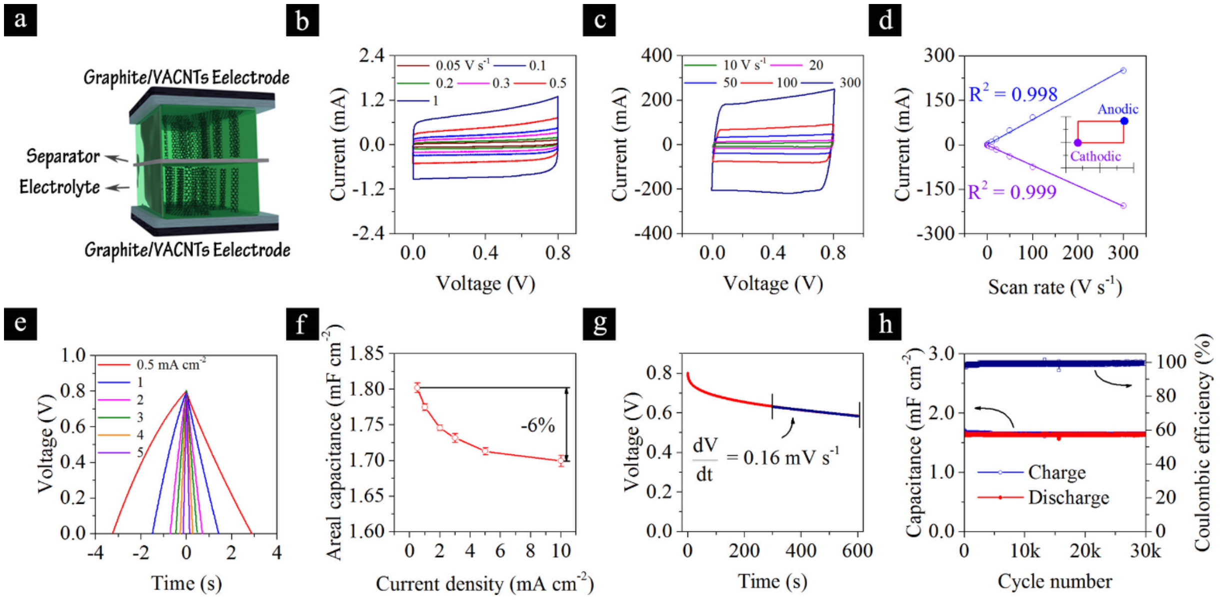

Figure 2. a) Schematic presentation of the EC structure. b – c) Cyclic voltammetry at specified scan rates. d) Anodic and cathodic currents as a function of scan rates. e) Galvanostatic charge/discharge curves at specified current densities. f) Areal capacitance as a function of current density. g) Self-discharge curve. h) Cycling stability at a current density of 2 mA cm^{-2}.

An EC device was constructed by stacking two graphite/VACNTs layers (of approximately equivalent dimension) with a glass fiber separator wetted by 6 M KOH electrolyte (Figure 2a). The cyclic voltammogram (CV) was obtained by varying the scan rates in a large range from 0.05 V s^{-1} up to 300 V s^{-1} in a voltage window of 0.8 V (Figure 2b-c). At all scan rates, the CV curves remain quasi-rectangular in shape which is expected for double layer behavior [1]. For a quantitative validation of the capacitive performance, the cathodic and anodic current response as a function of scan rate is plotted and linearly fitted (Figure 2d). The linear relationship remains up to an ultra-fast scan rate of at least 300 V s^{-1}, which is three orders of magnitude higher than those of conventional ECs [38].

Galvanostatic charge/discharge (GCD) measurements (Figure 2e) were conducted at current densities from 0.5 to 5 mA cm^{-2} (current densities lower than 0.5 mA cm^{-2} result in strong deviation from capacitive behavior, and currents higher than 5 mA cm^{-2} result in milisecond charge/discharge times). The maximum capacitance is approximately 1.8 mF cm^{-2} at the lowest current density (0.5 mA cm^{-2}). The capacitance is well retained with only a 6% loss when the current is increased by 10 times, demonstrating a good rate capability (Figure 2f).

The self-discharge behavior of ECs is a metric of major practical significance in their operation and the types of functions they may be required to fulfil [39]. Self-discharge is caused by leakage currents that leads to voltage decay of a charged EC over time. Figure 2g displays the self-discharge curve of the graphite/VACNTs based EC recorded after pre-charging the device to 0.8 V with a current of 0.5 mA cm^{-2} and constant voltage charging for only 5 minutes (for the interest of practical applications where fast charging/discharging switch are of immense importance [40]). The voltage decays to 0.63 V in the first 5 minutes and further to 0.58 V in the next 5 minutes. The segment from 5 to 10 minutes is linearly fitted and the rate of voltage change (slope of the fitted line) is about 0.16 mV s^{-1}. The average leakage current can be calculated by multiplying dV/dt by capacitance. For example, the leakage current is 1.6 µA after 5 minutes for a 10 mF device. The µA level leakage enhances the energy storage efficiency for miniaturized self-powered systems [40].

Cycle life is also an important criterion for ECs targeting IoT applications - the device will be charged and discharged 120 times/s for 120 Hz line filtering. As shown in Figure 2h, a satisfactory stability is evidenced by nearly zero capacitance loss over 30000 cycles of repeating charge/discharge (capacitance retention 99.8%).

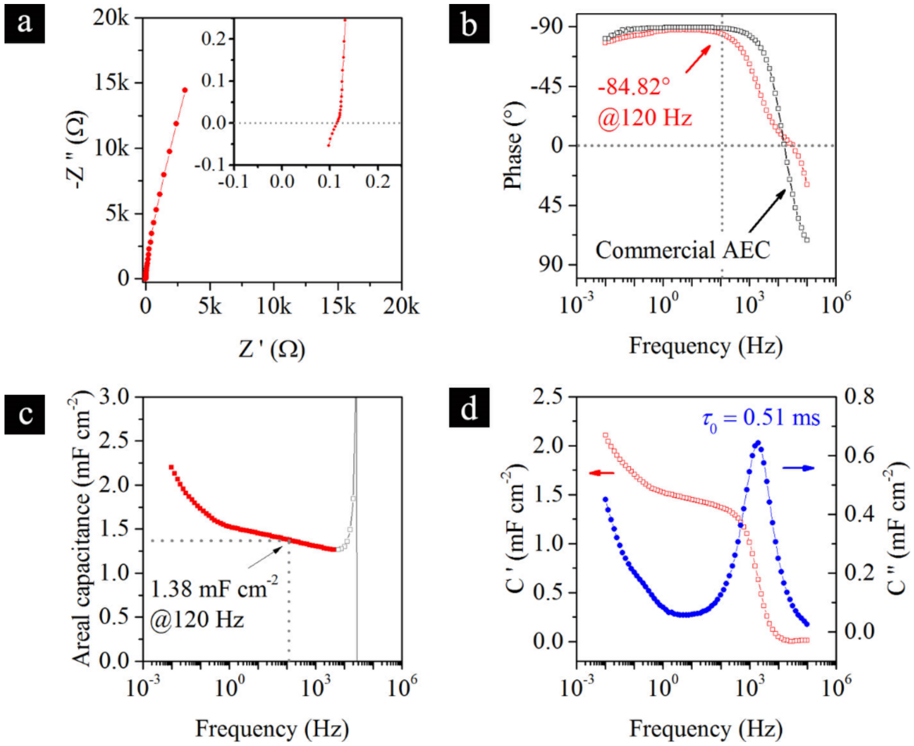

Figure 3. a) Nyquist plot of graphite/VACNTs based EC with 6 M KOH electrolyte. b) Impedance phase angle versus frequency. c) Areal capacitance versus frequency. d) C' and C'' versus frequency

To examine the frequency response, electrochemical impedance spectroscopy (EIS) was performed, and the data is presented in different forms (Figure 3). A Nyquist plot (Figure 3a) can be used to identify different kinetic processes in an electrochemical system. For porous carbon based ECs, the porous nature leads to asynchronous charging (adsorption of ions) and a 45° line intersecting the real axis of the complex-plane. The absence of the 45° line indicates almost no porous structure existing in the present system. Therefore, the charging process proceeds in a synchronous manner that is beneficial for high power capability and high frequency response. The impedance phase angle remains close to -90° within a fairly wide frequency range and drops rapidly to lower angles through one frequency decade (Figure 3b), indicating the transition from capacitive to resistive behavior. Of particular interest, the phase angle at 120 Hz is regarded as an important metric for AC-line filter ECs. The 120 Hz angle is as high as -84.82°, comparable to that of a commercial AEC (-88°). The cut-off frequency, i.e. the frequency at -45° phase where resistance and reactance have equal magnitudes, is approximately 2 kHz (1980 Hz). The impedance plot can be fitted with a series-RC model in which the resistance, *R*, is the real part of the impedance, Z', and areal capacitance, *C*, as a function of frequency (Figure 3c) is calculated as

$$C = \frac{-1}{2\pi f A Z''} \tag{4}$$

where *f* is frequency in Hz, *A* is the area of the device (i.e. the area of one electrode) in cm^2 and Z'' is the imaginary part of the impedance. In Figure 3c, the upturn behavior above 5000 Hz should be ignored because it is an artifact of the RC model (where Z'' passes through zero) [4]. According to the calculation, the capacitance could reach 2.25 mF cm^{-2} at an extremely low frequency (0.01 Hz) and decreases with increasing frequency. The high capacitance at 0.01 Hz could originate from VACNTs defects or catalyst residuals that lead to Faradaic energy contributions, and this value is unrealistic for high frequency applications. Nevertheless, 1.38 mF cm^{-2} is retained at 120 Hz and still 1.28 mF cm^{-2} at the cut-off frequency 1980 Hz. For the device prototype with 0.5 cm^2 footprint for the impedance measurement, the resistance at 120 Hz is measured to be only 0.13 Ω and the absolute capacitance is 0.69 mF, yielding an RC time constant

τ_{RC} of approx. 90 µs which is the lowest time constant among other reported devices [4, 13, 14, 20, 41-43]. High capacitance and short RC time constant are beneficial for high quality high voltage/current filtering. As a storage EC in energy autonomous systems, a smaller τ_{RC} also indicates the EC could be programmed for charging/discharging during shorter periods of time, which corresponds to high duty-cycle and thus e.g. high reliability of sensing [5].

The real (C') and imaginary parts (C'') of the "supercapacitance" (an admittance parameter [22]) are also extracted and displayed in Figure 3d. The relaxation time, τ_0, could be identified by the peak frequency of the plot of C'', which gives a τ_0 of 0.51 ms (reciprocal of cut-off frequency f_0), which is close to that of typical AECs and substantially smaller than most of ECs. The normalized performance metrics (areal capacitance $C_{\mathrm{A,\ 120Hz}}$ is normalized to the area of one electrode, volumetric capacitance $C_{\mathrm{V\text{-}e,\ 120\ Hz}}$ is normalized to the volume of active electrode materials and $C_{\mathrm{V\text{-}d,\ 120\ Hz}}$ is normalized to the volume of device, i.e. two electrodes including current collector) are compared with recent high frequency ECs in Table 1. The device based on graphite/VACNTs in this work is superior to many devices of its kind, especially in terms of areal and volumetric capacitances at a device level. Compared to previously reported CNTs based ECs [13-15, 18, 20, 44], the graphite/VACNTs device exhibited the highest areal capacitance while simultaneously maintaining a sufficiently fast frequency response even with approximately 40 µm long CNTs on a flexible substrate. Specifically, we observed a quasi linear increase of $C_{\mathrm{A,\ 120Hz}}$ as a function of CNT length, with fairly little changes in metrics of f_0 (Table S2). This is distinct from previous reports that frequency response decreases significantly when electrode thickness increases [8, 14, 18, 20]. The excellent performance of the device excludes having far from optimal electrical contact between its constituting components [13, 14], further supporting the suggestion of having obtained a covalent bonding structure between the graphite substrate and the VACNTs on top (Figure S4). Moreover, the choice of graphite substrate is found to play a key role in the resulted material structure and performance (Figure S5) – only with highly oriented graphite film can high frequency EC be obtained.

Table 1. Performance metrics comparison

Material	Electrolyte, Voltage	t_e a) (µm)	t_d b) (µm)	$\varphi_{\mathrm{120\ Hz}}$ (°)	f_0 (Hz)	τ_0 (ms)	$C_{\mathrm{A,\ 120\ Hz}}$ (mF cm^{-2})	$C_{\mathrm{V\text{-}e,\ 120\ Hz}}$ c) (mF cm^{-3})	$C_{\mathrm{V\text{-}d,\ 120\ Hz}}$ c) (mF cm^{-3})	Ref.
VACNTs on graphite	**KOH, 0.8 V**	**20** d)	**40** d)	**-84.82**	**1980**	**0.51**	**1.38**	**690**	**345**	**This work**
SWCNTs	H_2SO_4, 1.0 V	0.46 c)	-	-81	1425	0.7	0.601	13065	-	[13]
SWCNTs	TEA BF_4, 2.5 V	0.596	40.676	-82.2	1995	0.501	0.282	4732	69.3	[14]
Graphitic carbon / CNTs	TEA BF_4, 2.5 V	1.36	41.44	-80.3	1000	1	0.3	3947	72.4	[44]
Carbon nanofiber	KOH, 0.9 V	120	-	81 c)	1300	0.77 c)	2.25	187.5	-	[8]
VOGN e)	KOH, 1 V	1.2	72	-82	15000	0.06	0.175	1458	24.3	[4]
VOGN e)	KOH, 0.9 V	20	-	-83	10000	0.1	0.3	150	-	[43]
VOGN e)	KOH, 0.9 V	-	400	-82	4000	0.248	0.36	-	7.5	[45]
VOGN e)	KOH, -	-	154	-85	6300	0.16 c)	0.265	-	17.2	[46]
Holey graphene	KOH, 0.8 V	4	-	-81.2	1220	0.819	0.478	1200	-	[42]
rGO	KOH, 0.8 V	40.4	440.4	-84	4167 c)	0.24	0.283	70	6.4	[47]
Ketjen black	TEA BF_4, 2.8 V	1.56	41.64	-79.8	1000	1	0.574	3679	137.8	[41]

a) t_e – thickness of active material of both electrodes. b) t_d – thickness of both electrodes including current collectors. c) Estimated/inferred from presented data. d) After compression. e) VOGN stands for vertically oriented graphene nanosheets.

One major disadvantage of the current prototype EC is the small voltage window of the aqueous electrolyte, KOH, which could be a limitation to practical applications - especially for line filtering. However, this disadvantage can be mitigated by a bipolar design to increase the cell voltage while still maintaining an advantage in form factor [4, 48]. The thickness of the pristine active electrode material is about 60 µm (graphite substrate + VACNTs), but the thickness is greatly decreased when assembled in the stacked device since VACNTs are compressed and bend towards the substrate (Figure S6). The thickness is roughly 20 µm for a graphite/VACNTs film retrieved from a tested device. And further thickness reduction could be achieved by mechanically thinning down the graphite substrate with a thermal release tape technique. For a stacked device that comprises of two electrodes, 10 µm separator and twice the materials volume for packaging (parylene), the volumetric capacitance of the graphite/VACNTs EC *device* is on the order of 136 mF cm^{-3} (calculated by using the capacitance value at 120 Hz, 1.36 mF cm^{-2}). On the other hand, a 2.5 V rated commercial AECs (KEMET®, A750 series) has a capacitance density of approx. 2 mF cm^{-3}. The capacitance density decreases as $1/V^2$ (where V is the device operation voltage) with bipolar design for ECs, and as 1/V with spiral wound design for AECs [4, 48]. Therefore, the volume advantage of EC over AEC can be kept up to approximately 43 V (Figure S7). AECs rated at 2 V or higher are widely used today for bypass and filtering in portable electronics equipment [4].

It should be noted that efficient line filtering requires -90° phase angle at the switching frequency. The deviation from this ideal value implies losses in the form of heat generation, hence heat dissipation becomes an important issue to be considered. The graphite/VACNTs material has a thermal conductivity over 1600 W m^{-1} K^{-1} (Figure S8), which is an advantage in any application where excess heat has a detrimental impact and makes it possible to use one device for multiple functions in electronics (energy storage / line filtering and heat conduction).

3.3 Low loss storage ECs in miniaturized systems

3.3.1 As primary storage units

As a primary storage unit in miniaturized autonomous systems, ECs are charged up by the current from energy harvesters, the magnitude of which could be as low as µA or even nA [6, 7, 49]. The GCD measurements with a KOH electrolyte at current densities from 0.5 to 5 mA cm^{-2} (Figure 2e) have demonstrated good capacitive behavior, but the application as an energy storage EC in miniaturized IoT systems could still be improved. The concern comes from whether the device exhibits capacitive behavior also at very low currents. ECs are well known for fast charge/discharge and high power capability (i.e. excellent performance at high currents), however, their performance at low currents and low power exchange (µW) can be equally relevant in a miniaturized system. It can be noticed from previous reports that at low scan rates in the CV measurements [10, 42, 43, 45] (Figure S9), there is a clear deviation from a symmetric rectangular curve, which suggests that parasitic Faradaic reactions could have happened when the system dynamics are slow enough. The Faradaic reactions may originate from oxidizable or reducible impurities in the system (e.g. trace quantities of transition metals, Fe catalyst in this study, absorbed oxygen and functional groups in carbon materials), which contributes species for shuttling in both directions upon charging/discharging [50]. Correspondingly, the self-discharge (leakage current) is enhanced. If the leakage current is comparable to the working current, the ECs cannot be charged effectively. Therefore, Faradaic reactions are detrimental for charge storage in low power systems and should be minimized.

Faradaic processes, especially those caused by impurities, in an electrical double layer capacitor are governed by diffusion kinetics [50]. At low scan rates in CV measurements and low current densities in GCD measurement, the energy contribution from Faradaic reactions becomes predominant over the electrostatic storage. In contrast, the effect from Faradaic processes at high scan rates and high current densities is insignificant due to kinetic limitations. Accordingly, a viable strategy to limit Faradaic effects at low current conditions would be to slow down the kinetics further. Recently, M. Xia et al. [40] validated the suppression of diffusion and Faradaic processes that lead to self-discharge by taking advantage of electrorheological effect of liquid crystals. Here, we demonstrate that the suppression may also be achieved simply by using gel electrolytes. The kinetics of capacitive processes will unfortunately be compromised using this approach. Nevertheless, significant benefits can be gained in cycling stability, packaging capability and, most importantly, the incorporation of a gel (non-liquid) electrolyte enables improved compatibility with low power ASICs (application specific integrated circuits) and IoT systems.

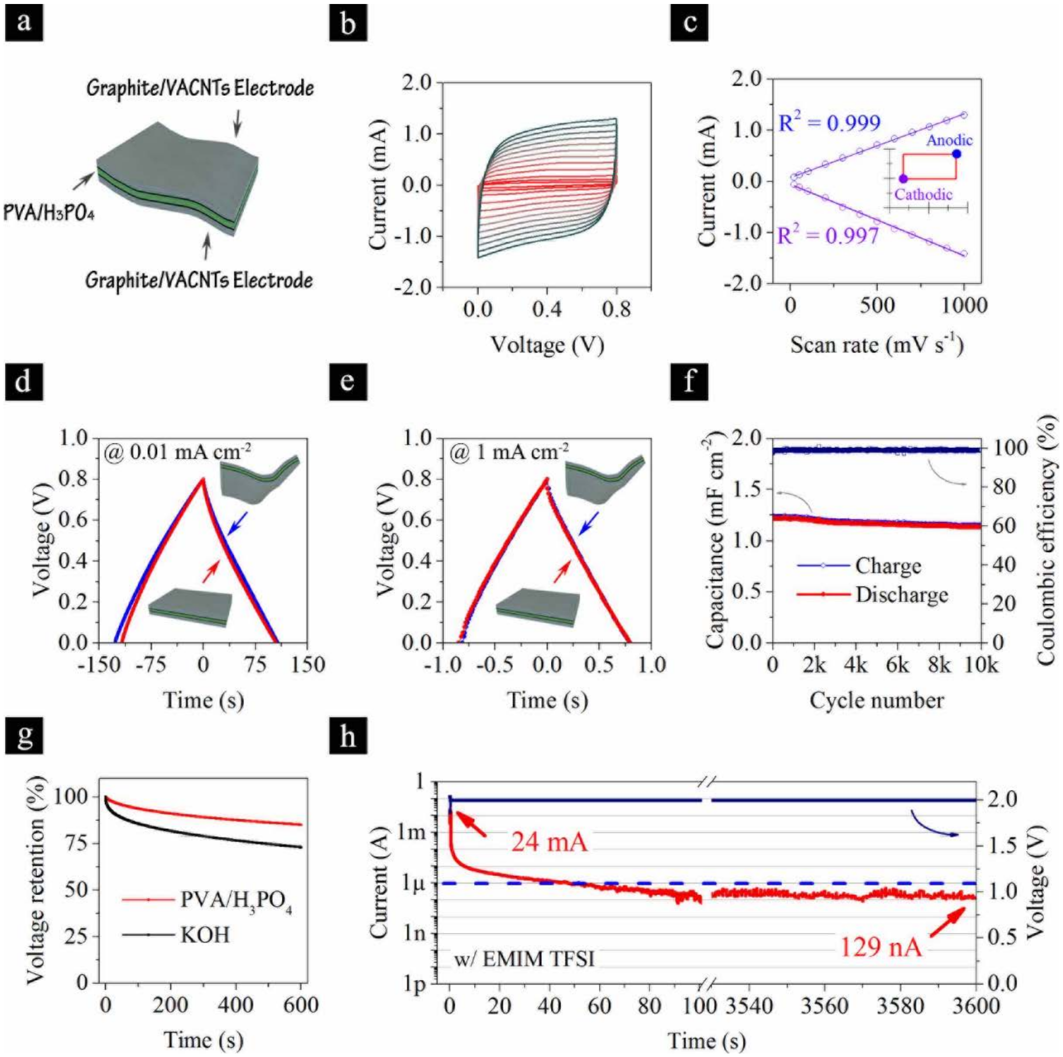

Figure 4. a) Schematic presentation of the solid-state EC. b) CV from 20 to 1000 mV s^{-1}. c) Anodic and cathodic current versus scan rates. d – e) Comparison of GCD curves between original and bent states at a current density of 0.01 mA cm^{-2} and 1 mA cm^{-2} respectively. f) Cycling stability at a current density of 0.1 mA cm^{-2}. g) Comparison of self-discharge with gel and liquid electrolyte. h) Leakage current at 2.0 V with an EMIM TFSI electrolyte.

A common PVA/H_3PO_4 gel electrolyte was used for the following demonstration, and a solid-state device was constructed as shown in Figure 4a. The device has a thickness of around 60 µm and was directly clamped to the potentiostat probes without adding a further current collector. CV scans from 20 to 1000 mV s^{-1} exhibit quasi-rectangular shapes, indicating the dominance of double layer capacitive behavior. The dominance is further evidenced by the linear fitting of the cathodic and anodic current as a function of scan rates that yield R^2 values of 0.999 and 0.997, respectively (Figure 4c). As expected, the device could be charged at a very low current density of 0.01 mA cm^{-2}, corresponding to 5 µA at a footprint of 0.5 cm^2, and capacitive behavior is well retained yielding an areal capacitance of 1.3 mF cm^{-2}. A flexibility measurement was also performed by bending the solid state device to 90° 100 times, and the performance was compared in bent and unbent states (Figure 4c-d), and no significant change was observed at either current density of 0.01 mA cm^{-1} or 1 mA cm^{-1} respectively. The durability of the device is further examined by repeating charging/discharging at 0.1 mA cm^{-2} for 10000 cycles, which resulted in a capacitance retention of 92%.

Further, the self-discharge behavior is compared to that of a KOH electrolyte (Figure 4i). The resulting self-discharge and leakage current of an EC depends on several factors including device dimension, type of separator and encapsulation method. For a fair comparison, a PVA/H_3PO_4 device was fabricated with 2 pieces of 0.5 cm^2 electrodes and a glass fiber separator in a Swagelok setup, which are the same as a KOH device except for the use of a gel electrolyte. As displayed in Figure 4i, 85% of initial voltage was retained after 10 minutes open circuit for the PVA/H_3PO_4 device, 12% higher than that with a KOH electrolyte. Accordingly, the rate of voltage change after 5 minutes is slower (1.1 mV s^{-1} versus 1.6 mV s^{-1} with KOH). In another comparison (Figure S10), mathematical analyses suggest that the self-discharge mechanism could have been altered by using a different electrolyte. For the gel electrolyte, the self-discharge curve can be fairly well fitted with a governing equation derived from Fick's law, i.e. voltage decays linearly with square root of elapsed time ($time^{1/2}$), suggesting that the self-discharge may mainly originate from diffusion controlled processes while ohmic or Faradaic processes contribute little. On the other hand, the curve of the device with a KOH electrolyte cannot well match any single mechanism, indicating its self-discharge is governed by multiple processes. A thermodynamic driving force for self-discharge exists in a charged EC because the free energy at the charged state is significantly higher than in the discharged state [50]. Therefore, it is impossible to eliminate self-discharge for a realistic device, but one can mitigate it by slowing down the kinetics of the relating processes. The results presented above demonstrate the possibility of achieving slower self-discharge / lower leakage current and capacitive behavior at extremely low current through the kinetics restriction in the electrolytes. However, it should be noted that the effectiveness of using a gel electrolyte for reducing self-discharge in *porous* structures may require special attention to device fabrication, especially to ensure the penetration of gel electrolyte into the porous matrix.

3.3.2 As buffer capacitors

Except for being a primary storage unit in micro systems, another type of function of ECs is to buffer the energy source when peak power exceeds the limits of primary energy source [5, 51]. IoT applications usually use low power energy source (e.g. energy harvester with a small battery), but need to support peak power loads for the purpose of RF transmissions, data acquisition, storage and micro-controller start-up, etc. The peak power (current) can be significantly higher than that a battery can handle. In this case, ECs are used in couple with the battery. The voltage of ECs are held at the value of the battery during sleeping mode, and a pulse high current is withdrawn from ECs during active mode (for e.g. data transmission), so that the lifetime of battery is prolonged. For such applications, it is important that ECs should be of low leakage current at a specified voltage, in order to reduce the energy loss during the sleeping mode of a sensor network. A graphite/VACNTs based EC with an EMIM TFSI electrolyte was fabricated to examine the leakage property and its dynamics. The device was held at 2 V for one hour and the leakage current was recorded. As displayed in Figure 4h, with a step voltage from 0 to 2 V, a current of 24 mA was withdrawn in the beginning for the 2 mF device. The huge initial current indicates a small resistance and a strong ability of working in pulse mode (high power intake/delivery). After the initial stage, the current dropped exponentially from mA to sub-μA within only 50 seconds, and then stabilized rapidly to 100-200 nA (the recorded value at the end of voltage holding is 129 nA) after approximate 100 seconds. Note that the initial leakage current, and hence energy loss, would be significantly reduced when applying a shallow voltage step (e.g. from 1.8 to 2 V) which is common in practical applications. The fast dynamics of leakage current stabilization is highly preferred for minimizing energy loss. The 100 seconds record for the 2 mF device reaching a stabilized 100 nA level leakage current (5 magnitudes reduction from initial value 24 mA) is remarkable compared to traditional electrochemical capacitors that may take tens of minutes or even several hours [52, 53], and superior to a 1 mF rGO based micro device of which the leakage current at 2.5 V decreases from ca. 30 μA to 300 nA in 10-20 minutes, and further below 200 nA after about 2 hours [39].

4. Conclusions

In summary, we have demonstrated a graphite/VACNTs hybrid as an electrode material for ECs targeted at line-filtering and energy storage units for miniaturized systems. Combining with a suitable electrolyte, the graphite/VACNTs based ECs exhibit superior performance for different type of function. An excellent frequency response for AC line-filtering has been obtained with a 6 M KOH liquid electrolyte, exhibiting both state-of-art device level areal capacitance (1.38 mF cm^{-2}) and volumetric capacitance (345 mF cm^{-3}) at 120 Hz, with phase angle of -84.82°. For the applications as energy storage in miniaturized systems, ECs employing a gel electrolyte is demonstrated for µA current charging and slow self-discharge (compared to a 6 M KOH liquid electrolyte) as primary storage units; The graphite/VACNTs based EC also exhibits fast dynamics during voltage holding, manifested by an example of a device containing EMIM TFSI electrolyte, of which a sub-µA leakage current could be obtained within only 50 seconds, and 100 nA level stabilized leakage after 100 seconds at a voltage step from 0 to 2 V, thus being a suitable buffer capacitor for supporting peak power loads. We believe that the excellent performance of the devices originates from a near optimal electrical contact between its constituting components including a covalent bonding between graphite and VACNTs. This work with emphases on application specified performance assessments should provide hints for the development and evaluation of electrochemical capacitors for miniaturized systems.

5. Acknowledgements

This work was supported by the EU Horizon 2020 research and innovation program Smart-MEMPHIS project with the contract No: 644378, the Vinnova UDI project Energy Harvesting Toolkit and Swedish Energy Agency. S, Sun, Y. Fu and J. Liu thank for the financial support from the Swedish Foundation for Strategic Research (SSF) under contract (Nos SE13-0061, GMT14-0045) and from the Production Area of Advance at Chalmers University of Technology, Sweden and EU Horizon 2020 project "Smartherm". S. Sun and J. Liu acknowledges the financial support by the Key R&D Development Program from the Ministry of Science and Technology of China with the contract No: 2017YFB040600 and Shanghai Municipal Education Commission (Shanghai University High Education Peak Discipline Program).

6. References

[1] P. Simon, Y. Gogotsi, Materials for electrochemical capacitors, Nat. Mater., 7 (2008) 845-854.
[2] R.R. Salunkhe, Y.H. Lee, K.H. Chang, J.M. Li, P. Simon, J. Tang, N.L. Torad, C.C. Hu, Y. Yamauchi, Nanoarchitectured graphene-based supercapacitors for next-generation energy-storage applications, Chemistry (Easton), 20 (2014) 13838-13852.
[3] A. Lahyani, P. Venet, A. Guermazi, A. Troudi, Battery/supercapacitors combination in uninterruptible power supply (ups), Ieee Transactions on Power Electronics, 28 (2013) 1509-1522.
[4] J.R. Miller, R.A. Outlaw, B.C. Holloway, Graphene double-layer capacitor with ac line-filtering performance, Science, 329 (2010) 1637-1639.
[5] S. Sudevalayam, P. Kulkarni, Energy harvesting sensor nodes: Survey and implications, Ieee Commun Surv Tut, 13 (2011) 443-461.
[6] H. Guo, M.H. Yeh, Y.C. Lai, Y. Zi, C. Wu, Z. Wen, C. Hu, Z.L. Wang, All-in-one shape-adaptive self-charging power package for wearable electronics, ACS Nano, 10 (2016) 10580-10588.
[7] H. Guo, M.H. Yeh, Y. Zi, Z. Wen, J. Chen, G. Liu, C. Hu, Z.L. Wang, Ultralight cut-paper-based self-charging power unit for self-powered portable electronic and medical systems, ACS Nano, 11 (2017) 4475-4482.
[8] N. Islam, S.Q. Li, G.F. Ren, Y.J. Zu, J. Warzywoda, S. Wang, Z.Y. Fan, High-frequency electrochemical capacitors based on plasma pyrolyzed bacterial cellulose aerogel for current ripple filtering and pulse energy storage, Nano Energy, 40 (2017) 107-114.
[9] S. Fletcher, V.J. Black, I. Kirkpatrick, A universal equivalent circuit for carbon-based supercapacitors, J. Solid State Electrochem., 18 (2013) 1377-1387.
[10] Z.S. Wu, Y.Z. Tan, S. Zheng, S. Wang, K. Parvez, J. Qin, X. Shi, C. Sun, X. Bao, X. Feng, K. Mullen, Bottom-up fabrication of sulfur-doped graphene films derived from sulfur-annulated nanographene for ultrahigh volumetric capacitance micro-supercapacitors, J. Am. Chem. Soc., 139 (2017) 4506-4512.
[11] J.P. Randin, E. Yeager, Differential capacitance study of stress‐annealed pyrolytic graphite electrodes, J. Electrochem. Soc., 118 (1971) 711-714.
[12] Y. Gogotsi, P. Simon, Materials science. True performance metrics in electrochemical energy storage, Science, 334 (2011) 917-918.

[13] Y. Rangom, X.S. Tang, L.F. Nazar, Carbon nanotube-based supercapacitors with excellent ac line filtering and rate capability via improved interfacial impedance, ACS Nano, 9 (2015) 7248-7255.

[14] Y. Yoo, S. Kim, B. Kim, W. Kim, 2.5 V compact supercapacitors based on ultrathin carbon nanotube films for AC line filtering, J. Mater. Chem. A, 3 (2015) 11801-11806.

[15] K.U. Laszczyk, K. Kobashi, S. Sakurai, A. Sekiguchi, D.N. Futaba, T. Yamada, K. Hata, Lithographically integrated microsupercapacitors for compact, high performance, and designable energy circuits, Adv. Energy Mat., 5 (2015) 1500741.

[16] Y. Zhu, L. Li, C. Zhang, G. Casillas, Z. Sun, Z. Yan, G. Ruan, Z. Peng, A.R. Raji, C. Kittrell, R.H. Hauge, J.M. Tour, A seamless three-dimensional carbon nanotube graphene hybrid material, Nat. Commun., 3 (2012) 1225.

[17] I.B. Dogru, M.B. Durukan, O. Turel, H.E. Unalan, Flexible supercapacitor electrodes with vertically aligned carbon nanotubes grown on aluminum foils, Prog. Nat. Sci.-Mater., 26 (2016) 232-236.

[18] A. Ghosh, V.T. Le, J.J. Bae, Y.H. Lee, Tlm-psd model for optimization of energy and power density of vertically aligned carbon nanotube supercapacitor, Sci. Rep., 3 (2013) 2939.

[19] J. Wojciechowski, L. Kolanowski, A. Bund, G. Lota, The influence of current collector corrosion on the performance of electrochemical capacitors, J. Power Sources, 368 (2017) 18-29.

[20] J. Lin, C. Zhang, Z. Yan, Y. Zhu, Z. Peng, R.H. Hauge, D. Natelson, J.M. Tour, 3-dimensional graphene carbon nanotube carpet-based microsupercapacitors with high electrochemical performance, Nano Lett., 13 (2013) 72-78.

[21] W. Gao, N. Singh, L. Song, Z. Liu, A.L. Reddy, L. Ci, R. Vajtai, Q. Zhang, B. Wei, P.M. Ajayan, Direct laser writing of micro-supercapacitors on hydrated graphite oxide films, Nat. Nanotechnol., 6 (2011) 496-500.

[22] P.L. Taberna, P. Simon, J.F. Fauvarque, Electrochemical characteristics and impedance spectroscopy studies of carbon-carbon supercapacitors, J. Electrochem. Soc., 150 (2003) A292-A300.

[23] C.L. Pint, N.T. Alvarez, R.H. Hauge, Odako growth of dense arrays of single-walled carbon nanotubes attached to carbon surfaces, Nano Research, 2 (2010) 526-534.

[24] K.S. Ahn, J.S. Kim, C.O. Kim, J.P. Hong, Non-reactive rf treatment of multiwall carbon nanotube with inert argon plasma for enhanced field emission, Carbon, 41 (2003) 2481-2485.

[25] A. Felten, C. Bittencourt, J.J. Pireaux, G. Van Lier, J.C. Charlier, Radio-frequency plasma functionalization of carbon nanotubes surface o_2, nh_3, and cf_4 treatments, J. Appl. Phys., 98 (2005) 074308.

[26] H. Ago, T. Kugler, F. Cacialli, W.R. Salaneck, M.S.P. Shaffer, A.H. Windle, R.H. Friend, Work functions and surface functional groups of multiwall carbon nanotubes, J. Phys. Chem. B, 103 (1999) 8116-8121.

[27] S. Kundu, Y.M. Wang, W. Xia, M. Muhler, Thermal stability and reducibility of oxygen-containing functional groups on multiwalled carbon nanotube surfaces: A quantitative high-resolution xps and tpd/tpr study, J. Phys. Chem. C, 112 (2008) 16869-16878.

[28] A.O. Lobo, F.R. Marciano, I. Regiani, S.C. Ramos, J.T. Matsushima, E.J. Corat, Proposed model for growth preference of plate-like nanohydroxyapatite crystals on superhydrophilic vertically aligned carbon nanotubes by electrodeposition, Theor. Chem. Acc., 130 (2011) 1071-1082.

[29] T.I.T. Okpalugo, P. Papakonstantinou, H. Murphy, J. McLaughlin, N.M.D. Brown, High resolution xps characterization of chemical functionalised mwcnts and swcnts, Carbon, 43 (2005) 153-161.

[30] Q. Li, G.S. Li, C.C. Fu, D. Luo, J.M. Fan, J. Zheng, D.J. Xie, L.P. Li, A study on storage characteristics of pristine li-rich layered oxide $li_{1.20}mn_{0.54}co_{0.13}ni_{0.13}o_2$: Effect of storage temperature and duration, Electrochim. Acta, 154 (2015) 249-258.

[31] D. Puthusseri, D.J. Babu, S. Okeil, J.J. Schneider, Gas adsorption capacity in an all carbon nanomaterial composed of carbon nanohorns and vertically aligned carbon nanotubes, Phys. Chem. Chem. Phys., 19 (2017) 26265-26271.

[32] M.S. Dresselhaus, A. Jorio, M. Hofmann, G. Dresselhaus, R. Saito, Perspectives on carbon nanotubes and graphene raman spectroscopy, Nano Lett., 10 (2010) 751-758.

[33] Z. Wei, R. Pan, Y. Hou, Y. Yang, Y. Liu, Graphene-supported pd catalyst for highly selective hydrogenation of resorcinol to 1, 3-cyclohexanedione through giant pi-conjugate interactions, Sci. Rep., 5 (2015) 15664.
[34] C.S. Yung, N.A. Tomlin, K. Heuerman, M.W. Keller, M.G. White, M. Stephens, J.H. Lehman, Plasma modification of vertically aligned carbon nanotubes: Superhydrophobic surfaces with ultra-low reflectance, Carbon, 127 (2018) 195-201.
[35] A.I. Lopez-Lorente, B.M. Simonet, M. Valcarcel, Raman spectroscopic characterization of single walled carbon nanotubes: Influence of the sample aggregation state, Analyst, 139 (2014) 290-298.
[36] L. Jiao, L. Zhang, X. Wang, G. Diankov, H. Dai, Narrow graphene nanoribbons from carbon nanotubes, Nature, 458 (2009) 877-880.
[37] Y.H. Yan, M.B. Chan-Park, Q. Zhou, C.M. Li, C.Y. Yue, Functionalization of carbon nanotubes by argon plasma-assisted ultraviolet grafting, Appl. Phys. Lett., 87 (2005) 213101.
[38] A. Kajdos, A. Kvit, F. Jones, J. Jagiello, G. Yushin, Tailoring the pore alignment for rapid ion transport in microporous carbons, J. Am. Chem. Soc., 132 (2010) 3252-3253.
[39] M.F. El-Kady, R.B. Kaner, Scalable fabrication of high-power graphene micro-supercapacitors for flexible and on-chip energy storage, Nat. Commun., 4 (2013) 1475.
[40] M.Y. Xia, J.H. Nie, Z.L. Zhang, X.M. Lu, Z.L. Wang, Suppressing self-discharge of supercapacitors via electrorheological effect of liquid crystals, Nano Energy, 47 (2018) 43-50.
[41] Y. Yoo, J. Park, M.-S. Kim, W. Kim, Development of 2.8 V ketjen black supercapacitors with high rate capabilities for AC line filtering, J. Power Sources, 360 (2017) 383-390.
[42] Q. Zhou, M. Zhang, J. Chen, J.D. Hong, G. Shi, Nitrogen-doped holey graphene film-based ultrafast electrochemical capacitors, ACS Appl. Mater. Interfaces, 8 (2016) 20741-20747.
[43] G.F. Ren, X. Pan, S. Bayne, Z.Y. Fan, Kilohertz ultrafast electrochemical supercapacitors based on perpendicularly-oriented graphene grown inside of nickel foam, Carbon, 71 (2014) 94-101.
[44] Y. Yoo, M.S. Kim, J.K. Kim, Y.S. Kim, W. Kim, Fast-response supercapacitors with graphitic ordered mesoporous carbons and carbon nanotubes for AC line filtering, J. Mater. Chem. A, 4 (2016) 5062-5068.
[45] G.F. Ren, S.Q. Li, Z.X. Fan, M.N.F. Hogue, Z.Y. Fan, Ultrahigh-rate supercapacitors with large capacitance based on edge oriented graphene coated carbonized cellulous paper as flexible freestanding electrodes, J. Power Sources, 325 (2016) 152-160.
[46] M. Cai, R.A. Outlaw, R.A. Quinlan, D. Premathilake, S.M. Butler, J.R. Miller, Fast response, vertically oriented graphene nanosheet electric double layer capacitors synthesized from c_2h_2, ACS Nano, 8 (2014) 5873-5882.
[47] K. Sheng, Y. Sun, C. Li, W. Yuan, G. Shi, Ultrahigh-rate supercapacitors based on eletrochemically reduced graphene oxide for ac line-filtering, Sci. Rep., 2 (2012) 247.
[48] J.R. Miller, R.A. Outlaw, B.C. Holloway, Graphene electric double layer capacitor with ultra-high-power performance, Electrochim. Acta, 56 (2011) 10443-10449.
[49] Y. Wang, Y. Yang, Z.L. Wang, Triboelectric nanogenerators as flexible power sources, npj Flexible Electronics, 1 (2017) 10.
[50] B.E. Conway, Electrochemical supercapacitors: Scientific fundamentals and technological applications, first ed., Springer Science & Business Media, New York, 2013.
[51] X. Jiang, J. Polastre, D. Culler, Perpetual environmentally powered sensor networks, Proceedings of the 4th international symposium on information processing in sensor networks, (2005) 65-70.
[52] K. Fic, G. Lota, M. Meller, E. Frackowiak, Novel insight into neutral medium as electrolyte for high-voltage supercapacitors, Energy Environ. Sci., 5 (2012) 5842-5850.
[53] R. Kotz, P.W. Ruch, D. Cericola, Aging and failure mode of electrochemical double layer capacitors during accelerated constant load tests, J. Power Sources, 195 (2010) 923-928.

Supporting Information

Compact and low loss electrochemical capacitors using a graphite / carbon nanotube hybrid material for miniaturized systems

Qi Li[1][+], Shuangxi Sun[1, 2, 3][+], Anderson D. Smith[1], Per Lundgren[1], Yifeng Fu[1],
Peng Su[1], Tao Xu[4], Lilei Ye[5], Litao Sun[4], Johan Liu[1, 2*], Peter Enoksson[1*]
[1] Electronics Materials and Systems Laboratory, Department of Microtechnology and Nanoscience,
Chalmers University of Technology, SE - 412 96 Gothenburg, Sweden
[2] SMIT Center, School of Mechanical Engineering and Automation, Shanghai University, 201800
Shanghai, P. R. China
[3] Fingerprint Cards AB, Kungsgatan 20, SE - 411 19 Gothenburg, Sweden
[4] SEU-FEI Nano-Pico Center, Key Lab of MEMS of Ministry of Education, Southeast University, 210096
Nanjing, P. R. China
[5] SHT Smart High Tech AB, SE - 411 33 Gothenburg, Sweden
*Email: johan.liu@chalmers.se; peter.enoksson@chalmers.se
[+] These authors contributed equally

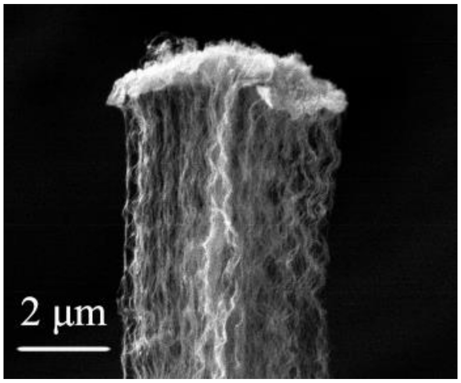

Figure S1. SEM image showing the Fe/Al_2O_3 layer residing at the tip of VACNTs

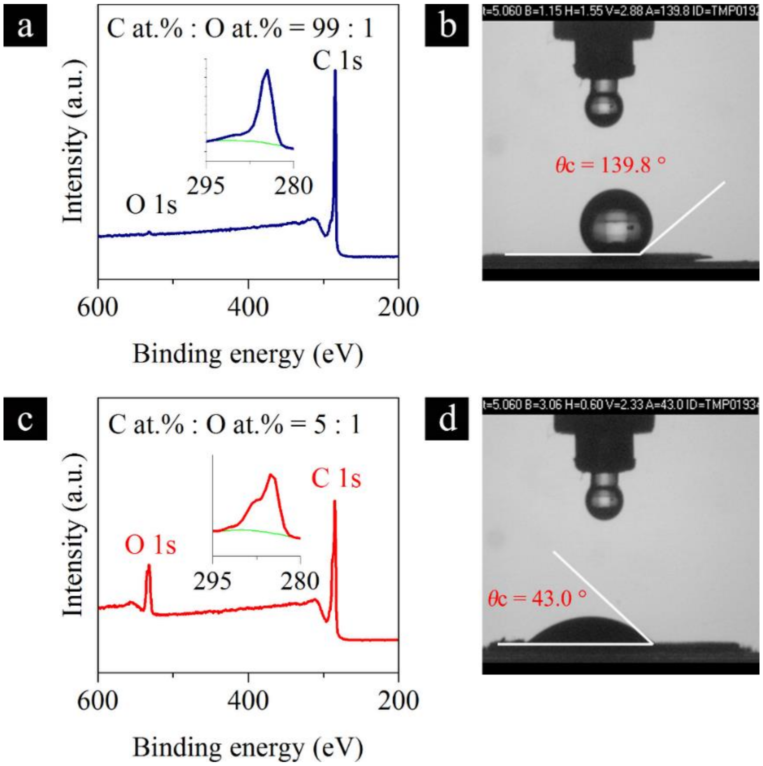

Figure S2. XPS survey spectrum and contact angle of the graphite/VACNTs a-b) before plasma treatment and c-d) after plasma treatment.

Table S1. XPS C1s core level curve fit summary. | Samples were analyzed by XPS employing a PHI 5000 Versa Probe system equipped with a monochromatic Al Kα X-ray source. Spectra were analyzed by MultiPak software. Spectra were calibrated setting the graphitic carbon to 284.8 eV. The CASA XPS program with a Gaussian-Lorentzian mix function (maximum 20% Lorentzian contribution) and Shirley background subtraction was employed to deconvolute the spectrum. For detailed analysis of the C1s spectrum, the components and restrictions summarized in Table 1 were employed. FWHM were restricted below 2.0 eV for all other components except for shake-ups.

Band	**Assigned to**	**Position**	**FWHM**	**%Gauss**	**%Area**	**χ^2**
1	Graphitic carbon	284.8	1.63	81	54.5	20.19
2	C-O	286.3	1.41	80	10.81	
3	C=O	287.8	2	80	15.35	
4	O-C=O	288.9	1.97	80	14.76	
5	π- π* shake-up	291.5	2.41	80	4.59	

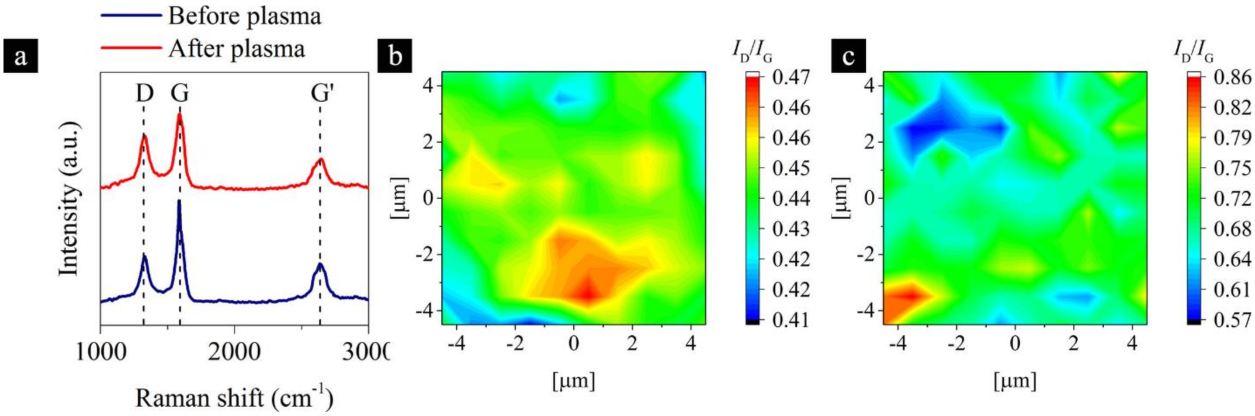

Figure S3. a) Representative Raman spectra of the graphite/VACNTs before and after plasma treatment. b) Raman mapping in a 10 × 10 μm^2 area of the material before plasma treatment. c) Raman mapping in a 10 × 10 μm^2 area of the material after plasma treatment.

Table S2 Frequency response of graphite/VACNTs with different CNT length. | By controlling the growth time during the CVD step, the length of VACNTs on the graphite substrate can be manipulated. The electrochemical characterization found that the frequency response performance shows little decrease with the increase of CNT length by 2 times, with cut-off frequency dropping from 2430 Hz to 1980 Hz. In contrast, areal capacitance at 120 Hz increased by 1.8 times, and volumetric capacitance remained around 360 mF cm^{-3}. The results suggest a semi linear capacitance increase as a function of CNT length, while frequency response is almost independent of CNT length.

VACNT length (μm)	Growth time (min)	$\phi_{120\ Hz}$ (°)	f_0 (Hz)	$C_{A,\ 120\ Hz}$ (mF cm^{-2})	$C_{V,\ 120\ Hz}$ (mF cm^{-3})
~ 40	5 min	-84.82	1980	1.38	345
~ 35	3 min	-83.95	2100	1.28	365
~ 20	0.5 min	-84.69	2430	0.76	380

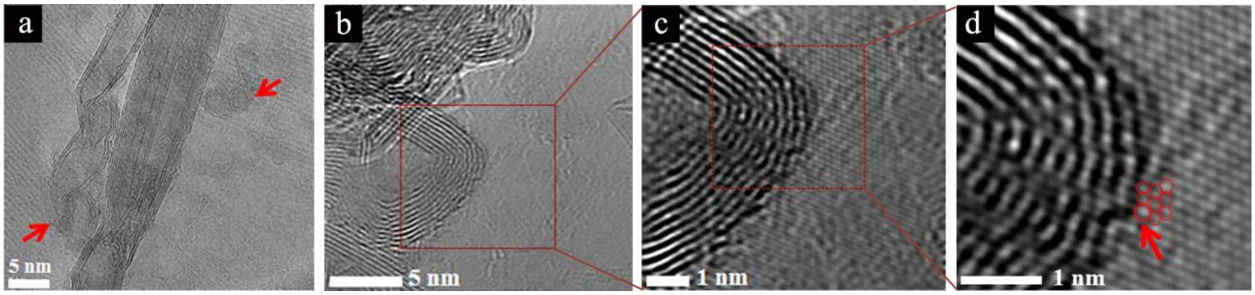

Figure S4. a) TEM images showing ring-like structures existing in the system. b-d) An inner ring-like shell at different magnifications. | The atomic scale nanostructure was examined by TEM and STEM (Figure S4) where the multiwall structure of the carbon nanotubes was clearly observed with a diameter range of 5-10 nm. Moreover, ring-like structures can be observed in Figure S4a, which are absent in VACNTs grown on Si. An inner ring-like shell positioned inside the VACNTs shells exists in the root region of VACNTs (Figure S4b). According to previous reports [1, 2], these ring-like structures are seen as a typical characteristic of covalent bonds between CNTs and graphene-like structures. STEM images were further captured to analyze the transition part between the VACNTs and the graphite film. As shown in Figure S4c-d, each white dot represents an aromatic ring [1]. The dots appear in an orderly arrangement around the shells of VACNTs. It is regarded as a seamless connection between the VACNT and the graphene-like structure due to the absence of any visible gap or crack at the interface except for some distorted white dots. These distorted white dots existing at the interface could be seven edge rings structure, marked by a red arrow, due to their out-of-plane orientations from the 2D planar graphene structure [3-5].

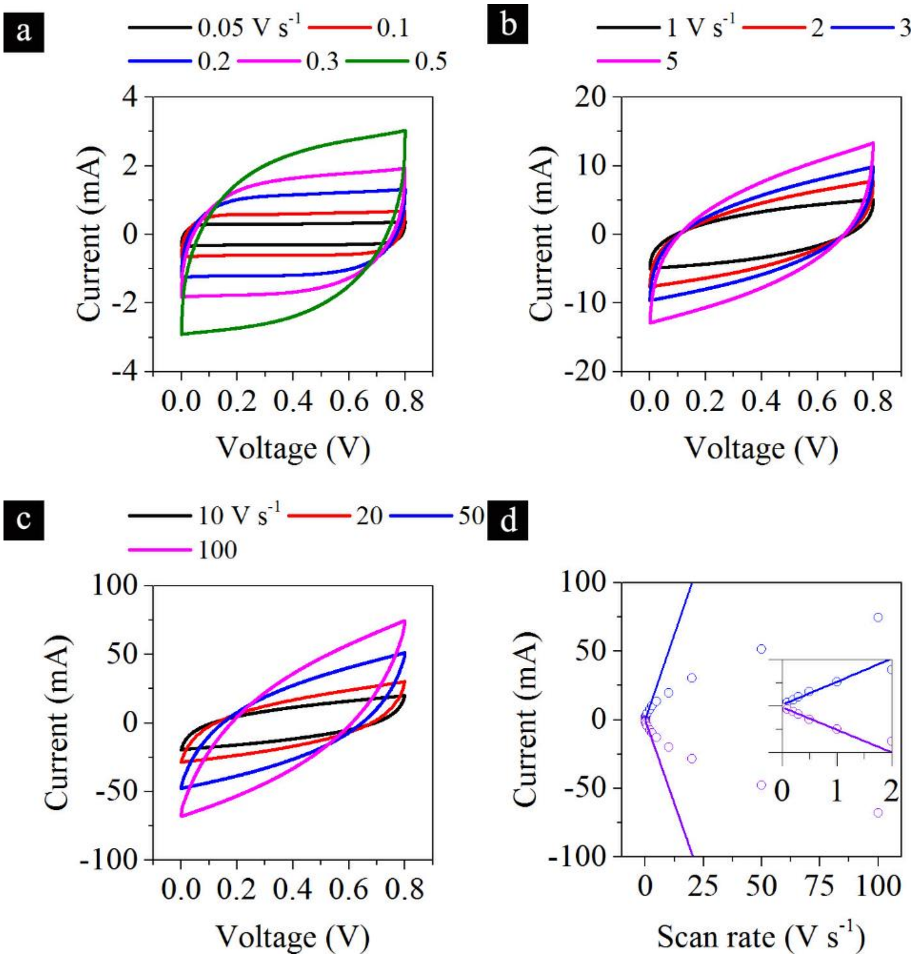

Figure S5. Electrochemical performance of a graphite/VACNTs material based on a laminated graphite film. a-c) CV scans at specified scan rates. d) Anodic and cathodic currents as a function of scan rates. | The current response to scan rate keeps linear until around 1 V s^{-1}. The performance of this material is much inferior to that of the material based on a highly oriented pyrolytic graphite (Figure 2).

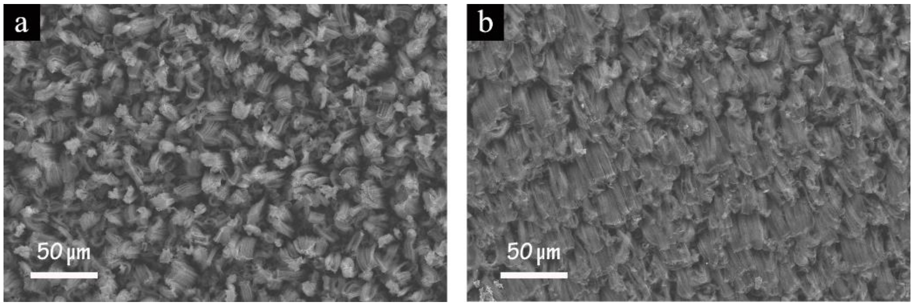

Figure S6. a) SEM image of pristine graphite/VACNTs. b) SEM image of compressed graphite/VACNTs.

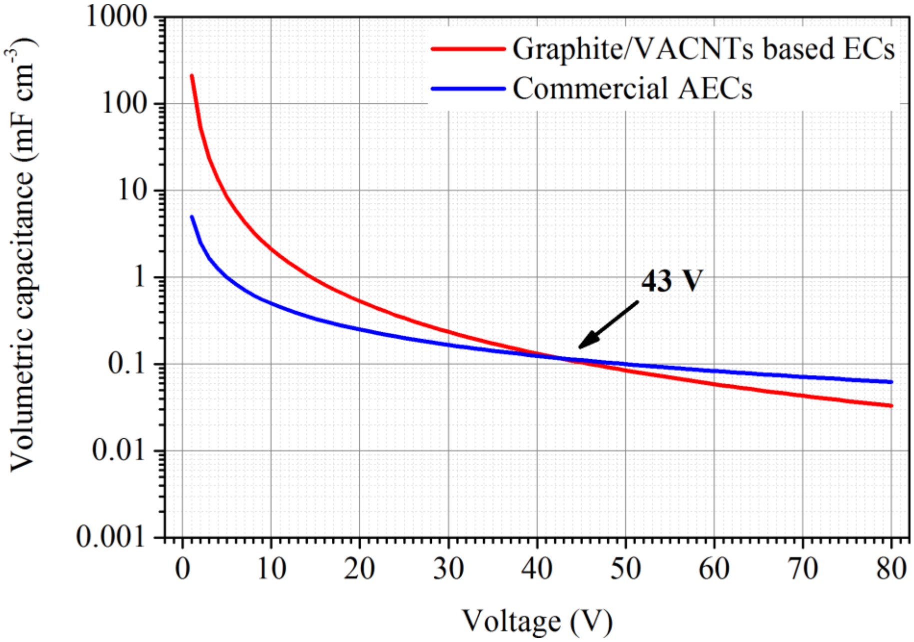

Figure S7. Comparison of volumetric capacitance between graphite/VACNTs based ECs and commercial AECs

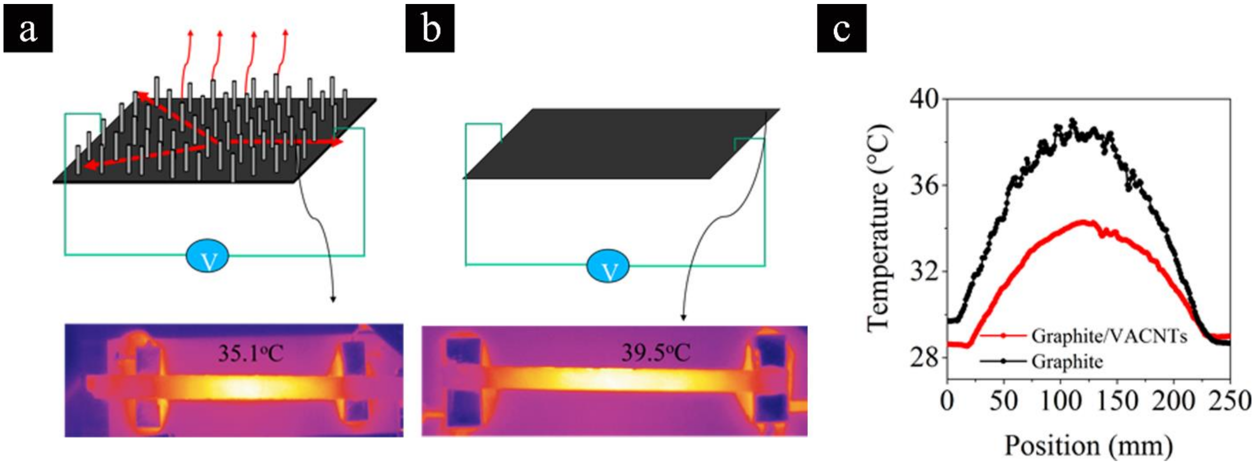

Figure S8. a) and b) Graphite/VACNTs and graphite strips are heated up through joule heating effect after loading the same power. The temperature distribution of the sample was captured by IR camera. c) The temperature distribution curves. | To compare the thermal conductivity of graphite/VACNTs and graphite substrate, so-called through bridge joule heating method was used to measure the temperature distribution of the bridge. The setup structure was shown in Figure S7a-b. The two terminals of the film were attached on the copper bulk by solder paste. Then the film was self-heated up by joule heating through loading current on the both terminals of the bridge. As shown in IR images, the maximum temperate always is located in the middle of bridge where is furthest away the copper cooler. Thus, the middle part would be cooled down in a relatively low efficiency due to extra heat resistance of half bridge long of film. According to the previous report, the difference of temperate between middle part and terminals can be used to deduce the thermal conduction capability of this film. Here the graphite can reach 1600 W m^{-1} K^{-1}, and graphite/VACNTs is even beyond pure graphite. After forming graphite/VACNTs hybrid structure, the maximum temperature decreased from 39.5°C to 35.1°C under the same power. This result indicated that the graphite/VACNTs has an excellent heat dissipation capacity.

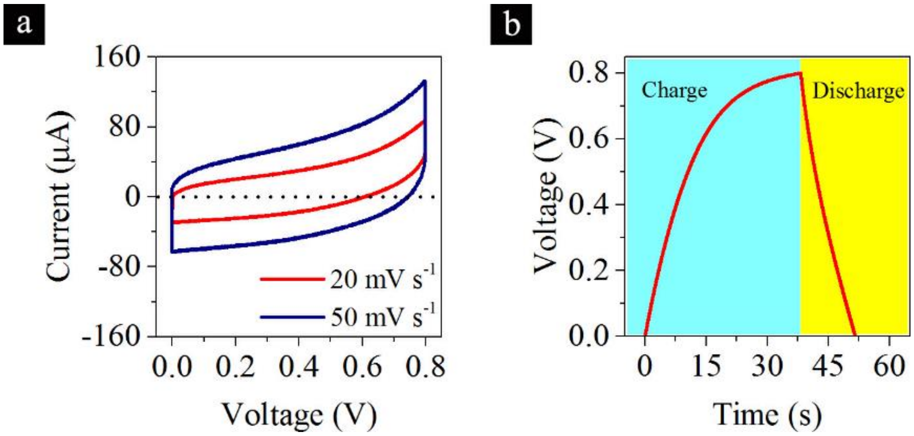

Figure S9. a) CV scans of graphite/VACNTs based EC with a KOH electrolyte at low scan rates. b) Galvanostatic charge/discharge of the same device at a current of 0.01 mA cm^{-2}.

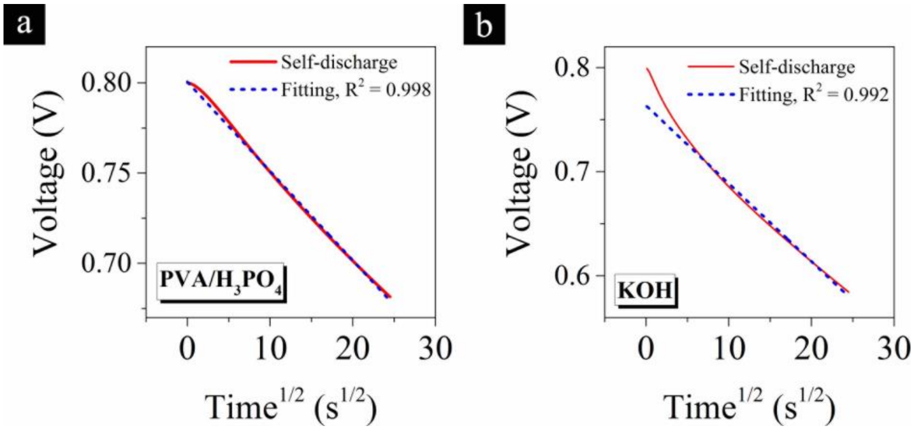

Figure S10. Voltage decline in time, as $t^{1/2}$, for the graphite/VACNTs device using a) PVA/H_3PO_4, b) 6 M KOH electrolyte. | Self-discharge of an EC can be categorized into three mechanisms with different governing equations [6]. (1) For self-discharge by activation-controlled Faradaic reactions, the dynamics is governed by Tafel equation in exponential form, and the voltage decay is in the mathematic form of

$$V = -\frac{RT}{\alpha F}\ln\frac{\alpha F i_0}{RTC} - \frac{RT}{\alpha F}\ln(t + \frac{C\tau}{i_0})$$

where V is the voltage at time t, R is the gas constant, T is the temperature, F is Faradaic constant, α is transfer coefficient, i_0 is the exchange current density, C is the capacitance and τ is an integration constant. Therefore, voltage declines with log t. (2) For self-discharge by an ohmic leakage resistance, the self-discharge can be treated by a parallel RC equivalent circuit, and then the voltage decay is in the mathematic form of

$$\frac{\mathrm{V}}{\mathrm{V}_0} = \exp(-\frac{t}{RC})$$

where V_0 is the initial voltage, R is the leakage resistance. Therefore, $\ln V$ declines with t. (3) For self-discharge by diffusion control, the dynamics of voltage decay is governed by Fick's law and in the mathematic form of

$$C(V_0 - V) = 2zFAD^{1/2}\pi^{1/2}c_0t^{1/2}$$

where A is the area of flux, D is the diffusion coefficient an c_0 is the initial concentration of the diffusive species. Therefore, V declines with $t^{1/2}$. Self-discharge mechanism can be distinguished by fitting the self-discharge curve in above equations.

For the comparison of self-discharge by using gel and liquid electrolyte, the devices were charged to 0.8 V and held for 5 minutes and left open circuit for 10 minutes. The data was treated using the above three equations of different mechanisms. It is found that for the gel electrolyte device, the self-discharge follows the linear trend as $t^{1/2}$, which is assigned to diffusion controlled process. On the other hand, the same treatment cannot produce the same fitting for the aqueous electrolyte. Though the confirmation shall be done by analyzing the individual curve of positive and negative electrodes in the three electrode setup, the brief comparison above indicates the different governing mechanisms by using the two different electrolytes.

References

[1] Y. Zhu, L. Li, C. Zhang, G. Casillas, Z. Sun, Z. Yan, G. Ruan, Z. Peng, A.R. Raji, C. Kittrell, R.H. Hauge, J.M. Tour, A seamless three-dimensional carbon nanotube graphene hybrid material, Nat. Commun., 3 (2012) 1225.

[2] C.-Y. Lin, Z. Zhao, J. Niu, Z. Xia, Synthesis, properties and applications of 3D carbon nanotube–graphene junctions, J. Phys. D: Appl. Phys., 49 (2016) 443001.

[3] F.D. Novaes, R. Rurali, P. Ordejón, Electronic transport between graphene layers covalently connected by carbon nanotubes, ACS nano, 4 (2010) 7596-7602.

[4] V. Varshney, S.S. Patnaik, A.K. Roy, G. Froudakis, B.L. Farmer, Modeling of thermal transport in pillared-graphene architectures, ACS nano, 4 (2010) 1153-1161.

[5] G.K. Dimitrakakis, E. Tylianakis, G.E. Froudakis, Pillared graphene: a new 3-D network nanostructure for enhanced hydrogen storage, Nano Lett., 8 (2008) 3166-3170.

[6] B.E. Conway, Electrochemical supercapacitors: scientific fundamentals and technological applications, first ed., Springer Science & Business Media, New York, 2013, pp. 557-595.